JOURNAL OF RESEARCH

OF THE U.S. GEOLOGICAL SURVEY

MARCH–APRIL 1974
VOLUME 2, NUMBER 2

Scientific notes and summaries of investigations in geology, hydrology, and related fields

U.S. DEPARTMENT OF THE INTERIOR

UNITED STATES DEPARTMENT OF THE INTERIOR
ROGERS C. B. MORTON, Secretary
GEOLOGICAL SURVEY
V. E. McKelvey, Director

For sale by the Superintendent of Documents, U.S. Government Printing Office, Washington, DC 20402. Order by SD Catalog No. JRGS. Annual subscription rate $15.50 (plus $3.75 for foreign mailing). Single copy $2.75. Make checks or money orders payable to the Superintendent of Documents.

Send all subscription inquiries and address changes to the Superintendent of Documents at the above address.

Purchase orders should not be sent to the U.S. Geological Survey library.

Library of Congress Catalog-card No. 72-600241.

The Journal of Research is published every 2 months by the U.S. Geological Survey. It contains papers by members of the Geological Survey and their professional colleagues on geologic, hydrologic, topographic, and other scientific and technical subjects.

Correspondence and inquiries concerning the Journal (other than subscription inquiries and address changes) should be directed to the Journal of Research, Publications Division, U.S. Geological Survey, National Center 321, Reston, VA 22092.

Papers for the Journal should be submitted through regular Division publication channels.

The Secretary of the Interior has determined that the publication of this periodical is necessary in the transaction of the public business required by law of this Department. Use of funds for printing this periodical has been approved by the Director of the Office of Management and Budget through February 11, 1975.

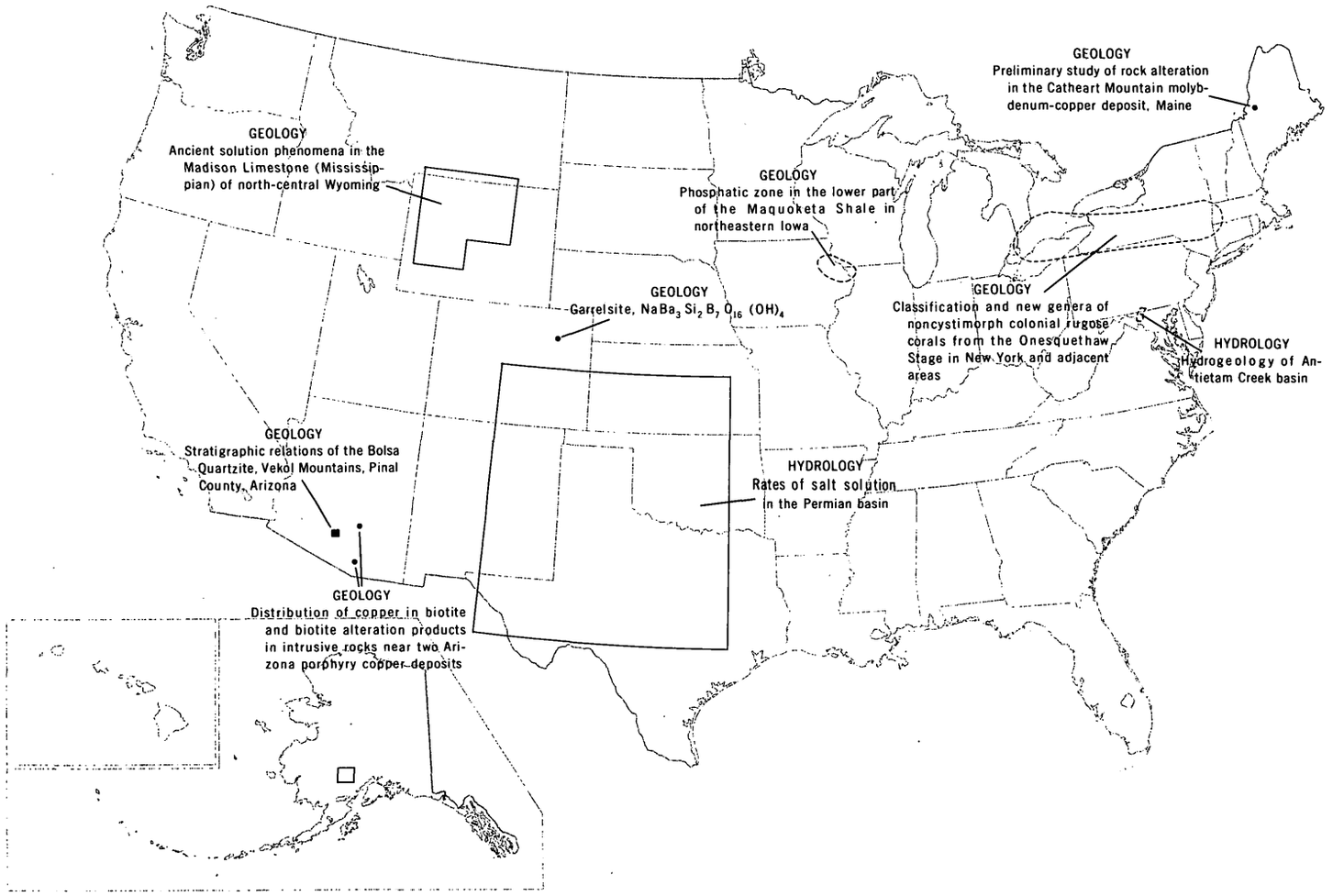

GEOGRAPHIC INDEX TO ARTICLES

See "Contents" for articles concerning areas outside the United States and articles without geographic orientation.

JOURNAL OF RESEARCH

of the

U.S. Geological Survey

Vol. 2 No. 2 Mar.-Apr. 1974

CONTENTS

ABBREVIATIONS

A	ampere
Å	angstrom
abs	absolute
ADP	ammonium dihydrogen phosphate
atm	atmosphere
Btu	British thermal unit
b.y.	billion years
°C	degree Celsius
cal	calorie
C.I.	color index
CIPW	Cross, Iddings, Pirsson, and Washington
cm	centimeter
cm^3	cubic centimeter
d	day
diam	diameter
emf	electromotive force
eu	entropy unit
F.D.&C.	Food, Drug, and Cosmetic [dye]
ft	foot
ft^2	square foot
ft^3	cubic foot
g	gram
γ	activity coefficient
gal	gallon
h	hour
in.	inch
J	joule
K	kelvin
kg	kilogram
km	kilometer
km^2	square kilometer
km^3	cubic kilometer
kV	kilovolt
l	liter
lb	pound
ln	logarithm (natural)
log	logarithm (common)
M	molarity; molar (concentration)
m	meter
m^2	square meter
m^3	cubic meter
m	molality; molal (concentration)
MA	megampere
mA	milliampere
mg	milligram
mGal	milligal
mi	mile
mi^2	square mile
min	minute
ml	milliliter
mm	millimeter
mmol	millimole
mo	month
mol	mole
mV	millivolt
m.y.	million years
µg	microgram
µm	micrometer
nm	nanometer
OD	outside diameter
PDB	Peedee belemnite
pH	measure of hydrogen ion activity
p/m	part per million
s	second
SMOW	standard mean ocean water
V	volt
W	watt
wt	weight
yd^3	cubic yard
yr	year

Jour. Research U.S. Geol. Survey
Vol. 2, No. 2, Mar.-Apr. 1974, p. 133–141

ANCIENT SOLUTION PHENOMENA IN THE MADISON LIMESTONE (MISSISSIPPIAN) OF NORTH-CENTRAL WYOMING

By WILLIAM J. SANDO, Washington, D.C.

Abstract.—A karst topography was developed on the Madison Limestone of north-central Wyoming during the middle Meramecian–early Chesterian time interval. Ancient karst features include enlarged joints, sinkholes, caves, and solution breccias that resulted from leaching of evaporitic beds in the upper 400 ft of the Madison bedrock. These features are predominantly phreatic rather than vadose. Most of the open spaces are filled by sand and residual products reworked by the early Amsden sea, which transgressed the area during the Chesterian.

An ancient karst surface developed on the Madison Limestone and equivalent rocks is a widespread feature in the Rocky Mountain region of the United States (Henbest, 1958, p. 37–38). Study of the Madison Limestone in north-central Wyoming has revealed many solution features related to this ancient karst topography. The purpose of this paper is to describe these solution features and to discuss their origin.

I am grateful to J. T. Hack for his critical examination of ideas expressed herein and to J. T. Dutro, Jr., and Mackenzie Gordon, Jr., for their review of the manuscript. Suggestions by S. S. Oriel, W. W. Mallory, and C. A. Sandberg are also gratefully acknowledged. Mackenzie Gordon, Jr., J. W. Huddle, and I. G. Sohn identified some of the fossils listed in the report.

STRATIGRAPHY

The Madison Limestone includes as much as 1,000 ft of predominantly carbonate strata of Early and Late Mississippian age (Kinderhookian–early Meramecian) in central Wyoming (Craig, 1972, p. 103). Ancient solution features discussed in this report occur in the upper two members of the Madison, which have an aggregate thickness of as much as 360 ft in the area studied. The Bull Ridge Member (Sando, 1968), uppermost of the two, consists of a lower unit of dolomitic siltstone, silty dolomite, and shale (upper solution zone of Sando, 1967a), overlain by limestone and dolomite that contain fossils of early Meramecian age (*Diphyphyllum* Zone of Sando, 1967a). The Bull Ridge may be as much as 120 ft thick. Underlying the Bull Ridge Member is an unnamed member that consists largely of cliff-forming cherty limestone and dolomite of Osagean age (*Spirifer madisonensis* Zone of Sando, 1967a). The lower part of this unnamed member consists of a solution zone made up of limestone and dolomite breccia in siltstone and shale matrix (lower solution zone of Sando, 1967a). The unnamed member ranges in thickness from about 80 to 240 ft.

The Madison is overlain disconformably by the Amsden Formation (Darton, 1904), which includes, in ascending order, the Darwin Sandstone Member (Blackwelder, 1918), the Horseshoe Shale Member (Mallory, 1967), and the Ranchester Limestone Member (Mallory, 1967). The Darwin is unfossiliferous, white to red, fine- to medium-grained, ordinarily crossbedded quartz sandstone of Chesterian age as much as 200 ft thick in the area studied. The overlying Horseshoe Shale Member consists of as much as 150 ft of red siltstone and shale containing sparse, discontinuous, thin beds of fine-grained quartz sandstone and fine-grained limestone. Fossils found in the Horseshoe range from Chesterian to Morrowan in age. The Horseshoe is succeeded by the Ranchester Limestone Member, a variable sequence of cherty dolomite and limestone, red and green shale and siltstone, and sandstone of Morrowan and Atokan age as much as 250 ft thick in the area studied.

Generalized stratigraphic relations of the beds above and below the Madison–Amsden contact and related Madison karst features are shown in figure 1. Great variation in the thicknesses of the Darwin Sandstone Member of the Amsden and the Bull Ridge Member of the Madison are largely dependent on the depth of the erosion surface.

SOLUTION FEATURES

Localities in north-central Wyoming where solution features were observed are shown in figure 2. These features are classified in four principal categories below, and their important characteristics are summarized in table 1.

ENLARGED JOINTS

Description.—Joint passages perpendicular or parallel to bedding of the carbonate strata are common in the upper Madison. These passages range from less than an inch to as much as a foot in width and are filled with red fine- to

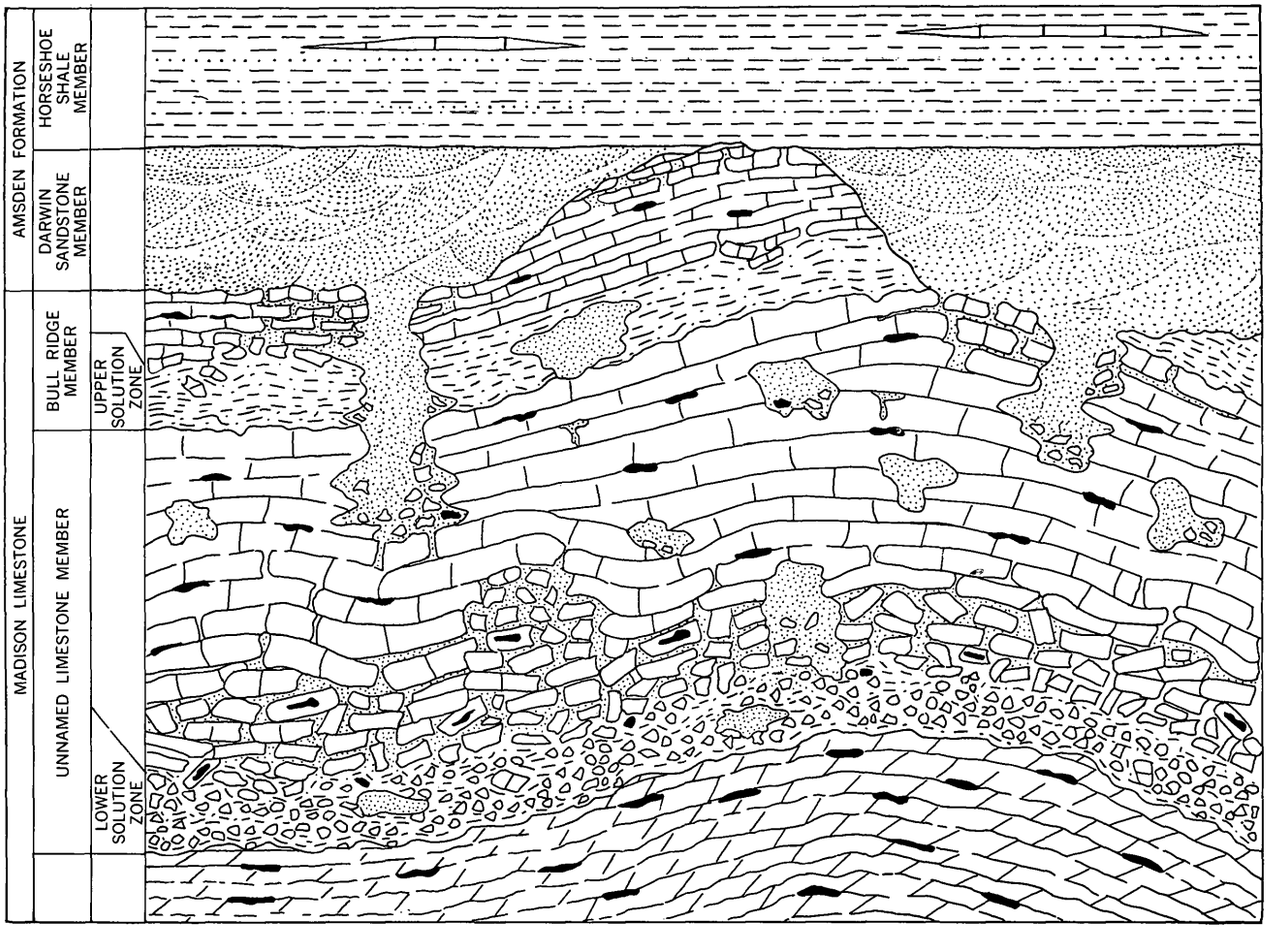

Figure 1.—Generalized sketch of solution features in the upper part of the Madison Limestone in north-central Wyoming.

medium-grained sandstone, siltstone, and shale. Reticulate networks of joint passages are common. Continuity with the post-Madison erosion surface is readily established at most localities. These filled joints are most common in the Bull Ridge Member but may extend considerable distances down into the upper part of the underlying unnamed limestone member of the Madison, particularly at localities such as Brown Spring Draw (table 1), where the Bull Ridge Member is absent. The observed maximum depth of these features below the disconformity ranges from 6 to 93 ft.

Origin.—The joint passages are the result of enlargement of fractures and were formed by meteoric waters that trickled down through the fractured carbonate rocks when the area stood above sea level during post-Madison uplift. Terrigenous fillings of these openings may have been derived partly from insoluble residues of the country rock and residual soil overlying the bedrock surface but are composed mostly of sand that entered during deposition of the overlying Darwin Sandstone Member.

SINKHOLES

Description.—Large cavities with demonstrable continuity with the regional disconformity have been observed at eight localities in north-central Wyoming (table 1). Although the exact shapes and dimensions of these features are difficult to determine because of poor exposures, they appear to be characterized by steep, nearly parallel walls, commonly having reentrants and overhangs. Angular blocks of carbonate rock similar to the adjacent wallrock occur at various levels in the cavities at some localities. Cavity fillings are principally poorly bedded fine- to medium-grained red sandstone and lesser amounts of red shale and siltstone. The sinkholes are found mainly in the Bull Ridge Member and tend to terminate at the base of this unit, but at North Crazy Woman Creek a sinkhole extends down into the underlying unnamed limestone member. The cavities are as much as 50 ft wide at the top and may extend as much as 90 ft below the post-Madison erosion surface.

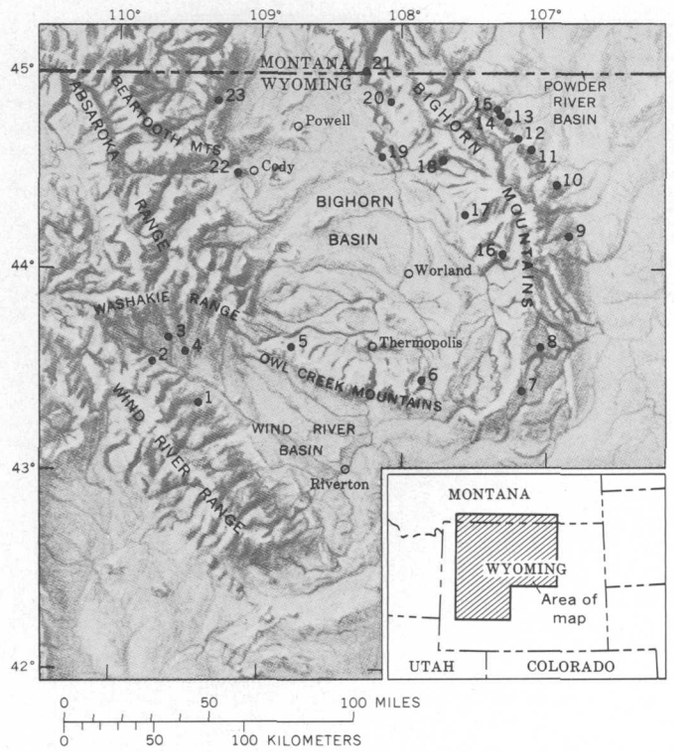

Figure 2.—Localities in Wyoming where Madison solution features were observed. See table 1 for detailed descriptions of the solution features.

Origin.—The sinkholes, like the enlarged joint passages, are clearly features that developed near the bedrock surface during subaerial exposure of the Madison Limestone. Although breccia of carbonate rock occurs in many of these cavities, no evidence of their origin by collapse of the roofs of caves was found. Probably they were formed mainly by intensive solution by meteoric waters along fractures, accompanied by collapse of parts of their walls. The sinkholes were partly filled with residual products of the solution process and breccia from the walls, but the principal fill material is sand deposited during deposition of the overlying Darwin Sandstone Member. The lack of deformational features such as those observed by Bretz (1940) in cavities in the Joliet Limestone seems to rule out post-Darwin origin of the cavities and injection of the fillings.

CAVES

Description.—Irregular-shaped solution cavities, lacking obvious connection to the erosion surface and ranging from less than a foot to tens of feet in maximum observed dimensions, are quite common throughout the Madison Limestone in north-central Wyoming. Many of these are open cavities undoubtedly related to Tertiary and Holocene land surfaces. However, caves are particularly abundant in the Bull Ridge and the unnamed limestone member of the Madison to a depth of 200 to 350 ft below the top of the formation; they are notably less common below this level. A noteworthy feature of many of the caves in the upper part of the Madison is their complete filling by red sandstone, siltstone, and shale (table 1), which suggests a pre-Amsden origin and distinguishes these caves from later ones. Reexcavation of some of the pre-Amsden caves during Tertiary and Holocene time, as suggested by Elliott (1963) in the Pryor Mountains, has obscured the origin of many of the observed features.

The exact geometry and dimensions of the pre-Amsden caves were not determined during this study. They appear on outcrop surfaces (principally in canyon walls) as irregularly shaped cavities without obvious connection or limitation to any narrow stratigraphic interval. Angular blocks of limestone and dolomite derived from the wallrock or roofrock are common, but the filling is predominantly red sandstone. The virtual absence of flowstone and dripstone deposits is particularly noteworthy.

Origin.—The sandstone fillings of the upper Madison caves indicate a pre-Darwin origin for the cavities, followed by an episode of sand accumulation during deposition of the overlying Darwin. Two features suggesting that the caves were excavated below the water table and remained below the vadose zone throughout most of their history are the absence of flowstone and dripstone deposits and the distribution of the caves with respect to the inferred topography of the post-Madison, pre-Amsden erosion surface. According to Davis (1930, p. 525) and Bretz (1956, p. 28–37) dripstone and flowstone are formed when caves are at or above the water table, where percolating carbonate-rich waters or free-flowing streams can deposit their dissolved load in a free-air environment.[1] Moreover, the maximum depth of stream valleys cut into the post-Madison, pre-Amsden land surface is an effective limit to the maximum depth of the vadose zone. Maximum relief is closely approximated by the total thickness of the Darwin Sandstone Member, which is about 200 ft in north-central Wyoming, whereas the deepest caves are about 100 ft below this level, and most of the caves occur below the deepest local base levels of the erosion surface. Undoubtedly, some of the highest caves were in the vadose zone for a short period of time, but even these were filled with sandstone from the Darwin cycle before characteristic vadose features were extensively developed.

[1] J. T. Hack (written commun., 1970) has pointed out that some of the Appalachian caves studied by him are lacking in flowstone and dripstone even though they are in topographic situations similar to other caves in which these features are well developed. He states that the presence of flowstone and dripstone is indicative of a vadose history but the absence of these features does not necessarily rule out a vadose history of the caves.

Table 1.—*Catalog of solution features in the upper part of the Madison Limestone in north-central Wyoming*
[Localities shown in fig. 2. Relief, dimensions, and depths are in feet]

Locality	Geographic location	Maximum local relief at top of Madison exclusive of sinkholes	Sinkholes: dimensions	Sandstone-filled joints: maximum depth below top of Madison	Upper solution zone: maximum depth below top of Madison of sandstone in lenses and matrix of breccia	Lower solution zone: maximum depth below top of Madison and nature of matrix of breccia	Sandstone-filled caves: dimensions and maximum depth below top of Madison
1. Dinwoody Canyon.	S1/2 sec. 1, T. 4 N., R. 6 W., Fremont County.	1	12 wide and 20 deep.	60	Lenses, 69 below top.	Lower solution zone absent.	10 high, 30 wide, and 40 below top; 6 wide, 7 high, and 128 below top.
2. Warm Spring Canyon.	SW1/4 sec. 31, T. 42 N., R. 107 W., Fremont County.	Not measured	None seen	None seen	Matrix of breccia, 75 below top.	272, red siltstone matrix.	Dimensions not measured, 150 below top.
3. Horse Creek.	SW1/4 sec. 19, T. 43 N., R. 106 W., Fremont County.	... do ...	... do ...	... do ...	None seen.....	360, red siltstone matrix.	None seen.
4. Wiggins Fork.	SW1/4 sec. 7, T. 42 N., R 105 W., Fremont County.	1–2	... do ...	61	Lenses, 119 below top.	341, red siltstone matrix.	Do.
5. Red Creek.	NE1/4 sec. 28, T. 8 N., R. 1 E., Hot Springs County.	Not measured	... do ...	25	None seen.....	208, rock flour and siltstone.	10 wide, 18 high, and 74 below top.
6. Brown Spring Draw.	Sec. 35, T. 41 N., R. 92 W., Hot Springs County.	... do ...	... do ...	71	Upper solution zone absent.	153, sandstone matrix.	Several caves 10 or more in diameter, 6–71 below top; one cave at least 90 wide, 60 high, and 138 below top.
7. Middle Buffalo Creek.	NE1/4 sec. 20 and SE1/4 sec. 21, T. 40 N., R. 86 W., Natrona County.	... do ...	30 deep	None seen	... do ...	77, siltstone and sandstone matrix.	None seen.
8. Blue Creek.	SE1/4 sec. 3, T. 42 N., R. 85 W., Johnson County.	5–15	None seen	... do ...	... do ...	182, sandstone and rock flour matrix.	Do.
9. North Crazy Woman Creek.	Secs. 17 and 28, T. 49 N., R. 83 W., Johnson County.	Not measured	25–30 wide and 90 deep.	25	None seen.....	172, sandstone, shale, and siltstone matrix.	Do.
10. South Rock Creek.	SW1/4 sec. 25, T. 52 N., R. 84 W., Johnson County.	... do ...	None seen	48	... do ...	160, shale and siltstone matrix.	20 wide, 12 high, and 48 below top.
11. Tepee Creek.	SE1/4 sec. 28, T. 54 N., R. 85 W., Sheridan County.	... do ...	50 wide and 50 deep.	None seen	Upper solution zone absent.	Not measured.....	None seen.
12. Big Goose Creek.	NE1/4 sec. 3 and NW1/4 sec. 2, T. 54 N., R. 86 W., and SW1/4 sec. 35, T. 55 N., R. 86 W., Sheridan County.	... do ...	None seen	... do ...	... do ...	137, sparry calcite matrix.	Many small caves throughout upper 70; one 10 wide, 12 high, and 342 below top.

Table 1.—*Catalog of solution features in the upper part of the Madison Limestone in north-central Wyoming*—Continued

[Localities shown in fig. 2. Relief, dimensions, and depths are in feet]

Locality	Geographic location	Maximum local relief at top of Madison exclusive of sinkholes	Sinkholes: dimensions	Sandstone-filled joints: maximum depth below top of Madison	Upper solution zone: maximum depth below top of Madison of sandstone in lenses and matrix of breccia	Lower solution zone: maximum depth below top of Madison and nature of matrix of breccia	Sandstone-filled caves: dimensions and maximum depth below top of Madison
13. Wolf Creek.	SE1/4 sec. 5, T. 55 N., R. 86 W., Sheridan County.	... do ...	30 wide and 71 deep.	35	None seen.....	Not measured.....	None seen.
14. Little Tongue River—U.S. 14.	NE1/4 sec. 27 and NW1/4 sec. 26, T. 56 N., R. 87 W., Sheridan County.	6	None seen	11	... do ...	290, siltstone matrix	Dimensions not measured, 175 below top.
15. Little Tongue River—U.S. 14.	SE1/4 sec. 15, T. 56 N., R. 87 W., Sheridan County.	2	... do ...	None seen	... do ...	Not measured.....	50 wide, 32 high, and 60 below top.
16. Tensleep Canyon.	Sec. 27, T. 48 N., R. 87 W., Washakie County.	3–4	... do ...	6	... do ...	165, siltstone matrix	Dimension not measured, 37 below top.
17. Paintrock Creek.	NW1/4 sec. 20, T. 50 N., R. 88 W., Bighorn County.	Not measured	... do ...	None seen	Sandstone matrix in collapse breccia, 19 below top.	241, siltstone and sandstone matrix.	None seen.
18. Shell Canyon.	S1/2 sec. 9 and E1/2 sec. 17, T. 53 N., R. 90 W., Big Horn County.	5	53 deep	93	None seen.....	175, siltstone and shale matrix.	Small cavities 90–130 below top; one cave 130 below top, dimensions not measured.
19. Sheep Mountain.	NW1/4 sec. 2, T. 53 N., R. 94 W., Big-Horn County.	Not measured	None seen	13	... do ...	290, siltstone and shale matrix.	None seen.
20. Cottonwood Canyon.	SW1/4 sec. 34 and SE1/4 sec. 33, T. 57 N., R. 93 W., Big Horn County.	... do ...	... do ...	22	... do ...	226, siltstone and shale matrix.	Do.
21. Devils Canyon.	Sec. 36, T. 9 S., R. 28 E., Big Horn County, Mont.	... do ...	50 deep	63	... do ...	223, siltstone matrix	20 wide, 21 high, and 106 below top.
22. Shoshone Canyon.	NE1/4 sec. 5, T. 52 N., R. 102 W., Park County.	16	None seen	None seen	Lenses, 38 below top.	192, siltstone matrix	30 wide, 9 high, and 51 below top.
23. Clarks Fork Canyon.	E1/2 sec. 6 and SW1/4 sec. 5, T. 56 N., R. 103 W., Park County.	Not measured	50 wide and 25–30 deep.	36	None seen	261, siltstone matrix	Many small caves in upper 50; one cave 50 wide, 20 high, and 50 below top.

Stratigraphic problems.—The irregularity of some sandstone-filled caves, particularly those that were developed along bedding planes, causes difficulty in determining age and stratigraphic relations at some localities. An example of such a problem may be seen at a locality on U.S. Highway 14 near the north end of the Bighorn Mountains (fig. 3).

Here the lowest beds exposed are predominantly thick-bedded, fine-grained, cherty limestone that clearly belongs to the Bull Ridge Member of the Madison Limestone. These beds contain the corals *Diphyphyllum*, *Syringopora*, and *Vesiculophyllum*, which are characteristic of the *Diphyphyllum* Zone of Sando (1967a). A bed of stromatolitic limestone and chert occurs near the top of the cliffy limestone outcrop. Overlying the limestone is 0.5 to 1.5 ft of red, fine-grained calcareous sandstone containing fine-grained limestone pebbles. The sandstone is overlain by 1 to 2 ft of silty, fine-grained, thin-bedded limestone, which is in turn overlain by 12.5 ft of red, fine-grained sandstone containing rounded limestone pebbles at the base and abundant angular limestone fragments in the upper half. Above the sandstone is about 5 ft of limestone that is medium grained, crossbedded, and bioclastic in the upper 1.5 ft. Friable white chert occurs in the upper foot of this unit. The uppermost limestone is overlain by at least 18 ft of yellowish-gray to red, poorly bedded, fine-grained sandstone containing limestone pebbles at the base.

All contacts between limestone beds and superjacent sandstone beds are irregular and overlain by limestone pebbles in the sandstone that appear to have been derived from the immediately subjacent bed. The uppermost limestone has an extremely irregular contact with the sandstone on which it rests. The sequence above the main limestone cliff has the appearance of a depositional series of interbedded sandstone and limestone marked by unconformities between each of the successive units. One might conclude that the base of the Darwin Sandstone Member is at the base of the lowest sandstone bed and that marine limestones are included in the lower 20 ft of the Darwin.

Fossils collected from the uppermost limestone and chert provide the basis for an alternative explanation of the history of this sequence. The fauna of the crossbedded limestone (USGS colln. 22659-PC, 22197-PC, 22198-PC, fig. 3) is as follows:

Schizophoria sp.
Pugnoides? sp.
Rhynchonelloid? brachiopod, indet.
Eumetria verneuiliana (Hall)
Beecheria? sp.
Falcodus? sp.
Neoprioniodus sp.
Ozarkodina cf. *O. laevipostica* Rexroad and Collinson
O. sp.
Diplodella sp.
Spathognathodus penescitulus Rexroad and Collinson
S. n. sp.
S. sp.

The fauna of the chert at the top of the uppermost limestone (USGS colln. 22199-PC, fig. 3) is:

Spiriferoid brachiopod, indet.
Serpulinid worm tubes
Sanguinolites? sp.
Paraparchites sp.

The brachiopods in the assemblage from the limestone are Mississippian types, but they do not indicate what part of the Mississippian System is represented. *Eumetria verneuiliana*, although a long-ranging Mississippian species, is not an Amsden form. Another *Eumetria*, *E. sulcata* Burk, is found in the

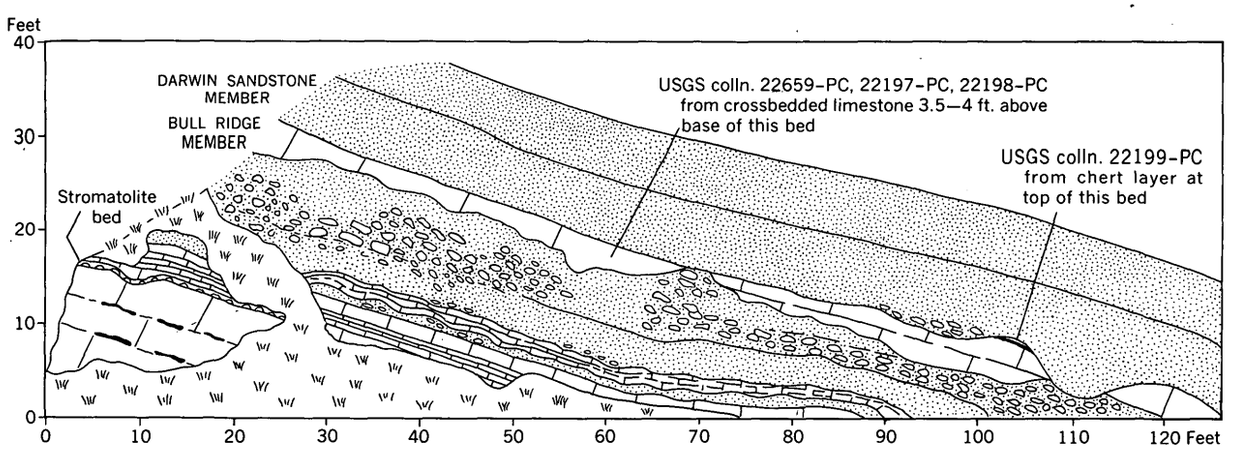

Figure 3.—Sketch of Bull Ridge Member of Madison Limestone and Darwin Sandstone Member of Amsden Formation exposed in roadcut on northwest side of U.S. Highway 14 in NW¼NE¼ sec. 22, T. 56 N., R. 87 W., Sheridan County, Wyo. Note positions of fossil collections discussed in text.

Mississippian part of the Amsden. According to J. W. Huddle (written commun., 1970), the conodonts from the limestone are indicative of a Salem–Warsaw age. *Spathognathodus penescitulus* is an exclusively Salem–Warsaw species. True *Ozarkodina laevipostica* occurs in the St. Louis Limestone, but similar forms are found in the Salem–Warsaw interval. *Falcodus*, *Diplodella*, *Prioniodina*, and *Neoprioniodus* are long-ranging genera whose ranges are compatible with a Salem–Warsaw age. The conodonts show no evidence of having been reworked.

Inasmuch as the Bull Ridge Member is also of Salem–Warsaw age (Sando and others, 1969, p. E22, fig. 7), the faunal evidence indicates that the limestone beds intercalated with sandstone at this locality belong in the Madison Limestone. This interpretation requires that the sandstone beds below the highest limestone represent deposition of the Darwin in solution cavities below the Darwin–Madison interface. The interpretation is compatible with the widespread solution effects observed in the upper part of the Madison and with the absence of marine limestone beds elsewhere in the Darwin. Moreover, all evidence bearing on the origin of the Darwin elsewhere indicates that the earliest sandstone deposits were fluvial.

SOLUTION ZONES

Description.—Stratigraphically limited brecciated carbonate rock having a terrigenous matrix is extensively developed at two levels in the Madison Limestone of north-central Wyoming. In the lower part of the Bull Ridge Member, a persistent interval of dolomitic siltstone, silty dolomite, and shale contains angular blocks of limestone or dolomite like that of the overlying carbonate interval at some localities (upper solution zone of Sando, 1967a). A more persistent and conspicuous breccia zone occurs at the base of the unnamed limestone member of the Madison in the area northward from the north end of the Wind River Range (lower solution zone of Sando, 1967a). The lower breccia is about 10 to 50 ft thick and consists of poorly sorted angular fragments of limestone and dolomite in a matrix of poorly bedded siltstone and shale. Less commonly, the matrix is quartz sandstone or occasionally fine-grained carbonate or sparry carbonate. The size of the fragments generally increases upward from an irregular but sharply defined base of the breccia zone. The lower breccia grades upward through an overlying breccia characterized by progressive decrease in the terrigenous content of the matrix, increase in size of the fragments to tens of feet in diameter, and increase in regularity of orientation of the fragments into well-bedded, unfragmented carbonate rock. Quartz sandstone is a common matrix in the higher levels of the breccia.

Origin.—Stratigraphically restricted breccias have been noted by many geologists in the Madison Limestone of Wyoming and Montana (Thom and others, 1935; Blackstone, 1940; Berry, 1943; Laudon, 1948; Tourtelot and Thompson, 1948; Denson and Morrissey, 1952, 1954; Severson, 1952; Sloss, 1952; Laudon and Severson, 1953; Nordquist, 1953; McMannis, 1955; Andrichuk, 1955, 1958; Hose, 1955; Richards, 1955; Norton, 1956; Strickland, 1956, 1957, 1960; Klepper and others, 1957; Freeman and others, 1958; Mapel, 1959; Middleton, 1961; Roberts, 1961, 1966; Robinson, 1963; Keefer and Van Lieu, 1966; Sando, 1967a, 1967b, 1968; McCaleb and Wayhan, 1969; Witkind, 1969). Although some geologists (Berry, 1943; Laudon, 1948; Strickland, 1956, 1957, 1960) regarded the breccias as evidence of an unconformity within the Madison, a more probable origin is post-Madison leaching and collapse of evaporite deposits that represented a part of late Madison deposition (Roberts, 1966, p. B17–B20). Interpretations of the upper Madison breccias have been reviewed recently by Roberts (1966, p. B17–B20) and Witkind (1969, p. 26–27). The present discussion is confined to critical observations bearing on the time and mode of origin of the breccias in north-central Wyoming.

In a study of breccias in the Mission Canyon Limestone near Livingston, southwestern Montana, Roberts (1966, p. B20–B21) distinguished between karst deposits formed during post-Mission Canyon, pre-Amsden erosion and solution breccia inferred to have formed during or after Late Cretaceous and early Tertiary uplift. According to Roberts (1966, p. B21), the solution breccia beds of Montana are restricted to areas of Late Cretaceous and early Tertiary uplift whereas correlative evaporite zones in the Madison are generally unaltered in nearby areas that were not uplifted. Moreover, he found a significant difference between the clay mineralogy of the karst deposits and that of the solution breccia. He noted a predominance of kaolinite in the karst deposits and a predominance of illite in the solution breccia; illite was also the chief clay mineral in the overlying Amsden Formation. Roberts reasoned that the kaolinite formed during development of an ancient soil on the uplifted surface of the Mission Canyon Limestone prior to deposition of the Amsden Formation, whereas the illite was deposited during marine deposition and was not changed during uplift or brecciation.

McCaleb and Wayhan (1969, p. 2104–2108) presented evidence that led to different conclusions in a subsurface study of the Madison Limestone in the Elk Basin oil field, which straddles the Wyoming-Montana State line at the north end of the Bighorn Basin. The upper 300 ft of the Madison in the Elk Basin field is characterized by extensive brecciation and a continuous solution breccia at the base of the brecciated interval. The solution breccia at the base of McCaleb and Wayhan's (1969, p. 2009) A zone is the lower solution zone of this report; a less conspicuous solution breccia noted by McCaleb and Wayhan (p. 2097) between their A_{1a} and A_{1b} zones is the upper solution zone of this report. McCaleb and Wayhan (1969, p. 2106) established vertical continuity of structural features from the solution zones to the karst deposits at the top of the Madison. At one well a sinkhole was developed as a result of collapse of the underlying lower

solution zone. Moreover, analysis of clay minerals from the Elk Basin cores yielded only illite throughout the Madison and in the overlying Amsden Formation, which suggests similar sources and origins for the clay minerals. McCaleb and Wayhan concluded that the development of karst deposits and the formation of solution breccias were phases of the same process, an event that took place during post-Madison, pre-Amsden time.

My interpretation of the age and origin of the solution breccias in the upper part of the Madison of north-central Wyoming coincides essentially with that of McCaleb and Wayhan. Leaching of soluble constituents of evaporite deposits at two levels in the upper part of the Madison produced open spaces that were filled largely by collapse of overlying carbonate beds. Fragments of carbonate rock of relatively small diameter are probably the brecciated remnants of thin carbonate beds within the evaporite deposits, whereas larger fragments, which increase in size and abundance upward in the breccia zones were derived by collapse of the roof rock. Poorly bedded siltstone and shale that forms the predominant matrix of the breccia was part of the original depositional sequence. Fine-grained carbonate matrix, an uncommon constituent, is thought to be finely crushed rock described as rock flour by Middleton (1961).

The occurrence of fine- to medium-grained quartz sandstone as matrix of the breccia and in irregular bodies and lentils within the breccia at some localities (table 1) is evidence of the pre-Darwin origin of the solution zones. Additional evidence bearing on the time of origin of the lower solution zone is the occurrence of a cave filled with red shale and siltstone approximately 200 ft below the lower solution zone at Big Goose Creek (table 1). The occurrence of this cave suggests that although the lower solution zone ordinarily marks the lowest level of pre-Amsden solution there were some areas where the solution process took place at even greater depth.

The depth of the lower solution zone beneath the top of the Madison ranges from about 80 to 360 ft (table 1). Inferred maximum relief on the post-Madison, pre-Amsden erosion surface was about 200 ft, and the solution zone occurs below the deepest local base levels. These relationships indicate a phreatic origin for the lower solution zone similar to that of the sandstone-filled caves.

SUMMARY OF MADISON KARST HISTORY

The geomorphic development of north-central Wyoming during middle Meramecian to late Chesterian time can be divided into several overlapping stages.

1. After predominantly carbonate deposition during Kinderhookian into early Meramecian time, the area was epiorogenically uplifted to form a land of low relief, and the Madison sea withdrew to a geosynclinal trough that lay to the west. The uplift took place between early Meramecian (middle Salem) and middle Chesterian time, as indicated by the youngest fossils found in the Madison Limestone and the oldest fossils found in the Amsden Formation. Local variations in the intensity of the epiorogenic process produced broad folds in the Madison strata.
2. A ground-water system, characterized by a shallow water table, developed in the carbonate terrane. Phreatic caverns were dissolved in the upper 400 ft of bedrock by ground water guided in part by readily soluble evaporite intervals in the carbonate sequence. The absence of flowstone and dripstone suggests that vadose circulation was never extensively developed. Solution breccias were formed by collapse of thin carbonate beds within the evaporite intervals and of roofs of large cavities, particularly in the lower of the two solution zones.
3. Continued uplift resulted in further karst development. Parts of the Bull Ridge Member of the Madison were eroded away, particularly toward the southeast. Although the main lines of surface drainage are not apparent, the valleys appear to have been dominantly synclinal, and maximum relief probably did not exceed 200 ft. The drainage pattern was probably complex and characterized by stream capture by numerous sinkholes, developed to a depth of about 100 ft, that formed in the bedrock surface. Red residual products from a thin soil cover infiltrated many of the solution cavities.
4. During the Chesterian, north-central Wyoming subsided and the Amsden sea swept eastward from the geosyncline across the karst surface. Initial reworking by the sea of stream deposits and residual soil was followed by deposition of a layer of sand derived largely from outside the Amsden basin. The sand covered all but a few isolated topographic highs that remained as islands and it infiltrated sinkholes and caves, filling most of the open spaces produced by prior solution.

REFERENCES CITED

Andrichuk, J. M., 1955, Mississippian Madison Group stratigraphy and sedimentation in Wyoming and southern Montana: Am. Assoc. Petroleum Geologists Bull., v. 39, no. 11, p. 2170–2210, 12 figs.

——1958, Mississippian Madison group stratigraphy and sedimentation in Wyoming and southern Montana, *in* Weeks, L. G., ed., Habitat of oil—a symposium: Tulsa, Oklahoma, Am. Assoc. Petroleum Geologists, June, 1958, p. 225–267.

Berry, G. W., 1943, Stratigraphy and structure at Three Forks, Montana: Geol. Soc. America Bull., v. 54, no. 1, p. 1–30, 1 pl., 5 figs.

Blackstone, D. L., Jr., 1940, Structure of the Pryor Mountains, Montana: Jour. Geology, v. 48, no. 6, p. 590–618.

Blackwelder, Eliot, 1918, New geological formations in western Wyoming: Washington Acad. Sci. Jour., v. 8, no. 13, p. 417–426.

Bretz, J. H., 1940, Solution cavities in the Joliet Limestone of northeastern Illinois: Jour. Geology, v. 48, no. 4, p. 337–384.

——1956, Caves of Missouri: Missouri Div. Geol. Survey and Water Resources [Rept.], v. 39, 2nd ser., 490 p.

Craig, L. C., 1972, Mississippian System: *in* Mallory, W. W., ed., Geologic atlas of the Rocky Mountain region, Denver, Rocky Mtn. Assoc. Geologists, p. 100–110.

Darton, N. H., 1904, Comparison of the stratigraphy of the Black Hills, Bighorn Mountains, and Rocky Mountain Front Range: Geol. Soc. America Bull., v. 15, p. 379–448, pls. 23–36.

Davis, W. M., 1930, Origin of limestone caverns: Geol. Soc. America Bull., v. 41, no. 3, p. 475–628.

Denson, M. E., Jr., and Morrissey, N. S., 1952, The Madison Group (Mississippian) of the Big Horn and Wind River Basins, Wyoming, *in* Wyoming Geol. Assoc. Guidebook, 7th Ann. Field Conf., 1952: p. 37–43, 8 figs.

——1954, Subsurface correlations within the Madison group, Bighorn and Wind River Basins, *in* Billings Geol. Soc. Guidebook, 5th Ann. Field Conf.: p. 44–49, 5 figs.

Elliott, J. K., 1963, Cave occurrences in the Mississippian Madison Limestone of the Pryor Mountains, Montana: Billings Geol. Soc. papers, p. 1–13, 16 figs.

Freeman, V. L., Ruppel, E. T., and Klepper, M. R., 1958, Geology of part of the Townsend Valley, Broadwater and Jefferson Counties, Montana: U.S. Geol. Survey Bull. 1042-N, p. 481–556, 5 pls., 1 fig.

Henbest, L. G., 1958, Significance of karst terrane and residuum in Upper Mississippian and Lower Pennsylvanian rocks, Rocky Mountain Region, *in* Wyoming Geol. Assoc. Guidebook, 13th Ann. Field Conf., 1958: p. 36–38, 1 fig.

Hose, R. K., 1955, Geology of the Crazy Woman Creek area, Johnson County, Wyoming: U.S. Geol. Survey Bull. 1027-B, p. 33–118, 8 pls., 15 figs., 6 tables.

Keefer, W. R., and Van Lieu, J. A., 1966, Paleozoic formations in the Wind River Basin, Wyoming: U.S. Geol. Survey Prof. Paper 495-B, 60 p., 6 pls., 23 figs., 8 tables.

Klepper, M. R., Weeks, R. A., and Ruppel, E. T., 1957, Geology of the southern Elkhorn Mountains, Jefferson and Broadwater Counties, Montana: U.S. Geol. Survey Prof. Paper 292, 82 p., 8 pls., 16 figs., 5 tables [1958].

Laudon, L. R., 1948, Osage-Meramec contact, *in* Weller, J. M., ed., Symposium on problems of Mississippian stratigraphy and correlation: Jour. Geology, v. 56, no. 4, p. 288–302, 3 pls., 12 figs.

Laudon, L. R., and Severson, J. L., 1953, New crinoid fauna, Mississippian, Lodgepole formation, Montana: Jour. Paleontology, v. 27, no. 4, p. 505–536.

McCaleb, J. A., and Wayhan, D. A., 1969, Geologic reservoir analysis, Mississippian Madison Formation, Elk Basin Field, Wyoming-Montana: Am. Assoc. Petroleum Geologists Bull., v. 53, no. 10, pt. 1, p. 2094–2113, 13 figs., 2 tables.

McMannis, W. J., 1955, Geology of the Bridger Range, Montana: Geol. Soc. America Bull., v. 66, no. 11, p. 1385–1430, 8 pls., 5 figs.

Mallory, W. W., 1967, Pennsylvanian and associated rocks in Wyoming: U.S. Geol. Survey Prof. Paper 554-G, 31 p., 3 pls., 16 figs.

Mapel, W. J., 1959, Geology and coal resources of the Buffalo-Lake De Smet area, Johnson and Sheridan Counties, Wyoming: U.S. Geol. Survey Bull. 1078, 148 p., 23 pls., 6 figs., 4 tables.

Middleton, G. V., 1961, Evaporite solution breccias from the Mississippian of southwest Montana: Jour. Sed. Petrology, v. 31, no. 2, p. 189–195, 3 figs.

Nordquist, J. W., 1953, Mississippian stratigraphy of northern Montana, *in* Billings Geol. Soc. Guidebook 4th Ann. Field Conf., Little Rocky Mountains, Montana, southwestern Saskatchewan, 1953. p. 68–82.

Norton, G. H., 1956, Evidences of unconformity in rocks of Carboniferous age in central Montana, *in* Billings Geol. Soc. Guidebook 7th Ann. Field Conf., central Montana, 1956: p. 52–66.

Richards, P. W., 1955, Geology of the Bighorn Canyon-Hardin area, Montana and Wyoming: U.S. Geol. Survey Bull. 1026, 93 p., 7 pls., 8 figs., 4 tables.

Roberts, A. E., 1961, Insoluble residues and Ca:Mg ratios in the Madison Group, Livingston, Montana, *in* Short papers in the geologic and hydrologic sciences: U.S. Geol. Survey Prof. Paper 424-B, p. B294–B296.

——1966, Stratigraphy of Madison Group near Livingston, Montana, and discussion of karst and solution-breccia features: U.S. Geol. Survey Prof. Paper 526-B, 23 p.

Robinson, G. D., 1963, Geology of the Three Forks quadrangle, Montana: U.S. Geol. Survey Prof. Paper 370, 143 p., 3 pls., 16 figs., 9 tables.

Sando, W. J., 1967a, Madison Limestone (Mississippian), Wind River, Washakie, and Owl Creek Mountains, Wyoming: Am. Assoc. Petroleum Geologists Bull., v. 51, no. 4, p. 529–557, 8 figs.

——1967b, Mississippian depositional provinces in the northern Cordilleran region, *in* Geological Survey research 1967: U.S. Geol. Survey Prof. Paper 575-D, p. D29–D38, 3 figs.

——1968, A new member of the Madison Limestone (Mississippian) in Wyoming: Geol. Soc. America Bull., v. 79, no. 12, p. 1855–1858, 2 figs.

Sando, W. J., Mamet, B. L., and Dutro, J. T., Jr., 1969, Carboniferous megafaunal and microfaunal zonation in the northern Cordillera of the United States: U.S. Geol. Survey Prof. Paper 613-E, 29 p., 1 pl., 7 figs., 1 table.

Severson, J. L., 1952, A comparison of the Madison Group (Mississippian) with its subsurface equivalents in central Montana: Wisconsin Univ., Ph. D. thesis, 87 p.

Sloss, L. L., 1952, Introduction to the Mississippian of the Williston Basin, *in* Billings Geol. Soc. Guidebook 3d Ann. Field Conf., 1952: p. 65–69.

Strickland, J. W., 1956, Mississippian stratigraphy, western Wyoming, *in* Wyoming Geol. Assoc. Guidebook 11th Ann. Field Conf., Jackson Hole, 1956: p. 51–57, 2 figs.

——1957, Summary of Mississippian and Devonian stratigraphy, Wind River Basin, Wyoming, *in* Wyoming Geol. Assoc. Guidebook 12th Ann. Field Conf., 1957: p. 20–27, 4 figs.

——1960, Summary of Mississippian stratigraphy, western Wyoming and vicinity, *in* Billings Geol. Soc. Guidebook 11th Ann. Field Conf., 1960: p. 217–225, 2 pls.

Thom, W. T., Jr., Hall, G. M., Wegemann, C. H., and Moulton, G. F., 1935, Geology of Big Horn County and the Crow Indian Reservation, Montana: U.S. Geol. Survey Bull. 856, 200 p.

Tourtelot, H. A., and Thompson, R. M., 1948, Geology of the Boysen area, central Wyoming: U.S. Geol. Survey Oil and Gas Inv. Map 91.

Witkind, I. J., 1969, Geology of the Tepee Creek quadrangle, Montana-Wyoming: U.S. Geol. Survey Prof. Paper 609, 101 p., 2 pls., 30 figs., 7 tables.

Jour. Research U.S. Geol. Survey
Vol. 2, No. 2, Mar.-Apr. 1974, p. 143–146

STRATIGRAPHIC RELATIONS OF THE BOLSA QUARTZITE, VEKOL MOUNTAINS, PINAL COUNTY, ARIZONA

By M. A. CHAFFEE, Denver, Colo.

Abstract.—A quartzite unit occurring between the rocks of the Precambrian Apache Group and those of the Cambrian Abrigo Formation in the Vekol Mountains, Pinal County, Ariz., has been called both Troy Quartzite (Precambrian) and Bolsa(?) Quartzite (Cambrian). Regional and local geologic relationships indicate that this intervening unit is definitely the Bolsa Quartzite. The Bolsa ranges in thickness from at least 200 ft at several localities in the Vekol Mountains to 0 ft over a positive area underlain by Precambrian diabase which has intruded the Apache Group. Previous observations that the diabase intruded the quartzite unit (thereby making this quartzite unit the Troy Quartzite) have been reinterpreted; all nonfaulted exposures of the basal contact of the quartzite unit show sedimentary relationships. No evidence was found to suggest that the Troy Quartzite was ever deposited in the Vekol Mountains.

The purpose of this report is to demonstrate that the clastic unit lying between the Apache Group of Precambrian Y age[1] and the Abrigo Formation of Cambrian age in the Vekol Mountains (fig. 1) is unconformable on the Apache Group and grades upward into the Abrigo. It is, thus, properly assignable to the Bolsa Quartzite of Cambrian age.

Before 1961 it was customary in southern Arizona to assign clastic rocks that intervened between the Apache Group and the Abrigo to the Troy Quartzite, whose age was variously interpreted as Precambrian, Cambrian, or Cambrian(?), and to assign clastic rocks that intervened between Precambrian crystalline rocks and the Abrigo to the Bolsa Quartzite of Cambrian age. In 1961, however, Krieger (1961) demonstrated that in the Galiuro Mountains area (fig. 1) clastic rocks between the Apache Group and the Abrigo contain a disconformity within them. She found that the clastic rocks beneath the disconformity were intruded by Precambrian diabase and are thus of Precambrian age, and she found that the clastic rocks above the disconformity are gradational into the Abrigo and are thus of Cambrian age. She placed the lower unit in the Troy Quartzite to which she assigned a definite Precambrian age, and the upper unit she placed in the Bolsa Quartzite.

[1] An interim scheme for subdivision of Precambrian time recently adopted by the U.S. Geological Survey assigns Precambrian Y time to the interval 1,600 to 800 m.y. ago.

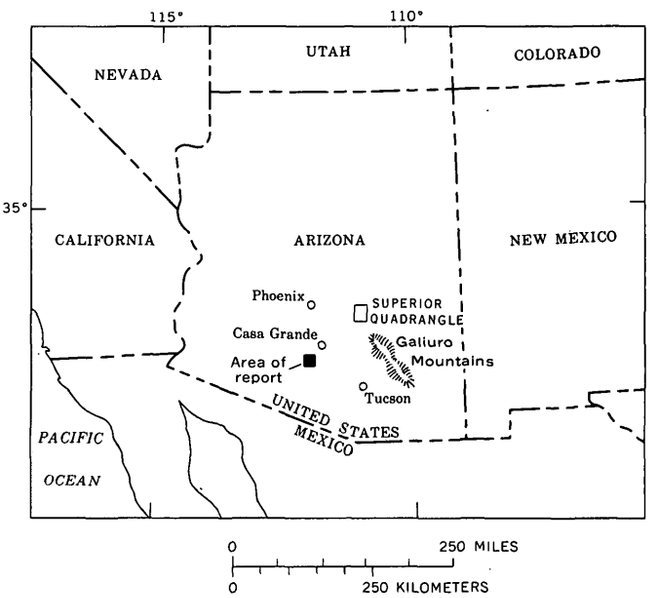

Figure 1.—Map of Arizona showing location of the report area in the Vekol Mountains.

After Krieger (1961) published her findings, it became desirable to reexamine relations in other areas in southern Arizona where Cambrian rocks overlie the Apache Group, and the Vekol Mountains are in such an area. The Vekol Mountains area is particularly important to broad regional studies because it contains both the westernmost and the most complete, little-disturbed section of Precambrian and Paleozoic sedimentary rocks in south-central Arizona. Furthermore, previous workers in the Vekols have disagreed about the relations of clastic rocks that intervene between strata definitely assignable to the Apache Group and strata definitely assignable to the Cambrian.

PREVIOUS INVESTIGATIONS

The first detailed geologic mapping in the Vekol Mountains was by Carpenter (1947). Following the practice of the time, Carpenter used the term Troy Quartzite for the clastic unit

found overlying the Apache Group rocks and underlying the Abrigo Formation as now defined.[2]

Carpenter (1947, p. 23, 47), without citing a particular area, further stated that Precambrian diabase, a unit which is commonly found as sill-like bodies in the Apache Group and in the Troy (see, for example, Shride, 1967), intruded much of the lower part of his Troy Quartzite. Where this intrusive relationship exists, it provides a good means of establishing the presence of Troy Quartzite, as now used, rather than Bolsa Quartzite (Krieger, 1968c).

Heindl and McClymonds (1964) made a regional reconnaissance study of some of the Precambrian and Cambrian units of south-central Arizona, including the Vekol Mountains. They were unable to find any evidence of diabase intrusion into the quartzite herein discussed and concluded that the clastic unit they mapped correlated more closely with the Bolsa Quartzite. Because they did not consider their findings conclusive, Heindl and McClymonds used the term Bolsa(?) Quartzite in their report (1964).

PRESENT INVESTIGATIONS

Recent field studies suggest a new interpretation for Carpenter's (1947) observations; accordingly, the query is herein dropped from the name Bolsa(?) Quartzite (Heindl and McClymonds, 1964).

Detailed mapping by Krieger (1968a, b, c) and Peterson (1969) has demonstrated that relief at the top of the Precambrian sections in central Arizona may be several hundred feet. This relief produces significant local variations in the thickness of the Bolsa Quartzite where it disconformably onlaps Precambrian hills. Measurement of the thickness of numerous sections of Bolsa Quartzite throughout the Vekol Mountains (fig. 2) clearly indicates that the topographic relief at the time of deposition of the quartzite there was similar to that described by Krieger (1968a, b, c) in the vicinity of the Galiuro Mountains and by Peterson (1969) in the Superior quadrangle (fig. 1).

The Bolsa Quartzite in the Vekol Mountains was measured wherever a reasonably complete section was expected. The base of the lowest clastic bed overlying either diabase of post-Apache age or basalt of the Apache Group was picked to be the base of the Bolsa. Where clastic rocks of the Dripping Spring Quartzite underlie the Bolsa (one location), the base of the lowest thick vitreous quartzite bed was taken to be the base of the Bolsa. In areas where the Bolsa directly overlies sedimentary formations of the Apache Group, the basal contact of the Bolsa is paraconformable. The top of the Bolsa

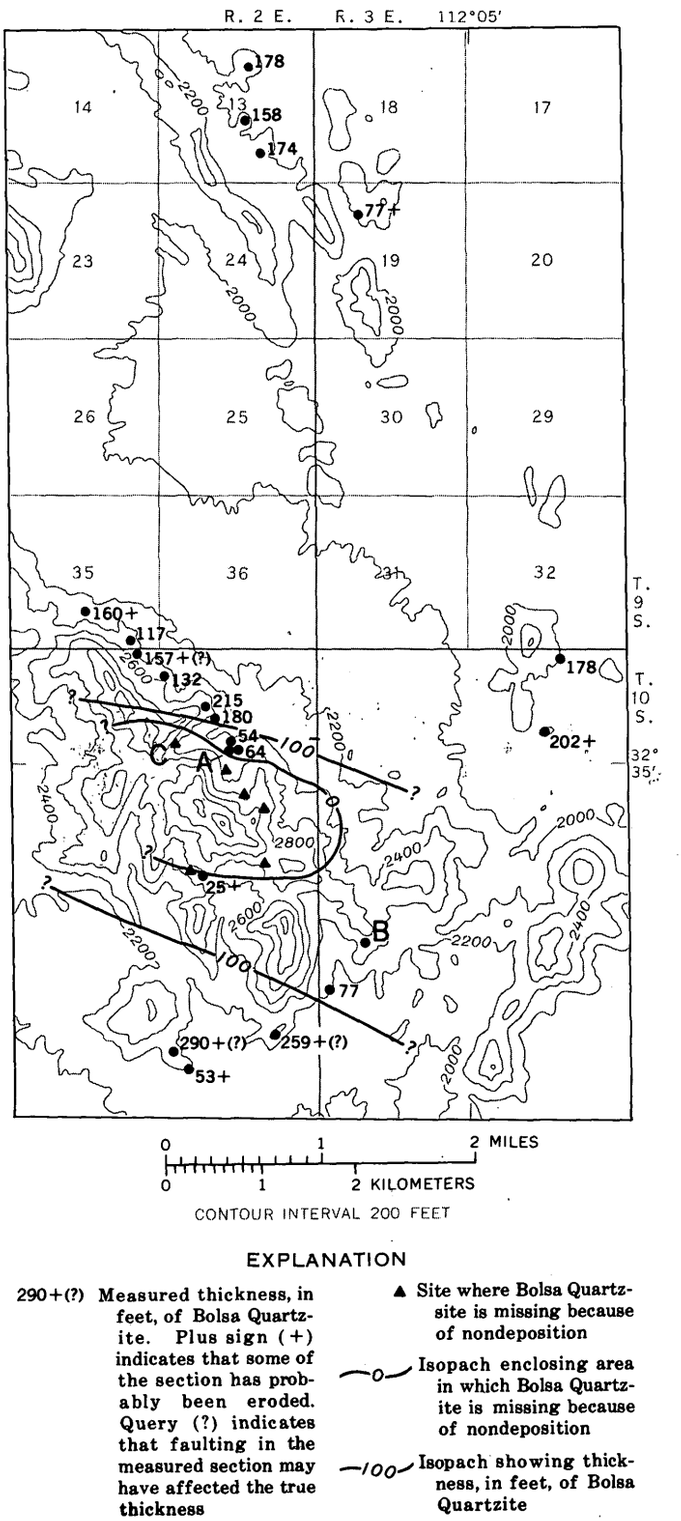

Figure 2.—Map showing sites and thicknesses of measured sections of Bolsa Quartzite in the Vekol Mountains. A, B, and C are localities referred to in text.

is gradational into the overlying Abrigo Formation and, therefore, the upper contact is somewhat arbitrary. The

[2] Carpenter used the stratigraphy of Stoyanow (1936) to describe the rocks occurring between his Troy Quartzite and the formations of Devonian age. Stoyanow divided the Abrigo into three separate formations. This scheme was never widely accepted and has now been abandoned.

contact was selected to be at the base of the lowest obvious carbonate bed or lowest interval where shaly beds predominate over quartzitic beds.

In areas in the Vekol Mountains where it does not appear to be abnormally thin because of onlap on buried hills, the thickness of the Bolsa Quartzite is probably in the range of 150–200 ft (fig. 2). The formation thins abruptly, however, in the central part of the mountains. This thinning, together with the lack of any evidence of erosion between the Bolsa and Abrigo Formations, must be the result of deposition on a surface of marked relief rather than deposition followed by erosion prior to Abrigo deposition. The differences in thicknesses of the Bolsa sections indicate the presence during Bolsa time of a Precambrian positive area with a relief of at least 200 ft. This positive area was a hill or ridge of Precambrian diabase and, to a lesser degree, the Precambrian Apache basalt, because all the sections in which Bolsa is absent or markedly thinned occur where diabase (and locally basalt) is the youngest Precambrian unit exposed and where the diabase is as much as several hundred feet thicker than normal. In exposures of the basal Cambrian contact where the Bolsa is missing, a thin-bedded basal unit of the Abrigo Formation immediately overlies weathered diabase (fig. 3). This basal unit contains interbedded carbonate and clastic beds ranging from shales to siltstones to conglomerates containing diabase fragments. Crossbedded calcareous quartzite is locally present in lenses at or near the contact.

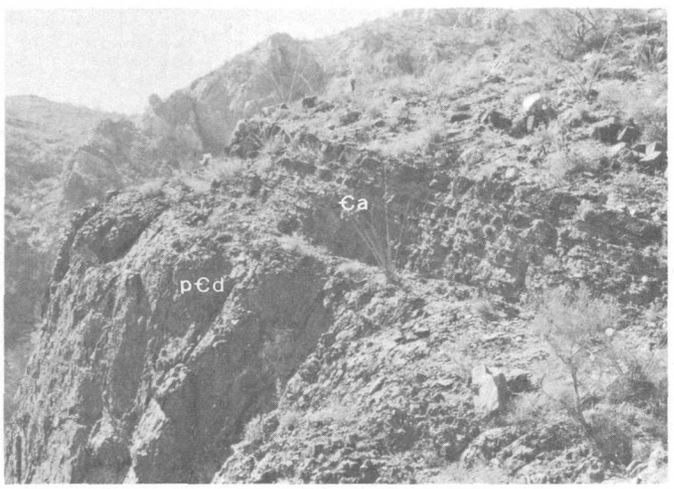

Figure 3.—Well-bedded Cambrian Abrigo Formation (Ca) in sedimentary contact with a massive Precambrian diabase sill (pCd). View west from locality C in figure 2.

No evidence of intrusion of the diabase into the Bolsa Quartzite was found at any exposure. The exposures at locality A (fig. 2) illustrate an unusually clear-cut example of the sedimentary nature of the basal Bolsa contact (fig. 4). Because of the presence of diabase boulders up to 3 ft in diameter near this contact, it would be possible, in poorly exposed areas, to interpret the contact as intrusive. Such a poorly exposed locality might have been one of the areas which led Carpenter (1947) to conclude that the diabase was intrusive into the quartzite.

Figure 4.—Subangular to rounded boulders of Precambrian diabase in a matrix of Cambrian Bolsa Quartzite, at locality A. The diabase boulders have been outlined with chalk for emphasis. Crossbedding is locally present in the matrix but is not visible in this photograph. Scale is 24 cm long.

In the vicinity of locality B (fig. 2) Carpenter (1947, p. 47–48) described a 1- to 3-ft-thick zone apparently near the basal Cambrian contact (as now defined) as containing "'hybrid' diabase with numerous small ghost-like quartzite fragments and individual quartz grains." This locality was reexamined in detail, and the "quartzite fragments" were actually found to be from a prominent quartzite bed near the middle of the Abrigo Formation where this bed is in fault contact with Precambrian diabase. The entire area is near a major regional tectonic lineament and, locally, diorite porphyry of Tertiary(?) age has intruded the Abrigo Formation. This combination of extensive faulting and igneous intrusion has widely metamorphosed the Abrigo shale, siltstone, and carbonate beds at locality B. These events also apparently caused a local remobilization of the diabase at its faulted contact with the Abrigo quartzite bed. This local remobilization produced the illusion that the diabase had intruded the quartzite (fig. 5).

CONCLUSIONS

Both regional and local geologic relationships indicate conclusively that the quartzite unit of the Vekol Mountains which is present stratigraphically between the rocks of the Apache Group and those of the Abrigo Formation is the Bolsa Quartzite. The Bolsa outcrops are similar in appearance nearly everywhere throughout the Vekol Mountains. None of the sections shows features similar to those described by Shride

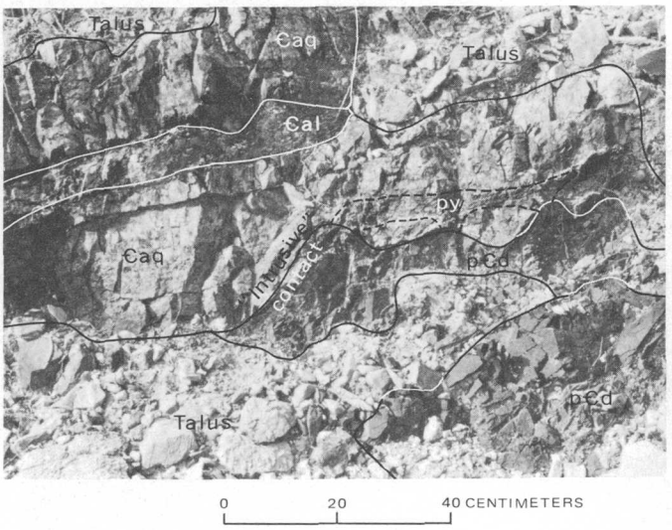

Figure 5.—Fault contact between Cambrian Abrigo Formation and Precambrian diabase showing "intrusion" of the diabase (pCd) into quartzite beds (Cam), at locality B. The zone of weathered pyrite casts (py) in the quartzite is probably related to remobilization of the diabase. In appearance the limestone bed (Cal) is typical of such beds in the Abrigo and unlike limestone beds in other formations in the region.

(1967) and Krieger (1961, 1968c) for the Troy Quartzite. If any Troy is present in the Vekol Mountains, it would have to occur within the lowermost few feet of the Bolsa sections where the base is not clearly exposed. No evidence exists now to indicate whether the Troy Quartzite as used by Krieger was ever deposited in the region of the Vekol Mountains. It is therefore recommended that the term Troy Quartzite not be used in the Vekol Mountains and surrounding region.

ACKNOWLEDGMENT

I thank C. W. Gale III, of the U.S. Geological Survey, for assisting me in measuring the thickness of many of the geologic sections.

REFERENCES CITED

Carpenter, R. H., 1947, The geology and ore deposits of the Vekol Mountains, Pinal County, Arizona: Palo Alto, Calif., Stanford Univ., Ph. D. thesis, 108 p.

Heindl, L. A., and McClymonds, N. E., 1964, Younger Precambrian formations and the Bolsa(?) Quartzite of Cambrian age, Papago Indian Reservation, Arizona, *in* Geological Survey research 1964: U.S. Geol. Survey Prof. Paper 501-C, p. C43–C49.

Krieger, M. H., 1961, Troy Quartzite (Younger Precambrian) and Bolsa and Abrigo Formations (Cambrian), northern Galiuro Mountains, southeastern Arizona, *in* Short papers in the geologic and hydrologic sciences: U.S. Geol. Survey Prof. Paper 424-C, p. C160–C164.

——1968a, Geologic map of the Holy Joe Peak quadrangle, Pinal County, Arizona: U.S. Geol. Survey Geol. Quad. Map GQ-669.

——1968b, Geologic map of the Saddle Mountain quadrangle, Pinal County, Arizona: U.S. Geol. Survey Geol. Quad. Map GQ-671.

——1968c, Stratigraphic relations of the Troy Quartzite (Younger Precambrian) and Cambrian formations in southeastern Arizona, *in* Southern Arizona Guidebook 3 – Geol. Soc. America Cordilleran Sec., 64th Ann. Mtg., Tucson, 1968: Arizona Geol. Soc., p. 22–32.

Peterson, D. W., 1969, Geologic map of the Superior quadrangle, Pinal County, Arizona: U.S. Geol. Survey Geol. Quad. Map GQ-818.

Shride, A. F., 1967, Younger Precambrian geology in southern Arizona: U.S. Geol. Survey Prof. Paper 566, 89 p.

Stoyanow, A. A., 1936, Correlation of Arizona Paleozoic formations: Geol. Soc. America Bull., v. 47, no. 4, p. 459–540.

Jour. Research U.S. Geol. Survey
Vol. 2, No. 2, Mar.-Apr. 1974, p. 147—158,

THERMAL INERTIA MAPPING FROM SATELLLITE—DISCRIMINATION OF GEOLOGIC UNITS IN OMAN

By H. A. POHN, T. W. OFFIELD, and KENNETH WATSON,
Denver, Colo.

Work done in cooperation with the National Aeronautics and Space Administration under Task 160-75-01-43-10

Abstract.—The Nimbus III and IV satellites provide reflectance and emittance data from the earth's surface at 8-km resolution. These data have been used to derive a physical property of geologic materials termed "thermal inertia" which appears to have great promise for discriminating surficial units. A thermal inertia map of part of Oman was produced from the Nimbus satellite measurements. Correlation of this map with a reconnaissance geologic map showed gross agreement with the major units but also suggested the need for some modifications of the reconnaissance map. Some of the anomalies were verified by comparison with a later, more detailed map; others remain unexplained and may indicate previously undiscriminated geologic units.

Radiometers on board the Nimbus III and IV meteorological satellites have provided measurements, at 8-km resolution, of radiation from the earth's surface in cloud-free areas. A Nimbus III experiment (High Resolution Infrared Radiometer, HRIR) recorded daytime reflectivity, and a Nimbus IV experiment (Temperature-Humidity Infrared Radiometer, THIR) recorded daytime and nighttime temperatures;[1] thus satellite data are available which offer some possibilities for discriminating geologic units on a broad scale. Two data formats are available—photofacsimile filmstrips and digital magnetic tapes. The filmstrips are of limited use for geologic analysis, owing to the image enhancement designed for cloud-cover studies. The digital data, however, preserve the entire dynamic range of recorded radiance values, and have already been used to study stream courses, ground moisture and vegetation variations, and broad soil-erosion patterns (Pouquet, 1969a, b; Rabchevsky, 1971).

In this report we extend these data by relating them to physical property information which should reveal differences in surficial material more directly than do the separate temperature and reflectivity measurements. To achieve this analysis, it was first necessary to develop a model for the thermal behavior of the ground.

The daily variation in ground temperature is induced primarily by absorption of solar energy and its subsequent reemission. Various factors determine the magnitude of this diurnal change, mainly the thermal properties of the ground, its albedo (reflectivity) and emissivity, and the circumstances of the solar heating (sun's declination, site latitude, and topographic slope). Secondary factors are sky radiation, conductive and convective heat transfer from the air, and geothermal heat. A thermal model constructed by Watson (1970a, 1970b) to study the behavior of different geologic material was qualitatively tested (Rowan and others, 1970; Watson and others, 1971). It is based on a relationship developed by Jaeger (1953) of surface flux to surface temperature for one-dimensional periodic heating of a half space. Only a single thermal parameter called the thermal inertia is required in this relationship. Thermal inertia is equal to $\sqrt{Ks}$, where K is the conductivity and s is the heat capacity.

Because albedo is an ambiguous parameter for distinguishing geologic materials,[2] maps based solely on albedo rarely portray the geology accurately. On the other hand, thermal inertia is more related to the bulk properties of material (it correlates strongly with density and interstitial water content). When thermal inertia is derived from the diurnal temperature change, it is averaged mainly over the top few centimeters,[3]

[1] The HRIR system actually recorded radiation simultaneously in three bands: 0.7–1.3, 2.3–3.0, and 2.4–4.2 μm. During daytime the reflected solar energy predominates. The THIR system recorded radiation in the 10.5–12.5 μm band. The operation of these systems was described in detail by Cherrix and Allison (1969) and McCulloch (1970).

[2] Albedo is generally determined not by bulk composition but rather by impurity (such as iron) in the crystal lattice, grain size, and texture. In addition, surface-coating effects such as lichen cover or desert varnish commonly mask the normal reflectance of even well-exposed rocks.

[3] This averaging occurs over only a fraction of the diurnal wavelength, which is about 1 m for rocks and about 50 cm for dry soils (Carslaw and Jaeger, 1959).

and thus is much less sensitive than albedo to thin surface coating and impurity effects. Because of this characteristic, thermal inertia provides important information for the remote discrimination of exposed rock and soil units.

For analysis of the Nimbus data we used a sun's declination appropriate to the time of observation and latitude of the study area, and we assumed zero topographic slope. The slope assumption is probably reasonable for the 8-km resolution of the spacecraft; it implies that varying slope orientations roughly cancel out over a large area.

Diurnal temperature curves were then generated on a computer for varying thermal inertias (Watson, 1970a) (fig. 1*A*), albedos (fig. 1*B*), emissivities (fig. 1*C*), and sky radiances (fig. 1*D*). Variations in sky radiance are, to a first approximation, equivalent to variations in ground elevation, because the thermal emission from the sky to the ground is less at higher elevations. Figure 1 illustrates that several parameters contribute to variations in the diurnal surface temperature of the ground. Some correction for ground elevation can be made using existing topographic maps and assuming a simple model of sky radiance; but, because no emissivity data are available at the scale of the Nimbus IV-THIR measurements, analysis of the thermal data requires another approach.

The amplitude of the diurnal temperature variations can be obtained from the Nimbus data by calculating ΔT, the day-night temperature difference. Examination of figure 1 shows that ΔT is reasonably independent of elevation and emissivity, moderately dependent on albedo, and strongly

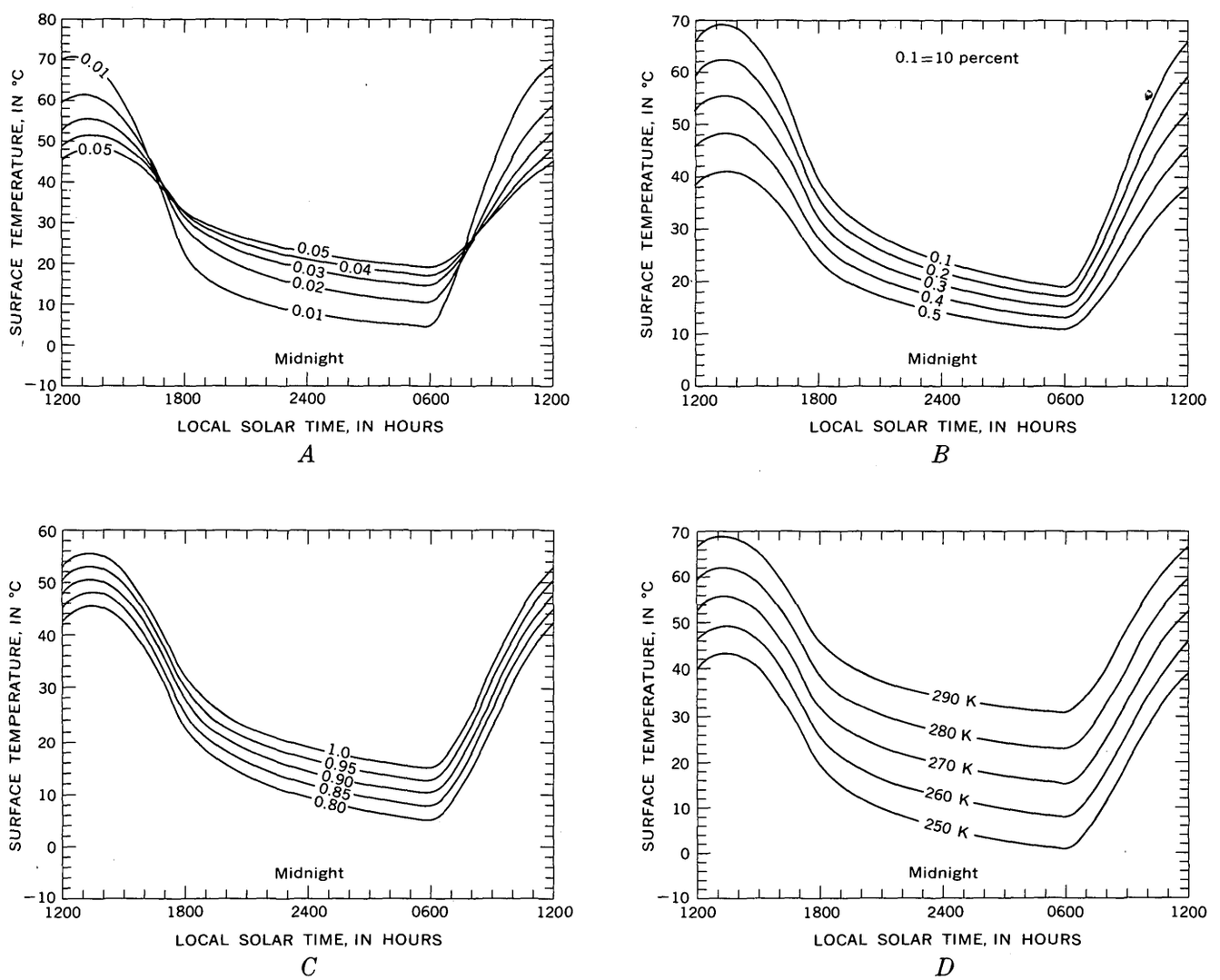

Figure 1.—Surface temperature versus solar time for materials with various thermal inertia values (*A*), albedos (*B*), emissivities (*C*), and sky temperature conditions (D) (but day and night temperatures equal). Albedo is assumed to be 30 percent for *A*, *C*, and *D*; emissivity 1.0 for *A*, *B*, and *D*; sky radiance temperature 270 K for *A*, *B*, and *C*; and thermal inertia 0.03 for *B*, *C*, and *D*.

dependent on thermal inertia (table 1). To first order the parameter ΔT is a function of only two rock properties: thermal inertia and albedo. Thermal inertia values, then, can be determined from Nimbus data by using an empirical curve based on the model results (fig. 2) in conjunction with albedos derived from reflectivity data (Nimbus III-HRIR) and temperature amplitudes (ΔT) computed from daytime and nighttime thermal data (Nimbus IV-THIR). A map of the thermal inertia values provides a representation of the thermal properties of exposed material which can be used to discriminate differences in composition, consolidation, and moisture content.

Table 1.—*Dependence of* ΔT *on elevation, albedo, emissivity, and thermal inertia*

	ΔT		ΔT
Elevation:[1]		Emissivity:	
0	32.3	1.	33.6
3,000	33.0	.95	33.4
6,000	33.6	.90	33.3
9,000	34.1	.85	33.1
Albedo:		Thermal inertia:	
0.1	42.1	0.01	61.1
.2	37.9	.02	44.0
.3	33.6	.03	33.6
.4	29.1	.04	26.9

[1] Elevations, in feet above sea level, were derived by assuming a 3°C atmospheric temperature change per 1,000 ft.

DATA ANALYSIS

To examine the utility of thermal inertia, as a remotely derived physical property for discriminating geologic materials, an initial test area was selected and computer printouts giving latitude, longitude, and reflectance or temperature of each resolution spot were obtained from the Goddard Space Flight Center. Nimbus IV-THIR data were used for day and night temperatures, and Nimbus III-HRIR data were used for reflectivity.

Choice of a test area was determined by several factors: (1) excellent exposures of rocks and soil unobscured by vegetation, (2) surface units large enough to be observed effectively at 8-km resolution, (3) geologic units expected to contrast thermally because of reflectivity and thermal property differences, (4) reasonably accurate geologic maps at scales appropriate to compare with maps made from Nimbus data, (5) topographic information to use in identifying possible thermal features due primarily to topography rather than to unit composition, and (6) minimum cloud cover and stable atmospheric conditions that would permit the best choice possible among the data available on magnetic tape.

The test area chosen was part of Oman, an extremely arid region of mountains and desert on the eastern tip of the Arabian Peninsula (fig. 3). A reconnaissance geologic map (U.S. Geological Survey, 1963) at a scale of 1:2,000,000 showed large units of eolian sand, gravel, limestone, dolomite, chert, and ultrabasic igneous rocks—all likely targets for discrimination on the basis of reflectance and thermal properties. The Nimbus orbits provided data at about 1100–1200

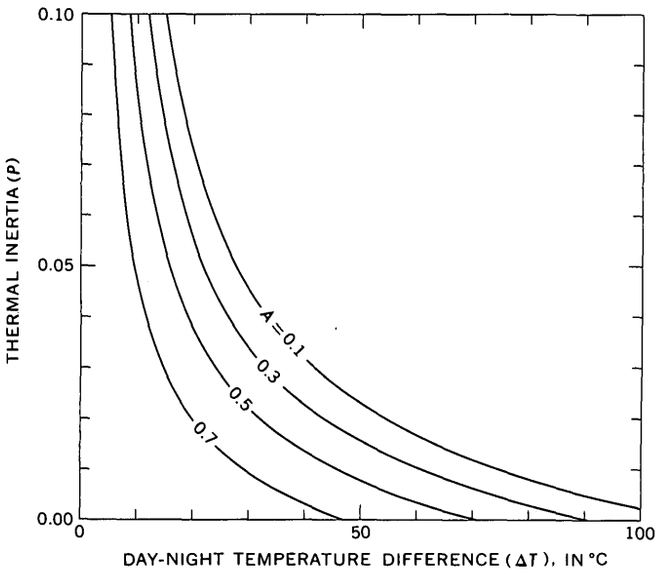

Figure 2.—Least-squares fit of thermal inertia (P) versus day-night temperature difference (ΔT) for different albedo (A). ΔT values computed from thermal model for given values of P and A. Form of functional fit $P = \alpha + B \times \Delta T + \lambda/\Delta T$.

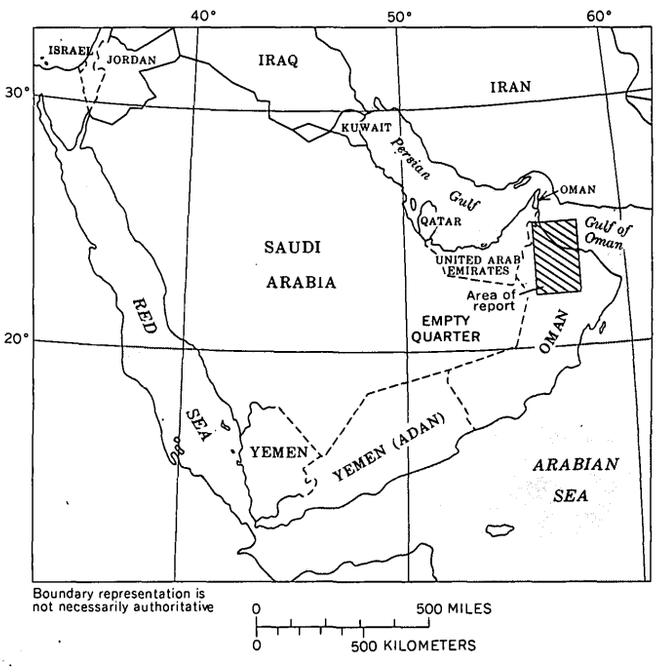

Figure 3.—Index map of Arabian Peninsula, showing Oman study area (patterned).

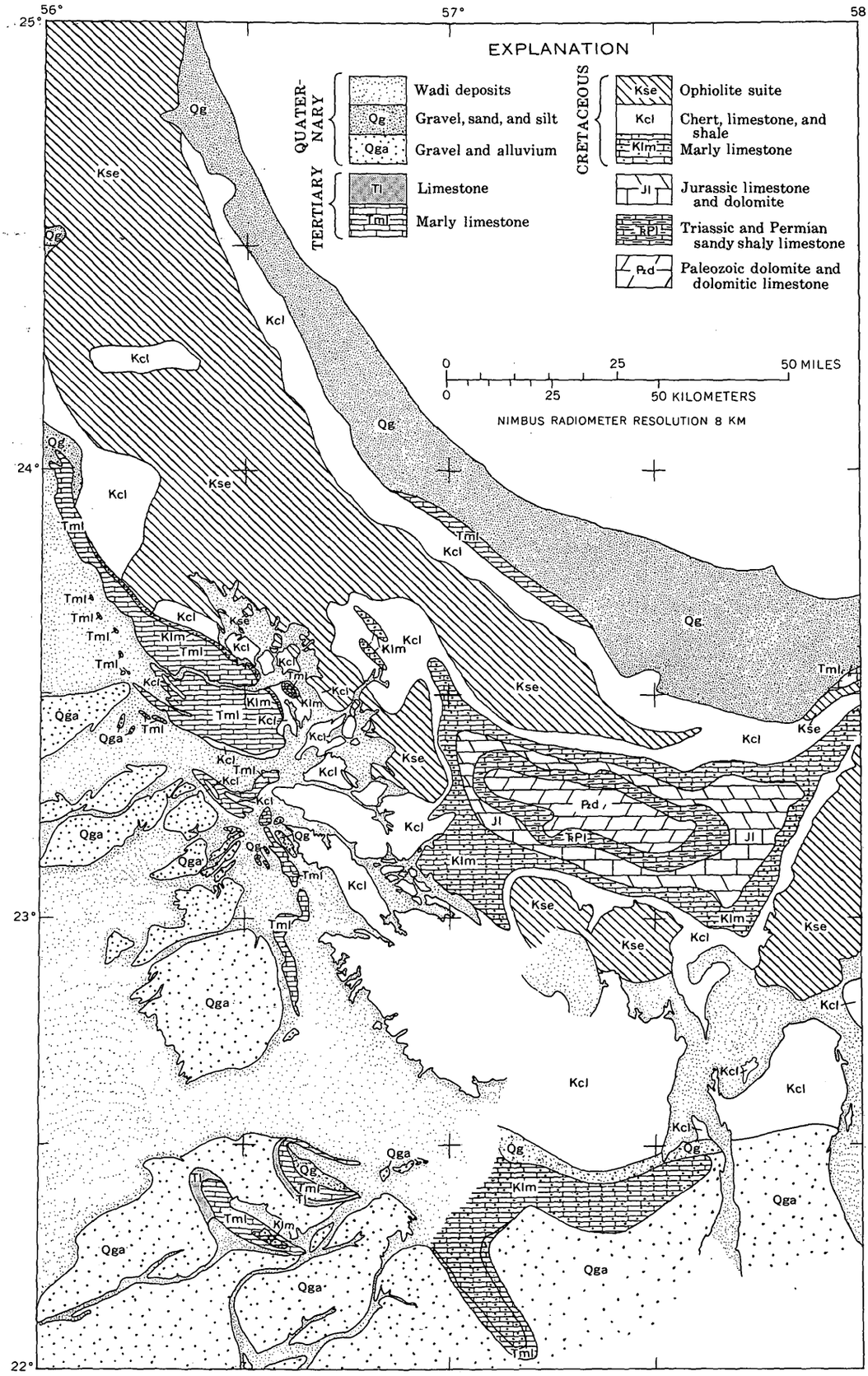

Figure 4.–Geologic map of a part of Oman (modified from U.S. Geological Survey, 1963; Glennie, 1970; Gemini IV photograph, June 4, 1965).

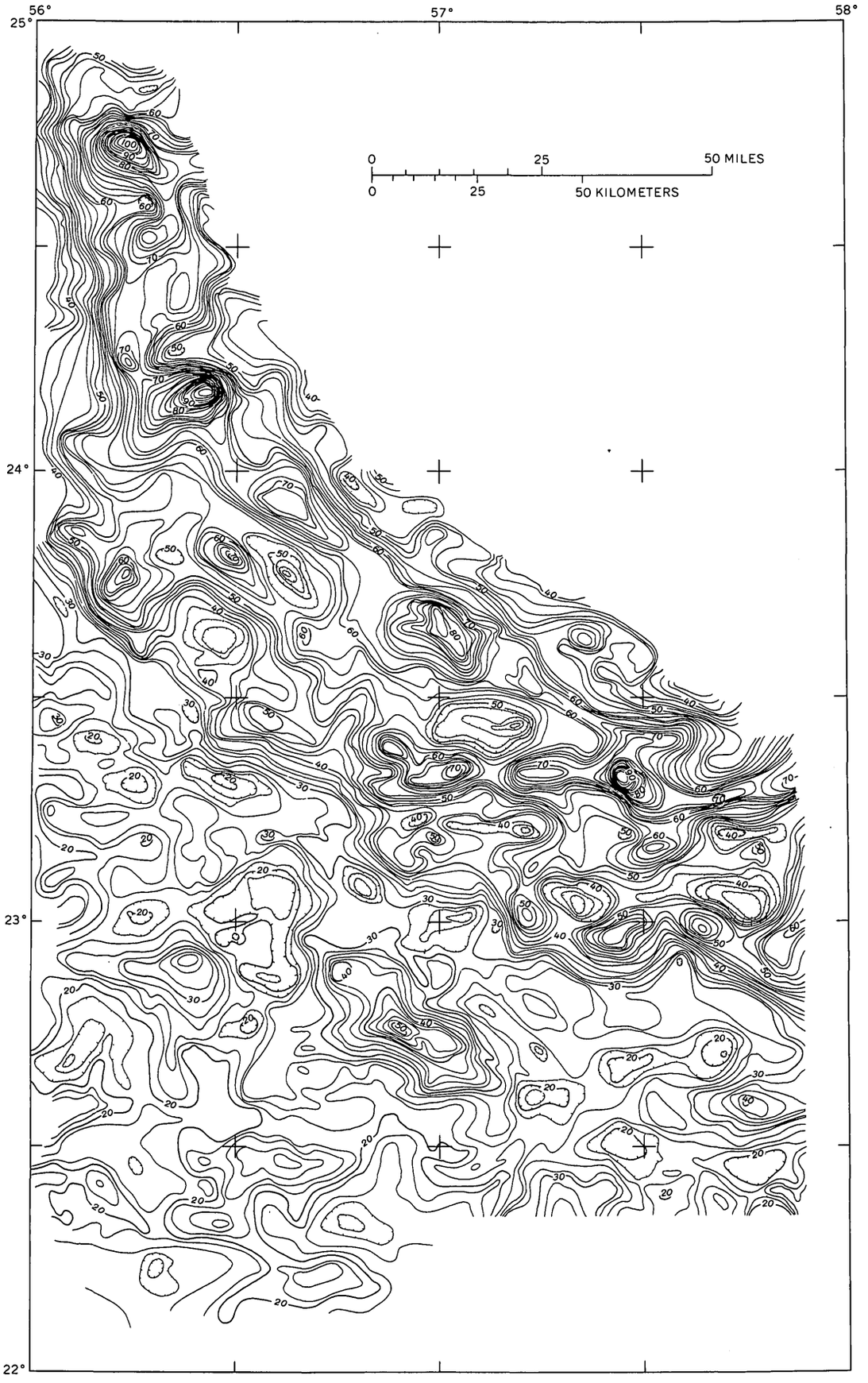

Figure 5.—Thermal inertia map of a part of Oman. Contour interval 2×10^{2} cal cm^{-2} $s^{-1/2}$. For true values multiply by 10^{-2}.

and 2300–2400 hours local time, offering approximately maximum and minimum surface-temperature measurements for Oman during the diurnal cycle.

Available reconnaissance maps at 1:2,000,000 scale for the whole area (U.S. Geological Survey, 1963) and 1:500,000 scale for the west half (Elberg and others, 1963) portrayed mostly bedrock configuration, rather than the surface materials sensed by the Nimbus radiometers, and so it was necessary to modify our base map. Some adjustments in geologic contacts and additions of stream-valley deposits were readily made by using topographic data from Aeronautical Chart and Information Center maps ONC H-7 and J-7. More details of wadi (stream-valley) deposits and other surficial materials were obtained from maps by Glennie (1970). These maps differentiated areas of sedimentation (primarily sand) from areas of deflation (primarily gravel), an important distinction from the aspect of thermal regimen. Other details of wadi deposits and geologic unit boundaries were added from Gemini IV color photograph S-65-34660. The resulting modified geologic map, prepared at a scale of 1:500,000, is shown in figure 4, for comparison with the various Nimbus maps.

Maps of reflectivity and day and night temperatures provided the basic data from which the final map showing thermal inertia could be produced. These maps were constructed by hand-plotting data from the computer listings. The reflectivity map was compiled from Nimbus III-HRIR daytime data taken November 11, 1969, on orbit 2829. The day and night temperature maps were plotted from Nimbus IV-THIR data from May 15, 1970 (orbit 497, day), and May 7, 1970 (orbit 396, night). Although 8 days elapsed between the two temperature-data acquisition times, careful examination of filmstrips showed that no major weather fronts moved through the study area during that period.

The basic maps display some obvious scale and shape discrepancies owing to radiometer pointing errors produced by small variations in spacecraft attitude. Other obvious discrepancies were caused by electronic variation in the tape recorders on board Nimbus. Basic-data maps and a discussion of corrections applied before using them in this analysis are given in the section on error analysis. These maps show only moderate correlations with the geologic map of the Oman area.

A temperature-difference (ΔT) map was constructed by superposing the positionally corrected day and night maps and subtracting the nighttime from the daytime temperatures at all points where contours on the two maps intersected. As explained in the previous section, the use of temperature amplitude minimizes the effects of emissivity and elevation differences, as ΔT is dependent primarily on thermal inertia and, to a lesser extent, on albedo. The ΔT map shows more detail (see section on error analysis) and has a stronger correlation with the modified geologic map than do the individual reflectivity and temperature maps.

The reflectivity and temperature-difference maps were then superposed, and the values were read at contour intersections. Thermal inertia values were then obtained for each intersection point from a look-up table derived by means of the computer model, and illustrated in figure 2. The thermal inertia map (fig. 5) produced by contouring the new data values has a much higher degree of correlation with the geologic map than do the basic-data maps. Contour shapes correspond well in many places to geologic contacts, and peak values of thermal inertia are fairly distinctive for several units. The high thermal inertia of the ophiolite suite, the intermediate thermal inertia of limestone units, and the low thermal inertia of wadi deposits and gravel units make these geologic materials readily distinguishable even at 8-km resolution.

To evaluate this correlation more quantitatively, means and standard deviations for ΔT and reflectivity were calculated for at least 50 points (selected by sample grid) within each of nine of the mapped rock, sand, and gravel units. These results are shown in figure 6. At least four different clusters of materials can be distinguished:

Cluster 1—Cretaceous ophiolite suite composed of ultramafic rocks, serpentinite, pillow lavas, gabbro, and diorite; also Paleozoic dolomite and dolomitic limestone.

Cluster 2—Predominantly Tertiary and Cretaceous marly and chalky limestones; mostly thick Cretaceous cherts but also detrital limestone, mudstone, breccia and some sandstones and shales (interestingly, the Cretaceous chert unit and the Cretaceous marly limestone are statistically similar, having

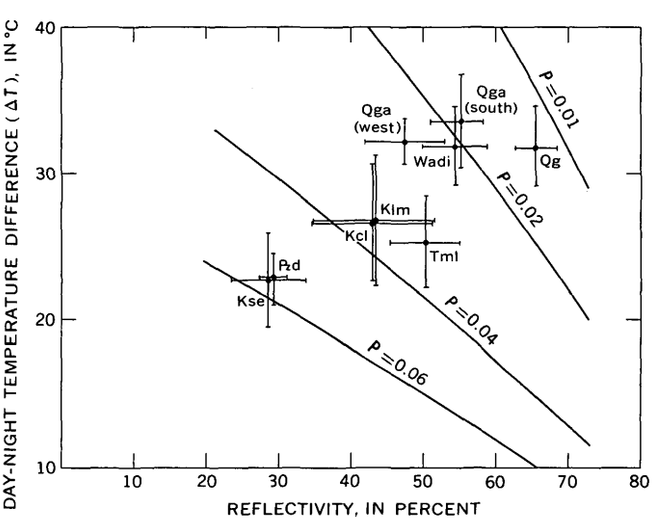

Figure 6.—Day-night temperature difference (ΔT) versus reflectivity for geologic units shown in figure 4 (means and standard deviations shown by crosses). *P*, thermal inertia, Qg, Quaternary gravel, sand, and silt; Qga, Quaternary gravel and alluvium; Tml, Tertiary marly limestone; Kse, Cretaceous ophiolite suite; Kcl, Cretaceous chert, limestone, and shale; Klm, Cretaceous marly limestone; Pzd, Paleozoic dolomite and dolomitic limestone.

identical means and standard deviations, and are trimodal in reflectivity and bimodal in ΔT).

Cluster 3—Primarily Quaternary gravel-dominated alluvial and wadi deposits in the west and south.

Cluster 4—Quaternary gravel, sand, and silt (including some dune sands) along the coast and just outside the west edge of the map area.

The geologic units cluster in different categories, indicating differences in thermal inertia and albedo. Curves of constant thermal inertia (derived from the thermal model) are drawn in figure 6 to illustrate the types of thermal inertia values associated with each cluster.

Even with the improvement provided by the thermal inertia map, conspicuous high-value anomalies not correlatable with the mapped geology were apparent along the ophiolite belt and in the area of the Jabal Akhdar massif (the anticlinal area centered on the Paleozoic rocks in the east-central part of the map). The good general correlation of thermal inertia and mapped rock units led us to suspect that the anomalous areas were ones where the 8-km Nimbus data might be more correct than the reconnaissance geologic map which in part was compiled on the basis of very widely spaced traverses. The Jabal Akhdar massif was shown on the geologic map as a domal area with a concentric distribution of sedimentary formations, yet the Nimbus data showed a single belt of high thermal inertia along the north side of the dome. This discrepancy was resolved upon examination of a more recent map of Jabal Akhdar by Wilson (1969). The new map showed that the massif was actually 15 km north of where it was located on the reconnaissance map, and that the high-thermal-inertia belt coincided with a central zone of quartzite and dolomite (fig. 7), both rock types which typically have high thermal inertia.

No information has been obtained to explain the other conspicuous anomalies within the ophiolite belt, but they are so sharply defined and of such high values that we believe they must be areas of unserpentinized ultramafic rock, or perhaps huge unmapped blocks of quartzite or dolomite. Thermal inertia lows within the ophiolite zone also may be unmapped rock units such as limestone or chert but are more likely explained as areas of talus or gravel cover.

CONCLUSIONS

This study demonstrates the feasibility of using satellite radiometer data for discrimination of geologic materials on the bases of thermal property differences. Even with data of 8-km resolution, the correlation of thermal inertia with mapped geology shown is more striking than might have been expected, and clearly indicates, we believe, the utility of the general technique. Thermal inertia mapping of geologic materials provides a means to discriminate some of these materials, and when thermal inertia is a diagnostic property of some material, identification also can be achieved. If these data are ambiguous, as for the unidentified Oman anomalies, additional data such as space photographs may provide enough information to decide among alternatives and identify materials remotely.

FUTURE APPLICATIONS

A significant advance can be achieved when Nimbus V data at 600-m resolution become available. Such information should permit rapid upgrading of reconnaissance geologic maps in some remote or poorly accessible part of the world. Because moisture in soils (not a significant factor in the Oman site) markedly affects their thermal inertias, Nimbus V data should provide an excellent opportunity to map and monitor changing near-surface moisture in many areas of hydrologic interest. With better resolution from aircraft altitudes, thermal inertia mapping can be applied to search for water-rich fracture zones, some kinds of ore bodies, and potential landslide areas.

ERROR ANALYSIS

Two primary sources of error were detected in the process of plotting the Nimbus data. The first was a pointing error owing to spacecraft attitude variations and was less than two resolution elements (16 km). The second source of error occurred in the individual scan lines and was apparently caused by flutter in the tape-recording system (A. W. McCulloch, NASA/Goddard, oral commun., 1971). Our previous study of thermal data in the Empty Quarter of Saudi Arabia (an area of seif dunes) showed that the magnitude of the flutter was equivalent to a temperature change of ±1.5°C. Although these effects were serious in the Empty Quarter where surface materials were relatively uniform and temperature contrasts were low, the scan-line anomalies caused by instrument noise in the Oman region were subdued, owing to the large temperature contrasts among differing rock units. Furthermore, topographic effects on temperature, especially during daytime, tended to mask some of the anomalies caused by tape-recorder flutter. The most conspicuous scan-line anomalies were smoothed by averaging with adjacent scan lines.

Basic-data maps made from the computer listings had to be corrected in varying degrees for pointing inaccuracies. Reflectivity, day temperature, and day-night temperature-difference maps are shown in figures 8, 9, and 10, and may be compared with the geologic map (fig. 4).

The reflectivity map (fig. 8) had coastline position discrepancies of less than one resolution element (8 km) within the study area. These small pointing errors were easily corrected by sliding the entire contour map to fit the true coastal outline and conspicuous inland features. The corrected reflectivity map has only a weak correlation with the geology; reflectivity values for the various geologic units clearly are not unique.

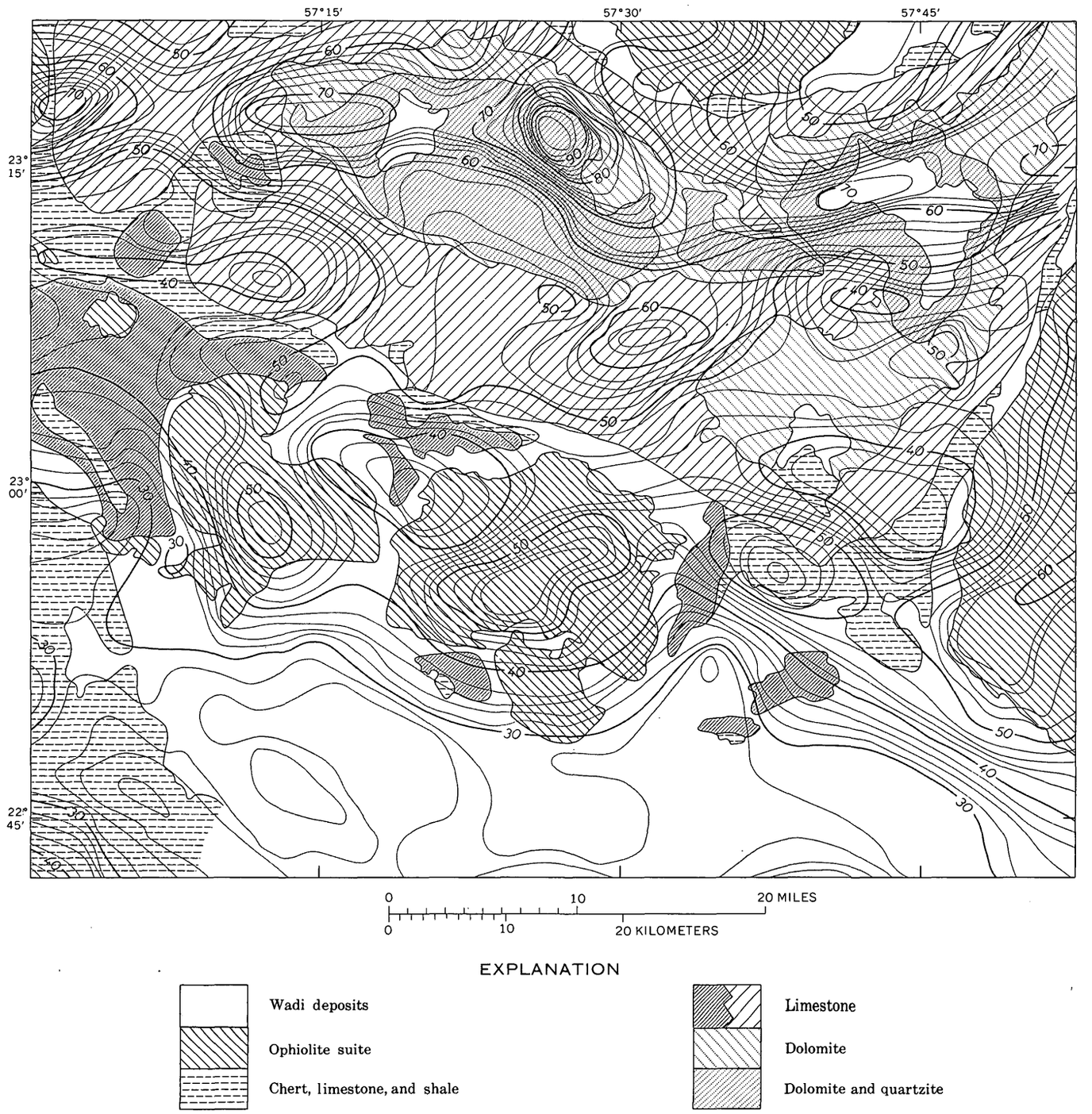

Figure 7.—Thermal inertia map at Jabal Akhdar, superposed on geologic map (Wilson, 1969). Contour interval 2×10^2 cal cm^{-2} $s^{-1/2}$.

Figure 9 shows the daytime temperature map, constructed from the raw data and not corrected for pointing error, but which nevertheless shows a modest correlation with the geologic map (fig. 4). The west-central part of the map exhibits large horizontal temperature gradients between the Tertiary marly limestone and the wadi deposits (fig. 9, area A) and between the wadi deposits and the Quaternary gravel and alluvium (areas B). The south-central part of the map (area C) shows steep gradients between the Cretaceous chert, limestone, and shale and the wadi deposits. In addition, the wadi deposits which extend into the Oman Mountains (area D) are represented by a clearly defined temperature anomaly. Finally,

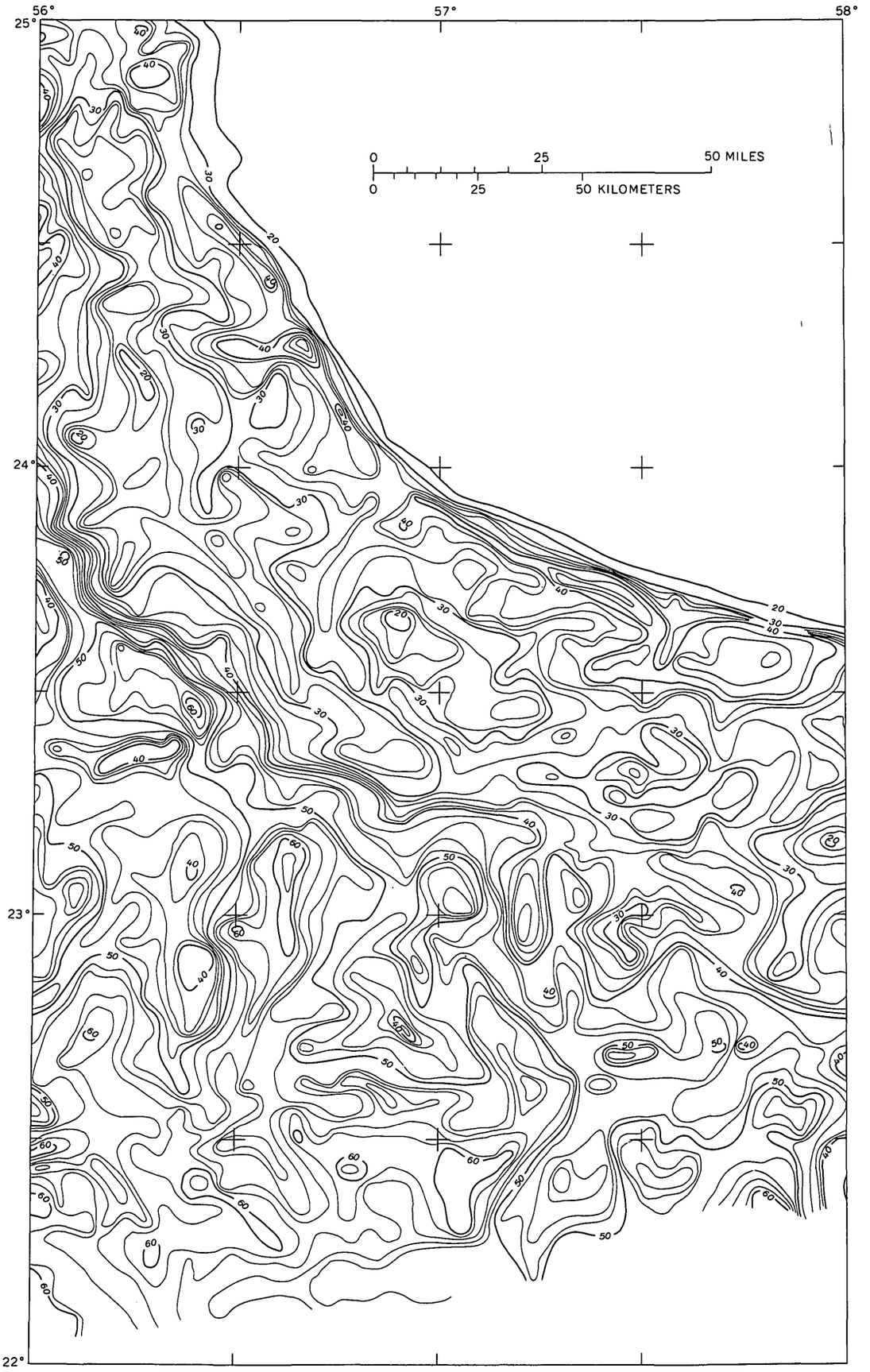

Figure 8.—Reflectivity map of a part of Oman. Compiled from Nimbus III-HRIR daytime data, November 11, 1969, orbit 2829. Contour interval 2 percent.

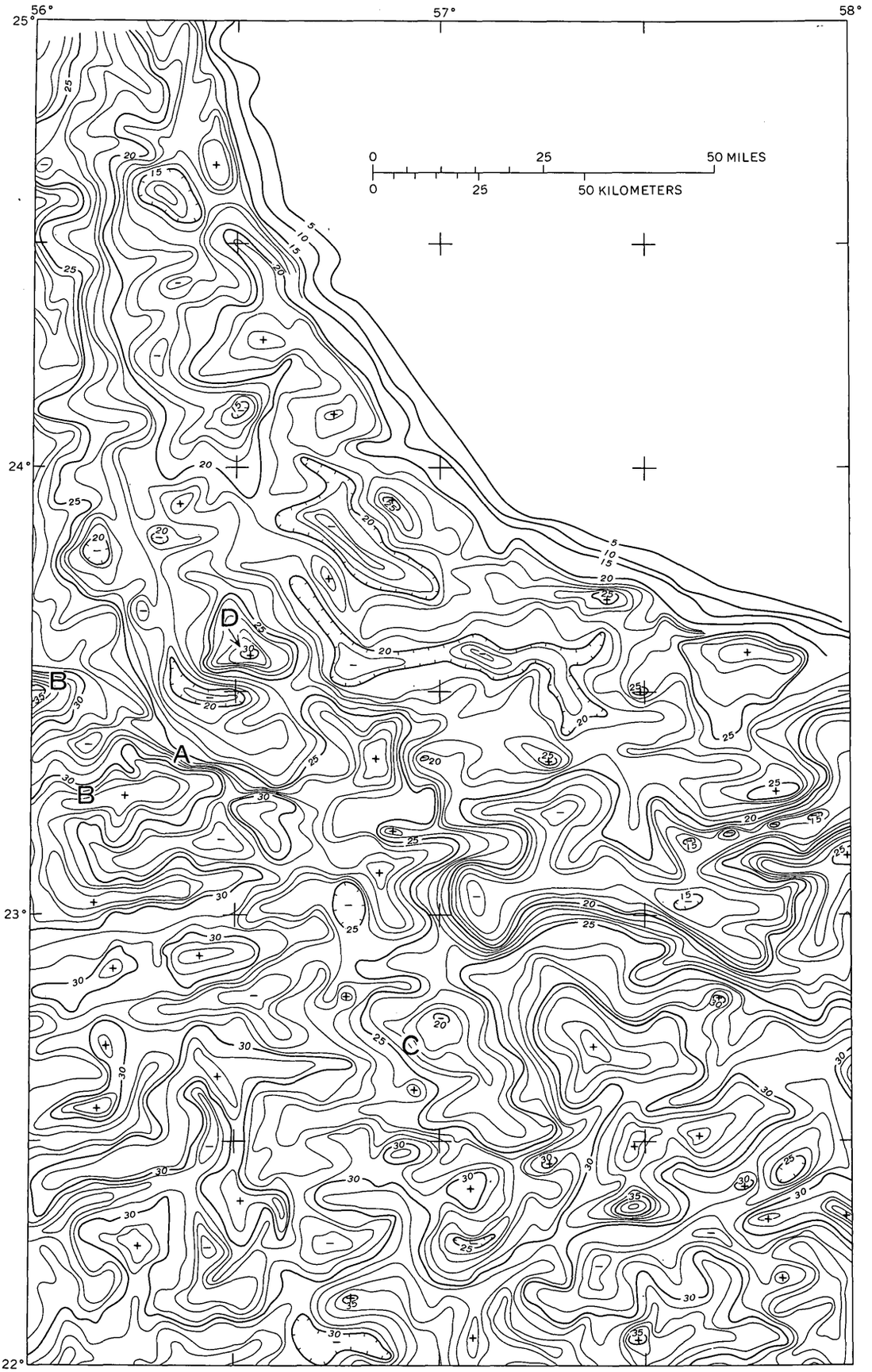

Figure 9.—Daytime temperature map of a part of Oman. Plotted from Nimbus IV-THIR data, May 15, 1970, orbit 497. Contour interval 1° C (add 300° C for correct values of absolute temperature). Hachured in closed areas of lower temperature.

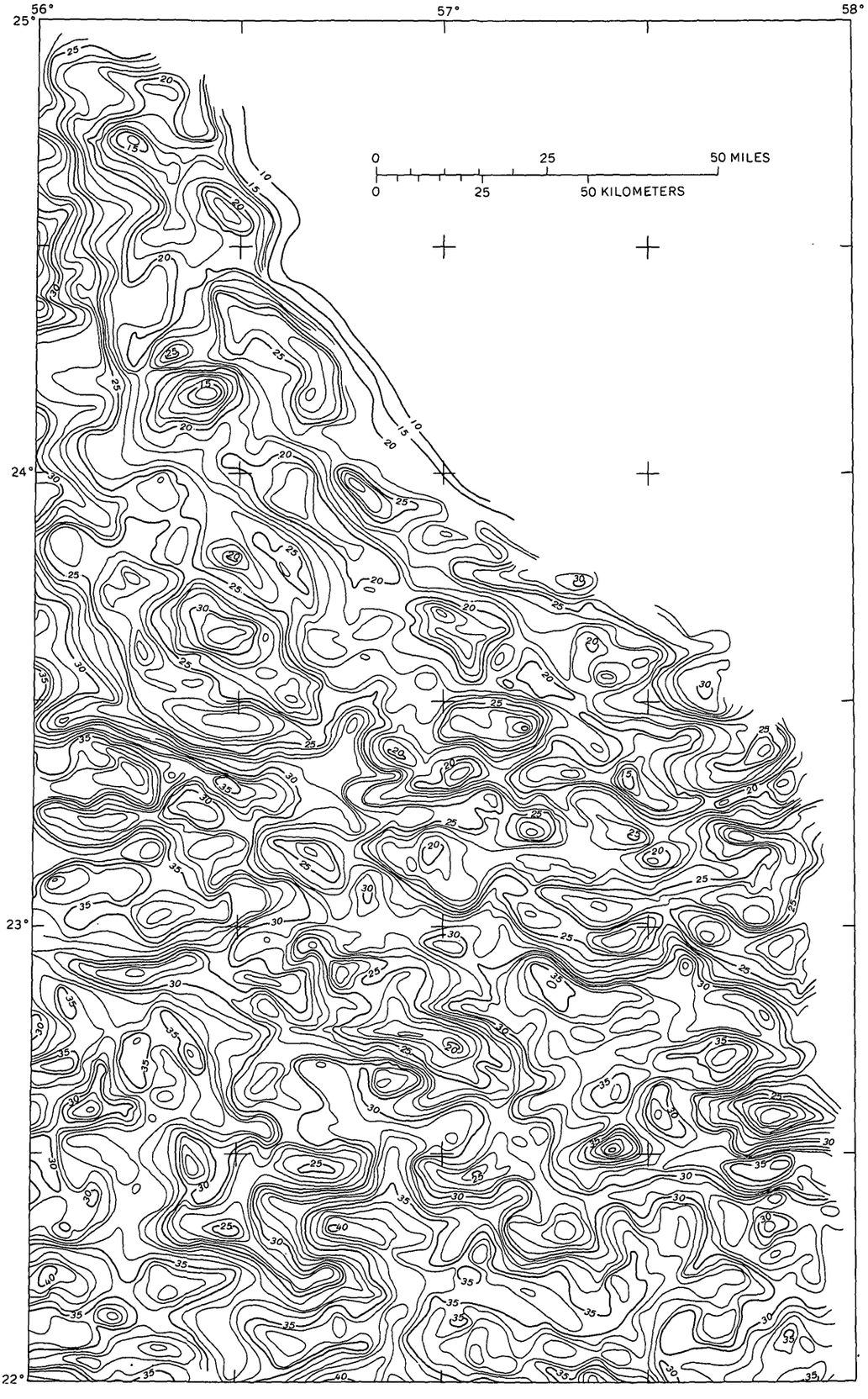

Figure 10.—Temperature difference (ΔT) of a part of Oman. Contour interval 1°C.

the coastline is well defined and its shape is a good approximation of the actual geography. Small-scale corrections for pointing error, however, were considered necessary for the detailed analysis described here. Different parts of the raw-data temperature map needed different directions and amounts of correction. The map was cut into three east-west strips which were separately adjusted to achieve a fit of contours to numerous topographic and geologic control points on the base map. Corrections generally were less than 8 km and no more than 16 km. The corrected map (not shown here) was used for the analysis described.

The nighttime temperature map (not shown) did not show the coastline, and had very few thermal anomalies that could be used as direct tie points to the geologic map. Several conspicuous anomalies, however, had shapes nearly identical with daytime anomalies which clearly correspond to topographic features. Thus the nighttime map could be corrected for positional inaccuracies simply by matching to the daytime temperature map.

Figure 10 shows the temperature-difference (ΔT) map constructed by superposing the positionally corrected day and night temperature maps and obtaining the temperature difference at each contour intersection.

ACKNOWLEDGMENTS

This research was supported by the National Aeronautics and Space Administration under Task 160-75-01-43-10. Acknowledgment is made to the National Center for Atmospheric Research (Boulder, Colo.), which is sponsored by the National Science Foundation, for part of the computer time used in this research. Paul Lowman, of Goddard Space Flight Center, brought the recent map of Jabal Akhdar to our attention; many other GSFC personnel were very helpful in providing the digital data and discussing problems encountered in using the data.

REFERENCES CITED

Carslaw, H. S., and Jaeger, J. C., 1959, Conduction of heat in solids: London, Oxford Univ. Press, p. 66, 401–402.

Cherrix, G. T., and Allison, L. J., 1969, The high resolution infrared radiometer (HRIR) experiment *in* Nimbus III user's guide: Natl. Aeronautics and Space Adm., p. 29–66.

Elberg, E. L., Gierhart, R. D., and Ramirez, L. F., 1963, Geologic map of the eastern Rub al Khali quadrangle, Kingdom of Saudi Arabia: U.S. Geol. Survey Misc. Geol. Inv. Map I-215A.

Glennie, K. W., 1970, Desert sedimentary environments, Volume 14 of Developments in sedimentology: Amsterdam, Elsevier, enclosure 3.

Jaeger, J. C., 1953, Conduction of heat in a solid with periodic boundary conditions, with an application to the surface temperature of the moon: Cambridge Philos. Soc. Proc., v. 49, pt. 2, p. 355–359.

McCulloch, A. W., 1970, The temperature-humidity infrared radiometer (THIR) experiment *in* Nimbus IV user's guide: Natl. Aeronautics and Space Adm., p. 25–63.

Pouquet, Jean, 1969a, Geomorphologie et ere spatiale: Zeitschr. Geomorphologie, v. 13, no. 4, p. 414–471.

——1969b, Geopedological features derived from satellite measurements in the 3.4–4.2 μ and 0.7–1.3 μ spectral regions: Internatl. Symposium on Remote Sensing of Environment, 6th, Ann Arbor, Mich. Proc., p. 976–988.

Rabchevsky, G. A., 1971, Hydrologic conditions viewed by the Nimbus meteorological satellite: Washington, U.S. Govt. Printing Office, Internatl. Workshop on Earth Resources Survey Systems, Proc., v. 2, p. 469–512.

Rowan, L. C., Offield, T. W., Watson, Kenneth, Cannon, P. J., and Watson, R. D., 1970, Thermal infrared investigations, Arbuckle Mountains, Oklahoma: Geol. Soc. America Bull., v. 81, p. 3549–3562.

U.S. Geological Survey, 1963, Geologic map of the Arabian Peninsula: U.S. Geol. Survey Misc. Geol. Inv. Map I-270A.

Watson, Kenneth, 1970a, Part A, Introduction and summary, and Part B, Data analysis techniques, *in* Remote sensor application studies progress report, July 1, 1968 to June 30, 1969: U.S. Dept. Commerce, Natl. Tech. Inf. Service, PB1-97 098.

——1970b, A thermal model for analysis of infrared images: Natl. Aeronautics and Space Adm. 3d Ann. Earth Resources Aircraft Program Rev., v. 1, sec. 13, 16 p.

Watson, Kenneth, Rowan, L. C., and Offield, T. W., 1971, Application of thermal modeling in the geologic interpretation of IR images: Internatl. Symposium on Remote Sensing of Environment, 7th, Ann Arbor, Mich., Proc., v. 3, p. 2017–2042.

Wilson, H. H., 1969, Late Cretaceous eugeosynclinal sedimentation, gravity tectonics, and ophiolite emplacement in Oman Mountains, southeast Arabia: Am. Assoc. Petroleum Geologists Bull., v. 53, no. 3, p. 626–671.

Jour. Research U.S. Geol. Survey
Vol. 2, No. 2, Mar.-Apr. 1974, p. 159—163

DENDRITIC DRY VALLEYS IN THE CONE KARST OF PUERTO RICO

By WATSON H. MONROE, San Juan, P.R.

Work done in cooperation with the Puerto Rico Department of Natural Resources

Abstract.—The depressions in the cone karst (Kegelkarst) of the area west of Ciales in the Lares Limestone are alined in dry valleys that have dendritic patterns. These valleys apparently record the former existence of a cover of noncalcareous clastic material that was deposited on the limestone in late Tertiary time. One system of dendritic dry valleys ends at an abandoned meander of the Río Grande de Manatí, which is about 60 m above the present floor of the river. Another system leads to large masses of "blanket sand" near the town of Florida. These valleys were apparently eroded during the late Pliocene or very early Pleistocene when sea level was at least 80 m higher than it is today.

Karst topography formed on the limestone formations of Oligocene and Miocene age in northern Puerto Rico includes large areas of cone karst or Kegelkarst, which commonly consists of steep-sided hills surrounded by irregularly shaped closed depressions. In the Ciales and Florida quadrangles (fig. 1), however, the cone karst contains continuous canyon-like dry valleys, which form dendritic patterns similar to those of consequent streams in nonkarst areas. These valleys occur in the Lares Limestone of Oligocene age. The strata exposed in the area are described in table 1 and shown in figure 2.

The area of cone karst west of Ciales was described by Lehmann (1954, p. 134, fig. 7) as typical of the type of Kegelkarst he designated "*gerichtete Karst*" or directed karst.

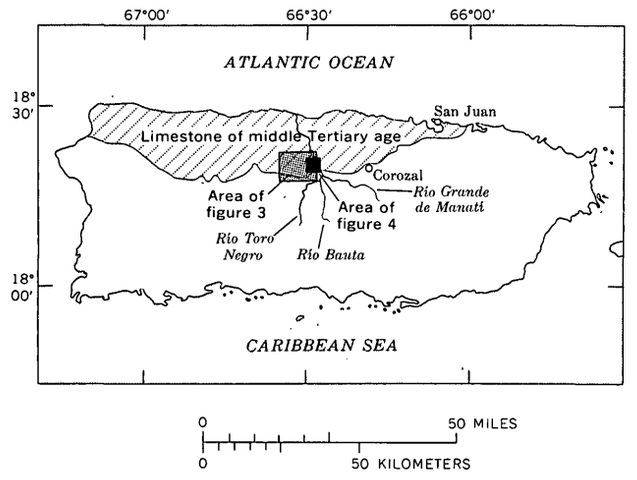

Figure 1.—Index map showing outcrop area of limestone of middle Tertiary age in northern Puerto Rico and areas of figures 3 and 4.

Table 1.—*Strata exposed in the Ciales—Florida area*

Age	*Unit and description*	*Thickness (meters)*
Quaternary...	Alluvium—sand, gravel, and cobbles.	0–5
Quaternary and Tertiary.	Blanket sand—mostly sandy clay	0–30
Miocene.....	Camuy Formation—sandstone and limestone, exposed north of area.	170
	Aymamón Limestone, exposed north of area.	200
	Aguada Limestone, exposed north of area.	90–115
	Cibao Formation—chalk and marl	10–180
	Montebello Limestone Member—friable pure calcarenite, indurated on exposure to an erosion-resistant limestone.	20–210
Oligocene....	Lares Limestone—crystalline limestone containing beds of fragmental limestone; basal part is thin-bedded limestone that contains grains of limonitic rock.	180–220
	San Sebastián Formation—mostly clay, subordinate amounts of sand and gravel.	0–70
Eocene to Cretaceous.	Several formations of tuffaceous and volcanic rocks, limestone, and intrusive rock.	Several thousand

He called attention to south-trending depressions arranged in long parallel lines between conical peaks, expecially in the Lares Limestone. He listed as reasons for the directed karst the influence of joint systems and outcrops of alternating resistant and less resistant strata. In other parts of the cone karst area of Puerto Rico, some of the trends in cone karst are probably related to jointing, but in the Ciales area they seem to have been superposed from a former cover of clastic material.

DESCRIPTION OF THE DRY VALLEYS

The dry valleys in the Ciales-Florida area form three distinct surface patterns (fig. 3). These patterns include a series of abandoned meanders of the Río Grande de Manatí and an eastern and a western dendritic system. In addition, there are several isolated fringing valleys, possibly related to the western system. The abandoned meanders of the Río Grande de Manatí are dry valleys now lined with swallow holes. The present

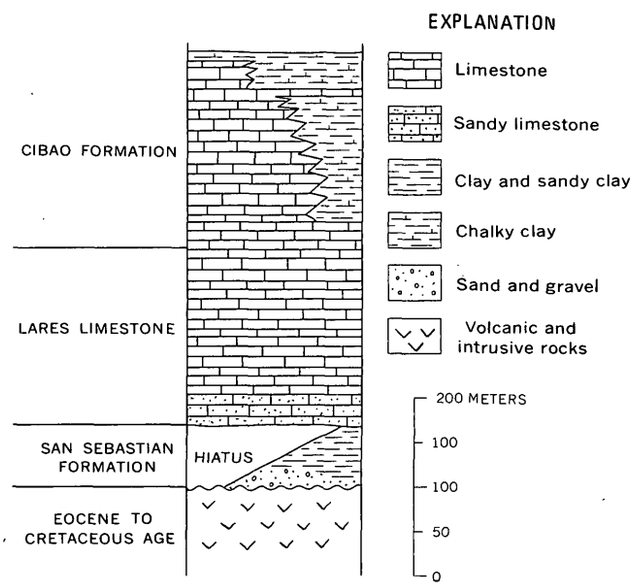

Figure 2.—Columnar section of rocks exposed in Ciales-Florida area.

altitude of the river valley is 25 m, some 500 m upstream from the bridge of Highway 149 (fig. 4). Altitudes of the abandoned meanders are approximately 30, 60, and 85 m above sea level.

The eastern system (fig. 4) consists of dry valleys that trend north and north-northeast from the top of the valley wall of the Río Cialitos to the dry abandoned meanders of the Río Grande de Manatí. The dry valleys in this system are rock canyons averaging about 50 m wide with walls about 70 m high (fig. 5). The canyons contain many swallow holes, so that there is no through drainage in any of these valleys; instead, all drainage is underground, except that after heavy rainstorms water flows to the nearest swallow hole downslope. The longest (about 4.9 km) of the dry valleys in the eastern system starts south-southeast of the Iglesia San Antonio at an altitude of about 310 m and trends generally north-northeast to an abandoned meander having an altitude of about 85 m.

The western system of dry valleys, which is within the Florida quadrangle (fig. 3), consists of one long dry valley, which has several tributary valleys, and some shorter dry valleys. The longest valley trends generally west past the longitude of the town of Florida and then bends abruptly north. The north-trending valley contains Highway 140 between Florida and Utuado, but the highway is omitted from figure 3. The bottom of the long valley, known for much of its length as Los Caños, drops from an altitude of 290 m at its southeastern end to an altitude of about 220 m at its junction with Highway 140, a drop of about 70 m in 11.4 km. Los Caños is a steep-sided valley whose limestone walls range in height from 35 to 115 m, averaging 75 m. The width of the canyon at the bottom is mostly less than 100 m, but at one place it widens to about 200 m. The bottom of the canyon is very irregular, as it is interrupted every 200 to 500 m by a swallow hole. The divides between the swallow holes generally become lower from southeast to northwest, but they are not very regular in their drop, as the lowest divide has an altitude

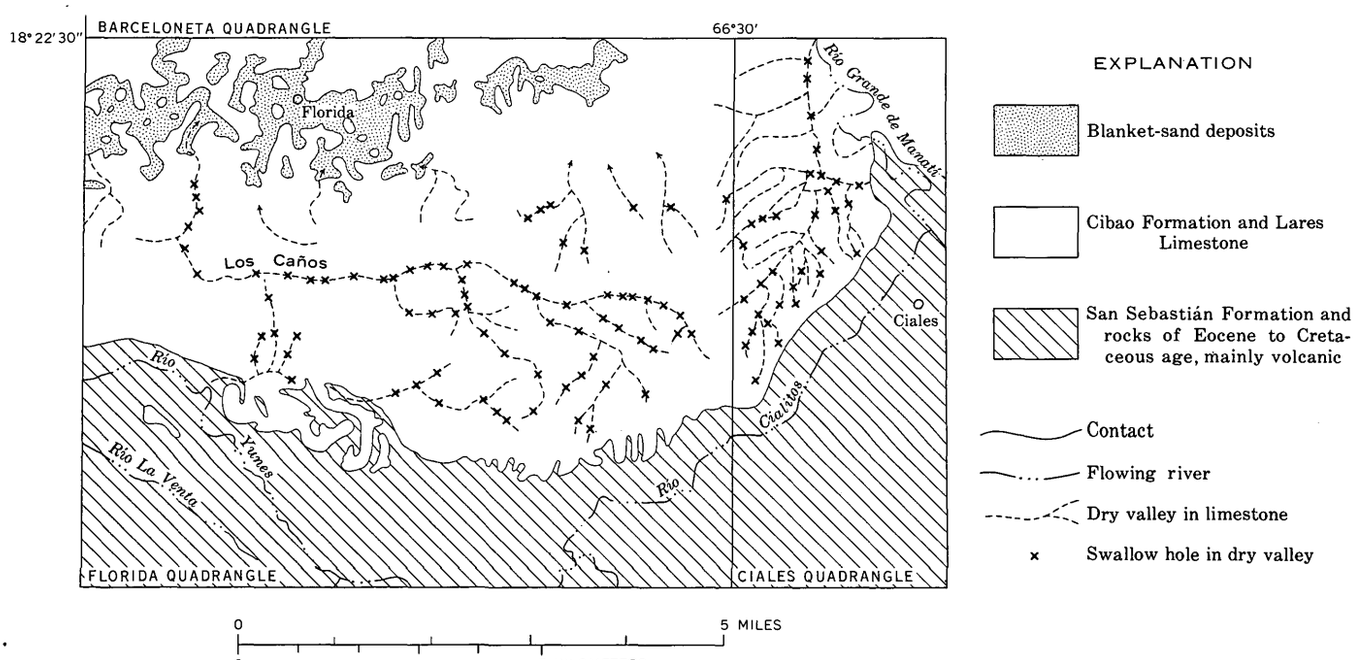

Figure 3.—Generalized geologic map of parts of the Florida and Ciales quadrangles showing dendritic pattern of dry valleys and locations of swallow holes.

Figure 4.—Part of the northwestern section of the Ciales 7½-minute quadrangle showing dendritic pattern of dry valleys (short-dashed lines) and of abandoned meanders of the Río Grande de Manatí long-dashed lines).

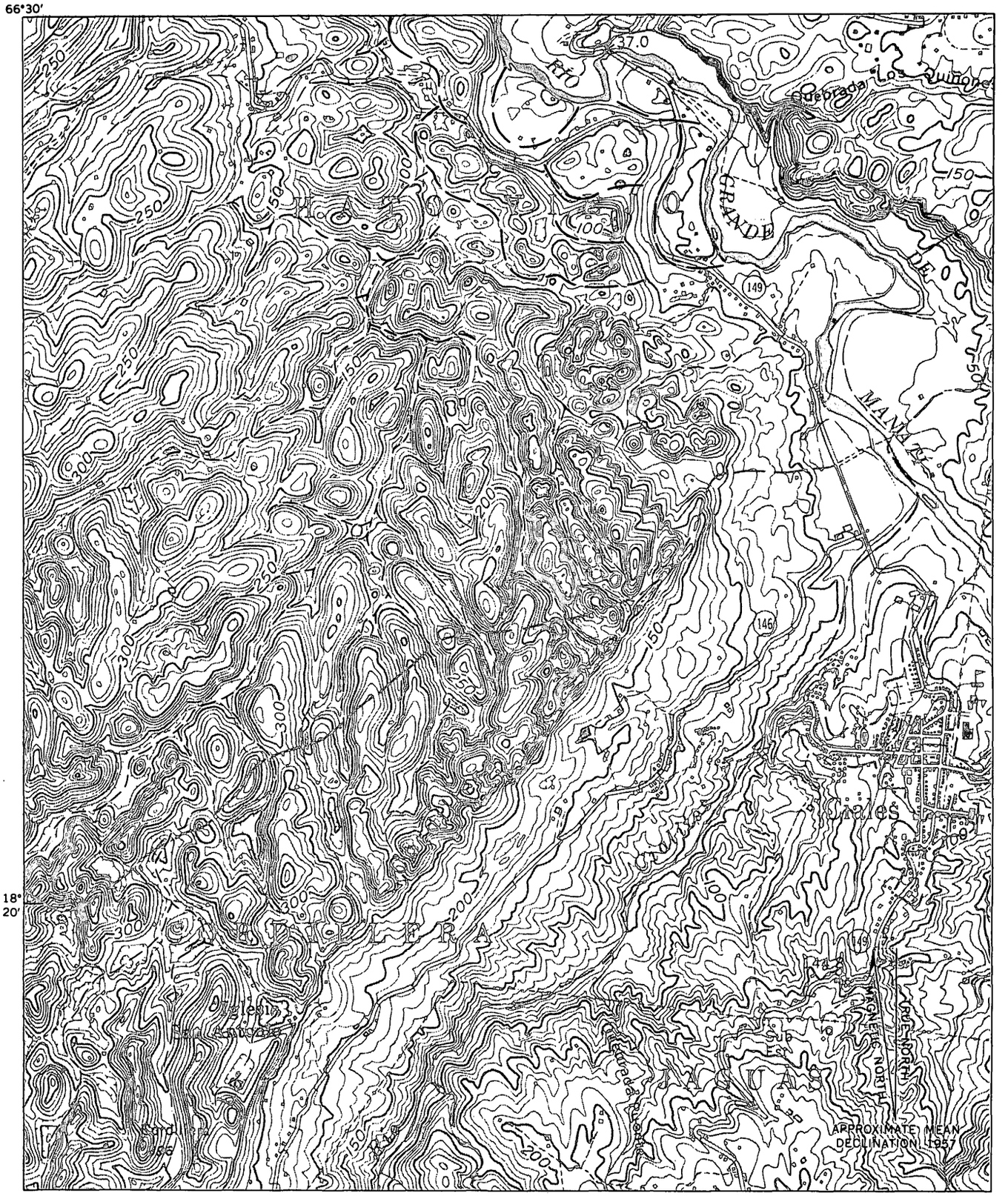
66°30'
18°
20'
RIO
GRANDE
DE
MANATI
Quebrada
Manatí
CORDILLERA
CENTRAL
MAGNETIC NORTH
APPROXIMATE MEAN
DECLINATION, 1957
0 ½ 1 MILE
0 ½ 1 KILOMETER
CONTOUR INTERVAL 10 METERS

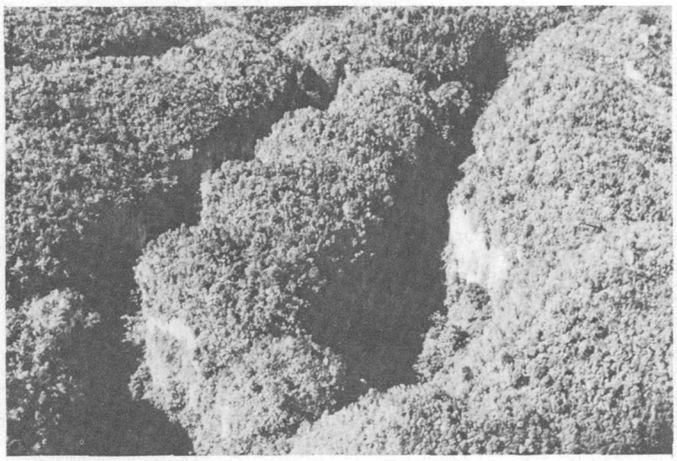

Figure 5.—Canyon at head of dendritic dry valley cut in Lares Limestone at top of northwest wall of Río Cialitos, west of Ciales.

of only 205 m, whereas divides nearby have altitudes of 215 m. The swallow holes along the canyon commonly consist of very small vertical or steep-sided holes in soil that has accumulated by washing downslope from the divides between the swallow holes. This mass of soil and alluvium is probably rather thin, but there are no cuts through it, so that its thickness is not known. The composition at most places consists entirely of clay, but in some of the deeper depressions a few grains of quartz were observed. Between the swallow holes the soil cover is rather thin, and at many places bare rock is at the surface.

Hildebrand (1960) collected about 10 samples of the clay at the bottom of this series of dry valleys. He found quartz, anatase, and kaolinite in nearly all samples; other minerals found in some samples include boehmite, goethite, hematite, halloysite, oligoclase, sanidine, and unidentified feldspars as well as organic matter. He believed that the deposits were derived from grains of volcanic rock carried into the area from the mountains to the south.

PROBABLE ORIGIN OF THE VALLEYS

The origin of the valleys in the Ciales quadrangle is undoubtedly related to the history of the Río Grande de Manatí, which acts today, and most likely has acted in the past, as the karst base level of the area. After deposition of the entire sequence of limestone of Oligocene and Miocene age, the river carved a part of its present valley, following a meandering course northward and depositing cobbles in terrace deposits. Many of the abandoned meanders can be recognized from place to place (fig. 4), and the terrace deposits are well shown on the geologic maps of the Ciales (Berryhill, 1965) and Manatí (Monroe, 1971) quadrangles.

While the river was cutting its valley, it seems likely that on the limestone upland at the sides of the river, solution may have been forming some kind of karst topography, but thus far it has not been possible to date any of the karst features with respect to the river except the dendritic dry valleys that are the subject of this paper.

The dendritic pattern of the karst valleys immediately southwest of Ciales (fig. 4) resembles the consequent drainage formed on an area of noncalcareous sedimentary rocks. If the drainage system began on a noncalcareous stratum that rested on the middle Tertiary limestones, the stratum must have been deposited at a time that the bed of the Río Grande de Manatí 2 km north of Ciales was at an altitude of about 100 m above sea level, or about 70 m above the present level. The valley of the Río Grande de Manatí was probably at this altitude during the Pliocene or the very early Pleistocene, that is, somewhat higher than the probable altitude of the coastline (80+ m) at about the time of the deposition of some of the blanket sand that is now found between ridges of Aymamón Limestone in the Barceloneta quadrangle (Briggs, 1965) to the northwest. The cover of clastic material itself was probably an alluvial-fan deposit washed off the upland of Cretaceous volcanic rocks (Nelson and Monroe, 1966) southwest of Ciales in the Florida quadrangle. This upland now has a ridge crest altitude of 500 to 600 m above sea level, but it has been deeply dissected by streams that appear to be extremely young in geomorphic terms. Conceivably an alluvial fan was deposited on the limestone surface at an altitude of slightly less than 400 m before the Río Cialitos had excavated its deep valley from the upland to the Río Grande de Manatí. The alluvial cover is postulated to have been very thin, less than 20 m thick; a dendritic drainage system formed rapidly, and such a drainage system had more or less the pattern shown in figure 4. Erosion soon exposed the hard limestone, and the drainage system that flowed to the Río Grande de Manatí began to entrench itself into the limestone. The form of the valleys was determined by the overlying drainage network, and steep-gradient streams heavily loaded with sediment caused fairly rapid erosion and entrenchment. As the water came in contact with the limestone, karstification began, and some water was lost to the underground. As the underground drainage network formed, more of the surface drainage went underground, and swallow holes got deeper, approaching the condition of today.

Presumably the Río Cialitos began as drainage on the more sandy beds in the lower part of the Lares Limestone. Erosion of these strata proceeded rapidly, and in a very short time the river reached the San Sebastián Formation and the underlying weathered rocks of the volcanic-intrusive complex. These rocks weather chemically faster than exposed hard limestone, for the limestone soon acquires a very hard surface crust (Monroe, 1966), which is resistant to solution and erosion and which sheds water rapidly during hard tropical rainstorms. The volcanic and intrusive rocks of Cretaceous to Eocene age do not form such a surface crust, and erosion proceeds as rapidly as weathering can take place. Consequently, throughout northern Puerto Rico, the lowermost limestone formation of the Oligocene-Miocene belt is bordered on the south by a deep

valley cut into the older rocks (Blume, 1970). An exception is in a few interstream divide areas where the San Sebastián Formation overlaps on the older rocks. This condition exists between the valleys of the Río Yunes and the Río Cialitos (fig. 3).

The rapid differential erosion by the Río Cialitos soon produced a steep-sided valley at the side of which the Lares Limestone formed a cliff face. Continued deepening of the valley encouraged landslides (Monroe, 1964) which today cover the upper part of the slope (Berryhill, 1965). Erosion by the ancestral Río Cialitos cut off all sources of alluvium and a large part of the former water supply for the dendritic valleys, and henceforth they received only the local rainfall. As the underground drainage network could handle this quantity of water very easily, surface flow, except for a few hundred meters upstream from the swallow holes, ceased.

Land sculpture in the area of figure 4 now results from (1) the breaking off of blocks of limestone at the top of the valley of the Río Cialitos and the slow sliding of these blocks down toward the river valley, accompanied by the breaking up of the large blocks into smaller blocks, (2) the gradual enlargement of swallow holes along dry valleys, (3) the spalling off of the limestone to form steeper slopes of the canyon walls as valleys deepen by solution and perhaps by a small amount of collapse of underground cavities, (4) the continued formation of meander scares by the heavily laden Río Grande de Manatí (note the recently abandoned meander just north of the road at the north edge of fig. 4), and (5) the continued deepening of the valley of the Río Cialitos to keep pace with deepening of the Río Grande de Manatí.

In the area to the west in the Florida quadrangle (fig. 3), a continuation of the alluvial fan covered the limestone, probably as far north as Florida. As no large river such as the Río Grande de Manatí was present, drainage probably was generally toward the north. After a very little erosion, northward drainage was barred when the erosion-resistant Montebello Limestone Member of the Cibao Formation was reached in the area just north of Los Caños. Drainage was then diverted to the west along the present course of Los Caños until the cuesta of the Montebello was breached. The fan may not have extended farther north than Los Caños, but, if so, it is difficult to account for the rather short branching dry valleys farther north.

North of the dry valleys, near Florida, is the southernmost belt in Puerto Rico of the "blanket sands," considered by Briggs (1966) to have had an alluvial origin. The blanket sands in the Florida area are considerably more clayey than those farther north; they consist of fairly acid clayey soils with a pH of 4.6 to 6.2 (Roberts and others, 1942). The main bodies of blanket sand farther north, in the outcrop belt of the Aymamón Limestone, are generally more sandy than the deposits near Florida.

The anomalous blanket sands of the Florida area are probably the highly weathered residue of the alluvium of the ancient alluvial fan, eroded from the surface by the Los Caños and other streams and deposited in the lowland near Florida, which is a short distance south of a prominent cuesta scarp of the Aguada Limestone.

Cone karst is present in some areas in Puerto Rico not near a trunk stream such as the Río Grande de Manatí. In these areas the depressions seem to be alined for short distances, but no dendritic pattern was detected on aerial photographs or topographic maps. The alinement in those areas is probably controlled by joint systems, as suggested by Lehmann (1954).

CONCLUSIONS

The dendritic patterns formed by dry valleys which consist of alined karst depressions suggest that the valleys are superposed from a former cover of clastic material. Such a cover could have consisted of alluvial fans deposited on the limestone during the late Tertiary, before incision of the minor tributaries of trunk rivers. The anomalous deposits of blanket sand near Florida may be remnants of these alluvial fans or, more likely, concentrations of the alluvium eroded from the dry valleys before all drainage passed underground.

Discovery of the dendritic dry valleys in Puerto Rico suggests that the cone karst areas of Jamaica, Java, and other tropical areas be reexamined to see whether such patterns are common to most areas of cone karst.

REFERENCES CITED

Berryhill, H. L., 1965, Geology of the Ciales quadrangle, Puerto Rico: U.S. Geol. Survey Bull. 1184, 116 p.

Blume, Helmut, 1970, Besonderheiten des Schichtstufenreliefs auf Puerto Rico: Kiel, Deutsche geog. Forschung Welt von Heute, Festschrift für Erwin Gentz, p. 167-179.

Briggs, R. P., 1965, Geologic map of the Barceloneta quadrangle, Puerto Rico: U.S. Geol. Survey Misc. Geol. Inv. Map I-421.

——1966, The blanket sands of northern Puerto Rico, in Caribbean Geol. Conf., 3d, Kingston, Jamaica, 1962, Trans.: Jamaica Geol. Survey Pub. 95, p. 60–69.

Hildebrand, F. A., 1960, Occurrences of bauxitic clay in the karst area of north-central Puerto Rico, *in* Short papers in the geological sciences: U.S. Geol. Survey Prof. Paper 400-B, p. B368–B371.

Lehmann, Herbert, 1954, Der tropische Kegelkarst auf den Grossen Antillen: Erdkunde, v. 8, no. 2, p. 130–139.

Monroe, W. H., 1964, Large retrogressive landslides in north-central Puerto Rico, *in* Geological Survey research 1964: U.S. Geol. Survey Prof. Paper 501-B, p. B123–B125.

——1966, Formation of tropical karst topography by limestone solution and reprecipitation: Caribbean Jour. Sci., v. 6, nos. 1–2, p. 1–7.

——1971, Geologic map of the Manatí quadrangle, Puerto Rico: U.S. Geol. Survey Misc. Geol. Inv. Map I-671.

Nelson, A. E., and Monroe, W. H., 1966, Geology of the Florida quadrangle, Puerto Rico: U.S. Geol. Survey Bull. 1221-C, 22 p.

Roberts, R.C., and others, 1942, Soil survey of Puerto Rico: U.S. Dept. Agriculture, Soil Survey Rept., ser. 1936, no. 8, 503 p.

Jour. Research U.S. Geol. Survey
Vol. 2, No. 2, Mar.-Apr. 1974, p. 165—174

CLASSIFICATION AND NEW GENERA OF NONCYSTIMORPH COLONIAL RUGOSE CORALS FROM THE ONESQUETHAW STAGE IN NEW YORK AND ADJACENT AREAS

By WILLIAM A. OLIVER, JR., Washington, D.C.

Abstract.—A proposed classification is outlined for 39 species of colonial rugose corals in 10 genera belonging to the families Stauriidae, Craspedophyllidae (including Cylindrophyllinae new subfamily and Craspedophyllinae), Disphyllidae?, and Zaphrentidae, from the Onesquethaw and lower Cazenovia Stages in New York and adjacent areas. These corals are described or redescribed in another report now in press. Three new genera, *Asterobillingsa, Grewgiphyllum,* and *Cyathocylindrium,* are described in this report.

A succession of coral faunas is present within the Onesquethaw and lower Cazenovia Stages in eastern North America. Corals are rare in the lower Onesquethaw (Siegenian and (or) Emsian Age). A homogenous and widespread middle Onesquethaw (Emsian) coral assemblage includes several colonial rugose corals. In New York this assemblage is found in the Schoharie and Bois Blanc Formations (fig. 1).

The Onondaga Limestone, except for its upper member, is late Onesquethaw (Eifelian) in age (fig. 1). The Onondaga, and equivalent formations in other parts of Eastern North America, contain a large variety of corals including many colonial rugose corals. The areal distribution of late Onesquethaw corals is partly controlled by facies, but similar successions of coral assemblages in New York, Ohio, and Kentucky provide the basis for biostratigraphic subdivision of the upper Onesquethaw. Colonial rugose corals are most numerous and diverse in bioherms within the Edgecliff Member of the Onondaga in New York and southwestern Ontario. They are fewer and less diverse in biostrome facies of the same age, but this facies is more widely developed. A still smaller colonial rugose coral assemblage in the higher Moorehouse Member of the Onondaga Limestone is also widespread.

The Seneca Member of the Onondaga Limestone is in the lower part of the Cazenovia Stage (Eifelian). Only one colonial rugose coral is known from this member in New York, but additional forms are known from other areas.

All colonial rugose coral species known from the Onesquethaw and lower Cazenovia Stages in New York and the Niagara Peninsula of Ontario, except the cystimorphs, have been described by Oliver (in press) on the basis of available specimens from all of Eastern North America. Some species

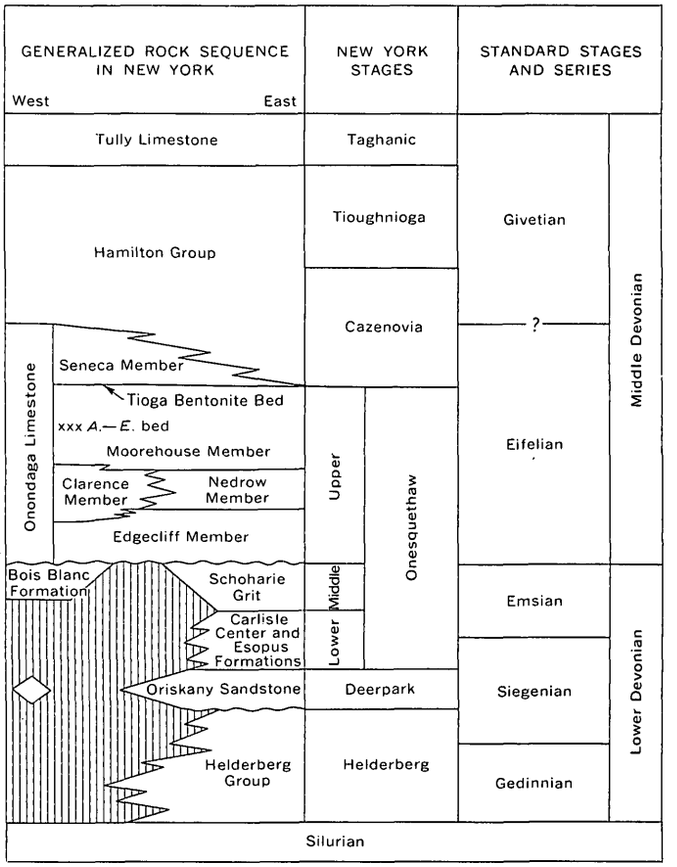

Figure 1.—Generalized stratigraphic column showing formations, members, and Eastern North American provincial stages mentioned in text. Correlations with standard European stages are shown, based on Oliver and others (1968, 1969). *(A.—E.* bed, *Acinophyllum-Eridophyllum* bed.)

from Kentucky, Ohio, Michigan, Quebec, and Venezuela are included in the same study because of their importance in understanding the New York-Ontario genera and species. The genera are described and interpreted on the basis of all known species. Most of the genera and all of the species are endemic to the Eastern Americas faunal realm. Their histories in the Eastern Americas Realm are outlined here and discussed in detail in the fuller account.

Acknowledgments.—Many individuals and institutions loaned specimens and provided other help in the systematic study of which this is a part. Specimens cited in this paper are deposited as follows: USNM, U.S. National Museum of Natural History, Washington; NYSM, New York State Museum, Albany; GSC, Geological Survey of Canada, Ottawa; AMNH, American Museum of Natural History, New York. W. J. Sando and J. T. Dutro, Jr., read the manuscript and made several suggestions that have been adopted in the final version.

CLASSIFICATION AND SYSTEMATIC DESCRIPTIONS

The new classification of Onesquethaw colonial rugose corals is given in outline form with an indication of the known stratigraphic and geographic range of the genera. Species described by Oliver (in press) are listed; named new species are listed as n. sp. unless also described here; those listed as sp. A, B, or C are so named in the bigger work. ENA is Eastern North America (east of the trans-continental arch). Taxa described or discussed in this report are marked with an asterisk(*).

Family Stauriidae M.-E. and H.[1]

Synaptophyllum Simpson (includes *Placophyllum* Simpson). ENA: late Onesquethaw; *S. arundinaceum* (Billings), *S. tabulatum* (Simpson), and *S.* n.sp. One additional species is known from Middle Devonian rocks in Washington State (Sorauf, 1972).

***Family Craspedophyllidae** Dybowski.

***Subfamily Cylindrophyllinae** n. subfam. Early Onesquethaw to Tioughnioga, ENA; middle or late Onesquethaw, Venezuela.

**Acinophyllum* McLaren. Middle and late Onesquethaw, ENA and Venezuela. ENA: middle Onesquethaw, *A. stokesi* (M.-E. and H.), *A. simcoense* (Billings); late Onesquethaw, *A. stramineum* (Billings), *A. segregatum* (Simpson), and *A. mclareni* Fagerstrom. Venezuela: *A. vermetum* (Weisbord).

**Cylindrophyllum* Simpson. Middle Onesquethaw to Tioughnioga, ENA; late Onesquethaw, Venezuela Scrutton, 1973, p.263–264). Possible occurrences in western North America and Viet Nam are discussed by Oliver (in press). ENA: middle Onesquethaw, *C.* n.sp.; late Onesquethaw, *C. elongatum* Simpson, *C. propinquum* Stewart, *C.* n. sp., *C.* sp. A.

**Prismatophyllum* Simpson. Middle Onesquethaw to Taghanic, ENA; (?)Middle Devonian, N. Africa. ENA: late Onesquethaw, *P. prisma* Lang and Smith, *P. ovoideum* (Davis); early Cazenovia, *P. annum* (Whitfield), *P. truncata* Stewart.

**Asterobillingsa* n. gen. Early Onesquethaw to Tioughnioga, ENA. Early Onesquethaw: *A. affinis* (Billings); middle and late Onesquethaw: **A. magdisa* n. sp., *A. rugosa* (Hall).

***Subfamily Craspedophyllinae** Dybowski. Middle Onesquethaw to Taghanic, ENA; Givetian, Morocco.

Eridophyllum M.-E. and H. (includes *Craspedophyllum* Dybowski, *Crepidophyllum* Nicholson and Thompson, and *Schistotoecholasma* Stewart). Late Onesquethaw to Taghanic, ENA; Givetian, Morocco. ENA: late Onesquethaw, *E. seriale* M.-E. and H., *E. conjunctum* (Davis), *E. subseriale* Stumm, *E.* n. sp., *E.* n. sp.

**Grewgiphyllum* n. gen. Middle to late Onesquethaw, ENA: *G. colligatum* (Billings).

***Family Disphyllidae** Hill. In ENA known only from Cazenovia and Tioughnioga Stages in Michigan, Hudson Bay Lowlands, and Quebec. Widespread in Old World Realm.

?*Disphyllum* Fromental. Same ENA range as family. Cazenovia: *D.? rectiseptatum* (Rominger), *D.? stummi* (Oliver).

***Family Zaphrentidae** M.-E. and H. ENA colonial forms range from middle Onesquethaw to Taghanic.

**Cyathocylindrium* n. gen. Middle to late Onesquethaw, ENA. Late Onesquethaw: *C. gemmatum* (Hall), **C. opulens* n. sp., *C.* n. sp. A.

**Heliophyllum* Hall. ENA colonial forms range from middle Onesquethaw to Taghanic. Middle Onesquethaw, *H.* n. sp., *H.* n. sp.; late Onesquethaw, *H. coalitum* (Rominger), *H. monticulum* (Ehlers and Stumm), *H.* n. sp., *H.* n. sp. B, *H.* n. sp. C.

Family Craspedophyllidae Dybowski, 1873

Diagnosis.—Solitary(?), phaceloid, cerioid, phaceloid-cerioid, astreoid, and thamnasterioid rugose corals having long or short, very attenuate major septa marked by zigzag carinae. The septa characteristically are composed of very fine monocanthine trabeculae and appear in most sections to have a dark axial zone with light tissue on either side. The major septa are deflected to form an aulos in the Craspedophyllinae but this structure is lacking in the Cylindrophyllinae. The dissepimentarium is formed by one to several rows of globose normal dissepiments. Tabulae are variable but commonly flat or slightly arched axially and downbent at the margin of the tabularium.

Included subfamilies.—Cylindrophyllinae new, and Craspedophyllinae.

Discussion.—The Craspedophyllidae as here recognized includes *Eridophyllum* (=*Craspedophyllum*) and related forms in the nominate subfamily, and a group of genera previously generally classified as Disphyllidae, here assigned to the new subfamily Cylindrophyllinae. The Cylindrophyllinae are the Billingsastraeinae of Jell (1969, p. 63), but this name is not available as the genus *Billingsastraea* is unrecognizable but probably a Silurian coral unrelated to the forms on which our concept of *Billingastraea* has been based.

The cylindrophyllinids differ from the disphyllids (s.s.) (essentially the Disphyllinae of Jell) in having strongly attenuate septa formed of fine monacanths with well-developed zigzag carinae. In contrast the disphyllids have thicker septa formed of coarse monacanths and generally lack such marked carinae.

Eridophyllum and its allies (Craspedophyllinae) differ from the Cylindrophyllinae only in the possession of an aulos and are also a distinctly Eastern North American development. It seems likely that the Craspedophyllinae were derived from the

[1] Milne–Edwards and Haime.

Cylindrophyllinae in middle Onesquethaw time. The degree of relationship between the Craspedophyllidae and the Disphyllidae is more difficult to analyze, but no true disphyllids are known from Eastern North American rocks older than the Cazenovia Stage.

Subfamily Cylindrophyllinae n. subfam.

part 1969 Billingsastraeinae Jell, p. 63.

Type genus.—*Cylindrophyllum* Simpson.

Diagnosis.—Craspedophyllids that lack an aulos.

Included genera.—*Cylindrophyllum* Simpson, *Prismatophyllum* Simpson, *Acinophyllum* McLaren, *Asterobillingsa* new genus (= part of *Billingsastraea* of most authors).

Discussion.—The earliest known cylindrophyllinid is *Asterobillingsa affinis* (Billings), from the Grande Grève Limestone (early Onesquethaw Age), Gaspé, Quebec, known from a single specimen. Except for this isolated occurrence, all four genera are first known at essentially the same time in the middle Onesquethaw. Similarities suggestive of intergeneric relationships are not particularly helpful in understanding evolution within the subfamily.

Genus *Acinophyllum* McLaren

Discussion.—McLaren (1959, p. 22–23) and Scrutton (1968, p. 272–273) considered that *Acinophyllum* might be or was a junior synonym of *Peneckiella* because of general similarities and "peneckielloid" dissepiments in the former. I consider *Acinophyllum* to be distinct from *Peneckiella* in the nature of its dissepiments as well as in other characters mentioned in the family diagnosis and discussion. Examination of hundreds of longitudinal sections of several species of *Acinophyllum* has produced no suggestion of peneckielloid, sigmoidal, or horseshoe dissepiments. *Acinophyllum* dissepiments are invariably globose, normal dissepiments, both in the characteristic peripheral row and in inner, supplemental rows. I consider it clear, that *Peneckiella* is a phillipsastraeid while *Acinophyllum* is not. Additional family level characters that separate the two genera are the microstructure and the presence of abundant septal carinae in *Acinophyllum*.

Genus *Cylindrophyllum* Simpson

Diagnosis.—Phaceloid cylindrophyllinids with relatively wide dissepimentarium commonly consisting of from three to eight rows of normal globose dissepiments. Zigzag to subyard-arm carinae are present to abundant on major and minor septa.

Genus *Prismatophyllum* Simpson

I agree with Jell (1969, p. 69) that *Prismatophyllum* differs from *Hexagonaria*, with which it has commonly been synonymized, in its attenuate septa composed of fine monacanthine trabeculae; in addition it commonly has a relatively broad dissepimentarium. *Hexagonaria* is typically disphyllid in its characters and its gross similarity to *Prismatophyllum* is interpreted as due to parallel or convergent evolution.

In Eastern North America, *Hexagonaria* is known only from rocks of Tioughnioga Age in Michigan and the Hudson Bay Lowlands; it is widespread in the Old World Realm. In contrast *Prismatophyllum* is known only from Eastern North America but from rocks of middle Onesquethaw to Taghanic age.

Genus *Asterobillingsa* n. gen.

not 1917 *Phillipsastraea (Billingsastraea)* Grabau, p. 957.

part 1937–1970 *Billingsastraea* of authors.

Type species.—*Asterobillingsa magdisa* n. sp., Schoharie Grit, Clarksville, Albany County, New York.

Diagnosis.—Astreoid to thamnasterioid cylindrophyllinid corals with calices having a central pit and a broad horizontal or reflexed peripheral platform, commonly with a raised zone around the pit. Septa are radially arranged and lightly to heavily carinate with zigzag to subyard-arm carinae. Major and minor septa extend from the periphery; minor septa terminate at the outer margin of the tabularium; major septa extend to or almost to the axis. At their peripheral ends the septa abut against those of adjacent corallites, are continuous into the next corallite, or more rarely are partly discontinuous. The tabularium is narrow and composed of closely spaced, more or less horizontal, complete and incomplete tabulae. The dissepimentarium is composed of gently to strongly globose dissepiments that are horizontally arranged except next to the tabularia where they are inclined toward the corallite axes.

Discussion.—*Asterobillingsa* is proposed to replace *Billingsastraea* Grabau which is unusable in its conventional concept and is a probable junior synonym of *Arachnophyllum* Dana. *Billingsastraea* was established by Grabau (1917, p. 957) who merely used the word in a list of fossils as "*Phillipsastraea (Billingsastraea) verneuili* E. and H." No description or other indication of his taxonomic concept was given. Clearly, the specific reference was to *Phillipsastraea verneuili* Milne-Edwards and Haime (1851, p. 447–448, pl. 10, fig. 5), stated to be from Wisconsin. The type specimen of this species has been assumed to be a drift specimen, originating in either the Onondaga or Bois Blanc Formation of Ontario or Michigan (Stumm, 1949, p. 35). None of the subsequent descriptions or diagnoses of the genus or species have been based on the holotype; all have been based on specimens of one or another of three species or subspecies of astreoid rugose corals from the Onondaga and Bois Blanc Formations in Ontario and New York.

I choose to use a new generic name for these three species and their congeners for the following reasons:

1. Inquiries and searches by interested specialists have failed to locate the holotype which was presumably in the deVerneuil Collection, École des Mines, Paris.
2. Although the Milne-Edwards and Haime specimen has not been found, Dr. P. Semenoff-Tian-Chansky located another specimen in the collection that is remarkably like the original in surface appearance (the only view of the original that was illustrated). This specimen is labeled as being from

an area, now in northeastern Iowa, that was a part of the Wisconsin Territory from 1836–1838. This second specimen is clearly an *Arachnophyllum* and probably from the Niagaran Hopkinton Dolomite that crops out in northeastern Iowa and southwestern Wisconsin. Therefore, it is possible (or probable?) that the holotype of *Billingsastraea verneuili* would prove to be an *Arachnophyllum* if found.

3. The only known local source for a Devonian coral in Wisconsin would be the small area of Devonian rocks at Milwaukee, Wis. However, no "*Billingsastraea*" are known from this area, and there is no indication that this area was known or that collections from this area were available before about 1860 (Cleland, 1911, p. 21).
4. The suggestion that the holotype of *Billingsastraea* is a drift specimen ultimately derived from Michigan or Ontario does not pass critical examination. Possible sources would be the Mackinac Straits area of the northern Lower Peninsula of Michigan, and southwestern Ontario. "*Billingsastraea*" occurs in both areas but transportation to Wisconsin would require southwesterly and westerly glacial movement across the Lake Michigan basin. Reference to the Glacial Map of North America (Flint and others, 1945) and other generalized sources suggests that ice movement was generally southerly, parallel to the Lake Michigan trough, and that a source east of the lake is unlikely for any drift specimen found in Wisconsin. A source in the Silurian of southwestern Wisconsin is far more likely.

Any one of these reasons is an adequate argument for abandoning *Billingsastraea* and starting fresh. A new start is long overdue and is logically made by basing a new genus on a species that will maintain, insofar as is practical, the present concept of "*Billingsastraea*". I have tried to do this by basing *Asterobillingsa* on the species most often referred to as "*verneuili*" and have selected a name for the genus that is reminiscent of both the first name applied to this genus by Vanuxem and the name under which it was known for so many years.

Other names that have previously been suggested to be synonyms of "*Billingsastraea*" are *Asterocycles* Vanuxem, 1842, *Radiastraea* Stumm, 1937, and *Keriophylloides* Soshkina, 1951.

Asterocycles Vanuxem and its type species (*A. confluens* Vanuxem, 1842, p. 136) were described but not illustrated. They were probably based on a specimen of *A. magdisa*, but the holotype is lost or unrecognizable and there is no way to be certain of its identity. Vanuxem's genus and species are indeterminate and not suitable as a replacement for *Billingsastraea.*

Radiastraea differs from *Asterobillingsa* in its incomplete tabulae, some of which are strongly arched in the periarial region, in lacking raised calice rims, and in its weak carinae. I now agree with Pedder (1964, p. 446–447) and Jell (1969, p. 63) that the two genera are distinct.

Keriophylloides was placed in synonymy with *Billingsastraea* by Soshkina and Dobrolubova (1962, p. 336). Most species assigned to the genus are phillipsastraeids as suggested by Jell (1969, p. 63). The structure of the type species is less clear, but spindle-shaped septa and trabecular fans are present and it is clearly not a craspedophyllid.

"*Billingsastraea*" as used for corals of Early and Middle Devonian age in Eastern North America has included astreoid forms that I interpret as belonging to two groups, cylindrophyllinids and zaphrentids. *Asterobillingsa* is established for the cylindrophyllinids and is considered to include the species listed in the table at the beginning of this section plus *A. canadensis* (Ehlers and Stumm) from the Tioughnioga Stage in southwestern Ontario.

Asterobillingsa magdisa n. sp.

Figures 2*a–e* and 3*a–d*

Occurrence of holotype.—Schoharie Grit, near Clarksville, Albany County, N.Y.

Diagnosis.—*Asterobillingsa* with small to medium-sized corallites; major septa extend to or nearly to the axis where a few commonly meet; zigzag carinae are strongly to weakly developed on all septa within the dissepimentarium.

Description.—Septa radially arranged. Major septa extend from margin of corallite nearly to the axis where two or more septa may join to form a simple axial structure. Minor septa are limited to the dissepimentarium. Peripherally the septa abut against those of the adjacent corallite, or in a few cases appear to be continuous; peripherally discontinuous septa are rare. All septa are attenuate and uniform in thickness in the dissepimentarium; in some colonies the major septa thicken slightly as they enter the tabularium. The mean and observed range of number of major septa per corallite (n), corallite diameter (d), and tabularium diameter (dt), in 10 or more corallites from 21 coralla is:

	n	d (mm)	dt (mm)
Mean	16.4	12.3	3.5
Observed range	14.4–19.8	8.0–16.9	2.6–4.3

Zigzag and occasional yard-arm carinae are long and closely spaced in most corallites of most coralla. On the sides of the septa and in properly oriented longitudinal sections, the carinae appear as low, flangelike ridges directed inward and upward, which are steepest toward the periphery.

The dissepimentaria occupy a large part of each corallum. In longitudinal sections the dissepiments are arranged in rows that are more or less horizontal except near the tabularia where they arch sharply upward, then down to form a crest at the tabularium-dissepimentarium boundary.

The tabularia are narrow; tabulae are incomplete forming a shallow W-shaped pattern that is gently arched axially and depressed peripherally. Tabulae are closely spaced, averaging several per millimeter.

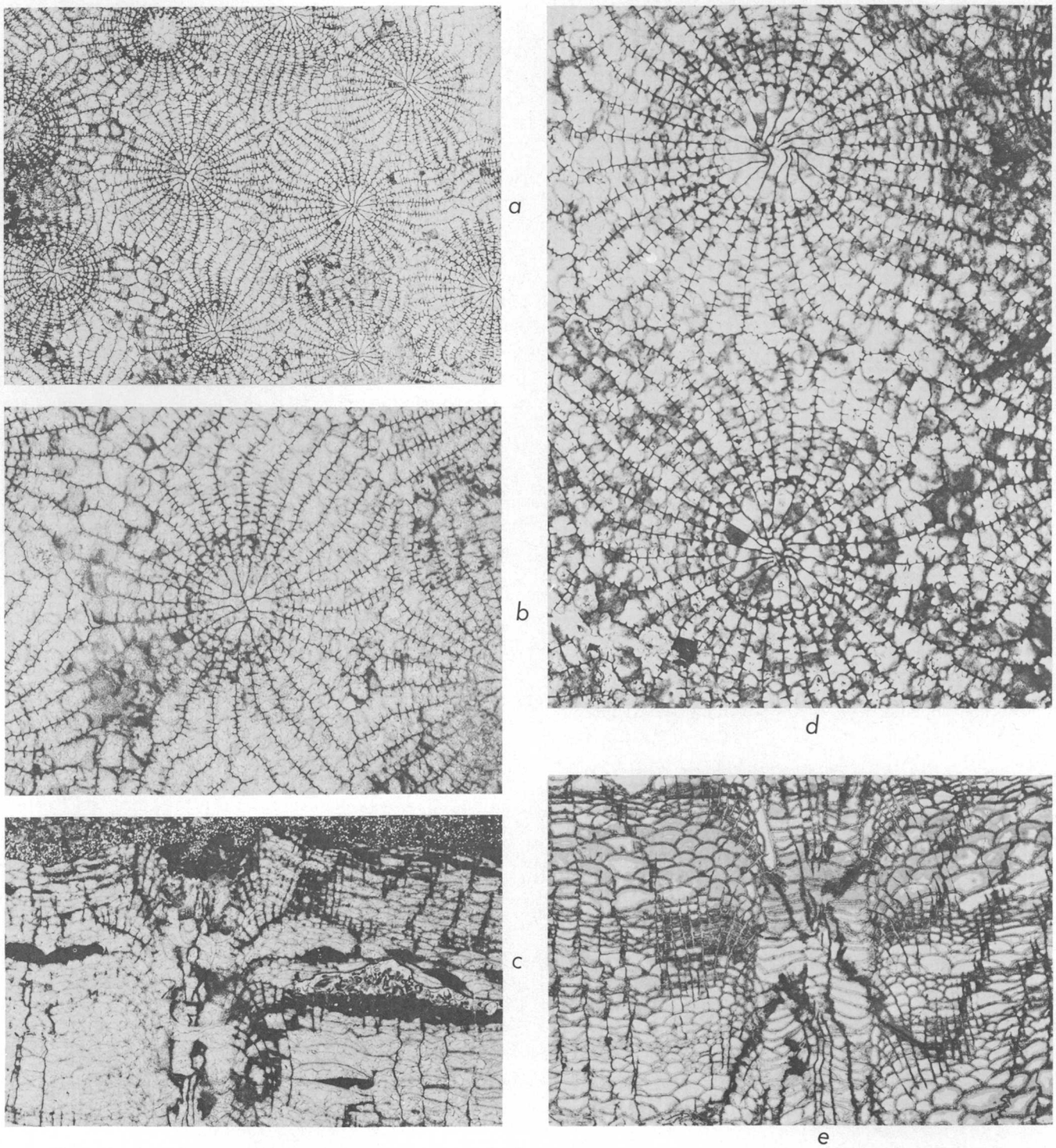

Figure 2.—*Asterobillingsa magdisa magdisa* n. gen., n. sp. and subsp.

a–c. Holotype, USNM 163419. Transverse, × 2½ and × 5, and longitudinal, × 5, thin sections. Schoharie Grit, Clarksville, N.Y.

d, e. Paratype, USNM 163420. Transverse and longitudinal thin sections, × 5. Bois Blanc Formation, Hagarsville, Ontario.

Chronological subspecies.—Specimens of *Asterobillingsa* occurring in the Schoharie-Bois Blanc Formations and in the Edgecliff Member of the Onondaga Limestone are similar in most respects but generally differ in the morphology of their dissepimentaria. There are local lonsdaleoid areas in most transverse sections of the older form (*A. magdisa magdisa*). These commonly occur where three or four corallites meet. In longitudinal sections the dissepiments are generally larger in the older form and may be quite large where the septa are peripherally incomplete. The younger form (*A. magdisa steorra*) has smaller dissepiments that are much more uniform in size and tend to be depressed. In other morphologic features, the two forms show considerable variation but have approximately the same range of variation.

All known Schoharie-Bois Blanc specimens have "large" dissepiments. Two additional "large" types are probably from the Bois Blanc but one is Edgecliff and another is probably Edgecliff. All specimens of the "small" dissepiment type are Edgecliff, Onondaga, or probably Onondaga in age.

A. magdisa differs from other species of the genus in its well-developed zigzag carinae, the arrangement of major septa at the axis, and its small to medium corallite size.

Asterobillingsa magdisa magdisa n. subsp.

Figures 2*a*–*e*

Diagnosis.—*A. magdisa* in which the largest dissepiments (measured in longitudinal thin section) are commonly 2.0 by 0.5 mm or larger.

Distribution.—Schoharie Grit, eastern New York, and Bois Blanc Formation, southwestern Ontario; Edgecliff Member of Onondaga Limestone, western New York and ?southwestern Ontario.

Material.—Holotype: USNM 163419 (fig. 2*a*–*c*) Paratypes: USNM 113264, 128016, 163420-23; NYSM 12827-28; GSC 31156; AMNH 641.

Asterobillingsa magdisa steorra n. subsp.

Figures 3*a*–*d*

Diagnosis.—*A.* magdisa in which the largest dissepiments (measured in longitudinal thin section) are commonly no larger than 1.0 by 0.4 mm.

Distribution.—Edgecliff Member, Onondaga Limestone, New York and Niagara Peninsula of Ontario. A single specimen from Woodstock, Ontario, is probably from the Amherstburg Limestone (Edgecliff equivalent).

Material.—Holotype: NYSM 12824 (figs. 3*a*, *b*). Paratypes: USNM 26000a, 113263, 143121, 172166-77; NYSM 12825-26; GSC 31155.

Subfamily Craspedophyllinae Dybowski, 1873

Type genus.—*Eridophyllum* Milne-Edwards and Haime, 1850 (=*Craspedophyllum* Dybowski, 1873)

Diagnosis.—Solitary(?) or compound craspedophyllids with general cylindrophyllinid characters except that major septa are deflected in the tabularium to form an aulos, separating the tabularium into axial and periaxial zones. Septa are thin and strongly carinate and may or may not enter the axial zone.

Included genera.—*Grewgiphyllum* n. gen. and *Eridophyllum* M.–E. and H.

Discussion.—The craspedophyllinids are morphologically close to the cylindrophyllinids and were probably derived from early members of that group within Eastern North America. At this time, I recognize only two genera. *Eridophyllum* (=*Craspedophyllum*), with a nearly perfect aulos, is limited to the Middle Devonian of eastern North America and Morocco. Early species are all phaceloid but later solitary(?) and cerioid species are tentatively included in the genus. A new genus *Grewgiphyllum*, ranges from the middle Onesquethaw into the lower upper Onesquethaw and is restricted to Eastern North America. It is characterized by an imperfect aulos and an alternately cerioid and phaceloid growth form. In these characters it is intermediate between *Eridophyllum* and the cylindrophyllinid *Prismatophyllum* (middle-upper Onesquethaw), and it seems likely that the morphologic series *Prismatophyllum* → *Grewgiphyllum* → *Eridophyllum* represents an evolutionary series as well.

Genus *Grewgiphyllum* n. gen.

Type species.—*Heliophyllum colligatum* Billings, 1859, p. 126–127. First illustrated by Nicholson, 1874, p. 28, pl. 5, figs. 3, 3a. "Rama's Farm, near Port Colborne [Ontario]" (Billings, 1859, p. 127). Presumably the Bois Blanc Formation, middle Onesquethaw.

Diagnosis.—Craspedophyllinids with an imperfect and irregular aulos formed by deflected major septa, some of which continue into the aulos and are irregularly bent and twisted. Colonial, with corallum composed of straight corallites that are at alternate levels expanded to form a cerioid stage and contracted to form a phaceloid stage. Increase is lateral.

Discussion.—*Grewgiphyllum colligatum* (Billings) (figs. 4*a*, *b*) has generally been assigned to *Eridophyllum* because of the presence of a distinct aulos. However, it differs from that genus in its imperfect aulos (possibly primitive) and in its distinctive growth form, not otherwise known in the Craspedophyllidae. It could be considered an early (primitive) *Eridophyllum*, but its distinct morphology and stratigraphic position can be emphasized by giving it a new generic name. It is the earliest known craspedophyllinid and may be the evolutionary intermediate between the cylindrophyllinid *Prismatophyllum* and *Eridophyllum* as discussed elsewhere in this paper.

Family Disphyllidae Hill, 1939

Diagnosis.—Solitary(?), phaceloid and cerioid rugose corals with thin or thickened major septa composed of coarse monacanthine trabeculae. The dissepimentarium is formed by

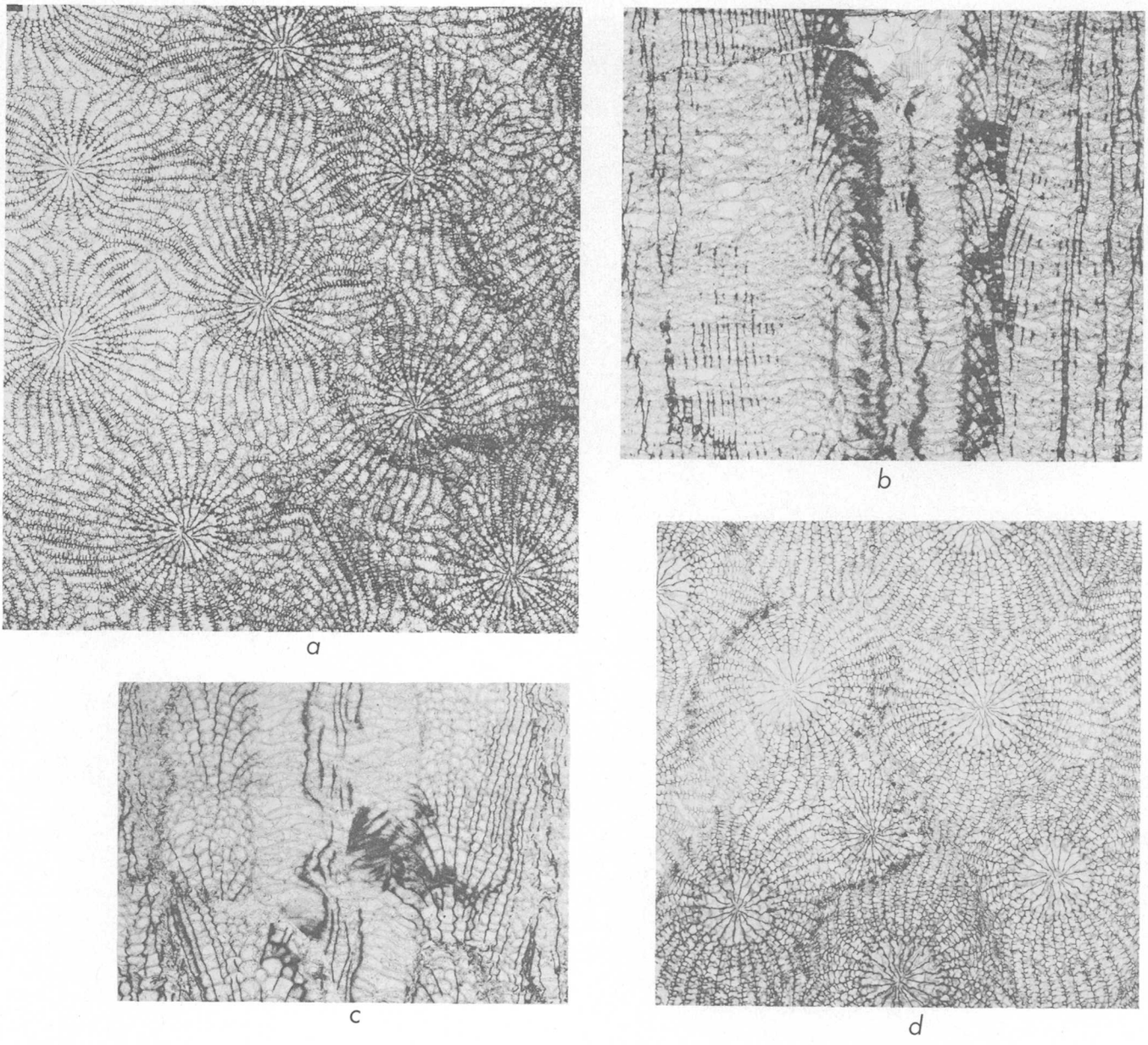

Figure 3.—*Asterobillingsa magdisa steorra* n. gen., n. sp. and subsp.
a,b. Holotype, NYSM 12824. Transverse, × 2½, and longitudinal, × 5, thin sections. Onondaga Limestone, Clarksville, N.Y.
c,d. Paratype, GSC 31155. Longitudinal, × 5, and transverse, × 2½, thin sections. Probably Amherstburg Limestone, Woodstock, Ontario.

one to several rows of normal, globose to vertically elongate dissepiments. Tabulae are variable but commonly incomplete with central, flat, horizontal tabulae and periaxial tabulae inclined toward the axis.

Discussion.—The above is not intended as a complete diagnosis and no description is offered of the family or its assigned genera. My interpretation of the family is conventional except for excluding the genera here grouped as the Cylindrophyllinze and those commonly known as phillipsastraeids (Phillipsastraeinae of Jell, 1969); it is essentially the Disphyllinae of Jell (1969) but excluding *Acinophyllum* which is clearly a craspedophyllid as discussed above.

Family Zaphrentidae Milne-Edwards and Haime, 1850

Discussion.—Tentatively, I am accepting the commonly assumed relationship between *Zaphrentis* and *Heliophyllum* but separating both from *Cyathophyllum* and the Cyathophyllidae. I consider the Zaphrentidae to consist of predominantly solitary forms but recognize that *Heliophyllum*, at least, includes small colonies within its type species (*H. halli* Milne-Edwards and Haime, 1850). I am also including Eastern North American colonial cyathophylloid species in *Heliophyllum* and in the new genus *Cyathocylindrium* but with some reservations.

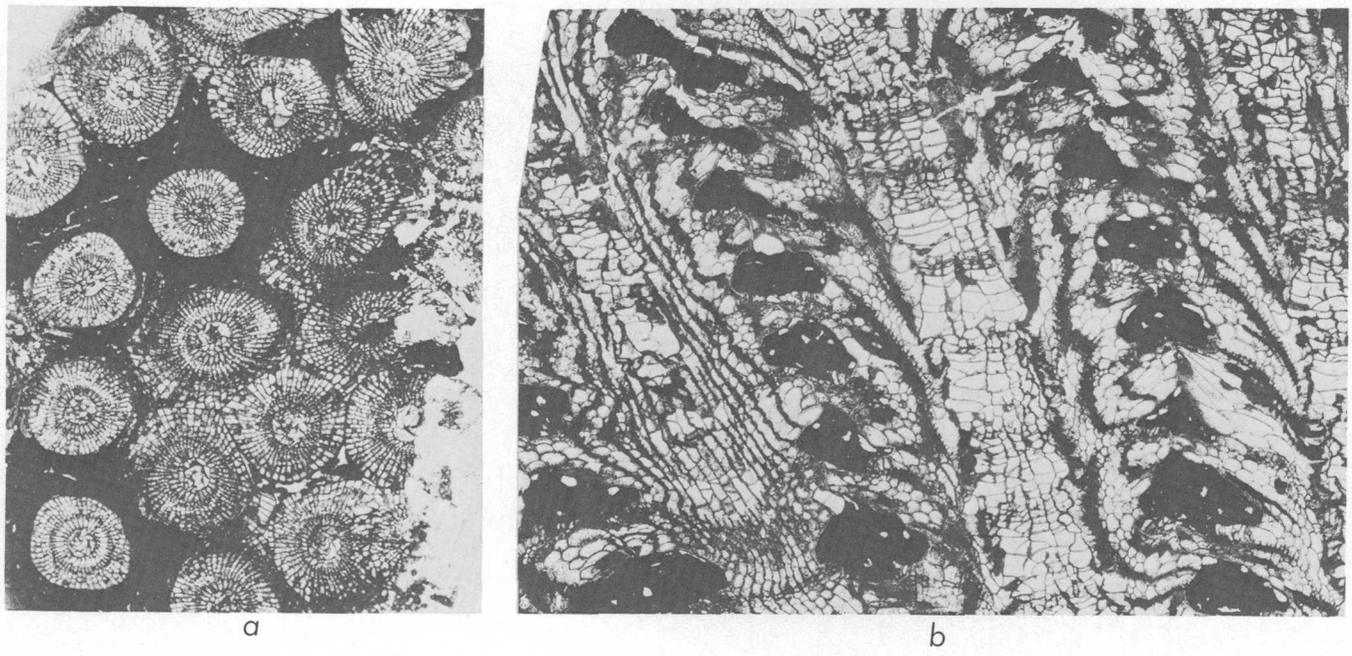

Figure 4.—*Grewgiphyllum colligatum* (Billings).
Lectotype, GSC 31158. Bois Blanc Formation, Walpole, Ontario. *a,b*, Transverse, × 1, and longitudinal, × 2½, thin sections.

Microstructure.—The fine structure of septa and walls in most of the zaphrentid species described by Oliver (in press) is similar to that of the craspedophyllids. This is particularly so where septa and walls are thin. Where the septal microstructure is well preserved, it appears as follows. A dark central area, approximately 0.03 mm thick, indents the epitheca and extends the full length of the septum. This is apparently composed of closely spaced "centers of calcification." On either side of the dark central zone is a light-colored zone composed of minute fibers directed away from the central zone and inclined slightly toward the axis of the corallite, giving a pinnate appearance in transverse section. Septa are separated from the wall by a dark line, but the light-colored zone is identical to the inner wall in texture. Septa are thickest at their peripheral ends; the light-colored tissue thins toward the inner part of the tabularium. Carinae form ridges on the sides of the septa and show the same structure as the septa in transverse section. Carinae and parts of septa between carinae are commonly composed of several parallel monacanths.

The size of the monacanths varies in some of the zaphrentids, so that a single carina or part of a septum between carinae may be formed by as few as two or three monacanths. In some *Heliophyllum* with dilated septa, carinae may be thickened, triangular, or diamond-shaped in cross section and formed by a single coarse monacanth. This is especially characteristic of *Heliophyllum halli*, less so of the colonial species. But in all these, very fine monacanths are the most common structural element. If medium or coarse monacanths are present in an individual, there is a complete gradation from very fine to medium or coarse.

Genus *Cyathocylindrium* n. gen.

Type species.—*Cyathocylindrium opulens* n. sp.; Onondaga Limestone, Edgecliff Member, bioherm facies; New York.

Diagnosis.—Dendroid or phaceloid rugose corals. Septa numerous, biradially or bilaterally arranged, long or variously withdrawn from the axis; attenuate and weakly to strongly carinate (zigzag); cardinal and counter septa commonly shorter than other major septa. Wide dissepimentarium is composed of many rows of very globose dissepiments. Tabulae arched, complete or incomplete, tending to be more complete in forms with shorter major septa.

Discussion.—This genus is established for species, formerly referred to *Cylindrophyllum* or *Heliophyllum*, that differ from species of the former in their larger size and decidedly more pronounced bilateral septal arrangement. In both of these characters, *Cyathocylindrium* is close to *Heliophyllum*. However, the latter differs in having predominant long, yard-arm carinae and dilated, early stage septa. *Cyathocylindrium* is most similar to *Cyathophyllum* from which it differs primarily in its more globose dissepiments and more variable carinae.

Cyathocylindrium opulens n. sp.

Figures 5*a–e*

Occurrence of holotype.—Onondaga Limestone, Edgecliff Member, bioherm facies, Thompson's Lake bioherm, 15 mi (25 km) west of Albany, N.Y.

Diagnosis.—Phaceloid and dendroid *Cyathocylindrium* in which the septal arrangement is strongly bilateral; major septa

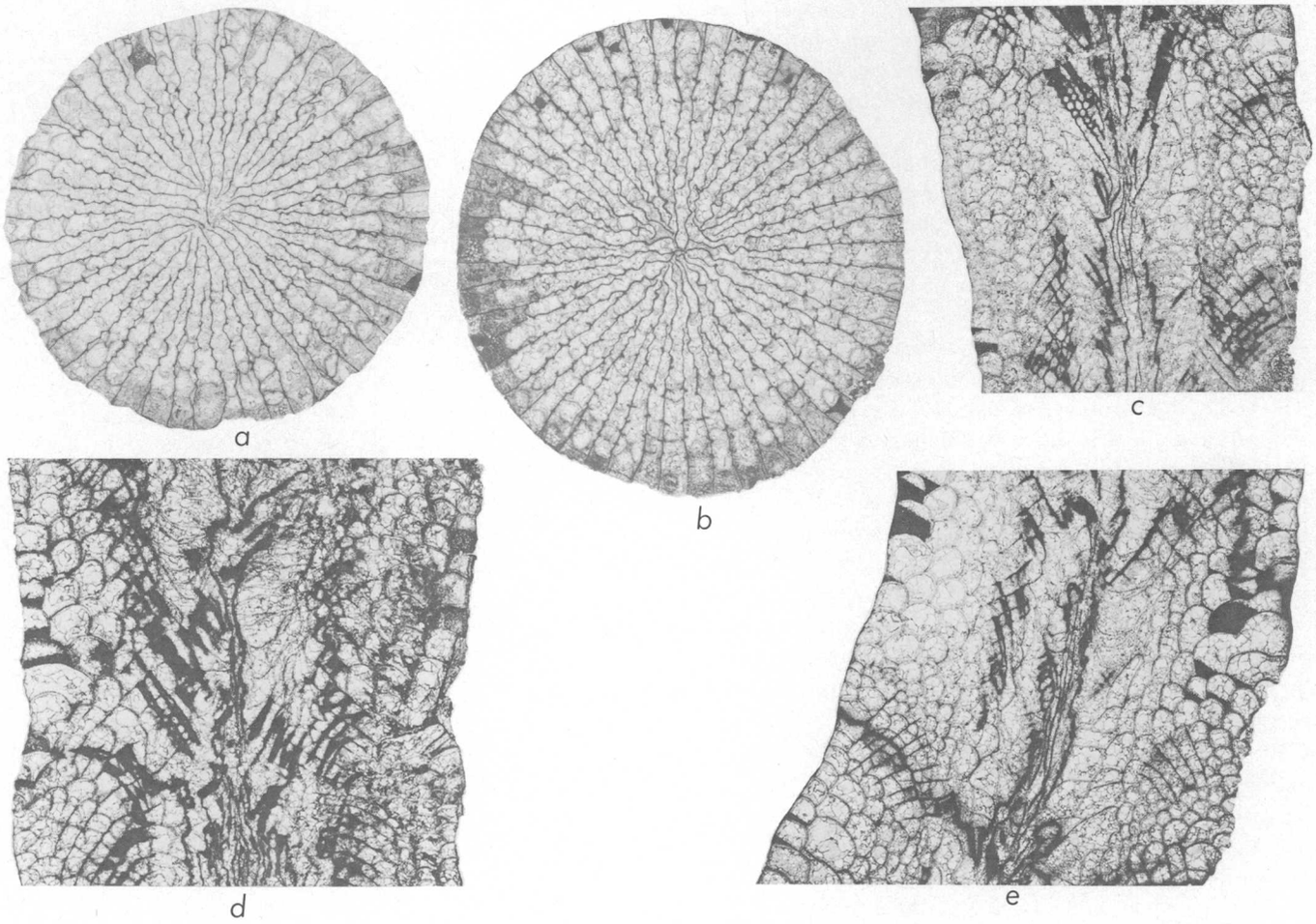

Figure 5.—*Cyathocylindrium opulens* n. gen., n. sp.
a–e. Five thin sections of holotype corallum (USNM 172197), × 2½. Onondaga Limestone, Edgecliff Member, bioherm facies, Thompson's Lake, N.Y.

extend to the cardinal-counter plane which is defined by short cardinal and counter septa. Tabulae are incomplete. Corallites are only rarely in contact.

External features.—Coralla are phaceloid or dendroid and composed of subparrallel or radiating corallites that are rarely in contact except at their lower ends; there are no lateral supports. Colony heights and diameters in excess of 60 cm are common.

Corallites are trochoid or ceratoid becoming cylindrical and are coarsely and more or less regularly rugose; finer encircling growth lines and longitudinal septal grooves are also present. Increase is lateral and peripheral. Of 33 colonies in which increase was observed, 24 offset laterally, 8 offset peripherally, and 1 was dominantly lateral with a single peripheral offset. Mode of increase was not determined in several additional specimens.

Calices are moderately deep (average one-half corallite diameter) with gently sloping walls and broad peripheral platforms that commonly slope inward but may be horizontal or reflexed in some individuals. A cardinal fossula is formed by a short cardinal septum. The calice floor is flat.

Internal features.—Septa are bilaterally arranged. The cardinal and counter septa are commonly shorter than the adjacent major septa, and one of these may be shorter than the other. In some sections the counter septum is flanked by long minor septa although other sections of the same corallite may not show this feature. Commonly the cardinal and counter septa are of approximately equal length and not individualized by the arrangement of other septa; a cardinal-counter plane is clearly defined, however. Adjacent major septa turn toward the symmetry axis at their axial ends and are longer toward the 90° positions so that the major septa tend to meet along the cardinal-counter plane but not at a point. Alar septa can be recognized only in some early (conical) stages where new septa are being introduced.

The length of the minor septa varies with position but is commonly one-half to two-thirds the length of the adjacent major septa. Major and minor septa are slightly thickened in the inner dissepimentarium and outer tabularium. Cylindrical parts of corallites range in diameter from 10 to 32 mm; 13

colony means range from 14 to 27 mm. Numbers of major septa range from 23 to 41; colony means range from 25 to 36. Carinae abound; they are predominantly zigzag but are locally yard-arm or nearly so; they are limited to the dissepimentarium.

The dissepimentarium consists of from 7 to 12 or more rows of globose dissepiments varying in height (as seen in longitudinal section) from 0.5 to 2.5 mm or more. Some dissepiments are elongate parallel to the carinae; near the inner margin of the dissepimentarium they tend to be less globose and may be elongate in the other direction.

The tabularium is clearly separated from the dissepimentarium. Tabulae are incomplete, short arched plates, forming an arched or double-arched pattern.

Distribution.—This is the most common colonial zaphrentid known from the Onondaga Limestone. It has been collected from every known Edgecliff bioherm area from Port Colborne, Ontario, to Albany, N.Y., and in the Edgecliff biostromal facies in the Niagara Peninsula (two specimens). Two specimens are known from the lower Jeffersonville Limestone (lower Edgecliff equivalent?) at the Falls of the Ohio. One specimen from the upper part of the Columbus Limestone in the subsurface of northeastern Ohio is tentatively assigned to the species.

Material.—Holotype: USNM 172197. Paratypes: USNM 172198-211, 182846-53; NYSM 12843-48; GSC 31159.

Genus *Heliophyllum* Hall

Diagnosis.—Solitary and colonial rugose corals, widely varying in shape and type of colony, characteristically with a moderately deep calice with broad axial pit, steeply inclined lower calice wall, a broad horizontal or gently inclined peripheral platform and a shallow fossula. Major septa tend to be long and are bilaterally arranged about the cardinal-counter plane; mature septa may be attenuate but but septa are moderately to heavily dilated at least in early ontogenetic stages. Carinae are abundant and prominent, commonly long yard-arm but short zigzag carinae may also occur; they are commonly, but not necessarily, limited to the dissepimentarium. Dissepiments are globose and in numerous rows. Tabulae are incomplete, commonly convex but forming a generally concave pattern.

Discussion.—The genus badly needs revision as its limits are poorly understood at present even though some "populations" of *H. halli* have been admirably described. Of Onesquethaw colonial corals, I am including phaceloid, cerioid, and astreoid species characterized by long yard-arm carinae and, in some cases, by septal dilation.

REFERENCES CITED

Billings, Elkanah, 1859, On the fossil corals of the Devonian rocks of Canada West: Canadian Jour., new ser., v. 4, p. 97–140, illus.

Cleland, H. F., 1911, The fossils and stratigraphy of the Middle Devonic of Wisconsin: Wisconsin Geol. Survey Bull. 21 (sci. ser.), 222 p., map.

Dybowski, W. N., 1873–1874, Monographie der Zoantharia schlerodermata rugosa aus der Silurformationen Estlands, Nord-Livlands und der Insel Gotland: Archiv. Naturkunde Liv-, Ehst-und Kurland, v. 5, p. 257–414, pls. 1, 2 (1873); v. 5, p. 415-532, pls. 3-5 (1874).

Flint, R. F., and others, 1945, Glacial map of North America. Part 1, Glacial map; Part 2, Bibliography and explanatory notes: Geol. Soc. America Spec. Paper 60, 37 p., map.

Grabau, A. W., 1917, Stratigraphic relationships of the Tully Limestone and the Genesee Shale in eastern North America: Geol. Soc. America Bull., v. 28, p. 945–958.

Hill, Dorothy, 1939, The Devonian rugose corals of Lilydale and Loyola, Victoria: Royal Soc. Victoria Proc., (new ser.), v. 51, p. 219–256, pls. 13–16.

Jell, J. S., 1969, Septal microstructure and the classification of the Phillipsastraeidae, *in* Campbell, K. S. W., ed., Stratigraphy and palaeontology; essays in honour of Dorothy Hill: Canberra, Australian Natl. Univ. Press, p. 50–73.

McLaren, D. J., 1959, A revision of the Devonian coral genus *Synaptophyllum* Simpson: Canada Geol. Survey Bull. 48, p. 15–33.

Milne-Edwards, Henri, and Haime, Jules, 1850, A monograph of the British fossil corals, Introduction: (Paleont. Soc. London Mon.), p. i–lxxxv.

——1851, Monographie des Polypiers fossiles des Terrains Palaeozoiques: Archiv. Mus. Historie Nat. Paris, v. 5, 502 p., 20 pls.

Nicholson, H. A., 1874, Report upon the palaeontology of the Province of Ontario: Toronto, 133 p., illus.

Oliver, W. A., Jr., in press, Non-cystimorph colonial rugose corals of the Onesquethaw and lower Cazenovia stages (Lower and Middle Devonian) in New York and adjacent areas: U.S. Geol. Survey Prof. Paper 869.

Oliver, W. A., Jr., deWitt, Wallace, Jr., Dennison, J. M., Hoskins, D. M., and Huddle, J. W., 1968, Devonian of the Appalachian Basin, United States, *in* Oswald, D. H., ed., Internat. Symposium on the Devonian System, Calgary, 1967, [Proc.]: Alberta Soc. Petroleum Geologists, v. 1, p. 1001–1040.

——1969, Correlation of Devonian rock units in the Appalachian Basin: U.S. Geol. Survey Oil and Gas Inv. Chart OC-64.

Pedder, A. E. H., 1964, Correlation of the Canadian Middle Devonian Hume and Nahanni Formations by tetracorals: Palaeontology, v. 7, pt. 3, p. 430–451, pls. 62–73.

Scrutton, C. T., 1968, Colonial Phillipsastraeidae from the Devonian of southeast Devon, England: British Mus. (Nat. History) Bull., Geology, v. 15, no. 5, p. 183–281, 18 pls.

——1973, Palaeozoic coral faunas from Venezuela, II, Devonian and Carboniferous corals from the Sierra de Perija: British Mus. (Nat. History), Bull., Geology, v. 23, no. 4, p. 221–282.

Sorauf, J. E., 1972, Middle Devonian coral faunas (Rugosa) from Washington and Oregon: Jour. Paleontology, v. 46, p. 426–439.

Soshkina, E. D., 1951, [Upper Devonian Rugosa corals, their systematics and evolution]: Akad. Nauk SSSR, Paleont. Inst. Trudy. v. 34, 122 p., 24 pls.

Soshkina, E. D., and Dobrolubova, T. A., 1962 [Order Evenkiellida, Order Columnarida], *in* Sokolov, B. S., ed., Osnovy Paleontologii, v. 2: Moscow, Akad. Nauk SSSR, p. 333–345, pls. 17–23, illus. 84–108.

Stumm, E. C. 1937, The lower Middle Devonian tetracorals of the Nevada Limestone: Jour. Paleontology, v. 11, no. 5, p. 423–443.

—— 1949, Revision of the families and genera of the Devonian tetracorals: Geol. Soc. America Mem. 40, 92 p., 25 pls.

Vanuxem, Lardner, 1842, Geology of New York, Part III, comprising the survey of the third geological district: Albany, 306 p., illus.

Jour. Research U.S. Geol. Survey
Vol. 2, No. 2, Mar.-Apr. 1974, p. 175—184

STABILITIES OF CALCITE AND ARAGONITE

By C. L. CHRIST; P. B. HOSTETLER,[1] and R. M. SIEBERT;[1]
Menlo Park, Calif.; Columbia, Mo.

Abstract.—A revaluation of the 25°C activity-product constants of calcite (K_C) and aragonite (K_A) was made on the basis of the known solubilities of these phases for which the activity of total dissolved calcium was corrected for the presence of the ion pair $CaHCO_3^+$ in the aqueous phase. The value of the dissociation constant of $CaHCO_3^+$ was taken to be $10^{-1.225\pm0.02}$. This value, combined with values of the analytical concentrations in solutions with partial pressure P_{CO_2}=0.97 atmosphere, leads to $K_C=10^{-8.52\pm0.04}$ and $K_A=10^{-8.36\pm0.04}$. Based on these K values, standard free energies of formation of calcite and aragonite were calculated to be −270,144±375 and −269,926±375 calories mole^{-1}, (−1,130,282±1,569 and −1,129,370±1,569 joules mole^{-1}), respectively. From the 25°C K values, using appropriate entropy and heat capacity data, values of K_C and K_A were calculated over the temperature range 0° to 200°C. Possible errors in interpretation of measured pH values and inferred P_{CO_2} values and the bearing of these errors on calculations of K values are discussed.

We have recently completed an investigation of the long-term aqueous solubility of aragonite at 51°C and at 90°C, at 1 atm total pressure. The experimental analytical results obtained in that study and the activity-product constants of aragonite, as a function of temperature, derived from these experimental results, will be the subject of another report. This paper presents some calculations of the variation of the activity-product constants with temperature for both calcite and aragonite. These calculations are based on the values of the respective activity-product constants at 25°C. In order to arrive at the "best" 25°C values, we have included corrections to the known solubilities of the two phases for the presence of the calcium bicarbonate ion pair, $CaHCO_3^+$, in the aqueous phase.

ACTIVITY-PRODUCT CONSTANT OF CALCITE AT 25°C

Preliminary considerations

The activity-product constant for calcite is given by the expression $[Ca^{2+}][CO_3^{2-}]=K_C$, where the bracketed ionic species represent the activities of the dissolved aqueous ions in equilibrium with calcite. Values of $[Ca^{2+}]$, the activity of hydrated, uncomplexed calcium ion can be calculated directly from the analytical values, provided that the distribution of aqueous calcium species can be predicted. Some possible ion pairs in solution are $CaOH^+$, $CaCO_3^\circ$, and $CaHCO_3^+$. For $CaHCO_3^+$, the equilibrium dissociation is given by the reaction

$$CaHCO_3^+=Ca^{2+}+HCO_3^-, \quad (1)$$

and the dissociation constant, $K_{CaHCO_3^+}$, by the expression

$$K_{CaHCO_3^+}=\frac{[Ca^{2+}][HCO_3^-]}{[CaHCO_3^+]}. \quad (2)$$

Corresponding expressions can be written for the dissociation constants of $CaOH^+$ and $CaCO_3^\circ$; pK values (negative logarithm values) for these latter are pK_{CaOH^+}=1.3 (Davies and Hoyle, 1951), and $pK_{CaCO_3^\circ}$=3.1 (Lafon, 1970). In the following, we will be concerned with the calculation of $pK_{calcite}$ (25°C) using analytical results obtained by other investigators on solutions saturated with respect to calcite at a nominal CO_2 pressure of 0.97 atm. For such solutions, the ion pairs $CaOH^+$ and $CaCO_3^\circ$ are present in insignificant concentrations, as can be noted from the values of the experimental parameters and the calculations given.

However, $CaHCO_3^+$ is present in significant concentrations in these solutions. Values for $pK_{CaHCO_3^+}$ have been obtained by several investigators. Greenwald (1941) was the first to determine an apparent value of this constant. He expressed the quantities in equation 2 in terms of concentrations rather than activities. Garrels and Thompson (1962) corrected Greenwald's concentrations to activities and obtained a $pK_{CaHCO_3^+}$ of 1.26, at 22°C. Nakayama (1968) recomputed Greenwald's data and calculated the value 1.24±0.02. In an independent investigation, Nakayama (1968) found the value 1.25±0.02, at 25°C. More recently, using a procedure differing from that of Greenwald and of Nakayama, we have found $pK_{CaHCO_3^+}$ to be 1.225±0.02, at 25°C (P. B. Hostetler and others, unpub. data, 1973). For any practical purposes, all these results are in good agreement. In calculations in the present paper the value 1.225 is used.

[1] Department of Geology, University of Missouri.

On the basis of a comprehensive review and revaluation of aqueous calcite solubility measurements, Langmuir (1968) concluded that the activity-product constant of calcite at 25°C and 1 atm is $10^{-8.40\pm0.02}$. In arriving at this conclusion Langmuir assumed that no significant concentrations of $CaHCO_3^+$ were present in the solutions. He found that values of $m_{Ca^{2+}}$ (m = molality), calculated from pH measurements in calcium bicarbonate solutions at P_{CO_2}=0.97 atm, agreed exactly with measured total dissolved calcium, $m_{Ca^{2+}(t)}$ and hence that the $CaHCO_3^+$ ion pair should be neglected. Thus, there is a seeming inconsistency between the value of $pK_{CaHCO_3^+}$, found to be nearly the same by three different methods of study, and the measured solubility of calcite. In the following we attempt to resolve this difficulty.

Calculation of $K_{calcite}$

In calculating the activity-product constant of calcite, use is made of the several equilibria involved in the CO_2-H_2O system, for which

$$\frac{[H_2CO_3]}{P_{CO_2}}=K_0\,, \tag{3}$$

$$\frac{[H^+][HCO_3^-]}{[H_2CO_3]}=K_1\,, \tag{4}$$

$$\frac{[H^+][CO_3^{2-}]}{[HCO_3^-]}=K_2\,. \tag{5}$$

The chosen K values at 25°C are $K_0=10^{-1.464}$ (Harned and Davis, 1943), $K_1=10^{-6.351}$ (Harned and Davis, 1943), and $K_2=10^{-10.329}$ (Harned and Scholes, 1941). These K values were obtained from voltage measurements in electromotive force (emf) cells of the Harned type; that is, cells without liquid-junction potential. The emf measurements were consistent to 0.2 mV, which corresponds to an error of $10^{\pm0.0003}$ in the K values. The final K values listed were obtained by straight-line extrapolation to infinite dilution of apparent K values derived from measurements of cells with finite concentrations of electrolytes; it is this extrapolation that leads to the largest overall error. It is difficult to judge what error should be assigned to these K values; however, the error is probably of the order of $10^{\pm0.002}$ to $10^{\pm0.003}$ for each K.

Wagman and others (1968) give free-energy values from which the values of K_0, K_1, and K_2 can be calculated. These values are $K_0=10^{-1.470}$, $K_1=10^{-6.362}$, and $K_2=10^{-10.328}$ (as listed in Langmuir, 1968). It is seen that these latter K values differ little from those of Harned and coworkers. However, the free-energy values are given without errors and are not referenced. Hence, it would seem more logical to use the K values of Harned and coworkers, and these are employed in most of the calculations that follow. Moreover, K values from Wagman and coworkers are available for 25°C only; the values of Harned and coworkers extend from 5° to 50°C. Because we will subsequently report results from investigations of carbonate equilibria at temperatures both below and above 25°C, consistency can be maintained among all the calculations by using the values of Harned and coworkers.

Combining equations 3, 4, and 5, we get

$$[CO_3^{2-}]=\frac{K_0K_1K_2P_{CO_2}}{[H^+]^2}\,, \tag{6}$$

and substituting the numerical K values of Harned and coworkers

$$[CO_3^{2-}]=\frac{10^{-18.144}P_{CO_2}}{[H^+]^2}\,. \tag{6a}$$

Also, combining equations 3 and 4,

$$[HCO_3^-]=\frac{K_0K_1P_{CO_2}}{[H^+]}\,, \tag{7}$$

$$[HCO_3^-]=\frac{10^{-7.815}P_{CO_2}}{[H^+]}\,. \tag{7a}$$

In the ensuing calculations, use is made of the activity coefficients of Ca^{2+} and HCO_3^-, that is, $\gamma_{Ca^{2+}}$ and $\gamma_{HCO_3^-}$. These are determined from the Debye-Hückel equation (Garrels and Christ, 1965, p. 61) as follows:

$$-\log\gamma_i=(Az_i^2\,I^{1/2})/(1+\mathring{a}_i\,BI^{1/2}). \tag{8}$$

For this equation, at 25°C, A=0.5095 and B=0.3284×10^8 (Helgeson, 1967); I is ionic strength in molal units. The value of $\mathring{a}_{HCO_3^-}$ is 5.5×10^{-8} (Christ and Hostetler, 1970). For Ca^{2+}, the value $\mathring{a}_{Ca^{2+}}=5.5\times10^{-8}$ was derived from the mean activity coefficients of $CaCl_2$ and KCl listed in Lewis and Randall (1961, p. 653) by a method fully described by Hostetler (1963) in arriving at the $\mathring{a}$ value for Mg^{2+}.

Beginning with Garrels, Thompson, and Siever (1968), a number of investigators have determined a value for K_C by measuring the equilibrium value of pH in a saturated solution of calcite through which pure CO_2 bubbled at a total pressure of 1 atm. Correcting for the vapor pressure of water, equal to 0.03 atm at 25°C (Weast, 1967, p. D-110), this corresponds to a nominal P_{CO_2}=0.97 atm. Garrels and coworkers determined the equilibrium pH to be 6.02. Langmuir (1964) and Berner (1967) found the pH to be 6.03; more recently, L. Niel Plummer (written commun., 1972) obtained the value 6.02. If the measured pH truly represents the thermodynamic value of the activity of hydrogen ion, $[H^+]$, through the relation pH=-log$[H^+]$, and the nominal P_{CO_2} equals the effective

P_{CO_2} then these experimental values can be used directly to calculate the activity-product constant of calcite, assuming the absence of significant concentrations of ion pairs in the solution. For $[H^+]=10^{-6.02}$ and $P_{CO_2}=0.97$ atm, from equation 6a, $[CO_3^{2-}]=10^{-6.118}$. The solution being considered is essentially a $Ca(HCO_3)_2$ one, so that we may write the charge balance equation

$$2m_{Ca^{2+}}=m_{HCO_3^-}. \quad (9)$$

From this, $I=\frac{1}{2}(4m_{Ca^{2+}}+m_{HCO_3^-})=3/2\,m_{HCO_3^-}$. The value of $[HCO_3^-]$ equal to $10^{-1.809}$ results from equation 7a. Starting with the approximation that $m_{HCO_3^-}=[HCO_3^-]$, a provisional value for I is found, a value for $\gamma_{HCO_3^-}$ is noted for this value of I, and a new $m_{HCO_3^-}$ calculated through the relationship $m_{HCO_3^-}=[HCO_3^-]/\gamma_{HCO_3^-}$. This process of iteration is repeated until a constant value of γ_{HCO_3} results (only three iterations were needed in the present problem). The final results yield the values $m_{HCO_3^-}=0.0180$, $I=0.027$, and $\gamma_{HCO_3^-}=0.861$. From these numbers we obtain $m_{Ca^{2+}}=0.0090$ $\gamma_{Ca^{2+}}=0.550$, and hence $[Ca^{2+}]=10^{-2.304}$. Then, $K_C=[Ca^{2+}][CO_3^{2-}]=10^{-2.304}\times10^{-6.118}=10^{-8.42}$. Langmuir (1968) and L. Niel Plummer (written commun., 1972) using the same constants for the CO_2–H_2O equilibria given in the foregoing, but slightly different γ-values, both found the constant to be $10^{-8.41}$.

The solubility of calcite at 25°C and $P_{CO_2}=0.97$ atm has been determined by a number of investigators. Langmuir (1968) discusses and evaluates the results in detail; following him, it seems safe to assume that $m_{Ca^{2+}(t)}$ is close to 9.1×10^{-3}. This number has been reaffirmed by Langmuir (1971) and by L. Niel Plummer (written commun., 1972). Langmuir (1968) argues convincingly that this experimental value for $m_{Ca^{2+}(t)}$ is in error by less than 1 percent. Note that the experimental value 9.1×10^{-3} is in good agreement with the value 9.0×10^{-3} calculated from pH and P_{CO_2}, in the foregoing, when $CaHCO_3^+$ is neglected. For this reason Langmuir (1968) concluded that this ion pair could be neglected.

At this point, we take a fresh approach to the problem of calculating the activity-product constant of calcite. We make the two basic assumptions that the molal concentration of total dissolved calcium, $m_{Ca^{2+}(t)}$, is 9.1×10^{-3} in the CO_2-saturated solution and that $pK_{CaHCO_3^+}$ is 1.225. The following relations hold, where $K_{CaHCO_3^+}\equiv K_d$:

$$\frac{[Ca^{2+}][HCO_3^-]}{[CaHCO_3^+]}=K_d \quad , \quad (2)$$

$$2m_{Ca_2^{2+}}+m_{CaHCO_3^+}=m_{HCO_3^-} \quad , \quad (10)$$

$$m_{Ca^{2+}}+m_{CaHCO_3^+}=m_{Ca^{2+}(t)}, \quad (11)$$

Equation 10 represents the charge balance, and equation 11 represents the mass balance for calcium, in the solution. Subtracting equation 11 from equation 10, we get

$$m_{Ca^{2+}}+m_{Ca^{2+}(t)}=m_{HCO_3^-} \quad . \quad (12)$$

Substitution into equation 2 yields the relation

$$\frac{(\gamma_{Ca^{2+}})(m_{Ca^{2+}})(\gamma_{HCO_3^-})(m_{Ca^{2+}}+m_{Ca^{2+}(t)})}{(\gamma_{CaHCO_3^+})(m_{Ca^{2+}(t)}-m_{Ca^{2+}})}=K_d \quad . \quad (13)$$

The value of $\mathring{a}$ for $CaHCO_3^+$ is not known; however, as discussed in the following, the assumption can be made that $\gamma_{CaHCO_3^+}=\gamma_{HCO_3^-}$ in the dilute solutions involved. Rearranging the terms in equation 13 we obtain

$$\left(m_{Ca^{2+}}\right)^2+\left(m_{Ca^{2+}(t)}+\frac{K_d}{\gamma_{Ca^{2+}}}\right)\left(m_{Ca^{2+}}\right)-\left(\frac{K_d}{\gamma_{Ca^{2+}}}\right)\left(m_{Ca^{2+}(t)}\right)=0 \quad . \quad (14)$$

Equation 14 is a quadratic equation that can be solved for $m_{Ca^{2+}}$ using the chosen value of $m_{Ca^{2+}(t)}$ and K_d and successive approximations to obtain a final value for $\gamma_{Ca^{2+}}$.

In deriving equation 14, several assumptions are made. In setting up the solution charge balance, expressed by equation 10, the contributions of H^+, OH^-, and CO_3^{2-} were neglected. However, the molalities of these ions are insignificant compared with those of Ca^{2+}, $CaHCO_3^+$, and HCO_3^-, as can be noted in the calculations that follow. There is no apparent way of calculating γ-values for the ion pair $CaHCO_3^+$ from mean activity coefficients. We have assumed that the free calcium ion exists in solution as $Ca(H_2O)_x^{2+}$, with a secondary sheath of H_2O molecules. If HCO_3^- replaces one of the primary H_2O molecules surrounding Ca^{2+}, then one can write the ion pair as $Ca(HCO_3)(H_2O)_{x-1}^+$, with a less strongly bound secondary sheath of H_2O molecules, because of the lower overall charge. Also, because of the lower charge on the ion pair, the number of primary H_2O molecules might be less than x-1. Thus, we assume that the two ions have approximately the same effective diameter. Since we have assigned the same value of $\mathring{a}=5.5$ to both Ca^{2+} and HCO_3^-, we can equate $\gamma_{HCO_3^-}$ to $\gamma_{CaHCO_3^+}$. Actually, on a numerical basis, the assumption that $\gamma_{HCO_3^-}=\gamma_{CaHCO_3^+}$ does not lead to significant error even if the $\mathring{a}$-values of the two ions are appreciably different. For example, at 25°C, when $I=0.03$ and $\mathring{a}=5.5$, the γ-value of a monovalent ion calculated by the Debye-Hückel equation is 0.856; for $\mathring{a}=8.0$, $\gamma=0.869$. Taking $\mathring{a}=5.5$ for HCO_3^- and assuming that $\mathring{a}$ for $CaHCO_3^+$ is as large as 8.0, then the ratio $(\gamma_{HCO_3^-})/(\gamma_{CaHCO_3^+})$ in equation 13 would be 0.985, rather than unity. This change would be insignificant in any ensuing calculations.

To a first approximation, $I=3m_{Ca^{2+}(t)}$, whence $I=0.0273$, and thus $\gamma_{Ca^{2+}}=0.549$. Substituting this latter value into equation 14, with $K_d=10^{-1.225}$, we calculate $m_{Ca^{2+}}=7.82\times10^{-3}$, and

therefore, $m_{CaHCO_3^+}=1.28\times10^{-3}$. The correct expression for I is

$$I=3m_{Ca^{2+}}+m_{CaHCO_3^+} \quad (15)$$

(neglecting the insignificant concentrations of H^+, OH^-, CO_3^{2-}, $CaOH^+$, and $CaCO_3^0$ present in the solution). A new value of I=0.0247 is calculated using equation 15, from which $\gamma_{Ca^{2+}}=0.562$, and then the whole process is repeated until a constant value of I is found. In the present example, this iteration requires only one additional step. For $m_{Ca^{2+}(t)}=9.1\times10^{-3}$, one obtains the final values I=0.0248, $m_{Ca^{2+}}=7.84_5\times10^{-3}$, $m_{CaHCO_3^+}=1.25_5\times10^{-3}$, and $\gamma_{Ca^{2+}}=0.562$. From these results, $[Ca^{2+}]=4.41\times10^{-3}$. Using equation 10, we find $m_{HCO_3^-}=16.95\times10^{-3}$. For I=0.0248, $\gamma_{HCO_3^-}=0.865$, whence $[HCO_3^-]=14.66\times10^{-3}$. This entire calculation was then repeated for $m_{Ca^{2+}(t)}=9.0\times10^{-3}$. The results for both series of calculations are collected in table 1; it can be noted from the values given there that a difference of approximately 1 percent in total dissolved calcium results in a change also of about 1 percent in $m_{Ca^{2+}}$ and $[Ca^{2+}]$. If in the above calculations an error in pK_d of ±0.02 is assumed, and the quantities listed in table 1 are recalculated using pK_d=1.245 instead of 1.225, no significant differences are found in the values of the quantities.

Table 1. *Concentrations and activities of ionic species present in saturated calcite solution at 25° C and at a nominal partial pressure of carbon dioxide of 0.97 atm*

[See text for definition of terms. Calculations are for pK_d=1.225 (eq 2)]

	For $m_{Ca^{2+}(t)}=9.0\times10^{-3}$	For $m_{Ca^{2+}(t)}=9.1\times10^{-3}$
I	0.0245	0.0248
$m_{Ca^{2+}}$	7.77×10^{-3}	$7.84_5\times10^{-3}$
$m_{CaHCO_3^+}$	1.23×10^{-3}	$1.25_5\times10^{-3}$
$\gamma_{Ca^{2+}}$	0.562	0.562
$[Ca^{2+}]$	4.37×10^{-3}	4.41×10^{-3}
$m_{HCO_3^-}$	16.77×10^{-3}	16.95×10^{-3}
$\gamma_{HCO_3^-}$	0.866	0.865
$[HCO_3^-]$	14.52×10^{-3}	14.66×10^{-3}

To recapitulate, our two basic assumptions are that the total concentration of calcium in solution, and pK_d, are known. These assumptions lead to the values listed in table 1. In particular, the value of $[HCO_3^-]$ is fixed for each of the two values of $m_{Ca^{2+}(t)}$. In turn, knowledge of the value of $[HCO_3^-]$ means that equation 7a can be solved for the thermodynamic values of $[H^+]$, for a series of P_{CO_2} values, or *vice versa*. Then, for each pair of $[H^+]$ and P_{CO_2} values, equation 6a can be solved for the corresponding values of $[CO_3^{2-}]$. Using these values of $[CO_3^{2-}]$ and the values of $[Ca^{2+}]$ from table 1, values of pK_C are calculated. The results are given in table 2.

Table 2.—*Calculated values of the activities of hydrogen ion, carbonate ion, and activity-product constant of calcite as a function of partial pressure of carbon dioxide at 25°C*

P_{CO_2}	For $m_{Ca^{2+}(t)}=9.0\times10^{-3}$, the −log of			For $m_{Ca^{2+}}=9.1\times10^{-3}$ the −log of		
(atm)	$[H^+]$	$[CO_3^{2-}]$	K_C	$[H^+]$	$[CO_3^{2-}]$	K_C
0.90	6.023	6.144	8.504	6.027	6.136	8.492
.92	6.013	-------	-------	6.017	-------	-------
.94	6.004	6.163	8.523	6.008	6.155	8.511
.96	5.995	-------	-------	5.999	-------	-------
.97	5.990	6.177	8.537	5.994	6.169	8.525
.98	5.986	-------	-------	5.990	-------	-------
1.00	5.977	6.190	8.550	5.981	6.182	8.538
1.02	5.968	-------	-------	5.972	-------	-------

Note.—The listing of calculated values to three decimal places does not mean that these values are considered to be that precise. The extended listing is given to enable the reader to more readily interpolate between values.

Examination of table 2 reveals several interesting points. It is seen there that the generally accepted values of P_{CO_2}=0.97 atm and pH=6.02 are not compatible. Actually, there have never been firm grounds for considering that these specific numbers can be taken at face value for thermodynamic computations. Although a number of investigators have found nearly the same value of pH (6.02 to 6.03) for a nominal pressure of CO_2 of 0.97 atm, this concordance implies reproducibility rather than accuracy, the experiments of the several investigators having been carried out in essentially the same way. To the point here is the fact that even a precisely measured pH value does not necessarily represent an equally *accurate* value of $-\log [H^+]$, in the sense that the activity of hydrogen ion so obtained is thermodynamically correct. The relationship between the conventionally measured pH and $-\log [H^+]$, and the errors involved in equating the two quantities, are discussed in detail elsewhere (Ives and Janz, 1961; Bates, 1964; Mattock and Band, 1967). Of the various factors that can contribute appreciably to errors in $-\log [H^+]$ values derived from measured pH values, probably the most important one for the kind of system under consideration is that due to liquid-junction potential effects (Mattock and Band, 1967, p. 19 and the following.) If, for example, the true P_{CO_2} is equal to the nominal P_{CO_2} of 0.97 atm in a saturated calcite solution, then from table 2, the correct $p[H^+]$ is 5.99. This differs from the measured pH=6.02 by 0.03 log units. The theoretical value relating the change of the emf of a H^+-sensitive glass electrode (measured against a reference electrode) with pH is 59.16 mV per pH unit (Garrels and Christ, 1965, p. 126). Thus, a change of 0.03 log units, represents a contribution of approximately 1.8 mV to the measured emf. Whether or not this value can be ascribed to liquid-junction potential, or a combination of this potential and potentials arising from other effects, is not known. We are presently attempting to evaluate liquid-junction potential

effects on measurements of pH in bicarbonate solutions in connection with our studies of ion-pairing and will reconsider the problem on the basis of the new experimental work.

On the other hand, the effective value of P_{CO_2} generally is not measured directly, but rather inferred from the conditions of the experiment. It seems possible that the correct value of P_{CO_2} to be used in calculating carbonate equilibria may be lower than the nominal value. The important point here is that what is really needed for accurate calculations is a knowledge of the value of the effective P_{CO_2} of rising gas bubbles near the immersed tip of the pH glass electrode. From table 2, we see that the calculated p[H^+] approaches the measured pH with lowering of P_{CO_2}. We suspect that the difference in the measured pH and the calculated p[H^+] arises from a combination of both of the effects discussed. In the present state of knowledge, we cannot really pin down either effect, and further discussion of the problem will have to await the results of any experiments designed specifically to test such effects.

Fortunately, the experimental values of the two basic quantities used in our calculations, namely, the value of the total calcium present in solution and the value of K_d, are much less subject to the kinds of errors discussed in the foregoing. The value $m_{Ca^{2+}(t)}=9.0$ to 9.1×10^{-3} is an analytically measured quantity, appropriate to a nominal value of $P_{CO_2}=0.97$ atm, and is accurate to approximately 1 percent. The value of $K_d=1.225\pm0.02$ was obtained (P. B. Hostetler and others, unpub. data, 1973) by a method that is based on changes in pH values and constancy of P_{CO_2} and not on the absolute values of these quantities.

Table 2 lists the calculated values of p[H^+], p[CO_3^{2-}], and pK_C for values of P_{CO_2} from 0.90 to 1.02 atm. The relatively small variation in pK_C enables us to pick what seems to be a reasonably accurate value for that quantity; we choose p$K_C=8.52\pm0.04$ as the "best" value at 25°C, and, in the following, calculate the temperature variation of pK_C on the basis of that value. The assigned error of ±0.04 log units is sufficiently large to include the variations in pK_C noted in table 2. These variations are probably the greatest source of uncertainty. Other possible errors included those in the values of K_0, K_1, K_2, $m_{Ca^{2+}(t)}$, and the $\mathring{a}$'s of Ca^{2+} and HCO_3^- used in the computations. It seems likely that such errors would be included in the ±0.04 figure (Langmuir, 1968). The pK_C values listed in table 2 are relatively insensitive to errors in the value of pK_d used. For example, if $m_{Ca^{2+}(t)}=9.1\times10^{-3}$ and pK_d is taken to be 1.285 (0.06 log units larger than the pK_d value of 1.225 used to calculate the values given in table 1), the results are $m_{Ca^{2+}}=7.70\times10^{-3}$, $m_{CaHCO_3^+}=1.40\times10^{-3}$, and $[Ca^{2+}]=4.33\times10^{-3}$. Comparing these numbers with the corresponding ones in table 1, it is seen that while $m_{CaHCO_3^+}$ increases approximately 11 percent for the more positive pK_d, $m_{Ca^{2+}}$ and $[Ca^{2+}]$ decrease only by approximately 1.8 percent. As a result, for example, p$K_C=8.533$ for p$K_d=1.285$ and $P_{CO_2}=0.97$ atm, compared with p$K_C=8.525$ for p$K_d=1.225$ (table 1). Thus, the assigned overall error of ±0.04 log units in pK_C will more than bracket errors of the order of ±0.1 log units in pK_d.

It may seem surprising that relatively large changes in a value of pK_d near 1.2 result in such small changes in the value of pK_C, in view of the fact that, if the $CaHCO_3^+$ ion pair is neglected, pK_C is near 8.4, whereas if pK_d is approximately 1.2, pK_C is near 8.5. However, this perhaps seeming inconsistency is easily explained. Equation 2 can be readily solved for K_d by assuming a value for $m_{CaHCO_3^+}$ that is insignificant compared to that of total dissolved calcium. If $m_{CaHCO_3^+}$ is taken to be of the order of 0.1 percent of $m_{Ca^{2+}(t)}$, then $m_{CaHCO_3^+}=10^{-5}$, and equation 2 yields $K'_d=10$. The ratio $K'_d/K_d=10/10^{-1.2}$ is 160. Thus, the first step in going from neglect of the ion pair $CaHCO_3^+$ to an even approximately correct value of K_d in calculating K_C is the most significant step. Of course, a precise knowledge of the value K_d is generally desirable but is not necessary for the present problem.

To this point, calculations have been made using the constants of Harned and coworkers for K_0, K_1, and K_2 (eq 3, 4, and 5). The reasons for using the Harned constants rather than those derived from the free-energy values of Wagman and others (1968) are given in the foregoing. However, it must be noted that if the Wagman constants (listed previously) are used, one finds that for saturated calcite solution at 25°C and $P_{CO_2}=0.97$ atm, the calculated p[H^+] is 6.01, nearly the same as the measured pH of 6.02. The use of the Wagman constants yields a calculated value of p$K_C=8.51$, in agreement with the previously chosen value of 8.52±0.04 (based on the Harned constants), so that for our primary purpose of obtaining the value of pK_C, it makes little difference which set of constants is used. Because the Wagman constants give a calculated p[H^+] in such good agreement with the measured pH, it might be argued that these constants are to be preferred to the Harned ones. Nevertheless, because the accuracy of the Harned constants can be assessed, while those of Wagman cannot, it seems necessary to make the detailed analysis that we have presented.

TEMPERATURE VARIATION OF THE ACTIVITY-PRODUCT CONSTANT OF CALCITE

Values of K_C were calculated over the temperature range 0° to 200°C, using the 25°C pK_C value of 8.52 together with entropy and heat capacity data, following the methods used in our studies of chrysotile (Hostetler and Christ, 1968) and magnesite (Christ and Hostetler, 1970). The value of K_C can be calculated at any temperature T, if the standard Gibbs free-energy change for the equilibrium reaction

$$CaCO_{3_{calcite}} = Ca^{2+} + CO_3^{2-} \qquad (16)$$

is known at that temperature; that is

$$\Delta G^\circ_T = -RT \ln K_C. \qquad (17)$$

The free-energy change of reaction at temperature T_2 can be calculated from that at T_1 by means of the equation

$$\Delta G^\circ_{T_2}=\Delta G^\circ_{T_1}-\Delta S^\circ_{T_1}(T_2-T_1)-T_2\int_{T_1}^{T_2}\Delta\overline{C}^\circ_P d\ln T+\int_{T_1}^{T_2}\Delta\overline{C}^\circ_P dT. \quad (18)$$

In equations 17 and 18 the standard thermodynamic quantities ΔG° (Gibbs free energy), ΔS° (entropy), and $\Delta\overline{C}^\circ_P$ (partial molal heat capacity) represent changes for the reaction; T is in K (kelvins), and R is the gas constant.

In general, values are not available for the partial molal heat capacities of ions at temperatures above 25°C. However, values of average heat capacities of common ions have been computed and tabulated by Criss and Cobble (1964).

If $\Delta\overline{C}^\circ_P\Big]_{25^\circ}^{t_2}$ is the average value of the heat-capacity change of reaction between temperatures 25°C and t_2°C, equation 18 can be rewritten as (Criss and Cobble, 1964)

$$\Delta(\Delta G^\circ)=\Delta G^\circ_{t_2}-\Delta G^\circ_{25^\circ}=\Delta S^\circ_{25^\circ}(t_2-25)+\Delta\overline{C}^\circ_P\Big]_{25^\circ}^{t_2}\times\left[(t_2-25)-T_2\ln\frac{T_2}{T_1}\right], \quad (19)$$

where T_1=298.15K.

Thus, a knowledge of ΔG° and ΔS° at 25°C and a value of the average heat-capacity change of reaction between that temperature and a higher temperature permit the calculation of ΔG° at the higher temperature. For the reaction of interest, the average heat-capacity change of reaction is given by

$$\Delta\overline{C}^\circ_P\Big]_{25^\circ}^{t_2}=\overline{C}^\circ_{P\,Ca^{2+}}\Big]_{25^\circ}^{t_2}+\overline{C}^\circ_{P\,CO_3^{2-}}\Big]_{25^\circ}^{t_2}-C^\circ_{P\,calcite}\Big]_{25^\circ}^{t_2}. \quad (20)$$

In the following discussion the units in which the thermodynamic quantities are expressed are: G° (cal mol^{-1}), S° (cal mol^{-1} deg^{-1}), standard enthalpy H° (cal mol^{-1}), and $\overline{C}^\circ_P$ (cal mol^{-1} deg^{-1}). The relationship between calories and absolute joules is given by the expression: 1 cal=4.1840 J.

For pK_C=8.52 at 25°C, from equation 17, $\Delta G^\circ_{25^\circ}$ is 11,624. The average heat-capacities of calcite were calculated from the enthalpy equation for calcite given by Kelley (1960, p. 42), using the definition

$$C^\circ_P\Big]_{25^\circ}^{t_2}=(H^\circ_T-H^\circ_{298.15})/(T-298.15). \quad (21)$$

Values used in calculating equation 19 (in addition to that for $\Delta G^\circ_{25^\circ}$) are listed in table 3. From the data listed in that table, for the reaction given by equation 16, ΔS°=−48.7, and the $\Delta C^\circ_P\Big]_{25^\circ}^{t_2}$ values are −107.4 (60°), −108.2 (100°), −100.0 (150°), and −107.6 (200°), where the temperature in parentheses denotes t_2 in °C. The appropriate values are substituted into equation 19 to calculate $\Delta(\Delta G^\circ)$ between 25°C and 60°, 100°, 150°, and 200°C, respectively. The $\Delta(\Delta G^\circ)$ values are 1,918; 4,604; 8,408; and 13,211. When these $\Delta(\Delta G^\circ)$ values and the value $\Delta(\Delta G^\circ)$=0, at 25°C, are plotted against the appropriate temperatures, a smooth curve results which yields the intermediate values of $\Delta(\Delta G^\circ)$ listed in table 4. From these $\Delta(\Delta G^\circ)$ values and the value $\Delta G^\circ_{25^\circ}$=11,624, the ΔG°_t values are calculated, and from these values, the values of pK_C are calculated (eq 17), also listed in table 4.

Table 3.—*Thermochemical data used in calculating the temperature variation of the activity-product constant of calcite*

Quantity[a]	Calcite[b]	Ca^{2+}[c]	CO_3^{2-}[d]
S°(25° C)	22.2	−13.2 −12.7	−13.6
$\overline{C}^\circ_P\Big]_{25^\circ}^{60^\circ}$	20.40	45	−132
$\overline{C}^\circ_P\Big]_{25^\circ}^{100^\circ}$	21.17	59	−146
$\overline{C}^\circ_P\Big]_{25^\circ}^{150^\circ}$	21.96	60	−138
$\overline{C}^\circ_P\Big]_{25^\circ}^{200^\circ}$	22.61	66	−151

[a] S° and $\overline{C}^\circ_P$ in cal mol^{-1} deg^{-1}.

[b] S° from Parker, Wagman, and Evans (1971, p. 45). Values of the average heat capacities calculated from the enthalpy equation given by Kelley (1960, p. 42).

[c] S°=−13.2 from Rossini and others (1952, p. 386); S°=−12.7 from Parker, Wagman, and Evans (1971, p. 30). An average value of S°=−12.95 was used to calculate the entropy change of reaction equal to −48.7 (see text). Average heat capacities from Criss and Cobble (1964).

[d] S° from Wagman and others (1968, p. 107). Average heat capacities from Criss and Cobble (1964).

It is difficult to assess the probable errors of the calculated pK_C values listed in table 4. Even if all the data used to construct the $\Delta(\Delta G^\circ)$ curve are accurate, there remains the problem of fitting a smooth curve through only five temperature points and then of reading intermediate values of $\Delta(\Delta G^\circ)$ from this curve. Points on the curve can be read to the nearest 10 calories, at best. We would judge that the values of $\Delta(\Delta G^\circ)$ listed in table 4 are precise (with respect to the $\Delta(\Delta G^\circ)$ curve) to about 30 calories, for the temperature range 25° to 200°C, and to about 40 calories below 20°C. Other sources of error may arise in the values of the entropies and heat capacities used to evaluate equation 19. The value of ΔS° used is −48.7 eu. Kelley and King (1961, p. 26) give the error in S° (25°) for calcite as ±0.2 eu. Estimating the total error in the sum of the entropies for calcium and carbonate ions to be

Table 4.—*Values of -log* K_C *calculated from the data in table 3* [1 cal = 4.1840 J]

t°C	$\Delta(\Delta G^\circ)$ (cal mol^{-1})	ΔG° (cal mol^{-1})	$-\log K_C$
0	-1,160	10,464	8.37
10	- 730	10,894	8.41
20	- 250	11,374	8.48
25	0	11,624	8.52
30	260	11,884	8.57
40	780	12,404	8.66
50	1,330	12,954	8.76
60	1,920	13,544	8.88
70	2,540	14,164	9.02
80	3,200	14,824	9.17
90	3,900	15,524	9.34
100	4,600	16,224	9.50
120	6,040	17,664	9.82
140	7,580	19,204	10.16
150	8,410	20,034	10.35
160	9,250	20,874	10.53
180	11,100	22,724	10.96
200	13,210	24,834	11.47

±0.3 eu, then for the dissolution reaction the error in ΔS° is ±0.5 eu. Criss and Cobble (1964) do not list errors for their values of the average heat capacities of Ca^{2+} but indicate the values for CO_3^{2-} given by them are to be considered as preliminary estimates. Taking all of these errors into account, the precision of the calculated -log K_C values given in table 4 is estimated to be of the order of ±0.05 units from 20° to 40°C and approximately ±0.08 units over the rest of the temperature range. Of course, these values are based on the 25°C value of -log K_C=8.52; any change in this 25°C value would cause a proportionate shift in the -log K_C values at other temperatures.

For temperatures above 100°C, the calculated values of the activity-product constant of calcite are applicable to the three-phase field, calcite plus solution plus vapor. For this system at 150°C, P_{H_2O} is approximately 5 atm, and at 200°C, about 15 atm. Thus, strictly speaking, corrections should be made to the thermochemical quantities for pressure; however, such corrections are insignificant.

ACTIVITY-PRODUCT CONSTANT OF ARAGONITE AT 25°C

The activity-product constant of aragonite at 25°C was calculated starting with a value for the total dissolved calcium and the value for the dissociation constant of the ion pair $CaHCO_3^+$, K_d, equal to $10^{-1.225}$, following the same procedure that was used to calculate the activity-product constant of calcite in the foregoing (equation 14 and ancillary equations).

Langmuir (1964) made a comprehensive review of the literature on the solubility of aragonite in water and concluded that the results obtained by Backstrom (1921) are definitive ones. Backstrom's measurements were determined reversibly in both undersaturated and supersaturated solutions, and both temperature and P_{CO_2} were carefully maintained. The aragonite he used was coarse enough to preclude particle-size effects, and he established that no significant amounts of calcite were being formed in the experiments. Backstrom obtained the value of 1.066 g/l, or $10.65\times10^{-3}m$, for the solubility of aragonite in pure water at 25°C and a nominal pressure of 1.00 atm of carbon dioxide. We have used this solubility value to calculate the activity-product constant of aragonite. The results of our calculations, in tables 5 and 6, were obtained in the same way as the results for calcite, in tables 1 and 2.

Table 5.—*Concentrations and activities of ionic species present in saturated aragonite solution at 25°C and at a nominal partial pressure of carbon dioxide of 1.00 atm*

[See text for definition of terms. Calculations are for pK_d=1.225 (eq 2)]

	For $m_{Ca^{2+}}(t)$ $=10.65\times10^{-3}$
I	0.0287
$m_{Ca^{2+}}$	9.03×10^{-3}
$m_{CaHCO_3^+}$	1.62×10^{-3}
$\gamma_{Ca^{2+}}$	0.542
$[Ca^{2+}]$	4.89×10^{-3}
$m_{HCO_3^-}$	19.68×10^{-3}
$\gamma_{HCO_3^-}$	0.858
$[HCO_3^-]$	16.88×10^{-3}

Table 6.—*Calculated values of the activities of hydrogen ion, carbonate ion, and activity-product constant of aragonite as a function of partial pressure of carbon dioxide at 25°C*

P_{CO_2} (atm)	The -log of $[H^+]$	The -log of $[CO_3^{2-}]$	The -log of K_A
0.90	6.089	6.012	8.322
.92	6.079	---	---
.94	6.070	6.031	8.341
.96	6.061	---	---
.97	6.056	6.045	8.355
.98	6.052	---	---
1.00	6.043	6.058	8.368
1.02	6.034	---	---

Note.—Calculations based on total dissolved calcium equal to $10.65\times10^{-3}m$. The listing of calculated values to three decimal places does not mean that these values are considered to be that precise. The extended listing is given to enable the reader to more readily interpolate between values.

Garrels, Thompson, and Siever (1960) measured an apparent equilibrium pH value of 6.08 for saturated aragonite solution, at a nominal value of P_{CO_2}=0.97 atm. From table 6 we see that these two values are not completely compatible, although

if we accept, for example, that the correct P_{CO_2} value is 0.97 atm., then the calculated $p[H^+]$ differs from the measured pH by only 0.02 units. The same sources of error stated in the foregoing discussion of calcite apply equally well to measurements on aragonite. Thus, in particular, it seems likely that neither the measured pH value nor the inferred P_{CO_2} value can be considered to be completely accurate, and as a result the calculated activity-product constant of aragonite cannot be pinned down as precisely as we would like. However, as in the case of calcite, the relatively small variation in the negative logarithm of the activity-product constant of aragonite, pK_A, enables us to choose a "best" value for that quantity. We have taken $pK_A=8.36\pm0.04$ at 25°C, and, in the following, calculate the temperature variation of pK_A on the basis of that value.

As for calcite, if the values of K_0, K_1, and K_2 derived from the free-energy values of Wagman and others (1968) are used to calculate the $p[H^+]$ for saturated aragonite solution at 25°C and $P_{CO_2}=0.97$, the difference between measured pH and calculated $p[H^+]$ practically disappears. Under these conditions the calculated $p[H^+]=6.07$ versus the measured pH=6.08. The calculated pK_A is 8.34 in good agreement with the selected value of 8.36±0.04.

From the solubility measurements of Backstrom (1921), and neglecting the ion pair $CaHCO_3^+$, Langmuir (1964), calculated pK_A to be 8.24. The pH and P_{CO_2} values of Garrels and others (1960) lead to a pK_A of 8.25, again neglecting $CaHCO_3^+$. As was shown in the foregoing, if ion-pairing is neglected in calculating the activity-product constant of calcite, the value $pK_C=8.40$ is obtained. Our calculations, based on the solubility of calcite, and a $pK_d=1.225$, lead to the value $pK_C=8.52$. There is a difference of 0.12 units in the values of pK_C, calculated by the two methods. For aragonite, this same difference is found; that is, 8.24 versus 8.36 for the values of pK_A calculated by the two methods.

TEMPERATURE VARIATION OF THE ACTIVITY-PRODUCT CONSTANT OF ARAGONITE

Values of the activity-product constant of aragonite were calculated over the temperature range 0° C to 200°C, using the 25°C $-\log K_A$ value of 8.36, and appropriate entropy and heat capacity data, in the same way that was used for calcite. The thermochemical data used are given in table 7. The entropy change for the dissolution of aragonite was taken as -47.8 eu, and values of the average heat-capacity change of reaction $\Delta\bar{C}_P^\circ\,]_{25^\circ}^{t_2}$ as -107.0 (60°), -107.6 (100°), -99.2 (150°), and -106.7 (200°), where the temperature in parentheses is t_2 in °C. Calculated values of $-\log K_A$, as a function of temperature, are listed in table 8.

Approximately the same estimated errors that apply to the calculated values of the activity-product constant of calcite as a function of temperature can be used for aragonite. Thus, the error in pK_A is of the order of ±0.05 units from 20° to 40°C and approximately ±0.08 units over the rest of the temperature range.

Table 7.—*Thermochemical data used in calculating the temperature variation of the activity-product constant of aragonite*

Quantity[a]	Aragonite[b]	Ca^{2+} [c]	CO_3^{2-} [d]
S°(25° C)	21.2	-13.2 -12.7	-13.6
$\bar{C}_P^\circ\,]_{25^\circ}^{60^\circ}$	20.00	45	-132
$\bar{C}_P^\circ\,]_{25^\circ}^{100^\circ}$	20.57	59	-146
$\bar{C}_P^\circ\,]_{25^\circ}^{150^\circ}$	21.18	60	-138
$\bar{C}_P^\circ\,]_{25^\circ}^{200^\circ}$	21.71	66	-151

[a] S° and $\bar{C}_P^\circ$ in cal mol^{-1} deg^{-1}.

[b] S° from Parker, Wagman, and Evans (1971, p. 45). Values of the average heat capacities calculated from the enthalpy equation given by Kelley (1960, p. 42).

[c] $S^\circ=-13.2$ from Rossini and others (1952, p. 386); $S^\circ=-12.7$ from Parker, Wagman, and Evans (1971, p. 30). An average value of $S^\circ=-12.95$ was used to calculate the entropy change of reaction equal to -48.7 (see text). Average heat capacities from Criss and Cobble (1964).

[d] S° from Wagman and others (1968, p. 107). Average heat capacities from Criss and Cobble (1964).

Table 8.—*Values of -log K_A calculated from the data in table 7*
[1 cal=4.1840 J]

t°C	$\Delta(\Delta G^\circ)$ (cal mol^{-1})	ΔG° (cal mol^{-1})	$-\log K_A$
0	-1240	10166	8.13
10	- 770	10636	8.21
20	- 280	11126	8.29
25	0	11406	8.36
30	280	11686	8.42
40	760	12166	8.49
50	1300	12706	8.59
60	1880	13286	8.72
70	2500	13906	8.86
80	3140	14546	9.00
90	3810	15216	9.16
100	4520	15926	9.33
120	5910	17316	9.62
140	7440	18846	9.97
150	8270	19676	10.16
160	9110	20516	10.35
180	10970	22376	10.79
200	13010	24416	11.28

DISCUSSION OF RESULTS

While it seems likely that the approach used here to calculate the 25°C values of the activity-product constants of calcite and aragonite to yield $pK_C=8.52$ and $pK_A=8.36$, is accurate to within ±0.04 units, our calculations of the temperature variations of these pK values are somewhat less accurate, as was pointed out in the foregoing. However, Donald Langmuir

and others (written commun., 1971) are carrying out reversed laboratory solubility measurements of calcite from 0° to 50°C, and are independently determining the dissociation constant of $CaHCO_3^+$. Our own studies of this dissociation constant are being extended to temperatures up to 90°C. When all these results become available, values of pK_C can be calculated directly at temperatures up to 50°C, and in this way the present calculation of the temperature variation of pK_C can be checked and modified if necessary.

From table 4, the standard free energy of the calcite dissolution reaction at 25°C is 11,624 cal mol^{-1}, with an assigned error of ±55 (corresponding to ±0.04 pK units). The most recently published value of the standard free energy of formation, ΔG_f°, for Ca^{2+} (aq) is -132,300 (Parker and others, 1971); Langmuir (1968) lists the value -132,350±250. ΔG_f° for CO_3^{2-} (aq) is given as -126,170 by Wagman and others (1968); Langmuir (1968) assigns an error of ±70 to this quantity. Using the value of Langmuir for ΔG_f° of Ca^{2+} (aq) and the values for ΔG_f° of reaction and ΔG_f° for CO_3^{2-} (aq) given in the foregoing, then the standard free energy of formation of calcite from the elements, ΔG_f° (calcite), is -270,144±375 cal mol^{-1}, at 25°C. Langmuir (1968) lists -269,980±260 for this quantity.

From table 8, the standard free energy of the aragonite dissolution reaction is 11,406 cal mol^{-1} for 25°C; again the assigned error is ±55. Following the procedure used for calcite, ΔG_f°(aragonite) is calculated to be -269,926±375 cal mol^{-1}.

Langmuir (1964) made an exhaustive evaluation of the standard free energy change of reaction for the transformation of aragonite to calcite, at 25°C. His general conclusion was that ΔG° for this reaction was -230±30 cal mol^{-1}. He affirmed this value recently (written commun., 1971). Langmuir's study was based upon published data on studies of solubility, heats of reaction, and high-temperature high-pressure equilibria. Our present results lead to a value for this ΔG° of -218±110 cal mol^{-1} (-11,624±55+11,406±55), a value in excellent agreement with Langmuir's, especially when our larger error is taken into account. If we take the value of ΔG_f° (calcite) of Langmuir (1968), and his estimate of ΔG° of transformation of aragonite to calcite, we calculate the value of ΔG_f° (aragonite) to be -269,750±290 cal mol^{-1}.

We have shown in this paper that there are certain inherent difficulties in determining very accurate values of activity-product constants of carbonates from solubility and pH measurements in CO_2 saturated solutions, even when the solubility of the carbonate phase and details of ion-pairing are known accurately. One additional parameter is needed; that is, an accurate value of either $p[H^+]$ or P_{CO_2}. Fortunately, for thermochemical purposes the value of a pK does not need to be known very accurately. As we pointed out, an error of ±0.04 pK units corresponds to an error of only ±55 cal, so that in determining the value of the free energy of formation of a solid phase, the error that can be attributed to the solubility measurements amounts to only ±55 cal.

ACKNOWLEDGMENTS

We are grateful to Prof. R. M. Garrels, University of Hawaii; Prof. Donald Langmuir, Pennsylvania State University; Prof. L. Niel Plummer, State University of New York at Buffalo; and A. H. Truesdell, U.S. Geological Survey, for much helpful discussion during the course of this work. We also thank Professors Langmuir and Plummer for the use of their unpublished data and Professor Garrels and Dr. Truesdell for their critical reviews of the manuscript. This research was supported in part by the Petroleum Research Fund of the American Chemical Society, Grant 5052-AC 2, and by the National Science Foundation, Grant GA 31231.

REFERENCES CITED

Backstrom, H. L. K., 1921, The solubilities of calcite and aragonite: Med. Vetenskapsakad. Nobelinst., v. 4, p. 11.

Bates, R. G., 1964, Determination of pH, theory and practice: New York, John Wiley and Sons, 435 p.

Berner, R. A., 1967, Comparative dissolution characteristics of carbonate minerals in the presence and absence of aqueous magnesium ion: Am. Jour. Sci., v. 265, p. 45–70.

Christ, C. L., and Hostetler, P. B., 1970, Studies in the system MgO-SiO_2-CO_2-H_2O–[Pt.] 2, The activity-product constant of magnesite: Am. Jour. Sci., v. 268, p. 439–453.

Criss, C. M., and Cobble, J. W., 1964, The thermodynamic properties of high temperature aqueous solutions–[Pt.] 5, The calculation of ionic heat capacities up to 200°C. Entropies and heat capacities above 200°C: Am. Chem. Soc. Jour., v. 86, p. 5390–5393.

Davies, C. W., and Hoyle, B. E., 1951, The dissociation constant of calcium hydroxide: Chem. Soc. [London] Jour., Jan., p. 233–234.

Garrels, R. M., and Christ, C. L., 1965, Solutions, minerals, and equilibria: New York, Harper and Row, 450 p.

Garrels, R. M., and Thompson, M. E., 1962, A chemical model for sea water at 25°C and one atmosphere total pressure: Am. Jour. Sci., v. 260, p. 57–66.

Garrels, R. M., Thompson, M. E., and Siever, R., 1960, Stability of some carbonates at 25°C and one atmosphere total pressure: Am. Jour. Sci., v. 258, p. 402–418.

Greenwald, Isidor, 1941, The dissociation of calcium and magnesium carbonates: Jour. Biol. Chemistry, v. 141, p. 789.

Harned, H. S., and Davis, Raymond, Jr., 1943, The ionization constant of carbonic acid in water and the solubility of carbon dioxide in water and aqueous salt solutions from 0° to 50°C: Am. Chem. Soc. Jour., v. 65, p. 2030–2037.

Harned, H. S., and Scholes, S. R., Jr., 1941, The ionization constant of HCO_3^- from 0° to 50°C: Am. Chem. Soc. Jour., v. 63, p. 1706–1709.

Helgeson, H. C., 1967, Solution chemistry and metamorphism, *in* Abelson, P. H., ed., Researches in geochemistry, v. 2: New York, John Wiley and Sons, p. 362–404.

Hostetler, P. B., and Christ, C. L., 1968, Studies in the system MgO-SiO_2-CO_2-H_2O–[Pt.] 1, The activity-product constant of chrysotile: Geochim. et Cosmochim. Acta, v. 32, p. 485-497.

Ives, D. J. G., and Janz, G. J., eds., 1961, Reference electrodes, theory and practice: New York, Academic Press, 651 p.

Kelley, K. K., 1960, Contributions to the data on theoretical metallurgy–[Pt.] 13, High-temperature heat-content, heat-capacity, and entropy data for the elements and inorganic compounds: U.S. Bur. Mines Bull. 584, 232 p.

Kelley, K. K., and King, E. G., 1961, Contributions to the data on theoretical metallurgy–[Pt.] 14, Entropies of the elements and inorganic compounds: U.S. Bur. Mines Bull. 592, 149 p.

Lafon, G. M., 1970, Calcium complexing with carbonate ion in aqueous solutions at 25°C and 1 atmosphere: Geochim. et Cosmochim. Acta, v. 34, p. 935–940.

Langmuir, Donald, 1964, Stability of carbonates in the system CaO-MgO-CO_2-H_2O: Cambridge, Mass., Harvard Univ., Ph. D. thesis, 142 p.

—— 1968, Stability of calcite based on aqueous solubility measurements: Geochim. et Cosmochim. Acta, v. 32, p. 835–851.

—— 1971, The geochemistry of some carbonate ground waters in central Pennsylvania: Geochim. et Cosmochim. Acta, v. 35, p. 1023–1045.

Lewis, G. N., and Randall, Merle, 1961, Thermodynamics, *revised by* K. S. Pitzer and Leo Brewer: New York, McGraw-Hill Book Co., 723 p.

Mattock, G., and Band, D. M., 1967, Interpretation of pH and cation measurements, *in* Eisenman, George, ed., Glass electrodes for hydrogen and other cations: New York, Marcel Dekker, p. 9–49.

Nakayama, F. S., 1968, Calcium activity, complex and ion-pair in saturated $CaCO_3$ solutions: Soil Sci., v. 106, p. 429–434.

Parker, V. B., Wagman, D. D., and Evans, W. H., 1971, Selected values of chemical thermodynamic properties: U.S. Natl. Bur. Standards Tech. Note 270-6, 119 p.

Rossini, F. D., Wagman, D. D., Evans, W. H., Levine, Samuel, and Jaffe, Irving, 1952, Selected values of chemical thermodynamic properties: U.S. Natl. Bur. Standards Circ. 500, 1,268 p. Part I. Tables, p. 1–822, reprinted in 1961.

Wagman, D. D., Evans, W. H., Parker, V. B., Halow, I., Baily, S. M., and Schumm, R. H., 1968, Selected values of chemical thermodynamic properties: U.S. Natl. Bur. Standards Tech. Note 270-3, 264 p.

Weast, R. C., ed., 1967, Handbook of chemistry and physics [48th ed.]: Cleveland, Chemical Rubber Publishing Co.

Jour. Research U.S. Geol. Survey
Vol. 2, No. 2, Mar.-Apr. 1974, p. 185–187

THERMAL CONDUCTIMETRIC DETERMINATION OF SUBMILLIGRAM AMOUNTS OF TOTAL WATER IN SILICATE AND CARBONATE MINERALS

By JOHN MARINENKO, Washington, D.C.

Abstract.—A simple and rapid method was developed for determining submilligram amounts of total water in silicate and carbonate minerals. Powdered samples are fused by heating with sodium tungstate–vanadium pentoxide flux in a Vycor combustion tube, and the evolved water vapor is absorbed on silica gel. After the water collection, the silica gel is heated at a controlled rate, and the released water vapor, carried by helium, is detected by thermal conductivity.

Since the turn of the century it has been a common practice to determine total water in minerals and rocks by the gravimetric method of Penfield (1894), or its variations (Harvey, 1939; Shapiro and Brannock, 1955; Wilson, 1962; Courville, 1962). These methods are described in a review by Harris (1972). The Penfield method or its variations, with the use of sufficiently large samples (0.1 to 1 g), give accurate results for total water in silicates, carbonates, and phosphates. A microdetermination of total water by the Penfield method is described by Sandell (1951). This method requires correction for loss of water by evaporation. Furthermore, the method does not account for procedural blanks. A microcoulometric method for determining total water in minerals (Cremer and others, 1971) has been applied to small samples. An infrared absorption method for determination of microgram amounts of fixed water (H_2O+) in rocks is described by Breger and Chandler (1969). This method, although very sensitive, has not been applied to minerals.

The method described here provides sufficient sensitivity and accuracy for determining major water (1 to 20 percent) on mineral samples weighing 5 to 10 mg and minor water (0.1 to 1 percent) on samples weighing 10 to 100 mg. An order-of-magnitude increase in sensitivity over the older gravimetric methods for total water is achieved without significant loss in accuracy.

REAGENTS

Sodium tungstate–vanadium pentoxide flux: Fuse 20 g of sodium tungstate dihydrate in platinum dish, cool, and grind to a fine powder. Heat 5 g of vanadium pentoxide to 700°C in porcelain crucible and cool in a desiccator. Mix the two powders in a covered weighing bottle and store in a desiccator over phosphorous pentoxide.

Aluminum foil: 0.0013 cm thick.

Barium chloride dihydrate: ACS (Am. Chem. Soc.) reagent, 99.0 percent assay.

APPARATUS

A schematic diagram of the apparatus is shown in figure 1. A gas chromatograph (Hewlett Packard[1] F and M Model 700) equipped with a tungsten thermal conductivity cell is used. Needle valves A and B are part of the standard equipment. An auxiliary valve, C, is installed to permit rapid switching of carrier gas flow without any adjustment of needle valve B. Externally, the carrier gas is controlled by a three-way valve, D; an on-off valve, E; and needle valve, F. The wheatstone-bridge output voltages are measured with a Minneapolis-Honeywell[1] Electronik 15 recorder.

Oven temperature is regulated with a temperature programer (Hewlett Packard[1] F and M Model 240). The columns are prepared by packing 43-cm-long stainless-steel tubing (0.6 cm OD) with an 8-cm plug of 30- to 60-mesh silica gel (Matheson, Coleman, and Bell Co.[1]). Pyrex wool is used to hold the silica gel plug in place, about 8 cm from the injection port. Helium is used as a carrier gas.

The combustion tube is made from Vycor tubing. The tube is closed with a rubber stopper through which a 2-mm-OD copper tube is inserted to introduce the carrier gas. Tubing for the delivery of carrier gas is made of copper with only one joint connected with minimum length of rubber tubing.

The furnace was constructed from a 240-W Nichrome filament wrapped inside a fused alumina cylinder. It attained 950° to 1,000°C in 5 min with 70 V applied with an autotransformer. Standards and samples are heated in porcelain boats (inside dimensions: length, 2.5 cm; width, 0.4 cm; height, 0.3 cm). Before use, the empty boats should be ignited to 900°C and cooled to room temperature in a desiccator.

[1] Use of model name is for descriptive purposes only and does not constitute an endorsement of the product by the U.S. Geological Survey.

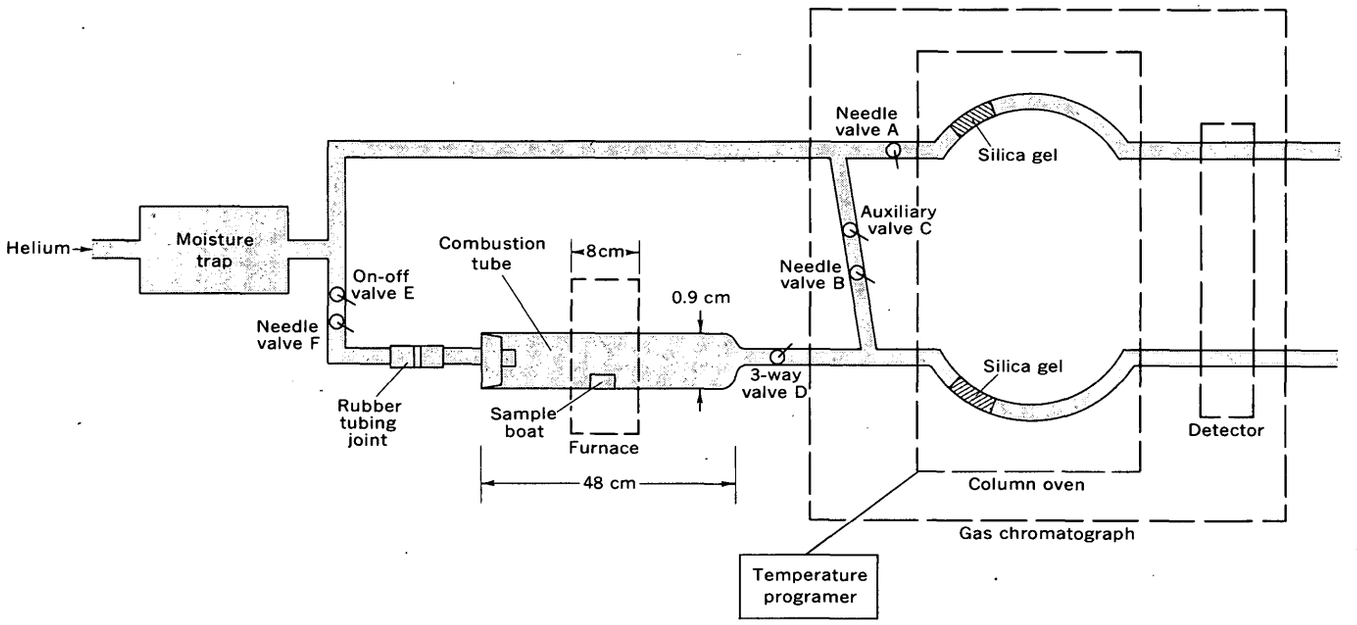

Figure 1.—Schematic diagram of apparatus for determining submilligram amounts of total water in silicate and carbonate minerals. Not drawn to scale.

PROCEDURE

Deliver helium carrier gas at 800 g/cm^2 and a flow rate of 60 ml/min through the sample and reference columns (valve E closed, valve F open, the combustion tube open to the atmosphere through valve D, and valves A, B, and C open). Set the attenuator control knob on the 16 position for the standards of 0.2 to 1.0 mg of water. Set the recorder speed at 2.5 cm/min, filament current at 200 mA, the detector temperature at 100° to 120°C, and the injection port at 90°C.

Open valve E to permit helium flow through the combustion tube and flush for 3 min to displace air. Close valve C and open valve D to allow carrier gas through the sample column. At this time check the rate of helium flow and, if necessary, adjust to a flow of 60 ml/min through the reference column with valve A and through sample column with valve F. Turn the furnace on and then turn it off after 7 min. Cool the furnace for 7 min with a fan. Set the temperature programer to heat the column oven at a rate of 30°/min and maximum temperature of 220° to 230°C. Turn the recorder on when the temperature of the oven reaches 110°C. The area under the curve is a measure of water content.

After the curve is registered on the chart, vent the combustion tube to the atmosphere with valve D, open valve C, and cool the oven to 50°C by setting the temperature programer back to the 50° mark and opening the oven door. This procedure should be repeated until the apparatus is free of residual water (area under the curve should not exceed 1 cm^2).

Accurately weigh three standards (2–7 mg of barium chloride dihydrate) into porcelain boats on a semimicrobalance or microbalance. Place the boat containing a standard into the combustion tube. Repeat the procedure described above for water evolution, collection, and detection.

Weigh the samples into porcelain boats and mix with 100 mg of flux. Use a pair of tweezers to cover the boats with 1 by 3 cm aluminum foil and then treat as described above for standards. Measure the area under the curve with a planimeter or an integrator and relate it to the area of the standards.

DISCUSSION AND RESULTS

A typical water signal as a function of temperature of the silica gel collector is shown in figure 2. Under the conditions given above, water is quantitatively released between 160° and 220°C.

The sodium tungstate–vanadium pentoxide flux is used to retain sulfur and fluorine. Vanadium pentoxide provides oxidizing melt. Carbon dioxide evolved from carbonates during sample fusion does not interfere.

Even though gas chromatographic equipment was used, the method described above is based on the collection rather than chromatographic separation of water. It is most applicable for determining total water in small mineral samples where conventional methods fail due to limited sensitivity.

Use of barium chloride dihydrate as a water standard was chosen because of its stability to changes in room temperature and humidity. Its stoichiometry of water can be determined

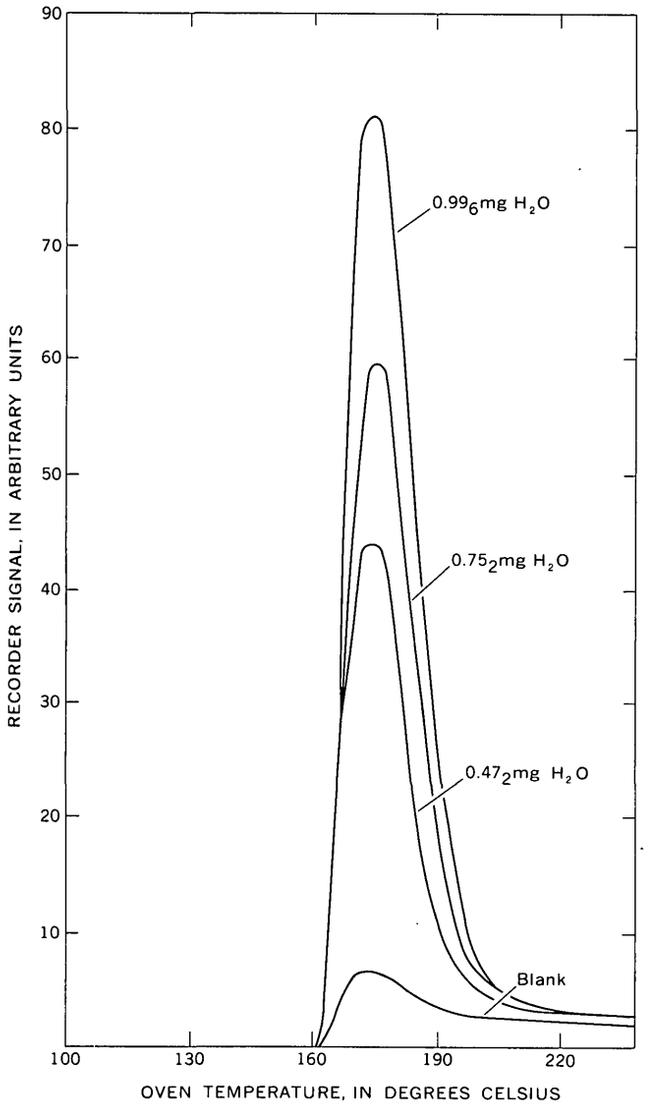

Figure 2.—Thermal conductivity signal of water released from silica gel collector as a function of temperature.

gravimetrically by difference after expulsion of water at 150°C, or it can be checked internally against water content of 99.7 percent potassium bicarbonate by the method described above. Use of potassium bicarbonate as a water standard is desirable because its weighing factor is more favorable than that of barium chloride dihydrate.

An aluminum foil cover is used to prevent H_2O- loss during the displacement of the air in the combustion tube with dry helium. Since the foil melts at about 660°C, it does not prevent the evolution of water from the samples.

The procedural blank for standards was evaluated over a period of 2 weeks by placing an empty boat into the combustion tube and repeating the determination of water as described above for standards. Thirteen determinations gave an average blank of 0.064±0.017 mg of water. Four blank determinations on boat, 100 mg flux, and aluminum foil gave an average procedural blank for samples of 0.069±0.012 mg of water.

The use of rubber tubing for connections was found to have a direct relationship to the magnitude of the procedural blank. Therefore, the surface of rubber tubing which contacts dry helium carrier gas should be minimized.

The procedure was tested on a selected group of rocks and minerals. Results are given in table 1. A small but consistent negative bias between the water determined by this method and other methods is due in part to unavoidable losses of adsorbed water (H_2O^-) during the displacement of air in the combustion tube with dry helium.

Table 1.—*Total water content of selected minerals and rocks determined by thermal conductimetry and other methods*

	Thermal conductimetric method			Total water by conventional methods[2] (percent)
	Approx sample weight (mg)	Total water (percent)	Coefficient of variation[1] (percent)	
Minerals				
Muscovite	13	4.27, 4.31	5	4.32
Biotite	15	5.29, 5.50	4	5.65
Antigorite	8	11.9, 12.4	2	[3]12.0
Magnesium carbonate hydrate	4	23.5, 23.2	1	23.7
Rocks				
Andesite (AGV-1)	30–60	1.70	9	[4]1.84
Granite (G-2)	60	.56	7	[4].66
Periodotite(PCC-1)	18	5.04	2	[4]5.17

[1] For minerals, calculated from the standard deviation derived from the formula for a set of duplicate determinations; four determinations for each rock.
[2] For minerals, total water determined by Penfield method.
[3] Analyst, Blanche Ingram, U.S. Geological Survey.
[4] Average value (Flanagan, 1969, table 4).

REFERENCES CITED

Breger, I. A., and Chandler, J. C., 1969, Determination of fixed water in rocks by infrared absorption: Anal. Chemistry, v. 41, p. 506–510.

Courville, Serge, 1962, Apparatus for total water determination by the Penfield method: Canadian Mineralogist, v. 7, pt. 2, p. 326–329.

Cremer, Marcelyn, Elsheimer, H. N., and Escher, E. E., 1971, Microcoulometric measurement of water in minerals: Anal. Chim. Acta, v. 60, p. 183–192.

Flanagan, F. J., 1969, U.S. Geological Survey standards–[pt.] II. First compilation of data for the new U.S.G.S. rocks: Geochim. et Cosmochim. Acta, v. 33, p. 81–120.

Harris, Clifford, 1972, Determination of water, a review: Talanta, v. 19, p. 1523–1547.

Harvey, C. O., 1939, Simple method for determination of water in silicates: Great Britain Geol. Survey Bull., no. 1, p. 8–12.

Penfield, S. L., 1894, On some methods for the determination of water: Am. Jour. Sci., 3d ser., v. 48, p. 30–37.

Sandell, E. B., 1951, Microdetermination of water by the Penfield method: Mikrochemie (Mikrochim. Acta), v. 38, p. 487–491.

Shapiro, Leonard, and Brannock, W. W., 1955, Rapid determination of water in silicate rocks: Anal. Chemistry, v. 27, p. 560–562.

Wilson, A. D., 1962, Determination of total water in rocks by a simple diffusion method: Analyst, v. 87, p. 598–600.

Jour. Research U.S. Geol. Survey
Vol. 2, No. 2, Mar.-Apr. 1974, p. 189—194

PRELIMINARY STUDY OF ROCK ALTERATION IN THE CATHEART MOUNTAIN MOLYBDENUM-COPPER DEPOSIT, MAINE

By ROBERT G. SCHMIDT, Washington, D. C.

Abstract.—Studies of drill cores from the Catheart Mountain molybdenum-copper deposit indicate that the deposit is of the porphyry type. Hydrothermal alteration and sulfide mineralization are probably distributed in complex but systematic alteration zones. Most or all mineralization at Catheart Mountain is in a medium-fine-grained quartz monzonite enclosed within a larger mass of Attean Quartz Monzonite; no ore and little hydrothermal alteration have been seen in the Attean. Much of the ore and hydrothermal alteration seem to be and presumably are spatially related to irregular intrusive masses of porphyry. Only certain porphyry intrusives are mineral bearing, however, and many have no associated ore and alteration. Studies of hydrothermal alterations in surface exposures supplemented by rock analyses of bulk samples indicate that alteration features and sulfide zone characteristics of an area northwest of the mountain crest are, when measured against accepted porphyry models, very favorable for the occurrence of ore. Even though this favorable area has already been tested by some drilling, the presence together here of the strong center of potassic enrichment, the well-developed pyrite zone, and the strong and extensive phyllic alteration suggest that some further evaluation may be warranted.

The Catheart Mountain molybdenum-copper porphyry deposit was discovered in 1963, and a major drilling program by Noranda Exploration Co., Ltd., has been carried out since 1966. Study of this deposit in Somerset County, northwest Maine (fig. 1), was started by the U.S. Geological Survey in 1970 and is continuing. The main objective has been to examine for evidence of hydrothermal alteration and zonation of copper and molybdenum mineralization. This report covers the preliminary results of this study.

The present study has consisted of two phases. First, more than 2,377 m (7,800 ft) of diamond-drill core from a limited area were examined and the visual characteristics were related, both manually and by computer correlations under the direction of J. A. Calkins, to chemical analyses for copper and molybdenum. Second, about 55 outcrop areas at Catheart Mountain were examined and described. Thin sections were studied from most of these areas, and rock analyses were made from bulk samples taken at 32 of them.

Acknowledgments.—The cooperation of Noranda Exploration Co., Ltd., and the Scott Paper Co. is gratefully acknowledged. They helped with access to the field area and provided drill cores and corresponding assay records for study.

Core logging in the field was done on a key-punch form prepared for this study by J. A. Calkins. The computer analysis of the field and laboratory data from drill cores that provided the information summarized in table 3 was planned and carried out by J. A. Calkins and N. A. Wright.

GENERAL GEOLOGY

Catheart Mountain is on the southeast flank of the Boundary Mountain anticlinorium and the northwest flank of the Moose River synclinorium (Albee and Boudette, 1972, p. 7–8).

Two plutonic types of quartz monzonite and one or more types of near-surface or subvolcanic rock form the bedrock in the area of Catheart Mountain. Catheart Mountain lies within the area mapped as Attean Quartz Monzonite described by Albee and Boudette (1972, p. 23) as "a mottled pink and green medium- to coarse-grained porphyritic quartz monzonite characterized by large phenocrysts of potassium feldspar." Chemical analyses of this rock are given in table 1. Outcrops of typical Attean Quartz Monzonite were seen only along the southeast side of the study area, but the rock was penetrated by drill holes on the northwest side. No Attean Quartz Monzonite was recognized in the areas of principal mineralization.

The west end of Catheart Mountain is underlain by a different quartz monzonite of uniformly medium fine granitic texture which contrasts with the coarser Attean Quartz Monzonite. Both quartz monzonites are cut by dikes and irregular masses of fine-grained feldspar-quartz porphyry. The medium-fine-grained quartz monzonite is referred to simply as quartz monzonite in the rest of this report. All the ore deposits are confined to the quartz monzonite and the fine-grained feldspar-quartz porphyry.

The quartz monzonite is gray and uniformly medium fine grained, and the major minerals are quartz, potassium feldspar, and plagioclase. Chlorite, epidote, and calcite derived from biotite by metamorphism indicate that biotite was originally a common mineral. Fairly abundant muscovite is probably mostly the product of metamorphism and hydrothermal alteration, but some may have been a primary rock mineral. This rock is distinguished from the Attean Quartz Monzonite by the generally finer grain size and the absence of large (1–2 cm) feldspars. Chemical analyses of both rocks are given in table 1.

The quartz monzonite is similar to rock exposed near Pyrite Creek and on part of the ridge west of Pyrite Creek (fig. 1).

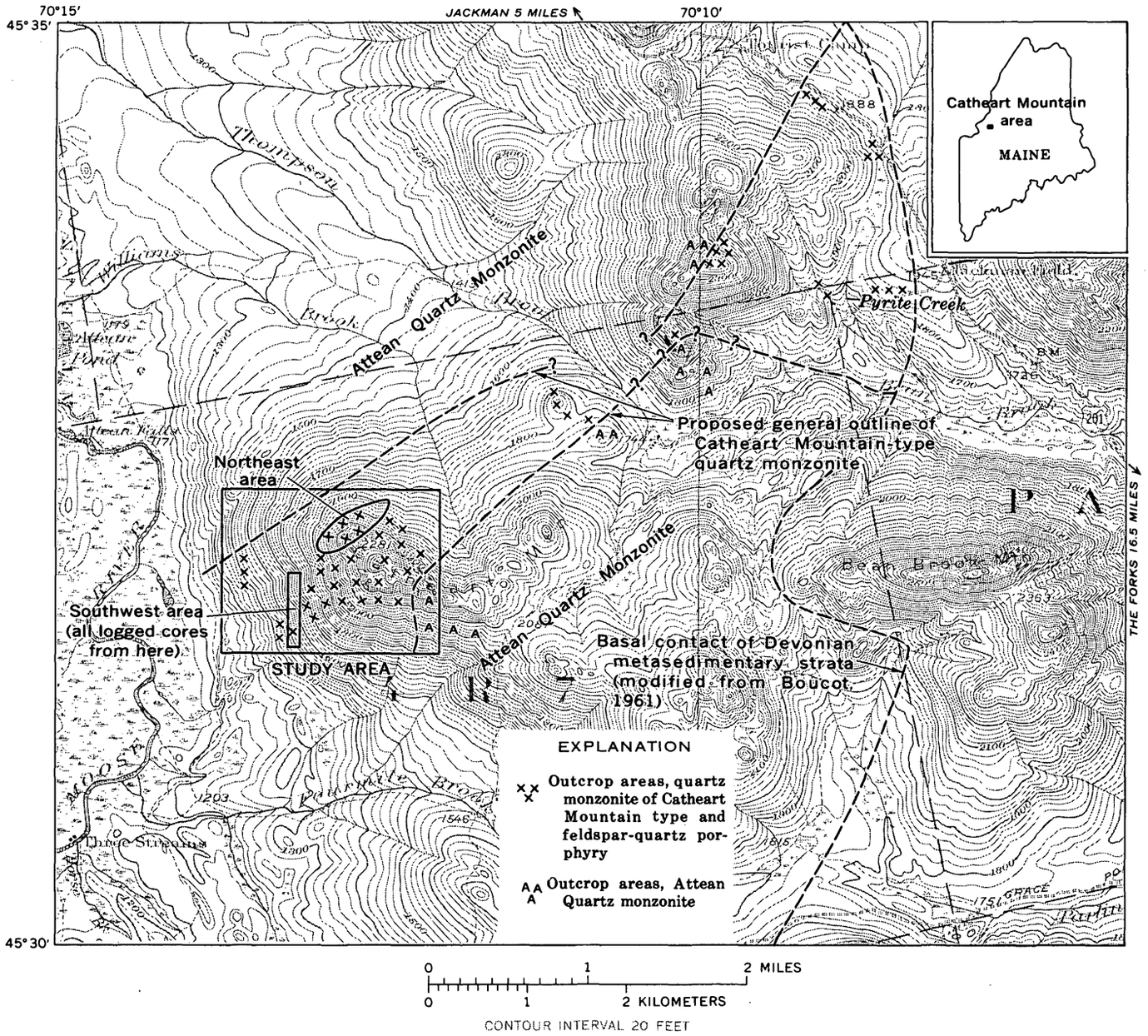

Figure 1.—Topographic map showing Catheart Mountain area, Maine.

Boundaries of the quartz monzonite trend northeastward at Catheart Mountain. Although I have examined only part of the rock exposures in the intervening area near the heads of Williams Brook and Thompson Brook, I think it probable that the quartz monzonite forms a narrow belt or a succession of patches up to 2.4 km (1.5 mi) wide and at least 9.6 km (6 mi) long from the southwest slope of Catheart Mountain to roadcut exposures along U.S. Highway 201 (fig. 1).

Small, probably subvolcanic intrusive bodies of feldspar porphyry and feldspar-quartz porphyry, the latter with some rounded phenocrysts of quartz, are abundant on Catheart Mountain and near Pyrite Creek. Plagioclase is the only feldspar in both types. The porphyries are locally intensely hydrothermally altered, but many similar porphyry bodies are not altered and have no related mineralization. I have not identified any age relationships between unaltered and altered porphyries. There are several unaltered porphyry masses within the Attean Quartz Monzonite on the east end and south sides of Catheart Mountain.

The Attean Quartz Monzonite is regarded by Albee and Boudette as probably Ordovician in age, and they attribute three radiometric ages of 356±15, 366±10, and 373±10 m.y.

Table 1.—*Analyses of bulk rock samples from the Catheart Mountain area*

[Sample BA-766 is from a point on Attean Mountain, south of the west end of Attean Pond, about 7 mi northwest of Catheart Mountain (Albee and Boudette, 1972, p. 24). The rest of the samples are from the study area on Catheart Mountain]

	Attean Quartz Monzonite	Quartz monzonite of Catheart Mountain								Quartz porphyry and some quartz monzonite	
	Metamorphosed rock, perhaps some propylitic alteration	Metamorphosed rock, perhaps some propylitic alteration				Phyllic and potassic alteration				Phyllic and potassic alteration	
Field No.	BB-2526b, BA-766[1]	SM90138[2]	SM90140[2]	SM90057[3]	SM90137[2]	SM90143[2]	SM90128[4]	SM90113[2]	SM90133[4]	SM90129[2]	SM90108[2]	SM90114[2]
SiO_2	70.2	70.3	69.5	70.8	69.1	70.0	67.8	72.7	70.4	71.2	68.5	70.4
Al_2O_3	14.5	14.4	14.8	14.8	15.1	14.2	15.7	13.6	15.1	13.3	15.6	14.1
Fe_2O_3	1.4	1.3	.80	1.6	.70	1.1	.90	1.2	1.4	1.6	1.6	1.1
FeO	1.3	3.4	2.2	.80	3.8	2.4	2.1	1.3	1.1	1.2	1.5	4.1
MgO	.87	1.2	1.5	.90	1.4	1.4	1.6	1.2	.92	.96	1.4	.96
CaO	3.1	.75	1.6	2.1	.81	1.7	2.7	.66	.67	.30	.45	.81
Na_2O	3.2	2.2	3.3	2.7	2.6	3.3	3.3	2.2	1.5	2.5	1.4	1.6
K_2O	3.8	4.9	4.4	4.1	4.9	4.3	3.9	5.7	6.0	5.4	7.3	5.4
H_2O+	.83	1.3	1.8	1.6	1.5	1.4	1.6	1.2	1.3	1.9	1.9	1.3
H_2O-	....	.04	.03	.16	.07	.03	.12	.03	.10	.07	.09	.03
TiO_2	.47	.27	.28	.23	.30	.28	.38	.24	.34	.28	.31	.22
P_2O_5	.26	.12	.12	.18	.13	.13	.14	.10	.11	.12	.12	.12
MnO	.06	.04	.02	.02	.02	.03	.08	.01	.03	.00	.01	.04
CO_2	<.05	.08	.04	<.05	.04	.06	.08	.08	.02	.08	.08	.21
Total	100	100	100	100	100	100	100	100	99	99	100	100

[1] Albee and Boudette (1972, p. 24); no analyst cited.

[2] Single-solution method described by Shapiro (1967); analyst, Sam Botts.

[3] Method described by Shapiro and Brannock (1962), supplemented by atomic absorption; analysts, Paul Elmore, G. Chloe, J. L. Glenn, James Kelsey, H. Smith.

[4] Single-solution method described by Shapiro (1967); analyst, Lowell Artis.

(1972, p. 32–33 and 87) to regional metamorphism. Boone, Boudette, and Moench (1970, p. 19) assigned an Early Ordovician age. The Attean Quartz Monzonite is overlain uncomformably by conglomerate of Late Silurian age on eastern Sally Mountain (Albee and Boudette, 1972, p. 42) in the adjacent Attean quadangle. The quartz monzonite of Catheart Mountain is probably intrusive into the Attean Quartz Monzonite, but the intrusive relations need confirmation.

Coarse white mica associated with hydrothermal alteration and ore yielded ages of 433 and 457 m.y., or Late Ordovician to Early Silurian age (Boone, Boudette, and Moench, 1970, p. 19).

All rocks on Catheart Mountain have been modified by chlorite-grade regional metamorphism, presumably later than the hydrothermal alteration and mineralization.

ECONOMIC GEOLOGY

Disseminated molybdenum and copper sulfides and associated potassic and phyllic alteration are present in rocks on western Catheart Mountain. Spatial relationship established by a study of drill cores strongly suggests that the hydrothermal alteration and ores are related to intrusion of certain of the porphyry bodies, but the small size and very irregular shape of these intrusive bodies make a positive correlation difficult. Ores and alteration types are present in irregular zones within and adjacent to several small porphyry bodies in a relatively large area, rather than being concentrated around one center of intensity. Zones of alteration minerals a few centimeters or meters in width can be recognized, but larger zonal successions and the relationship of zones to ore grades can be only roughly generalized in drill cores.

The sulfide minerals present are pyrite, chalcopyrite, and molybdenite, in decreasing order of abundance. All three minerals occur in fine siliceous veinlets and as disseminated grains, and much of the rock examined contains both. Molybdenite commonly occurs as gray streaks and smoky stains in the veinlets. In some small quartz veins the molybdenite is in rosettes 1 to 2 cm across, and locally the pyrite and chalcopyrite in veins are in masses several centimeters across, but these coarse sulfides probably do not have much total economic significance. The least amount of total sulfide, less than 1 percent, and the least molybdenum, about 0.01 percent, are associated with rock in which almost all the sulfide is in fractures. Where most sulfide is in disseminated grains, the total sulfide is about 3 percent and the molybdenum about 0.04 percent. Copper tends to be equally distributed in the two ore types but is perhaps a little more abundant in the disseminated ore.

The rock alteration of quartz monzonite and porphyry in the drill cores was classified into 16 categories which were later grouped into 5 major alteration types—propylitic, outer phyllic, phyllic, quartzose potassic, and potassic—and 2

relatively minor alteration types—argillic(?) and propylitic-potassic. The general characteristics of the alteration types are given in table 2. Generally each alteration type is gradational into other types, and the distinctions made in logging mixed rocks are arbitrary. Pink and orange-brown coloration was used to estimate the amount of potassium feldspar, although some potassium feldspar is gray. Categorization of alteration type seemed generally easier in quartz monzonite than in feldspar-quartz porphyry. The amount and types of sulfides were logged as separate characteristics and were not used in the classification of the alteration types. Argillic alteration is shown with a query because, although it contains much clay, it has no biotite and little potassium feldspar and is therefore not like the argillic zone described by Lowell and Guilbert (1970, p. 383).

Veinlets in propylitically altered quartz monzonite tend to be surrounded by narrow alteration zones. In those where I could recognize zonation, the central zone enclosing the vein and the main sulfide mineralization is quartz-sericite, surrounded by a narrow zone in which the total potassium feldspar has probably been increased. The inner edge of the potassium feldspar is a sharp boundary against the quartz-sericite; outward the potassium feldspar decreases gradually to the normal amount in the country rock. Thus, the relative positions of phyllic and potassic zones seem reversed in the observed small zones surrounding veinlets in comparison to the Lowell-Guilbert model (Lowell and Guilbert, 1970).

CORRELATION OF ORE AND ALTERATION TYPES

Alteration types, as judged during visual examination of drill cores, were machine correlated with crude, visual total-sulfide estimates, with chemical analyses for copper and molybdenum, as well as with the ratios of copper to molybdenum. The results of these correlations, summarized under seven alteration types and type-groups, are shown in table 3. The arrangement of the groups is arbitrary and based on the Cu:Mo ratio and the total amount of mineralization because no particular order was determined on the basis of the core-log data alone. This results in a synthetic zonation that is only indirectly related to field observations (fig. 2) but is not unlike the zonal arrangement in the well-known Lowell-Guilbert model (Lowell and Guilbert, 1970) where the

Table 2.—*Characteristics of the alteration type*

Alteration type	Macroscopic characteristics used in logging	Essential minerals	Distinctions from similar types, and comments
Propylitic	Rock texture unmodified. Most feldspar pale green to bright waxy green; some pink feldspar commonly present. No primary biotite remaining but positions marked by dark spots. No new quartz.	Quartz, plagioclase, potassium feldspar, chlorite, epidote, and ± calcite.	Distinguished by gray-green background. Abundant new muscovite and potassium feldspar are lacking. Chlorite, epidote need not both be present. Also includes rock logged in field as metamorphosed.
Argillic(?)	Rock texture generally unmodified. Feldspar dull to soft and chalky; light gray to tan.	Not determined	Distinguished by chalky appearance. Commonly soft, crumbly. Zonal position significance not clear. A minor type represented by only a little core.
Outer phyllic	Rock texture generally unmodified; quartz about the same as original rock. Generally gray, minor new pink or orange feldspar.	Quartz, muscovite, ± potassium feldspar, and ± plagioclase.	Distinguished by gray color, unmodified quartz content, and texture. New potassium feldspar is lacking.
Phyllic	Rock texture little to much modified; quartz visibly more abundant than in original rock. Mostly gray.	Quartz, muscovite, ± potassium feldspar, and ± plagioclase.	Distinguished by gray color, high quartz content, and lack of new potassium feldspar. All feldspar may have been replaced by quartz and muscovite.
Propylitic-potassic	Both green coloration and new potassium feldspar present. Dark spots mark former biotite.	Probably same as propylitic plus some new quartz and potassium feldspar.	Original rock commonly not identified. A minor poorly defined type that I would try to reclassify into other categories in future logging.
Quartzose potassic	Rock texture commonly modified; mostly gray and pink or orange brown.	Potassium feldspar, muscovite, quartz, and ± plagioclase.	Distinguished by abundance of new muscovite and potassium feldspar as well as quartz. Original rock commonly obscured. New potassium feldspar commonly anomalous orange brown or salmon.
Potassic	Rock texture commonly modified, mostly gray and pink or orange brown. Relatively low quartz content.	Potassium feldspar, muscovite, quartz and ± plagioclase.	Similar to quartzose potassic but quartz is less conspicuous.

characterizing alteration minerals from the exterior inward are as follows:

Propylitic zone: Chlorite, epidote, carbonate.
Argillic zone: Quartz, kaolin, chlorite.
Phyllic zone: Quartz, sericite, pyrite.
Potassic zone: Quartz, potassium feldspar, biotite, with or without sericite and anhydrite.

Table 3.—*Copper, molybdenum, and iron sulfide relationships in principal types of altered rock*

Type	Total core represented (m)	(ft)	Cu (percent)	Mo (percent)	Cu:Mo	Pyrite-chalco-pyrite	Total sulfide (percent)
Propylitic	259	850	0.108	0.016	6.8	8.0	1.0
Argillic(?)	47	155	.225	.030	7.5	3.5	1.8
Outer phyllic.	195	640	.182	.018	10.1	6.2	2.3
Phyllic . . .	265	874	.234	.037	6.3	6.5	2.2
Propylitic potassic.	83	272	.147	.026	5.6	6.5	1.4
Quartzose potassic.	480	1,587	.243	.045	5.4	4.9	2.2
Potassic . .	620	2,054	.229	.048	4.8	5.0	2.1

More work on field distribution of alteration types should be done before judging how well the alteration zones on Catheart Mountain fit the Lowell-Guilbert model. Because of the interaction of alteration from many intrusive porphyry bodies, the internal complexity may be such that zone distinctions are impossible to map, at least in the southwestern part of the deposit.

Figure 2 shows the relationship of sulfide mineralization to five types of rock alteration observed in the drill core. (The argillic(?) and propylitic-potassic groups are omitted because their relative positions are not clear and the total core length they represent is relatively small.) The figure shows that the amount and type of sulfide and the amount and ratio of copper and molybdenum in the core are related to the type of rock alteration. The highest combined copper and molybdenum contents are found in rocks with potassic alteration. Table 3 indicates that the logged cores lack a distinct pyritic zone. Surface samples taken in the same area as the studied cores (southwest area, fig. 1) contained, at the most, 5.9 percent K_2O, but bedrock exposures are sparse or lacking over what may be the most potassic part of the southwest area, and no analyses for potassium have been made on the core.

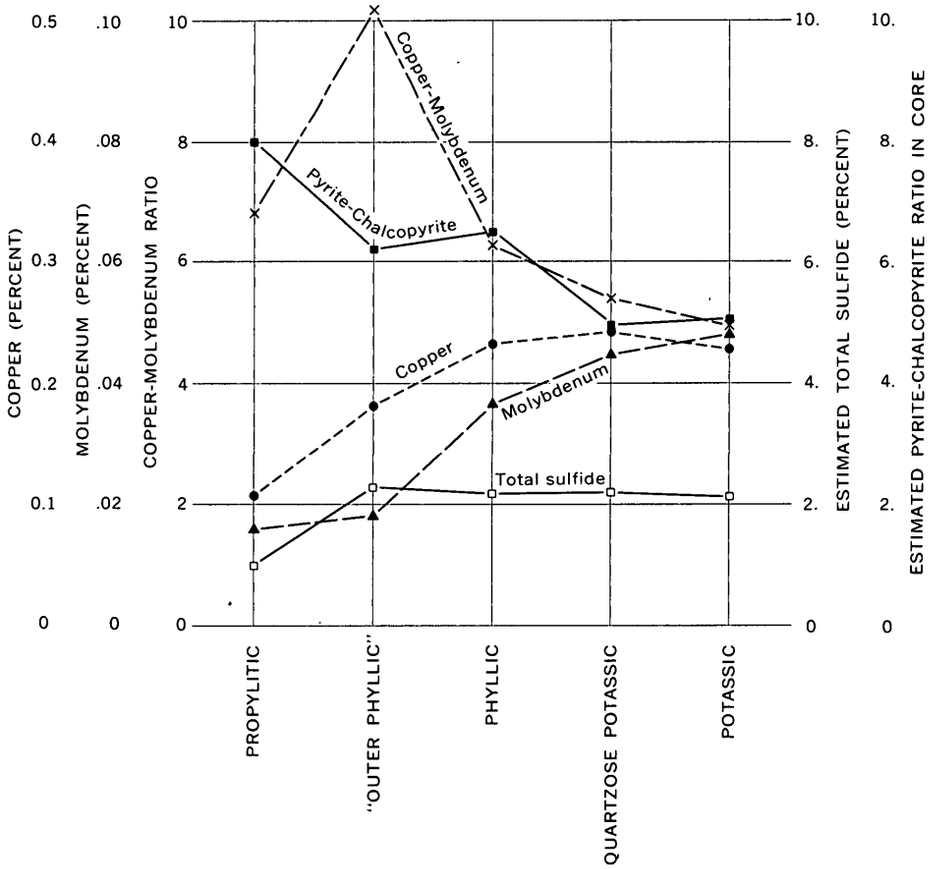

Figure 2.—Copper, molybdenum, and iron sulfide relationships in five selected types of rock alteration, Catheart Mountain drill cores. The relative placement of the alteration types from propylitic to potassic is based on Cu:Mo ratio and total Cu+Mo; this synthesized zonation is similar to zonal arrangements in other deposits (Lowell and Guilbert, 1970).

ECONOMIC POTENTIAL OF THE NORTHEAST PROSPECT AREA

Although no pyrite-rich zone was identified in the southwest area, a large and well-developed sulfide zone is present in the northeast prospect area (fig. 1). The northeast area also has a strong center of potassic enrichment and perhaps more phyllic alteration than the southwest area; however, the bulk surface samples tested only a relatively small part of the southwest area.

Most of the northeast area is pyrite rich; the average of 18 field estimates of pyrite content is 4.4 percent. Highest sulfide contents are on the southeast side of the northeast area, where the gradient to "background" of perhaps 0.1–0.5 percent is much steeper than on the northwest side. Highest estimates were 8 and 10 percent total sulfide.

Within the pyritic area there are also potassic enriched surface rocks where six bulk samples contained at least 7.0 percent K_2O and one sample contained 10.0 percent K_2O. This potassium oxide enriched area correlates fairly well with an anomalously potassic area detected by a U.S. Geological Survey airborne gamma radiation survey.

The northeast area also has the most phyllic (quartz-sericite-potassium feldspar) alteration, both in area and in intensity, and seems to have extensive depletion of Na_2O and CaO.

The potassic enrichment, pyrite-rich zone, and alteration pattern are all considered favorable features in exploration for porphyry-copper deposits in other regions.

CONCLUSIONS

The detailed study of a small selected part of the diamond drill cores combined with a general study of rock exposures on Catheart Mountain show that at this deposit there is a definite correlation of ore with certain types of alteration. The northeast area on the mountain has favorable types of alteration and strong potassic enrichment, both shown to be associated with ore in the southwest area, and also a distinct zone of pyrite enrichment, thought to be a common associate of copper-porphyry mineralization at other deposits. Although several holes have already been drilled in the northeast area, further evaluation appears to be warranted.

REFERENCES CITED

Albee, A. L., and Boudette, E. L., 1972, Geology of the Attean quadrangle, Somerset County, Maine: U.S. Geol. Survey Bull. 1297, 110 p.

Boone, G. M., Boudette, E. L., and Moench, R. H., 1970, Bedrock geology of the Rangeley Lakes-Dead River basin region, western Maine, *in* Boone, G. M., ed., New England Intercollegiate Geological Conference, 62nd Ann. Mtg., Rangeley, Me., Oct. 2–4, 1970, Guidebook for fieldtrips in the Rangeley Lakes-Dead River basin region, western Maine; Syracuse, New York, p. 1–24.

Boucot, A. J., 1961, Stratigraphy of the Moose River synclinorium, Maine: U.S. Geol. Survey Bull. 1111-E, p. 153–188.

Lowell, J. D., and Guilbert, J. M., 1970, Lateral and vertical alteration-mineralization zoning in porphyry ore deposits: Econ. Geology, v. 65, no. 4, p. 373–408.

Shapiro, Leonard, 1967, Rapid analysis of rocks and minerals by a single-solution method, *in* Geological Survey research 1967: U.S. Geol. Survey Prof. Paper 575-B, p. B187–B191.

Shapiro, Leonard, and Brannock, W. W., 1962, Rapid analysis of silicate, carbonate, and phosphate rocks: U.S. Geol. Survey Bull. 1144-A, 56 p.

Jour. Research U.S. Geol. Survey
Vol. 2, No. 2, Mar.-Apr. 1974, p. 195—211

DISTRIBUTION OF COPPER IN BIOTITE AND BIOTITE ALTERATION PRODUCTS IN INTRUSIVE ROCKS NEAR TWO ARIZONA PORPHYRY COPPER DEPOSITS

By NORMAN G. BANKS, Menlo Park, Calif.

Abstract.—Biotite and its alteration products (primarily chlorite) from igneous rocks around the Ray and Esperanza (Esperanza-Sierrita) porphyry copper deposits, Arizona, were analyzed for copper by electron microprobe. The copper occurs in amounts >90 p/m (limit of detection) in most of the chlorites analyzed, is concentrated at the optical and chemical boundary of chlorite and biotite, and is not associated with sulfur. Most unaltered igneous and hydrothermal biotites analyzed contain <90 p/m Cu, and except for one sample, all copper that was detected can be explained as contamination by copper from chlorite grains. The paucity of detectable copper in igneous and hydrothermal biotite and its presence in daughter chlorite suggest that the positive association noted by some workers between the proximity of an ore deposit and the copper content of biotite might be partly the result of increased amounts of chloritization of biotite near a deposit coupled with difficulty in physically cleaning the biotite separates. Additionally, previous speculations that (1) part of the copper in a deposit may come from altered biotite, and (2) copper in biotite indicates how copper behaves in a differentiating magma, are of doubtful value if based on data derived from analyses of bulk mineral separates.

The copper, sulfur, and major-element contents of biotite and its alteration products from igneous rocks associated with the Ray and Esperanza (Esperanza-Sierrita) porphyry copper deposits were determined by microprobe analyses. The results do not agree with some of the published data about the distribution of copper in biotite nor with some of the speculations drawn from that data.

The Ray samples, collected 2–11 km from the deposit, consist of 2 ore specimens and 21 igneous rocks representing 5 intrusive types. All five intrusive types are cut by sulfide-bearing veinlets in and around the Ray deposit. The deposit is located about 120 km north of Tucson, Ariz. The intrusive rocks temporally associated with the deposit range in composition and texture from hornblende diorite (andesite) to quartz monzonite (quartz latite) (Cornwall and others, 1971; Banks and others, 1972). Intrusion began about 70 m.y. ago and continued to about 60–61 m.y. ago—the Laramide age of the youngest intrusive body (Granite Mountain Porphyry) within the commercial limits of the deposit (Creasey and Kistler, 1962; Banks and others, 1972; Banks and Stuckless, 1973). Sulfide mineralization followed, and the deposit cooled below 100°C about 60 m.y. ago (Banks and Stuckless, 1973).

The Esperanza deposit, about 40 km south of Tucson, is associated with the Ruby Star Granodiorite, also Laramide in age (Creasey and Kistler, 1962; Damon and Mauger, 1966). T. G. Lovering kindly supplied igneous biotite, separated from seven samples collected from this intrusive body, 0.8–4 km from the center of mining activity at Esperanza.

ANALYTICAL METHODS

Extreme care was taken to eliminate contamination of copper by external sources. Rock chips (Ray samples) and mineral grains (Esperanza samples), plastic mounted onto glass slides and cut to 40- to 50-μm thickness by diamond saw, were ground and polished on glass plates in several steps, using diamond powder as an abrasive to remove any copper smeared onto the specimens from brass in the saw blade. Between each step, the slides were agitated in an ultrasonic cleaner, then positioned so that the direction of polishing was 90° from the previous direction. Finally, the slides were polished four more times on nylon over glass with alumina powder, agitated in an ultrasonic cleaner, and again rotated 90° between each polishing step.

Several mounts were polished on a lead-bronze lap with diamond powder, analyzed, repolished by use of the four-step alumina method, and finally reanalyzed to check if any copper physically smeared onto the sample was actually removed by the polishing with alumina. Copper in erratic but measurable concentrations (parts per million) was detected on some biotite grains in the slides polished on the lead-bronze lap (not on well-polished nonlayer silicates) but was not detected on the same grains after the alumina polishing. Thus, sample contamination by copper sources external to the sample is believed to have been eliminated by this polishing.

Contamination of minerals by copper from other minerals in the slide could not be eliminated. However, the sources of contamination are identified, and as explained later, the contamination does not alter the conclusions drawn here.

The copper and sulfur analyses were made with an ARL (Applied Research Lab.) model EMX-SM electron microprobe

using a LiF crystal for copper and an ADP crystal for sulfur, an excitation voltage of 20 kV, a sample current of 3×10^{-8} A on brass, and chalcocite (Cu_2S) as a standard. Integration times of 200±2 s were obtained by termination of counting on fixed-beam current. For most analyses the electron beam was fully focused. Buildup of carbon contamination and noticeable loss of volatile components were avoided by moving the beam with magnetic deflectors to sweep areas as much as 10 by 8 μm. If the shape of the grain did not permit sweeping of areas of at least 5 by 4 μm, a defocused beam (2–3 μm diam) was used, and the sample was moved under the beam about once every 20 s.

X-ray intensity data (counts) were obtained by averaging 2–40 (usually 6–8) observations on each grain. Initially, correction of the raw intensity data was done by computer and included drift, background, and matrix corrections (mass absorption, secondary fluorescence, and atomic number effects; Beeson, 1967; Beaman and Isasi, 1970). Individual backgrounds for each grain were determined by observing counts above and below the peak wavelengths of copper and sulfur. Major-element data required for the corrections and data in table 3 and figures 6 and 7 were obtained at an excitation voltage of 15 kV and count times of 20±0.5 and 40±1 s. It developed, however, that the computer correction factor for trace amounts of copper and sulfur (50–5,000 p/m) is nearly constant for each mineral type studied regardless of its exact major-element composition. Thus, in the later part of the study and for most of the data on tables 1 and 2, a matrix correction for copper and sulfur in each mineral type (derived in the initial study) was applied by hand. During this stage of the study, usually magnesium or potassium was monitored as a check on the purity of the mineral grains.

A homogeneous synthetic glass containing about 400 p/m Cu and 520 p/m S was repeatedly analyzed under the above operating conditions. The one standard deviation of error from the average amount of copper present in the glass was 10 percent (8 percent for S), and the maximum deviation was 20 percent (15 percent for S). Detection levels were established at three times the square root of the average background counts (Birks, 1963); thus, copper is considered detectable at about 90 p/m (50 p/m for S) at the above operating conditions in the minerals analyzed.

COPPER AND SULFUR CONTENTS OF THE MINERALS

The copper and sulfur contents of hydrothermal biotite from the Ray deposit and of igneous biotite and its alteration products (chlorite, epidote, sphene, and hydrogarnet?) from five intrusive rock types located near the deposit are listed in table 1. Similar data for igneous biotite and its alteration products from the Ruby Star Granodiorite near the Esperanza deposit are presented in table 2.

Chlorite formed by alteration of biotite near both the Ray and Esperanza deposits contains significantly more copper than the unaltered igneous biotite analyzed (fig. 1). Most of the biotite grains (80 percent of the Ray and 75 percent of the Esperanza biotite), including those of hydrothermal origin, do not contain detectable amounts of copper, whereas 65 percent of the Ray chlorite grains analyzed and 90 percent of the Esperanza chlorite grains analyzed contain detectable amounts of copper.

LOCATION OF COPPER IN CHLORITE

Sulfur and copper in the biotite and chlorite were monitored during the analyses on a memory oscilloscope or on Polaroid film over a nonrecording oscilloscope to determine whether sulfide or sulfate inclusions might account for the copper in the chlorite or biotite. With one possible exception (a chlorite grain in sample 2GM14, not listed in table 1), no such inclusions were found. Furthermore, it is unlikely that the copper is present in sulfide or sulfate grains that are smaller than can be detected on the oscilloscope because increases in the amount of copper in either biotite or chlorite are not accompanied by corresponding increases in the amount of sulfur (fig. 2). For example, the ratio of copper to sulfur should be 1 to 1 if the copper were present in chalcopyrite inclusions and 4 to 1 if the supposed inclusions were chalcocite; these ratios are not found (fig. 2). In addition, several quantitative analyses for Mo, Zn, Pb, Mn, Cl, and F (by microprobe) indicate that the copper in the grains also is not associated with these elements. The presence of copper carbonates or nitrates was not checked directly because the sections were carbon coated, and an analyzing crystal suitable for nitrogen analyses was not immediately available. A direct check for the presence of copper silicates and an indirect check for the presence of copper carbonates, oxides, and nitrates by analyzing the grains for silicon and oxygen was not possible because the copper occurs in a silicon-oxygen matrix (biotite and chlorite) having approximately the same silicon or oxygen contents as the known copper carbonates, oxides, nitrates, and silicates. Thus, any variations in silicon or oxygen intensity data caused by the presence of minute quantities (parts per million range) of these minerals would be masked by analytical uncertainty in such data. Quantitative analyses for Se, W, As, Sb, Te, I, V, and P (the other elements occurring in known copper-bearing minerals) were not made, but qualitative scans were. As noted in the tables, the copper in chlorite is often distributed inhomogeneously and, as discussed below, is locally concentrated in sufficient quantities so that X-ray images of its distribution can be observed on and photographed from an oscilloscope. Similarly, if Se, W, As, Sb, Te, I, V, or P were present in amounts comparable to the copper, they could be observed on the X-ray images; they were not.

Table 1.—*Copper and sulfur in biotite and its alteration products from the intrusives near the Ray porphyry copper deposit, Arizona*

[Values in regular type denote element is present at or above detection level (about 90 p/m for Cu and 50 p/m for S). Values in italic type indicate real or fictitious element contents resulting from higher-than-background counts at the peak wavelength of the element. Copper and sulfur values are not significant to three figures. Precision is lower in grains in which copper and sulfur are not homogeneously distributed]

Rock type	Sample	Grain	Mineral	Copper (p/m ±10 percent)	Sulfur (p/m ±10 percent)
Tortilla Quartz Diorite.	217-1	1BI	Biotite	*0*	
		2BI	.. do ..	*0*	
		3BI	.. do ..	*0*	138
		5BI	.. do ..	*0*	161
		2CL	Chlorite	*0*	
		4CL	.. do ..	*42*	*20*
		5CL	.. do ..	*16*	*0*
		6CL	.. do ..	*0*	*0*
		7CL	.. do ..	*24*	*23*
		6EP	Epidote	*42*	52
		7EP	.. do ..	*0*	*0*
	217-28	1BI	Biotite	386*	167
		3BI	.. do ..	*39*	199
		4BI	.. do ..	*52*	
		5BI	.. do ..	109	
		BTM1	.. do ..	*21*	199
		1CL	Chlorite	206*	59
		2CL	.. do ..	244*	
		4CL	.. do ..	149	86*
		5CL	.. do ..	120	*45*
		4M	Hydrogarnet?	151*	79
		3EP	Epidote	*40*	*28*
	248-29	2CL	Chlorite	*60*	
		3CL	.. do ..	190	
Rattler Grano-diorite.	246-99B ..	3BI	Biotite	697	172
		1CL	Chlorite	569	74
		2CL	.. do ..	432	50
	46-11G ..	BI	Biotite	*0*	
		CL	Chlorite	2237	
		EP	Epidote	2000*	
	246-11G ...	1BI	Biotite	*26*	
		3BI	.. do ..	*28*	199
		4BI	.. do ..	*0*	181
		7BI	.. do ..	110	146
		BTM1	.. do ..	*0*	197
		1CL	Chlorite	626	
		5CL	.. do ..	*51*	*1*
		6CL	.. do ..	105	*0*
		CLM1	.. do ..	*0*	*10*
		CLM2	.. do ..	*0*	*6*
		2EP	Epidote	*10*	*41*
		6SP	Sphene	*53*	82*
	61-25	BIGM	Biotite	*0*	
		BI1	.. do ..	*0*	
		BI2	.. do ..	*0*	
		CL2	Chlorite	291	
		EP2	Epidote	157	
	261-25	1BIA	Biotite	*0*	209
		1BIB	.. do ..	*0*	283
		3BI	.. do ..	*0*	184
		5BI	.. do ..	*0*	156
		2CLA	Chlorite	*0*	*0*
		2CLB	.. do ..	*0*	*0*
		4CL	.. do ..	*0*	*5*
		5CL	.. do ..	*0*	*0*
		1EP	Epidote	*0*	*0*
		4EP	.. do ..	*0*	*0*
Rattler Grano-diorite—Con.	260-113D ..	2BI	Biotite	*0*	189
		3BI	.. do ..	*0*	256
		4BI	.. do ..	*0*	190
		5BI	.. do ..	*0*	254
		3CL	Chlorite	*0*	*0*
		4CL	.. do ..	*0*	*0*
		3M	Hydrogarnet?	*0*	*0*
		1EP	Epidote	*0*	*0*
		5EP	.. do ..	*0*	*15*
	246-11A ...	1BI	Biotite	256*	
		1BIA	.. do ..	245	
		2BI	.. do ..	*0*	A313
		4BI	.. do ..	405*	
		5BI	.. do ..	*57*	294
		5BIA	.. do ..	119*	
		BIM1	.. do ..	496*	280
		BIM2	.. do ..	*0*	282
		1CL	Chlorite	2218*	*21*
		1CLA	.. do ..	1368	
		3CL	.. do ..	460	*14*
		3CLA	.. do ..	2000*	*10*
		4CL	.. do ..	405	
		4CLA	.. do ..	3138*	
		4CLB	.. do ..	617	
		5CLA	.. do ..	2397*	
		5CLB	.. do ..	4118*	
		5CLC	.. do ..	8340*	
		CLM1	.. do ..	1432*	*20*
		CLM2	.. do ..	9842*	*0*
	260-96A ...	1BI	Biotite	*52*	214
		3BI	.. do ..	*0*	191
		4BI	.. do ..	*0*	220
		5BI	.. do ..	*0*	185
		2CL	Chlorite	754*	254
		2CLA	.. do ..	416	262*
		3CL	.. do ..	1160*	54
		6CL	.. do ..	674*	112*
		1EP	Epidote	608*	*22*
		6SP	Sphene	*94*	*0*
Rhyodacite dike	2GM100...	1BI	Biotite	*51*	290
		2BI	.. do ..	*36*	243
		3BI	.. do ..	*15*	274
		2CL	Chlorite	*0*	*44*
		4CL	.. do ..	102	105
		5CL	.. do ..	*66*	117
		4EP	Epidote	*0*	*0*
		5EP	.. do ..	130*	*0*
		4SP	Sphene	*0*	*0*
		5SP	.. do ..	*0*	*0*
Granite Mountain Porphyry.	GM14.....	BI	Biotite	*0*	
		CL1	Chlorite	*0*	

Table 1.—*Copper and sulfur in biotite and its alteration products from the intrusives near the Ray porphyry copper deposit, Arizona*—Continued

Rock type	Sample	Grain	Mineral	Copper (p/m±10 percent)	Sulfur (p/m±10 percent)
Granite Mountain Porphyry—Con.	GM14	CL2	..do..	582	
		CL3	..do..	*34*	
		EP	Epidote	*0*	
		SP6	Sphene	*0*	
	2GM14....	1BI	Biotite	*20*	311
		2BI	..do..	*0*	
		2BIA	..do..	*0*	202
		3BI	..do..	198	273
		4BI	..do..	*0*	237
		6BI	..do..	*0*	
		BTM1	..do..	*0*	158
		2CL	Chlorite	110	*0*
		5CL	..do..	*42*	*11*
		6CL	..do..	*5*	68
		CLM1	..do..	*79*	75
	GM12R....	2BIX	Biotite	*0*	208
		3BI	..do..	111	237
		3BIA	..do..	144	180
		4BI	..do..	110	156
		5BI	..do..	125	152
		3CL	Chlorite	699	*26*
		3CLA	..do..	294	*26*
		4CL	..do..	297	*44*
		5CL	..do..	527	98
	GM6GR ...	BI1	Biotite	*0*	
		BIA	..do..	*0*	
		3BIA	..do..	*0*	120
		4BIA	..do..	*0*	190
		3CLA	Chlorite	3440*	*0*
		4CLA	..do..	*80*	*0*
		CLA	..do..	266	
	2GM6GR ..	2BIM	Biotite	*0*	190
		3BIM	..do..	*0*	
Granite Mountain Porphyry—Con.	2GM6GR..	4BIM	..do..	*0*	
		3CLM1	Chlorite	261	
		3CLM 2	..do..	442	
		4CLM	..do..	125	
	3GM6G....	BI1	Biotite	*0*	
		BI2	..do..	*0*	
		BI3	..do..	*0*	
		CL1	Chlorite	385	
		CL2	..do..	382	
		CL3	..do..	414	
	2GM4V....	BIB	Biotite	110	
		1BIA	..do..	*0*	
		3BIA	..do..	*0*	
		3BIB	..do..	*0*	
		1CL	Chlorite	915*	
		1CLA	..do..	818*	
		3CL	..do..	105	
	2GM1A....	2CL	..do..	324	
		2CLA	..do..	275	
		2CLB	..do..	311	
		CLM	..do..	1537*	
Teapot Mountain Porphyry.	TTM.....	ICL	Chlorite	1235*	
		3CL	..do..	1172*	
		CLM1	..do..	1006*	
		1SP	Sphene	145	
		3SP	..do..	124	
Hydrothermal biotite.	2P70-22 ...	1BI	Biotite	*80*	90
		2BI	..do..	*46*	486
	T123R	BI1	Biotite	*26*	189
		BI2	..do..	*37*	113
		BI3	..do..	*64*	156
		BI4	..do..	*30*	197
		BI5	..do..	*33*	191

*Element not distributed homogeneously in the grain. Criterion used was whether standard deviation from mean of counts divided by the square root of the average counts is >3 (Boyd, 1969).

The copper reported for chlorite in tables 1 and 2 was probably not smeared over the chlorite from other copper-bearing phases in the mounts because (1) the distribution of copper in the chlorite (discussed next) precludes such a source, (2) the copper content of the chlorite grains does not reflect the proximity, size, or even presence of copper sulfides in a given slide (always <200 p/m including chalcopyrite), and (3) except for sample 246-99B (table 1), copper was not found in other igneous silicate, oxide, or phosphate phases in the samples in amounts equal to or greater than that found in chlorite. Contamination of the chlorite with copper from chalcopyrite in veinlets was avoided by using probe mounts that contain no veinlets.

The amount of copper in chlorite is highest near the chlorite-biotite contact. Chlorite more than 50 μm from the mineral contact contains about 600–1,000 p/m Cu, biotite more than 50 μm from the contact contains copper in amounts just at or below the detection level, and about 1.5 percent Cu is found in the chlorite at the mineral contact (fig. 3A, sample 2GM4V, grain 1 CL). The amount of copper (about 1.5 percent) at the mineral contact is probably low because the material excited by the beam and secondary radiation extends beyond the visible mineral contact. Likewise, the broadness of the copper peak (fig. 3A) may be partly the result of excitation of copper in the contact zone by secondary radiation from points located in chlorite and biotite near the mineral contact.

The concentration of copper in chlorite along another biotite-chlorite boundary is shown as X-ray images photographed from an oscilloscope (fig. 4). The chlorite contains about

Table 2.—*Copper and sulfur in biotite and its alteration products from Ruby Star Granodiorite near the Esperanza porphyry copper deposit, Arizona*

[Values in regular type denote element is present at or above detection level (about 90 p/m for Cu and 50 p/m for S). Values in italic type indicate real or fictitious element contents resulting from higher-than-background counts at the peak wavelength of the element. Copper and sulfur values are not significant to three figures. Precision is lower in grains in which copper and sulfur are not homogeneously distributed]

Sample	Grain	Mineral	Copper (p/m, ±10 percent)	Sulfur (p/m, ±8 percent)	Chlorite in separate (percent)
T454R....	BT5	Biotite	*63*	106	*0.1*
	BTM1	..do..	*0*	180	
	BT5A	..do..	*0*	139	
	BT5C	..do..	*0*	138	
	BT5C1	..do..	*0*	125	
	CL5	Chlorite	*0*	*17*	
T455R....	BT1	Biotite	*21*	141	*3.5*
	BT2	..do..	*45*	126	
	BT3	..do..	*73*	126	
	BT4	..do..	*6*	160	
	BT5	..do..	200*	87	
	CLM1	Chlorite	4758*	68	
	CLM2	..do..	161	*0*	
	CL1	..do..	2040*	*6*	
T465R....	BT1	Biotite	*0*	69	*0.7*
	BT2	..do..	145	119	
	BT3	..do..	*0*	156	
	BTM1	..do..	*0*	140	
	BTM2	..do..	*0*	102	
	BTM3	..do..	*0*	125	
	CL1	Chlorite	175	*20*	
	SP1	Sphene	255	56	
T467R....	BT1	Biotite	654*	172	*11.2*
	BT2	..do..	511*	140	
	BTM1	..do..	*28*	275	
	BTM2	..do..	173	263	
	BTM3	..do..	*43*	232	
T467R.....	BTM4	Biotite	152	243	
	BTM5	..do..	*0*	197	
	CL1	Chlorite	766*	*0*	
	CL2	..do..	3418*	*0*	
	CL3	..do..	3024*	*7*	
	CLM1	..do..	1335	*0*	
	CLM2	..do..	1060	*14*	
T468R....	BT1	Biotite	*49*	201	*12.4*
	BT2	..do..	*3*	345	
	BT3	..do..	*0*	239	
	BT4	..do..	*0*	221	
	CL1	Chlorite	924*	*0*	
	CL2	..do..	9700*	96	
	CL3	..do..	10,000*	*36*	
	CL4	..do..	4500*	*32*	
T8R.....	BT1	Biotite	*0*	141	*17.6*
	BT2	..do..	616*	97	
	BT3	..do..	*0*	167	
	BT4	..do..	*32*	125	
	BT5	..do..	129	109	
	CL1	Chlorite	403	*0*	
	CL2	..do..	323*	*16*	
	CL3	..do..	669*	*0*	
	CL4	..do..	1656*	*30*	
	CL5	..do..	429	*10*	
	SP1	Sphene	*57*	*23*	
	SP2	..do..	333	65	
	SP4	..do..	*0*	*49*	

*Element not distributed homogeneously in the grain. Criterion used was whether standard deviation from mean of counts divided by the square root of the average counts is >3 (Boyd, 1969).

5,000 p/m Cu at the mineral contact and about 500 p/m (average) away from it. Although sulfur counts were collected for longer times than the copper counts, corresponding sulfur counts (fig. 4*C*, *F*) are lacking where the copper is concentrated. Background sulfur in biotite (300 p/m) was not detected in figure 4*C* and *F*.

Figure 3*B* shows a paucity of copper in compositionally pure biotite, a high concentration of copper in chlorite at the compositional chlorite-biotite contact, and a decrease in amount of copper in chlorite as it becomes chemically purer (as demonstrated by loss of K). Thus, copper is both spatially and compositionally associated with the biotite-chlorite transition, which implies that the copper was introduced in the fluids that destroyed the biotite and formed the chlorite. The fact that other elements known to coexist in previously described copper minerals were not concentrated with the copper suggests that the copper probably is present in either lattice or more loosely attached sites in the chlorite or other silicate minerals formed during transition of the biotite to chlorite. In the compositionally purer chlorite, the copper may be partly in exchangeable sites and partly in lattice sites. Dodge, Smith, and Mays (1969) and Parry and Nackowski (1963) point out that the radius of Cu^{+2} is appropriate for its camouflage in Fe^{+2} and Mg^{+2} (octahedral) positions. In the transitional material, the amount of copper present and the fact that cold concentrated nitric acid leaches copper from the Esperanza biotite-chlorite grains exposed in a rock-slab surface (T. G. Lovering, oral commun., 1972) might suggest a cation exchange position for part of the copper. The nature of the attachment of copper in this transitional material is discussed more fully in a later section.

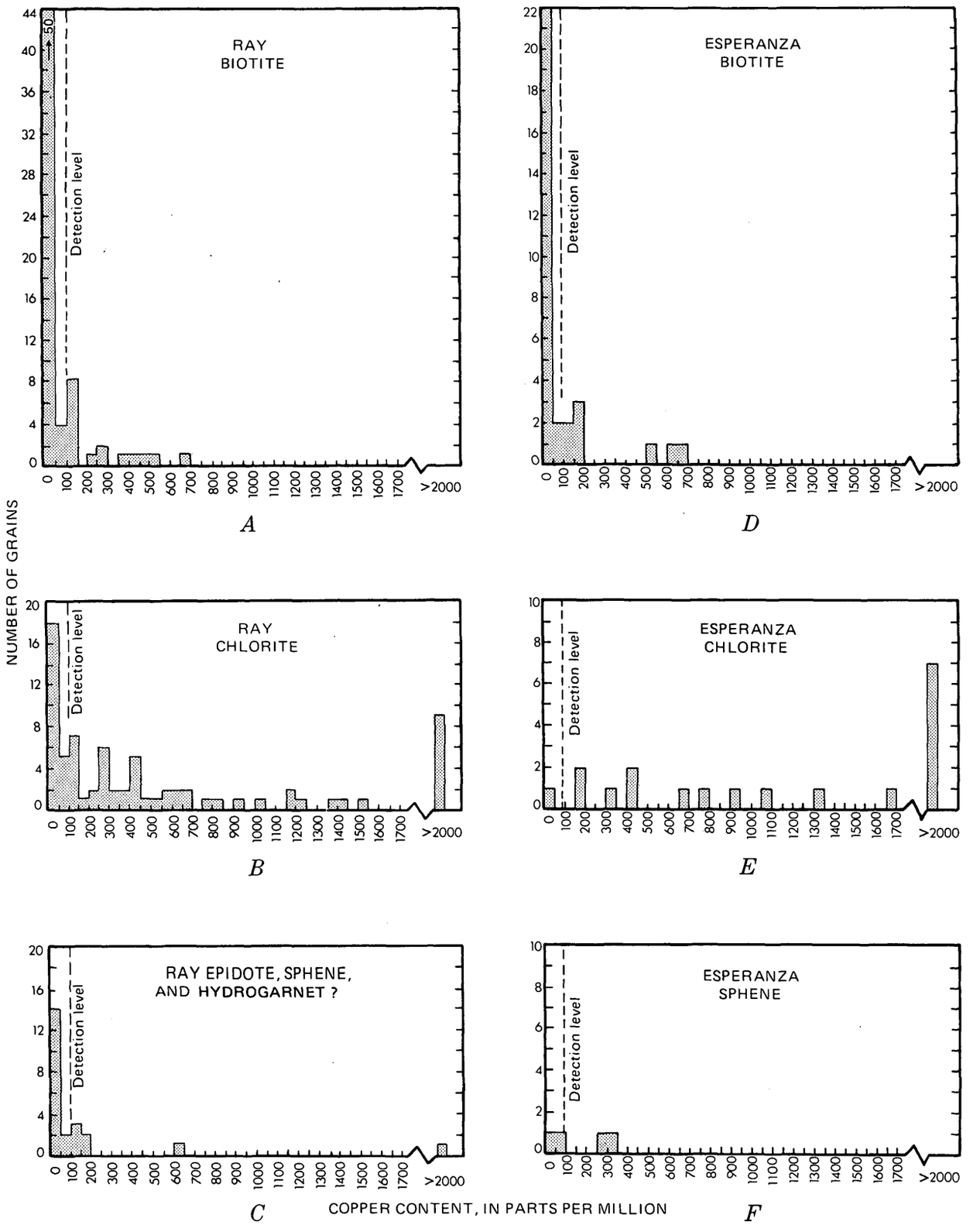

Figure 1.—Frequency histograms showing copper contents of biotite (*A* and *D*), chlorite (*B* and *E*), epidote, sphene, and hydrogarnet? (*C*), and Sphene (*F*) from Laramide intrusive rocks near the Ray and Esperanza copper deposits, Arizona. Detection levels established at three times the square root of the average background counts (Birks, 1963).

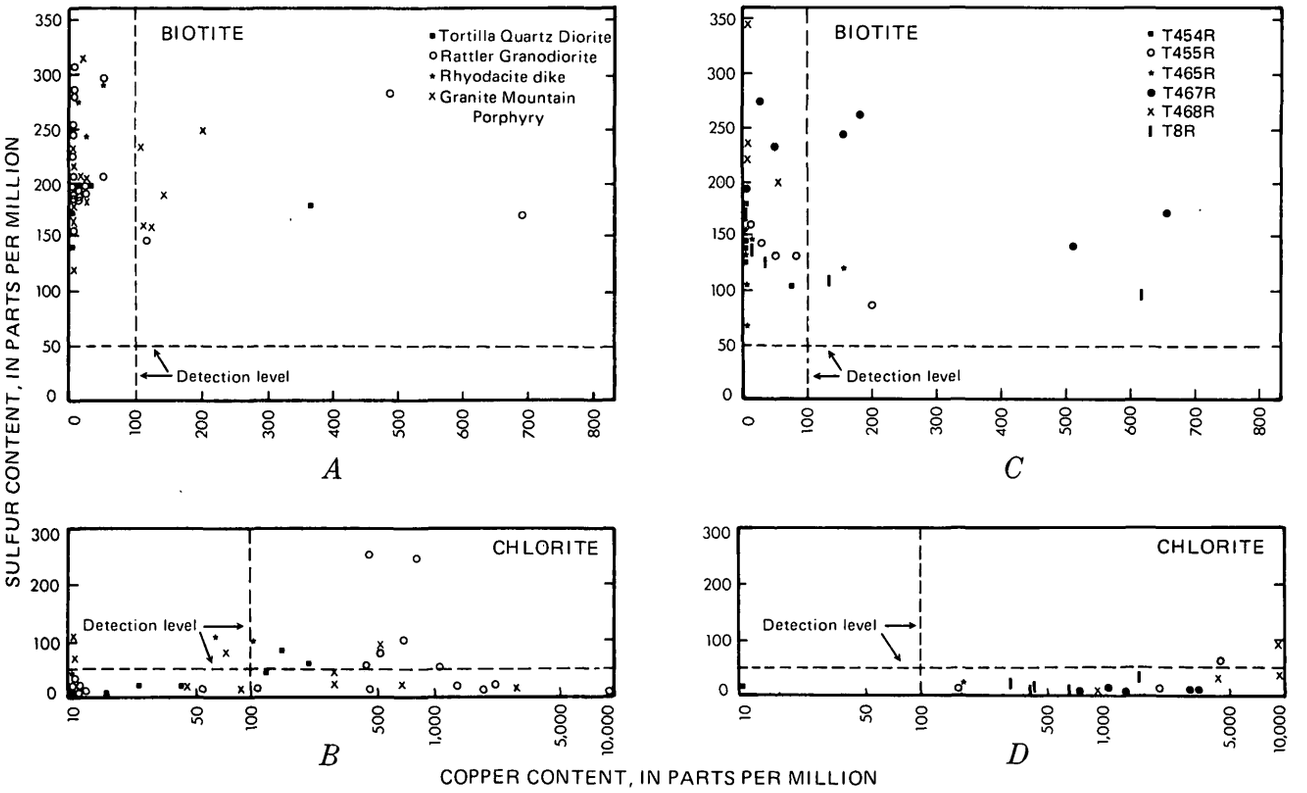

Figure 2.—Plots of copper versus sulfur contents of igneous biotite (*A* and *C*) and chlorite (*B* and *D*) derived from the biotite from rocks near the Ray and Esperanza copper deposits, Arizona. Note that different scales are used to plot copper in chlorite and copper in biotite. Three points from the Rattler Granodiorite and one from the Tortilla Quartz Diorite plot at the origin of *B*. Some points are slightly offset for plotting purposes. Detection levels were established at three times the square root of the average background counts (Birks, 1963).

CONTAMINATION ORIGIN FOR COPPER IN BIOTITE

The increase in copper content from parent biotite to daughter chlorite is probably even more striking than figure 1 shows because most biotite grains having detectable amounts of copper come from samples that contain chlorite having considerably more copper than the biotite. Thus part or all of the detectable copper reported for biotite may be copper from chlorite that has been smeared over the biotite during polishing. There is no simple relation between the degree of alteration of biotite in a sample and the presence or number of copper-bearing biotite grains analyzed in a sample. This is not surprising because the amount of copper smeared over the biotite would depend upon the proximity of copper-bearing chlorite, the amount of copper in the chlorite, and the position of a biotite grain relative to a copper-bearing chlorite and the final direction of polishing. However, the samples that have very little biotite alteration or that have no chlorite grains with detectable copper also have no biotite grains with detectable copper. In addition, biotite precipitated from copper-bearing fluids (hydrothermal biotite, table 1) does not contain detectable copper except immediately adjacent to chalcopyrite (these analyses were not reported in table 1 because of likelihood of copper contamination from the sulfide). Therefore, it is likely that the igneous biotite (with the possible exception of sample 246-99B, grain 3BI) does not contain copper in amounts detectable by the probe and that the copper in all but one biotite reported in tables 1 and 2 may be best explained by autocontamination. The exception, sample 246-99B, grain 3BI, is not easily explained by contamination with copper from chlorite because only the two grains of chlorite, both completely chloritized with no biotite-chlorite contact, occur in the sample, and the biotite contains more copper than the chlorite (table 1). Copper in this biotite also is not easily explained by contamination with copper from sulfides because no chalcopyrite occurs in the probe sample, and the pyrite contains less copper (300 p/m) than the biotite. Hornblende in the sample may contain copper (<95-percent confidence), but also in lesser amounts than the biotite.

The significance of the presence of copper in biotite and its possible presence in hornblende in sample 246-99B is not

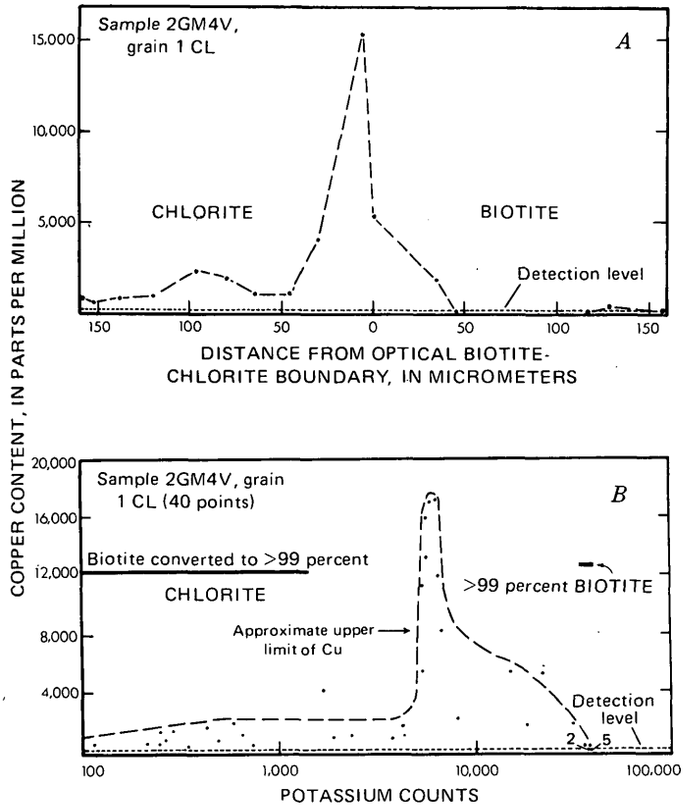

Figure 3.—Distribution of copper in biotite, chlorite, and transitional material. Bars indicate range of potassium (K) counts that designates relatively pure chlorite (<0.1 percent K_2O) and biotite (K counts equal to the average of K counts for biotite grains with no chloritization in the same mount). Counting time is 200 s, terminated on fixed beam current. Detection level was established at three times the square root of the average background counts (Birks, 1963). *A*, Distribution of copper in biotite and chlorite relative to the optical mineral boundary. *B*, Distribution of copper in chlorite, biotite, and transitional material relative to concentration of potassium.

clear. The sample is from the most mafic facies (diorite) of the Rattler Granodiorite, a fact that might suggest that copper actually is incorporated in biotite in mafic bodies during crystallization. However, biotite in equally mafic rock (Tortilla Quartz Diorite, table 1) and more mafic rock (diabase, unpub. data) does not contain detectable copper. Thus no trend of increasing copper content of biotite with decreasing silica content of the host rock is established for the rocks of the Ray area.

COPPER-RICH BLEACHED ZONES IN BIOTITE

Some biotite grains in the Granite Mountain Porphyry and older Laramide intrusive rocks have bleached (golden colored) zones oriented parallel to the (001) plane. The zones are sometimes offset along fractures that developed in the biotite prior to consolidation of the magma. Many of these zones are obvious extensions of chloritized layers, but others do not grade into optically perceivable chlorite at either the middle of the bleached zone or the edge of the grain. Some of the bleached zones contain unexpectedly large amounts of copper (table 3). A copper X-ray image of two such zones is shown in figure 5*A*. The wider zone is the one analyzed in mount 3GM6G of table 3.

As the small amounts of sulfur in the copper-rich zones indicate (table 3 and fig. 5*C*), the copper is not present in the form of submicroscopic copper sulfide or sulfate inclusions. In addition, X-ray images of the following elements indicate that they are not present in more than parts per million amounts in the bleached zones: F, Na, P, Cl, Ca, Sc, V, Cr, Co, Ni, Zn, Ga, Ge, As, Se, Br, Rb, Sr, Y, Nb, Mo, Tc, Ru, Rh, Pd, Ag, Cd, In, Sb, Te, I, Cs, Ba, La, Hf, Ta, W, Re, Os, Ir, Pt, Au, Hg, Tl, Pb, Bi, Th, Pa, and U.

Because of the carbon coating and lack of a suitable analyzing crystal, it could not be determined directly whether carbonates or nitrates account for the copper in the zones. However, the amount of silica in the zones suggests that the copper is not explained by the presence of known carbonates and nitrates, or even known oxides and silicates. Significantly less silica is present in such minerals than in chlorite (0–20 versus 26–27 percent). Therefore, if the zones were simply a mixture of known copper carbonates, nitrates, oxides, silicates, chlorite, and biotite, the amount of silica in the zones having appreciable amounts of copper (analyses G, O, P, Q, R, S, table 3) should be, but is not, measurably less than the amount of silica in chlorite.

It is not within the scope of this report to determine the exact mineralogic composition of the zones, but some speculation is warranted. The zones are assumed to represent incipient chloritization of biotite by fluids that may or may not carry copper, because chlorite occurs at grain edges along many of the zones and copper is concentrated at many optical biotite-chlorite boundaries (figs. 3, 4). However, except for SiO_2 and K_2O, the amounts of individual constituents and structural formulas of the copper-rich zones (analyses B, E, G, H, K, L, O, P, Q, R, S, U, and V, table 3) are not uniformly intermediate between the amounts of individual constituents and structural formulas of the parent biotites (analyses A, D, F, J, N, and T, table 3) and those of chlorite along the same zone or in the same rock sample (analyses C, I, M, and W, table 3). Although an increase in density of the zones relative to chlorite and biotite resulting from replacement of K, Ti, Mg, Fe, and Mn by Cu could account for some of the discrepancies in the nonuniform transition in chemistry between the zones and chlorite and biotite, the density shift is somewhat compensated by the amount of water required in the zones in order to arrive at reasonable totals of the constituents (the qualitative scans eliminate significant contribution to the totals of elements other than H and O). Thus it is apparent that the material in the zones is more than a simple mixture of well-formed chlorite and biotite. In addition, the large amount

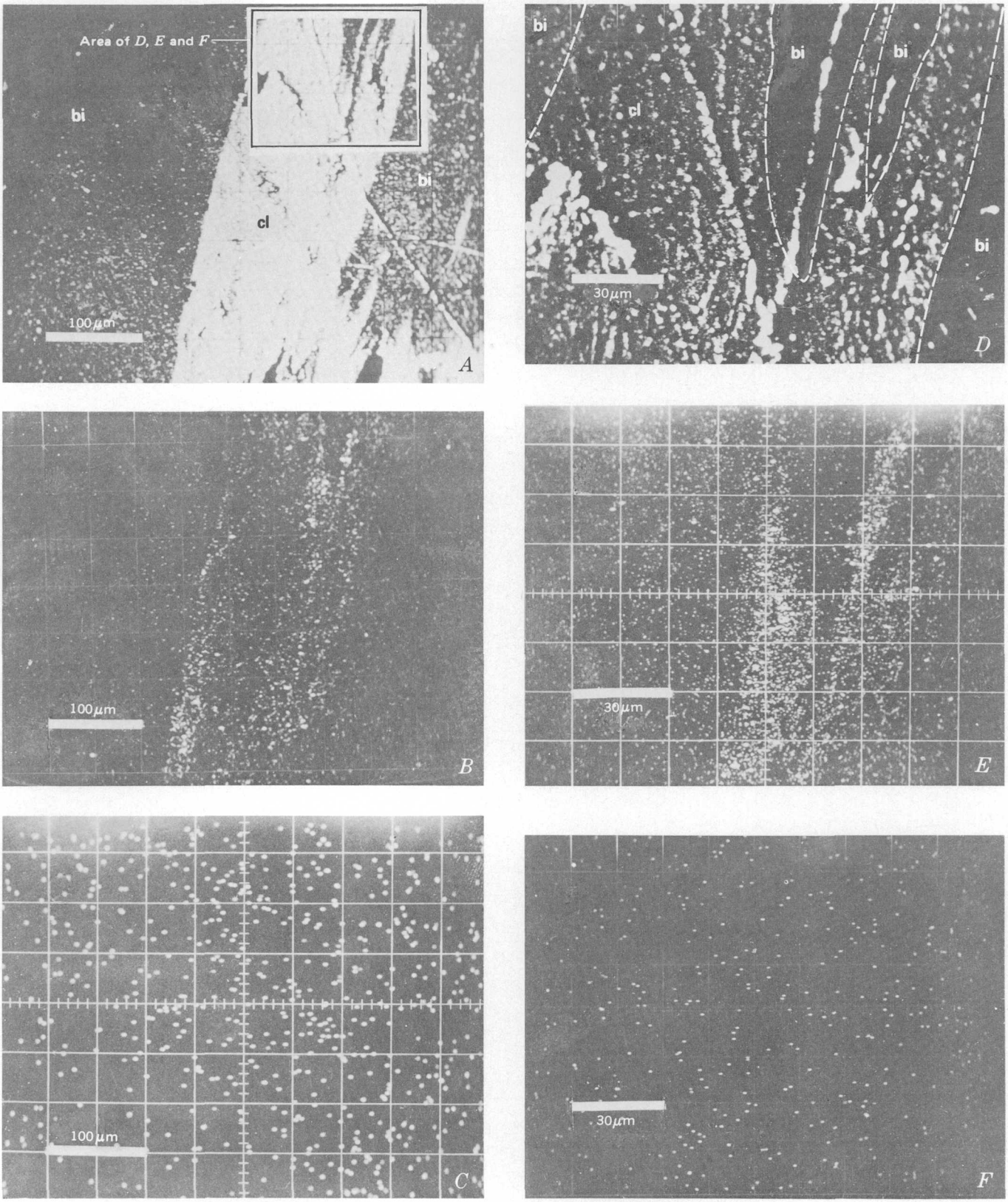

Figure 4.—Photographs of electron-beam scans of a biotite-chlorite grain in sample 46-11a. *A*, Scan for sample current of biotite-chlorite grain. The lighter area represents chlorite (cl), and dark areas are biotite (bi). *B*, Scan for copper (same area as *A*), showing its concentration at the mineral boundaries. Exposure time, 2 minutes. *C*, Scan for sulfur (same area as *B*). Note lack of sulfur at the mineral boundaries. Exposure time, 8 minutes. *D*, Scan for sample current of area designated in *A*. *E*, Scan for copper in same area as *D*. Exposure time, 1 minute. *F*, Scan for sulfur in same area as *E*. Exposure time, 4 minutes.

Table 3.—*Microprobe analyses and structural formulas for biotite, chlorite,*

Mount No.	2GM4V					GM6G
Grain No.	1			3		
Area analyzed	BIA	BI	CL	BIA	BI	BIA
Mineral	Biotite	Copper-rich zone	Chlorite	Biotite	Copper-rich zone	Biotite
Letter reference in text	A	B	C	D	E	F
Microprobe analysis (percent)						
SiO_2	37.6±0.2	32.7±1.2	27.4±0.3	38.1±0.3	37.2±0.4	36.5±.03
Al_2O_3	15.5±0.1	15.6±0.5	16.8±0.2	14.5±0.1	15.0±0.2	15.6±0.1
FeO[1]	17.4±0.2	19.4±0.7	24.3±0.2	17.6±0.1	17.6±0.1	18.4±0.2
MgO	11.4±0.1	14.4±0.4	16.2±0.1	12.4±0.1	11.5±0.05	11.4±0.1
CaO	(2)	.....	.....	.....	.....	.....
MnO	.46±0.01	.32±0.03	.64±0.02	.42±0.02	.42±0.02	.59±0.05
CuO	ND[3]	1.1±0.2	.11±0.02	ND	1.4±0.4	ND
TiO_2	3.2±0.1	.74±0.41	.09±0.010	3.4±0.03	3.5±0.1	2.5±0.1
K_2O	9.7±0.1	2.3±0.07	.09±0.018	9.9±0.1	9.0±0.5	9.5±0.2
Cl	.02±0.004	ND	ND	.03±0.006	.03±0.008	.02±0.006
F	.77±0.06	.18±0.17	.16±0.03	.86±0.04	.81±0.05	.66±0.06
S	.....	.....	.....	.....	.....	.01±0.001
Σ	96.1	86.7	85.8	97.2	96.5	95.2
Less O≡Cl+F	.3	.1	.1	.4	.3	.3
Σ	95.8±0.4	86.6±1.7	85.7±0.4	96.8±0.4	96.2±0.8	94.9±0.5
Structural formulas[4]						
Anions per formula	22	22	28	28	22	22	28	22
Si^{+4}	5.68	5.35	6.82	5.91	5.71	5.64	7.17	5.60
Al^{IV}	2.32 } 8.00	2.65 } 8.00	1.18 } 8.00	2.09 } 8.00	2.29 } 8.00	2.36 } 8.00	.83 } 8.00	2.40 } 8.00
Al^{VI}	.45	.37	2.65	2.18	.27	.32	2.58	.43
Ti^{+4}	.36	.09	.12	.01	.38	.40	.51	.29
Mg^{+2}	2.57	3.51	4.47	5.21	2.77	2.60	3.31	2.61
Cu^{+2}	..... } 5.64	.13 } 6.80	.17 } 11.46	.02 } 11.94	.... } 5.68	.16 } 5.76	.20 } 11.72	.... } 5.77
Fe^{+2}	2.20	2.66	3.38	4.38	2.21	2.23	2.84	2.36
Mn^{+2}	.06	.04	.06	.12	.05	.05	.07	.08
K^{+1}	1.87	.48	.61	.02	1.89	1.74	2.21	1.86

[1] Total Fe calculated as FeO.

[2] Blanks indicate no analysis was made for the component.

and copper-rich zones in biotite from Granite Mountain Porphyry

GM6G—Continued					
3—Continued			4		
Cul	Cu3	CLA	BIA	Cul	Cu3
Copper-rich zone		Chlorite	Biotite	Copper-rich zone	
G	H	I	J	K	L
Microprobe analysis (percent)—Continued					
32.9±2.4	34.9±2.3	26.6±0.4	37.0±0.4	33.4±2.9	36.3±0.7
13.5±0.7	14.3±0.7	17.3±0.2	14.7±0.2	13.5±1.3	14.0±0.3
15.3±0.9	17.0±0.7	24.2±0.2	17.6±0.1	16.2±0.3	17.4±0.4
9.5±1.3	11.3±0.7	16.4±0.1	11.9±0.1	10.6±0.2	11.4±0.5
.....	.....	.....	.....	.....	.....
.46±0.05	.51±0.05	.86±0.03	.56±0.01	.46±0.03	.05±0.028
13.5±0.9	4.6±0.9	.43±0.04	ND	1.0±0.6	5.3±0.8
3.5±0.7	4.8±3.8	.08±0.02	3.8±0.1	3.0±0.6	3.5±0.1
4.6±1.9	7.7±1.9	.09±0.03	9.4±0.1	5.5±0.7	8.1±1.2
ND	ND	ND	.03±0.006	.06±0.03	.04±0.007
.70±0.13	.79±0.17	.09±0.08	.69±0.04	.86±0.14	.73±0.09
.01±0.001	.01±0.001	ND	.02±0.002	.02±0.002	.02±0.002
94.0	95.9	86.1	95.7	84.6	96.8
.4	.3	.....	.3	.4	.3
93.6±3.7	95.6±5.1	86.1±0.5	95.4±0.5	84.2±3.4	96.5±1.8
Structural formulas[4]—Continued					
22 28	22 28	28	22	22 28	22 28
5.69 6.80 8.00 8.00	5.40 6.87 8.00 8.00	5.74 8.00	5.63 8.00	5.69 7.24 8.00 8.00	5.57 7.09 8.00 8.00
2.31 1.20	2.60 1.13	2.26	2.37	2.31 .76	2.43 .91
.40 2.09	.01 2.19	2.14	.26	.40 2.69	.10 2.31
.38 .54	.56 .71	.01	.43	.38 .49	.40 .51
2.69 2.92	2.61 3.32	5.28	2.70	2.69 3.42	2.61 3.32
.13 5.98 2.10 11.59	.54 5.99 .68 11.72	.07 12.05	.... 5.70	.13 5.98 .16 11.30	.61 6.02 .78 11.79
2.31 2.65	2.20 2.80	4.37	2.24	2.31 2.94	2.23 2.84
.07 .08	.07 .09	.16	.07	.07 .08	.07 .01
1.19 1.21	1.52 1.93	.02	1.82	1.19 1.52	1.59 2.02

[3] ND means component not detected at the following amounts: 0.01 percent CuO, 0.03 percent TiO_2, 0.005 percent S, 0.01 percent Cl, 0.04 percent F.

[4] Structural formula calculated on an anhydrous basis using computer program of Jackson and others (1967). Formulas exclude Ca, S, Cl, and F.

Table 3.—*Microprobe analyses and structural formulas for biotite, chlorite,*

Mount No.	GM6G-Con.	3GM6G			
Grain No.	4-Con.	1			
Area analyzed	CLA	G	A	C	D
Mineral	Chlorite	Biotite	Copper-rich zone		
Letter reference in text	M	N	O	P	Q
Microprobe analysis (percent)—Continued					
SiO_2	26.6±0.2	37.4±0.2	31.1±0.9	30.4±0.2	30.8±0.8
Al_2O_3	19.2±0.2	14.9±0.2	14.5±0.1	14.4±0.1	14.1±0.6
FeO[1]	22.5±0.3	18.5±0.2	14.5±0.3	13.9±0.2	13.5±0.6
MgO	16.4±0.2	12.3±0.1	10.3±0.2	9.8±0.1	9.7±0.4
CaO	.....	ND	.34±0.07	.24±0.05	.15±0.03
MnO	.96±0.07	.50±0.02	.32±0.02	.31±0.02	.28±0.02
CuO	.01±0.001	ND	12.6±0.6	12.1±0.4	14.4±0.8
TiO_2	.16±0.03	3.9±0.1	3.0±0.1	3.0±0.1	3.0±0.1
K_2O	.11±0.03	9.6±0.3	2.2±0.5	1.8±0.2	1.9±0.4
Cl	ND	.....	.....	.....	.....
F	.16±0.03	.....	.....	.....	.....
S	ND	.....	.....	.....	.....
Σ	85.9	97.1	88.9	86.0	87.8
Less O≡Cl+F	.1	.....	.....	.....	.....
Σ	85.8±0.5	97.1±0.5	88.9±1.3	86.0±0.6	87.8±1.2
Structural formulas[4]—Continued					
Anions per formula	28	22	22	28	22	28	22	28
Si^{+4}	5.66	5.58	5.22	6.65	5.25	6.68	5.25	6.68
Al^{IV}	2.34 → 8.00	2.42 → 8.00	2.78 → 8.00	1.35 → 8.00	2.75 → 8.00	1.32 → 8.00	2.75 → 8.00	1.32 → 8.00
Al^{VI}	2.48	.21	.09	2.30	.17	2.40	.08	2.28
Ti^{+4}	.03	.44	.38	.48	.39	.50	.38	.49
Mg^{+2}	5.20	2.74 → 5.76	2.58 → 6.75	3.28 → 11.34	2.52 → 6.71	3.21 → 11.21	2.46 → 6.73	3.14 → 11.30
Cu^{+2}	.... → 11.92	....	1.60	2.03	1.58	2.01	1.85	2.36
Fe^{+2}	4.01	2.31	2.04	2.59	2.01	2.55	1.92	2.45
Mn^{+2}	.17	.06	.06	.06	.04	.04	.04	.05
K^{+1}	.03	1.83	.47	.60	.40	.50	.41	.53

[1] Total Fe calculated as FeO.

[2] Blanks indicate no analysis was made for the component.

and copper-rich zones in biotite from Granite Mountain Porphyry —Continued

3GM6G—Continued		GM12			
1—Continued		2			3
E	F	BIX	BIA	BIB	CL
Copper-rich-zone—Continued		Biotite	Copper-rich zone		Chlorite
R	S	T	U	V	W
Microprobe analysis (percent)—Continued					
30.7±0.6	31.4±0.7	37.1±0.1	37.0±0.5	37.3±0.8	27.4±0.2
14.6±0.2	15.1±0.2	14.4±0.4	13.5±0.4	13.4±0.3	17.9±0.3
15.1±0.5	14.8±0.3	18.0±0.1	14.9±0.5	14.9±0.3	22.9±0.2
9.8±0.3	10.2±0.3	11.8±0.1	13.1±0.4	13.3±0.4	17.2±0.1
.25±0.24	.17±0.02	.....	.....	.....	.....
.30±0.02	.35±0.04	.69±0.05	.46±0.2	.45±0.03	.93±0.03
15.3±0.7	10.1±1.5	ND	.19±0.04	.19±0.04	.09±0.01
3.1±0.1	3.3±0.1	4.1±0.1	3.2±0.1	3.3±0.1	.05±0.009
2.6±0.1	4.2±0.5	9.4±0.1	7.3±0.2	7.6±0.1	.18±0.03
.....	.....	.03±0.01	.03±0.02	.01±0.007	ND
.....	.....	.69±0.05	.90±0.13	.91±0.12	.14±0.02
.....	.....	.02±0.002	.01±0.001	.01±0.001	.....
91.8	89.6 . . .	96.2	90.6	91.4	86.8
.....	.....	.3	.4	.4	.1
91.8±1.1	89.6±1.8	95.9±0.5	90.2±0.9	91.0±1.0	86.7±0.4
Structural formulas[4] —Continued					
22: 5.09, 2.86 → 7.95; 28: 6.48, 1.52 → 8.00; .... , .39, 2.42, 1.91, 2.09, .04 → 6.85; 2.11, .49, 3.08, 2.44, 2.66, .05 → 11.53; .55, .70		22: 5.21, 2.79 → 8.00; 28: 6.63, 1.37 → 8.00; .16, .41, 2.52, 1.27, 2.05, .04 → 6.45; 2.39, .52, 3.21, 1.61, 2.62, .06 → 11.54; .89, 1.13		22: 5.63, 2.37 → 8.00; .20, .47, 2.67, ... , 2.28, .09 → 5.71; 1.82		22: 5.82, 2.18 → 8.00; 28: 7.41, .59 → 8.00; .32, .38, 3.07, .02, 1.96, .06 → 5.81; 2.59, .48, 3.91, .03, 2.49, .08 → 11.44; 1.46, 1.86		22: 5.82, 2.18 → 8.00; 28: 7.41, .59 → 8.00; .29, .39, 3.10, .02, 1.95, .06 → 5.81; 2.55, .49, 3.94, .03, 2.48, .08 → 11.50; 1.51, 1.93		28: 5.80, 2.20 → 8.00; 2.27, .01, 5.43, .01, 4.06, .17, .05 → 12.00	

[3] ND means component not detected at the following amounts: 0.01 percent CuO, 0.03 percent TiO_2, 0.005 percent S, 0.01 percent Cl, 0.04 percent F.

[4] Structural formula calculated on an anhydrous basis using computer program of Jackson and others (1967). Formulas exclude Ca, S, Cl, and F.

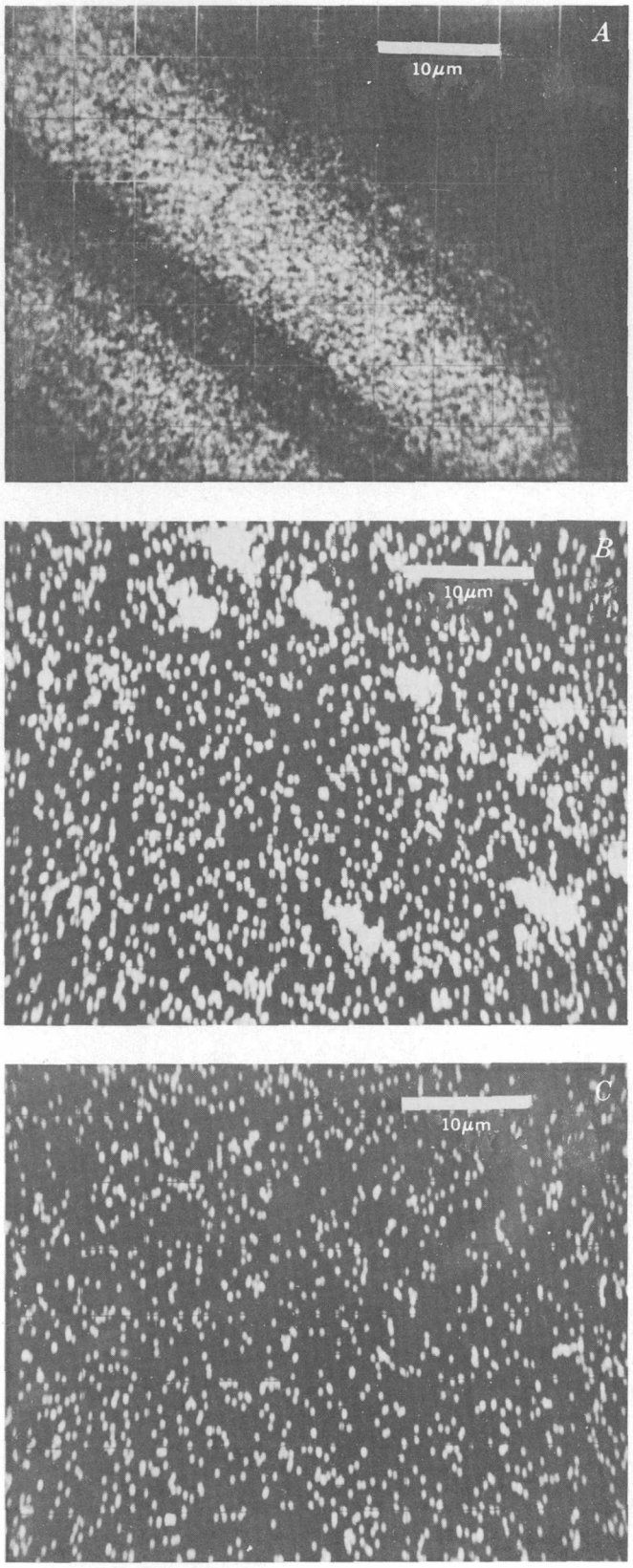

of copper in the transitional material is not easily explained by either substitution or attachment of copper in well-formed chlorite and biotite in view of the relatively low amount of copper in well-formed chlorite and biotite (fig. 3; tables 1 and 2).

Whether the material is partly destroyed biotite, poorly formed chlorite, another well or poorly formed sheet silicate, or a mixture of these cannot be determined from existing data. However, the data do restrict the type or amount of possible sheet silicates that could make up the material in the bleached zones. The silica content of the zones, being less than biotite, indicates that if no chlorite is present in the zones and biotite either is or is not present, the sheet silicates that could make up the zones are septechlorite, clintonite, xanthophyllite, margarite, silica-poor montmorillonite, or vermiculite. The small amount of calcium in the zones (analyses O, P, Q, R, and S, table 3) indicates that of these, margarite, clintonite, and xanthophyllite probably are not present. On the basis of the color of the zones, their refractive index, birefringence, the leachability in acid of copper in biotite-chlorite grains (mentioned earlier), and the number of exchange sites available, vermiculite or montmorillonite seem to be more likely alternatives to septechlorite, if indeed another sheet silicate is present in the zones. Montmorillonite is possibly less likely than vermiculite because smaller amounts of alumina are expected in silica-poor montmorillonite. Alternatively, if chlorite composes part of the zones, the data do not negate the presence of a sheet silicate having more silica than biotite; however, the amount of such a silicate that could be present is limited by the amount of chlorite required to dilute the higher amounts of silica in these minerals to those observed in the zones. Thus if most of the copper were present in a high-silica silicate, the amount required is much more than that required in vermiculite.

The zones often include apatite grains and are wider around them. In addition, the zones commonly contain or are near swarms of suboptical-sized apatite as determined by electron-beam scans of the zones for calcium and for phosphorus (fig. 5*B*). Thus it is suspected that the bleached zones (which range in thickness from <1 to 20 μm) extend completely through 3-mm-sized biotite grains and in places are offset along fractures that developed prior to consolidation of the magma because of favorable permeability conditions in the biotite resulting from the deformation and expansion of the grains by the apatite inclusions.

Figure 5.—Photographs of electron-beam scans of copper-rich zones in mount sample 3GM6G. *A*, Scan for copper. Exposure time, 1 minute. *B*, Scan for phosphorus of same area as *A*. Exposure time, 1 minute. *C*, Scan for sulfur of same area as *A*. Exposure time, 10 minutes.

COMPARISON OF MAJOR-ELEMENT CHEMISTRY OF THE COPPER-RICH AND COPPER-POOR CHLORITES

The presence or absence of copper in chlorite could possibly be attributed to its formation at different times or from different fluids; hence, the resulting chlorites might be differentiated on the basis of chemistry. However, preliminary data indicate that except for the presence of copper, chlorite that contains copper is similar in chemistry to chlorite that does not contain copper (fig. 6). In fact, the composition of chlorite appears dependent in larger part on the composition of the parent biotite than on the copper-depositing characteristics of the altering fluid (fig. 7). Preliminary observations also revealed no optical dissimilarity between copper-bearing and copper-poor chlorite. Thus it could not be established whether chlorite formed in the rocks at two different times from two fluids.

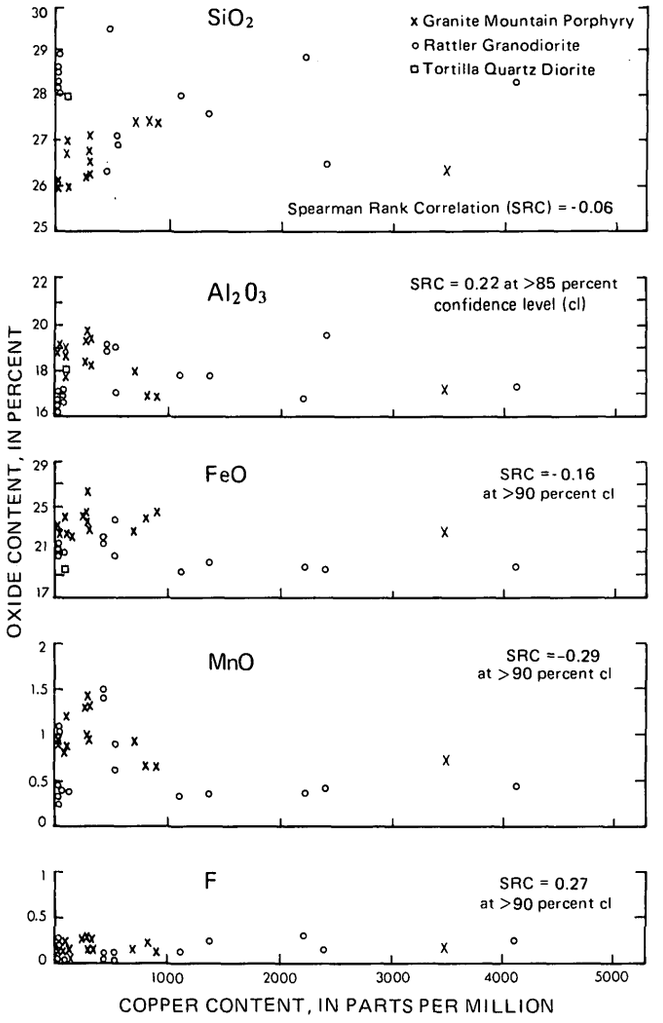

Figure 6.—Graphs showing amounts of representative chemical components in chlorite in relation to amount of copper in chlorite. Some points are offset slightly for plotting purposes. Four additional points (three for Rattler Granodiorite and one for Tortilla Quartz Diorite) plot near the origin of the F versus Cu diagram.

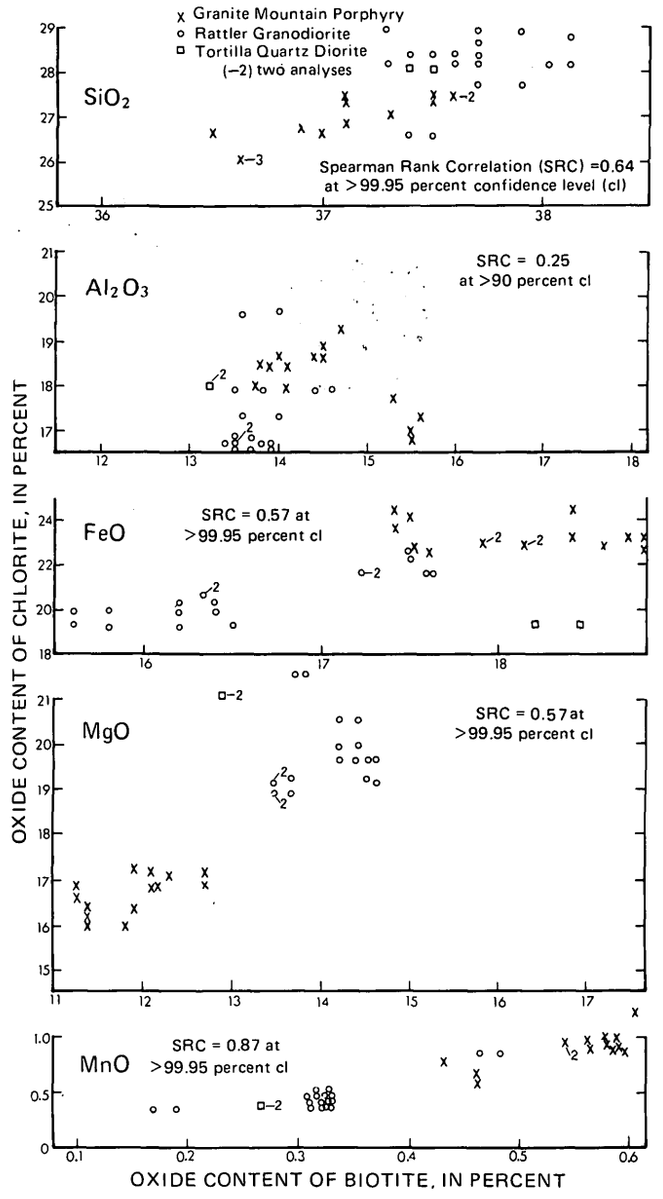

Figure 7.—Graphs showing the amount of oxide in biotite in relation to the amount of oxide in chlorite derived from the biotite. Some points are slightly offset for plotting purposes. The statistics include two biotite-chlorite pairs that plot off the diagrams.

VALUE OF THE COPPER CONTENT OF CHLORITE AS AN INDICATOR OF ORE

The occurrence of copper-bearing chlorite derived from igneous biotite near two ore deposits suggests that the amount of copper in chlorite might serve as a geochemical indicator for

a nearby copper ore deposit. However, copper in chlorite does not seem to show a simple positive relation with the proximity of the sample to a presently recognized deposit (fig. 8). This lack of correlation may result from inadequate data or from the possibility that the copper content of chlorite depends on factors other than, or in addition to, the distance of the chlorite grain from a minable deposit.

Inadequacy in the data is suggested by the extreme variation in the amount of copper in chlorite both between grains in the same probe mount (thin section, 1-in. diam) and within

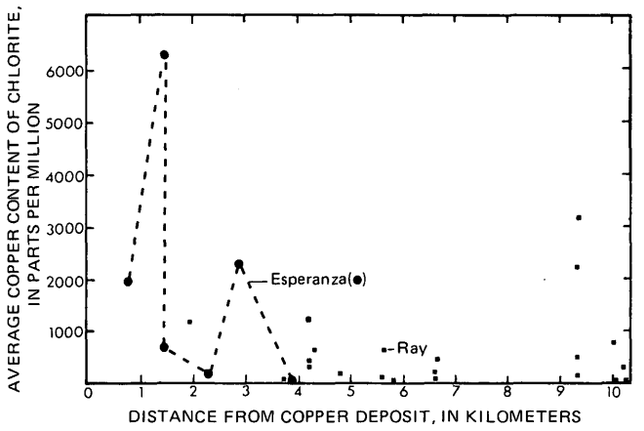

Figure 8.—Plot of average amount of copper in chlorite in a given sample in relation to distance of the sample from the nearest recognized commercial deposit.

individual grains (figs. 3, 4; tables 1, 2). Thus determination of the true average abundance of copper in chlorite in each rock sample is too expensive to refine with microprobe analyses because a prohibitive number of grains must be analyzed in a prohibitive number of mounts. The alternative method of determining the true abundance of copper in chlorite by conventional analyses of separates may also be limited by the various types of bias that are built into mineral separations (magnetic, electrostatic, specific gravity, and optical)—the resulting separation may be 100 percent chlorite, but in view of the irregular distribution of copper in chlorite and of the fact that much copper resides in the more poorly crystallized chlorite, the mineral separate is likely to contain copper in an amount not representative of the average.

These observations do not rule out the potential use of copper abundance in chlorite as a geochemical indicator. If standardized separation techniques are used, it is still possible that the content of either leachable or total copper in mica or chlorite separates may correlate roughly with proximity of the sample to a deposit. Additionally, the copper content of chlorite may be of limited usefulness as a broader indicator of ore; that is, it might point out potential copper-producing provinces. For example, the copper content of chlorite from Sierra Nevada rocks (Dodge, 1973) with no known associated porphyry-type deposits is much less than that of chlorites reported here. However, this again may reflect mineral separation problems because Dodge analyzed clean mineral separates that probably were relatively free of poorly crystallized chlorite.

Finally, assuming that the true average abundance of copper in chlorite (or an abundance determined by analysis of concentrates separated in a standardized way) could be determined, caution should be used in its application as a geochemical indicator of ore because there is reason to suspect that this abundance could be influenced by factors other than the distance of the sample from a minable copper deposit. These factors include the rate of chloritization, percentage of partial chloritization, number and size of grains chloritized, the number of potential fluid conduits (fractures) per unit volume of rock, the proximity of the chlorite to a fracture, and the concentration of copper in the fluid immediately adjacent to the biotite; the first three factors would control the number of sites suitable for copper capture, and the latter three are measures of the availability of the chlorite to the copper in the supplying fluid.

CONCLUSIONS

Copper occurs in chlorite derived from igneous biotite in Laramide intrusions around two Arizona porphyry copper deposits and, further, is concentrated at the boundary between parent biotite and chlorite. However, the copper content of igneous and hydrothermal biotite near these deposits was found to be much less than that of chlorite and was not detected in most of the grains analyzed. In view of the difficulty in cleaning chlorite from biotite separates, these observations suggest that caution should be used in speculations about what the abundance of copper in biotite derived from bulk-analyzed mineral separates might mean with respect to the genesis or proximity of ore deposits and with respect to the behavior of copper in a differentiating magma. Additionally, because a potentially large part of the copper in a whole-rock sample of "granitic" rock may be in alteration products of biotite and thereby conceivably have had its source outside the analyzed sample, caution should be applied to petrologic and genetic interpretations of whole-rock copper abundance data.

ACKNOWLEDGMENTS

The manuscript benefited greatly from thoughtful reviews by N. J Page and R. P. Ashley. T. G. Lovering kindly supplied the biotite separates from Esperanza-Sierrita samples. Hydrothermal biotite from the Ray deposit was collected with the helpful cooperation of the staff of the Kennecott Copper Corp., Ray Mines Division. Walter S. Snyder aided in construction of the illustrations.

REFERENCES CITED

Banks, N. G., Cornwall, H. R., Silberman, M. L. Creasey, S. C., and Marvin, R. F., 1972, K-Ar ages, pt. 1 *of* Chronology of intrusion and ore deposition at Ray, Arizona: Econ. Geology, v. 67, p. 864–878.

Banks, N. G., and Stuckless, J. S., 1973, Fission-track ages, pt. 2 *of* Chronology of intrusion and ore deposition at Ray, Arizona: Econ. Geology, v. 68, p. 657–664.

Beaman, D. R., and Isasi, J. A., 1970, A critical examination of computer programs used in quantitative electron microprobe analysis: Anal. Chemistry, v. 42, p. 1540–1568.

Beeson, M. H., 1967, A computer program for processing electron microprobe data: U.S. Geol. Survey open-file rept., 10 p.

Birks, L. S., 1963, Electron-probe microanalysis: New York, John Wiley and Sons, 253 p.

Boyd, F. R., 1969, Electron probe study of diopside inclusions in kimberlite: Am. Jour. Sci., v. 267A, p. 50–69.

Cornwall, H. R. Banks, N. G., and Phillips, C. H., 1971, Geologic map of the Sonora quadrangle, Pinal and Gila Counties, Arizona: U.S. Geol. Survey Geol. Quad. Map GQ-1021.

Creasey, S. C., and Kistler, R. W., 1962, Age of some copper-bearing porphyries and other igneous rocks in southeastern Arizona, *in* Short papers in geology, hydrology, and topography: U.S. Geol. Survey Prof. Paper 450-D, p. D1–D5.

Damon, P. E., and Mauger, R. L., 1966, Epeirogeny-orogeny viewed from the Basin and Range province: Soc. Mining Engineers Trans., v. 235, p. 99–112.

Dodge, F. C. W., 1973, Chlorites from granitic rocks of the central Sierra Nevada batholith, California: Mineralog. Mag., v. 39, p. 58–64.

Dodge, F. W. C., Smith, V. C., and Mays, R. E., 1969, Biotites from granitic rocks of the central Sierra Nevada batholith, California: Jour. Petrology, v. 10, p. 250–271.

Jackson, E. D., Stevens, R. E., and Bowen, R. W., 1967, A computer-based procedure for deriving mineral formulas from mineral analyses, *in* Geological Survey research 1967: U.S. Geol. Survey Prof. Paper 575-C, p. C23–C31.

Parry, W. T., and Nackowski, M. P., 1963, Copper, lead, and zinc in biotites from Basin and Range quartz monzonites: Econ. Geology, v. 58, no. 7, p. 1126–1144.

Jour. Research U.S. Geol. Survey
Vol. 2, No. 2, Mar.-Apr. 1974, p. 213–218

GARRELSITE, $NaBa_3Si_2B_7O_{16}(OH)_4$

By CHARLES MILTON[1] and ADOLF PABST,[2]
Washington, D.C., Berkeley, Calif.

Abstract.—Garrelsite, $NaBa_3Si_2B_7O_{16}(OH)_4$, originally described in 1955, has recently been reexamined by Charles Milton and Adolf Pabst and by Subrata Ghose and Horst H. Ulbrich. The latter have reanalyzed the mineral and determined the structure; the powder pattern is indexed on the basis of their 1972 cell constants. These were refined in 1973 to a=14.639 A, b=8.466 A, c=13.438 A, β=114.21°, space group $C2/c$. Garrelsite has been found in two drill cores penetrating the Green River Formation (Eocene) at two localities in Uintah County, Utah, and in the borate deposits of the Kramer district, Kern County, Calif. The original description of the morphology has been corrected, and the optical orientation has been redetermined.

Garrelsite was first briefly described in an abstract (Milton, Axelrod, and Grimaldi, 1955). The quality of the specimens then available was poor; later, good crystals became available for analytical and definitive crystallographic study (Ghose and Ulbrich, 1972, 1973). This paper reviews the older data, with reference to the new, and summarizes what is now known about garrelsite.

OCCURRENCE

Garrelsite was first discovered in a core from the Sun Oil Co. South Ouray Unit 1 well, Uintah County, Utah (Milton, Axelrod, and Grimaldi, 1955) and was more recently found in another Green River Formation core (Wosco Rx-1) in Uintah County. A third occurrence is in the Kramer borate district of Kern County, Calif., where "a few colorless, subhedral, prismatic grains, 0.1 by 0.6 mm in size, have been found in ulexite * * * some prismatic crystals and small disc-like grains with a sugary appearance have also been recovered from the tailings * * *" (Morgan and Erd, 1969).

Garrelsite occurs in Utah in brown dolomitic marlstone as authigenic, small (generally 2–3 mm), steeply four-sided, bipyramidal crystals, with characteristic diagonal striations. The crystals are clear and glassy, except where semiopaque and brown because of innumerable matrix inclusions. In addition to the garrelsite, the marlstone contains nahcolite, shortite, searlesite, and wurtzite. However, neither leucosphenite nor reedmergnerite (both fairly common Utah Green River borosilicates) have been found in association with garrelsite.

In the Utah cores, there appear to be two modes of occurrence, the first being sparsely disseminated crystals in fine-grained brown dolomitic marlstone. Most crystals are single; a few are composites (fig. 1). Although these crystals appear to be homogeneous, they invariably include a very large proportion of marlstone matrix material, with little if any of the crystallographically zoned distribution usually seen in other Green River borosilicates such as reedmergnerite and leucosphenite. Figures 2*A* and 2*B* show such garrelsite crystals in thin section; figure 2*C* shows an extreme case of such matrix inclusion. Because such inclusions make separation of pure garrelsite most difficult, if not impossible, interpretation of the analysis of these crystals (table 1, col. A) was subject to error even though every effort was made to obtain a sample consisting of microscopic particles free from visible matrix. All the Uintah County garrelsite from the two wells, with one exception, is of this matrix-inclusion type.

This exception, the second mode of occurrence, is in one small core sample labeled "South Ouray No. 1, 2,606 ft" which was obtained some years after publication of the original description in 1955. Here, lining a vertical fissure in the marlstone, the garrelsite is not sparsely disseminated but occurs fairly abundantly as clear, vitreous crystals almost, if not wholly, free from matrix inclusions. These crystals were (partly) analyzed (table 1, col. B), and their structure was determined, leading to a revised formula (Ghose and Ulbrich, 1973) $NaBa_3Si_2B_7O_{16}(OH)_4$.

Figures 1 and 2 show the material reported by Milton, Axelrod, and Grimaldi in 1955, and figure 3 illustrates the core sample with the crystals studied by ourselves and by Ghose and Ulbrich in 1972–73.

CHEMICAL ANALYSES AND INTERPRETATION OF DATA

The 1955 analysis by Blanche Ingram (table 1, col. A), made on the best available but still impure material (only 27 mg by

[1] U.S. Geological Survey and The George Washington University.
[2] Department of Geology and Geophysics, University of California.

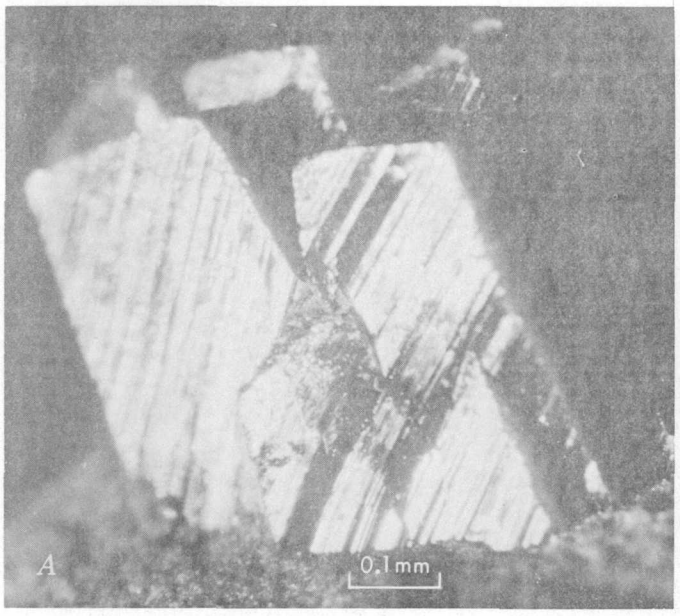

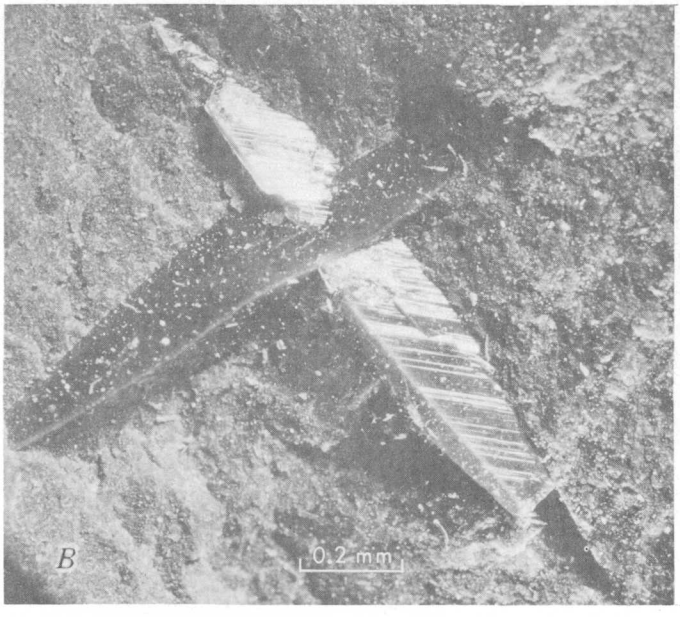

Figure 1.—Garrelsite crystals from Sun Oil Co. South Ouray Unit 1 well, Uintah County, Utah. *A*, Composite of several stubby prismatic crystals showing diagonal striations; from a depth of 2,178 ft. *B*, Composite of two crystals simulating twinning; note tapering prismatic habit and diagonal striations; from a depth of 2,185 ft.

"wet" methods), is now superseded by analyses of the inclusion-free crystals described above as the second mode of occurrence. The inclusion-free samples underwent partial microprobe analysis by H. H. Ulbrich (table 1, col. B), and Na_2O content of similar samples was determined by Blanche Ingram (table l, footnote 2). These new analytical data agree well with the theoretical composition derived from crystallographic study by Ghose and Ulbrich (1973).

Analysis A (table 1) yields the formula $(Ba_{0.65}\ Ca_{0.29}Mg_{0.06})_4\ H_6Si_2B_6O_{20}$ which Christ (1959) compared with those of other borosilicates; he suggested that garrelsite might be part of a homologous series that also includes bakerite, datolite, homilite, and herderite; while Strunz and Tennyson (1970) grouped garrelsite with the heterotypal borosilicate group including kornerupine, dumortierite, serendibite, howlite, and others. The theoretical composition of garrelsite, based on crystallographic studies (table 1, col. C) and supported by more reliable analytical data (table 1, col. B), gives the formula $NaBa_3Si_2B_7O16(OH)_4$, thus rendering the 1955 formula obsolete. As Christ and also Strunz and Tennyson used the data on the impure mineral, the relation of garrelsite to other minerals must now be reconsidered in the light of Ghose and Ulbrich's (1973) structural study.

The 1972 formula and cell dimensions by Ghose and Ulbrich, as listed in table 3, col. C, give a cell volume of 1,521.199 A, a cell weight of $5{,}917.35\times10^{-24}$ g, and a density of 3.890 g/cm^3. These cell dimensions have subsequently been refined by Ghose and Ulbrich (1973) on a single crystal automatic diffractometer, using higher angle reflections. The new values are shown in table 3, col. D.

Table 1.—*Chemical analyses of garrelsite*

	First mode of occurrence (impurities present)	Second mode of occurrence	Theoretical composition
	A	B	C
BaO	46.1	51.41, 51.50	51.64
CaO	7.7	Not found	.....
MgO	1.2	Not found	.....
B_2O_3 ...	24.0	.....	27.36
SiO_2 ...	14.6	13.49, 13.57	13.48
H_2O	[1]5.9	.....	4.04
R_2O_3 ...	.06	.....	.....
Na_2O ...	.....	.....	[2]3.48
K_2O	.....	Not found	.....
Total	100.1	.....	100.00
Density (measured)	3.68	.....	.....
Density (calculated)	.....	.....	3.890

[1] Loss on ignition at 800° C.

[2] Analysis of 1.1 mg of clear garrelsite crystals, similar to those inclusion-free samples analyzed by microprobe and crystallographic study by Ghose and Ulbrich, was made by Blanche Ingram (U.S. Geological Survey, written commun., 1973) who found (by atomic absorption photometry) 3.5 percent Na_2O. This value is in excellent agreement with the theoretical value of 3.48 percent.

A. Blanche Ingram, USGS analyst, on 27 mg (reported in Milton, Axelrod, and Grimaldi, 1955); Katherine E. Valentine, USGS analyst, spectrographic semiquantitative—Ca, 1 to 5 percent, Na and Mg, 0.1 to 0.5 percent; Charles Annell, USGS analyst, spectrographic semiquantitative Al, Ca, Mg, and Na, 1 to 5 percent. Reported formula is now obsolete.

B. Microprobe analysis, H. H. Ulbrich (written commun., July 1972).

C. Calculated from structural formula $NaBa_3Si_2B_7O_{16}(OH)_4$ (Ghose and Ulbrich, 1973).

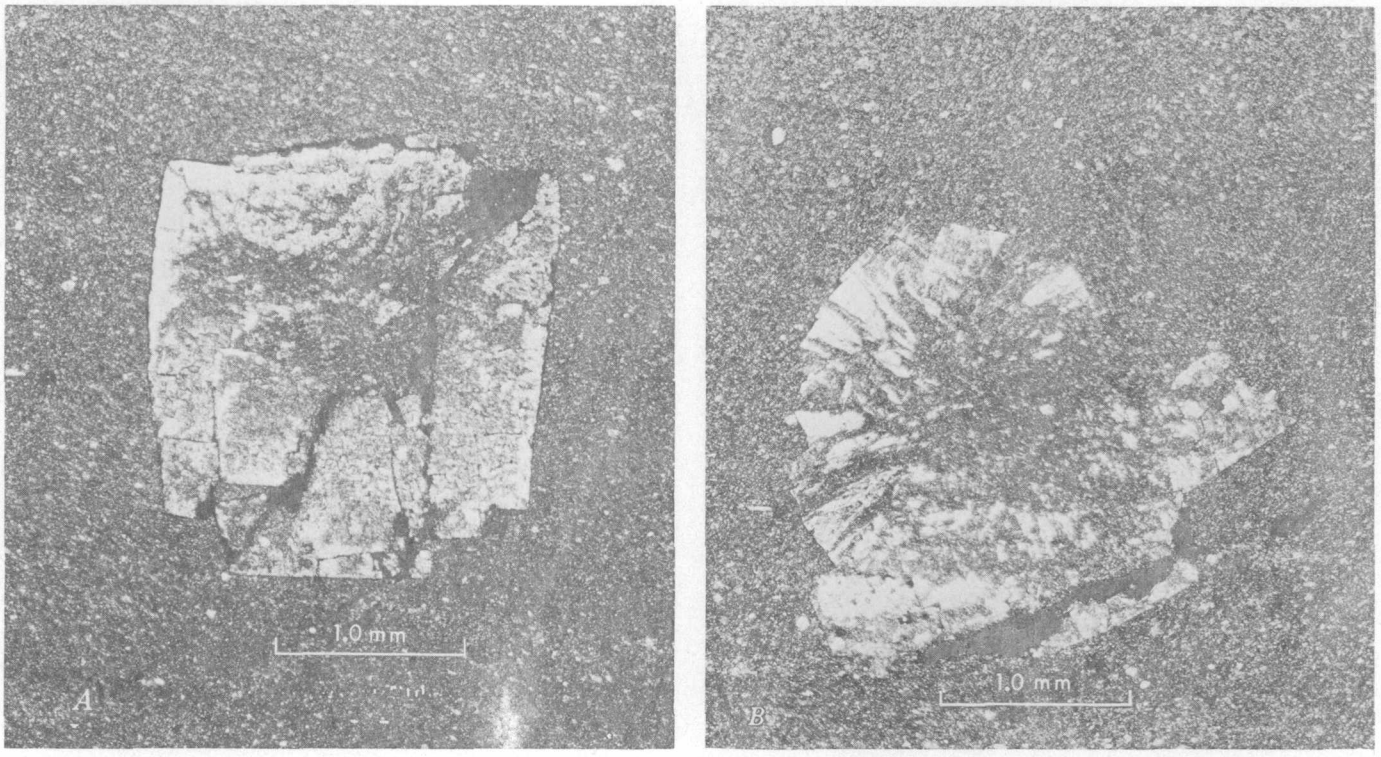

Figure 2.—Photomicrographs of thin sections of garrelsite from a depth of 2,185 ft, Sun Oil Co., South Ouray Unit 1 well, Uintah County, Utah. *A*, *B*, Showing composite growth and matrix inclusions. *C*. Showing skeletal growth of garrelsite crystal crowded with matrix inclusions. Plane-polarized light.

The discrepancy between the 3.890 value for density and the older measured value of 3.68 (table 1) may reflect the considerable admixture of lighter impurities (quartz, 2.65, dolomite, 2.87, and calcite 2.71).

X-RAY DATA

Table 2 records a measured powder pattern on clear crystals of garrelsite from Utah, with calculated pattern from the unit cell derived from the measured pattern; from this unit cell, the pattern is indexed. The indexed pattern calculated by Ghose and Ulbrich (written commun., 1972) from their single crystal data (Ghose and Ulbrich, 1972) is also given. Table 3 records five unit cell determinations on garrelsite.

MORPHOLOGY AND PHYSICAL PROPERTIES

The crystal habit was originally described as "steep bipyramidal" (Milton, Axelrod, and Grimaldi, 1955), and figure 4 shows this habit, which suggests overall morphological symmetry $2/m$. The striations are external features; no indication of twinning or intergrowth was seen. Under the microscope the clear crystals are free of visible deformation or mosaic structure.

In the gnomonic projection (fig. 5), crystal drawing (fig. 4), and angle table (table 4), the reference system of the original description is used, with angle calculations based on the reported (1955) cell dimensions.

The principal forms observed are $\{\bar{1}11\}$ and $\{\bar{2}11\}$; minor forms (rare) are $\{101\}$, $\{\bar{1}13\}$ and $\{001\}$. The characteristic

Table 2.—*X-ray data for garrelsite (clear crystals) from Utah*

Powder Cu/Ni radiation, 114.6-mm-diameter camera			Single crystal (Ghose and Ulbrich, 1972)		
I	*d*(observed)	*d*(calculated)[1]	*hkl*	*d*(calculated)[2]	*hkl*
vvw . .	7.184	7.156	110	7.148	110
vvw . .	6.697	6.679	200	6.665	200
mw . . .	6.125	6.135	002	6.122	002
vw . . .	5.906	5.882	$\bar{2}02$	5.870	$\bar{2}02$
w	5.662	5.662	111	5.654	111
mw . . .	4.232	4.238	020	4.234	020
vvw . .	4.056	4.055	$\bar{3}12$	4.048	$\bar{3}12$
mw . . .	3.944	3.942	310	3.935	310
				3.655	$\bar{2}21$
vs	3.636	3.626	$\bar{4}02$		
				3.618	$\bar{4}02$
vw . . .	3.489	3.487	022	3.483	022
vvw . .	3.347	3.339	400	3.336	400
				3.249	113
w	3.255	3.255	113		
				3.244	221
				3.070	$\bar{1}14$
vvs . . .	3.053	3.046	$\bar{2}23$	3.061	004
				3.042	$\bar{2}23$
vw . . .	2.938	2.941	$\bar{4}04$	2.935	$\bar{4}04$
ms . . .	2.873	2.874	312	2.869	312
				2.762	130
ms . . .	2.757	2.755	$\bar{4}22$		
				2.751	$\bar{4}22$
w	2.713	2.716	$\bar{5}11$	2.711	$\bar{5}11$
w	2.653	2.648	131	2.646	131
vw . . .	2.535	2.528	402	2.523	402
				2.496	$\bar{5}14$
vvw . .	2.487	2.485	024		
				2.481	024
vw . . .	2.435	2.433	204	2.428	204
vw . . .	2.269	2.271	$\bar{2}25$	2.267	$\bar{2}25$
				2.202	133
vw . . .	2.209	2.205	133		
				2.187	$\bar{4}06$
				2.120	025
vw . . .	2.121	2.119	040		
				2.117	040
				2.088	$\bar{1}16$
w	2.086	2.088	041		
				2.086	041
S_b . . .	2.026	2.028	$\bar{6}24$	2.027	241
					$\bar{5}16$
vw . . .	1.981	1.983	$\bar{7}14$	1.979	$\bar{7}14$
				1.952	241
vw . . .	1.946	1.946	$\bar{4}26$		
				1.943	$\bar{4}26$
				1.915	$\bar{1}35$
w	1.913	1.914	$\bar{6}25$	1.911	$\bar{6}25$
				1.906	$\bar{2}43$
				1.858	710
mw . . .	1.864	1.862	710		
				1.858	602
w	1.834	1.834	531	1.832	531
vw . . .	1.813	1.813	$\bar{8}04$	1.809	$\bar{8}04$

Table 2.—*X-ray data for garrelsite (clear crystals) from Utah*—Continued

Powder Cu/Ni radiation, 114.6-mm-diameter camera			Single crystal (Ghose and Ulbrich, 1972)		
I	*d*(observed)	*d*(calculated)[1]	*hkl*	*d*(calculated)[2]	*hkl*
				1.759	135
mw . . .	1.760	1.762	135		
				1.759	206
vvw . .	1.733	1.736	424	1.732	424
vvw . .	1.707	1.709	532	1.707	532
vvw . .	1.675	1.674	$\bar{8}06$	1.671	$\bar{8}06$

[1] Table 3, column B.

[2] Table 3, column C.

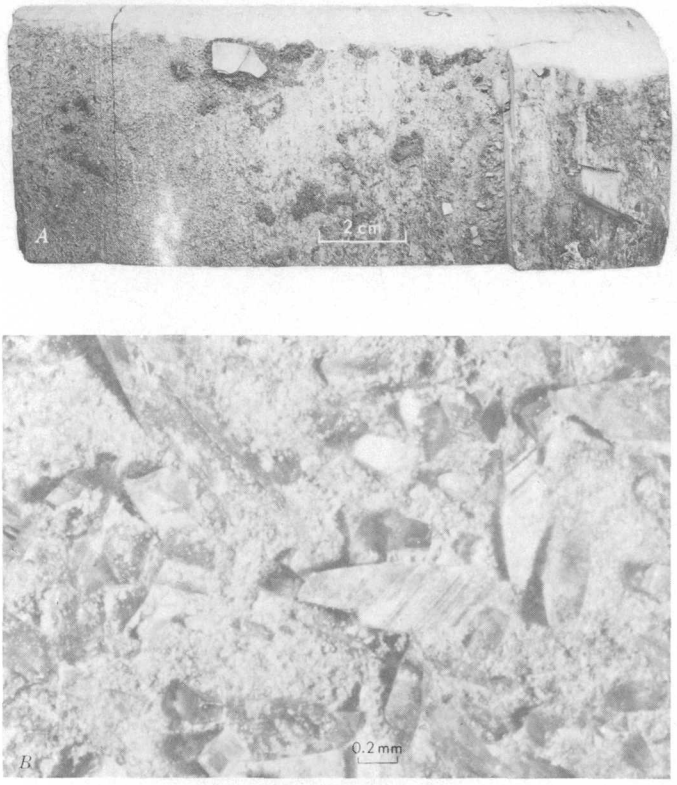

Figure 3.—Garrelsite. *A*, Core containing vertical fissure lined with garrelsite. *B*, Crystals of garrelsite from the fissure are nearly free of matrix inclusions. From a depth of 2,606 ft, Sun Oil Co. South Ouray Unit 1 well, Uintah County, Utah.

diagonal striations are mostly on $\{\bar{1}11\}$, less often on $\{\bar{2}11\}$ which is generally unstriated. Perfect $\{001\}$ cleavage is recognized.

The optical data are as follows: Colorless; indices of refraction α=1.620, β=1.633, γ=1.640 (all ±0.003) as previously reported; $2V_\alpha$ (measured) is 55°±2°; the $2V$ previously reported, 72°, was calculated from the indices; in

Table 3.—*Unit cell dimensions for garrelsite*

	A	B	C	D	E
a	13.43 A	14.655±.008 A	14.628 A	14.639 A	14.51 A
b	8.45	8.480±.008	8.469	8.466	8.524
c	14.01	13.460±.01	13.435	13.438	13.32
β	114°19′	114°18±03′	114°18′	114°13′	114°08′
Space group					
Aa or *A2/a*	. . . . .		*Cc*	*C2/c*	*C2/c* or *Cc*
Z	4	. . . . .	4	4	----------

A. Original material from Utah (Milton, Axelrod, and Grimaldi, 1955). (These data are now obsolete).
B. Clear crystals from Utah; calculated from powder data in table 2.
C. Clear crystals from Utah (Ghose and Ulbrich, 1972).
D. Clear crystal from Utah (Ghose and Ulbrich, 1973).
E. Garrelsite from California (R. C. Erd, written commun., 1968).

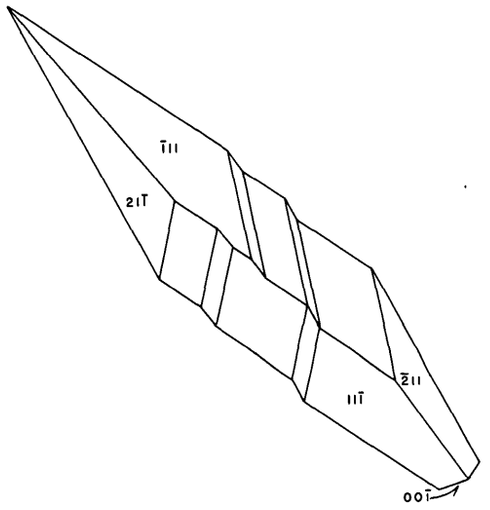

Figure 4.—Side view of typical garrelsite crystal showing steps of $\{\bar{2}11\}$ on $\{\bar{1}11\}$, giving rise to striations. Lower tip broken off along $\{001\}$ cleavage.

cases of low or moderate birefringence the uncertainty of the indices, ±0.003, leads to an uncertainty of the calculated $2V$ far greater than that of the measured $2V$ (shifts of the reported indices by about 0.0013, or 40 percent of the estimated uncertainty, are sufficient to achieve agreement between observed and calculated $2V$); the optic orientation as shown in the gnomonic projection (fig. 5) is $\beta=b$ (not $\gamma=b$ as previously reported), with $\gamma\wedge[101]$ (the edge of the $\{\bar{1}11\}$ form) = 33°; one optic axis is nearly normal to this edge.

Cell constants of garrelsite have been determined as shown in table 3.

Garrelsite just barely scratches glass and readily scratches steel; the hardness is therefore about 6.

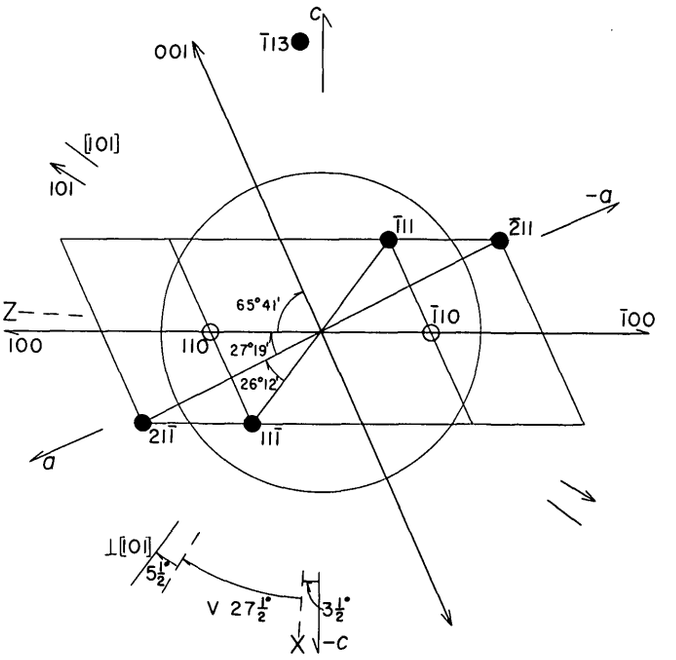

Figure 5.—Optic orientation and morphology of garrelsite in gnomonic projection on (010). Projection constants calculated from cell dimensions reported by Milton, Axelrod, and Grimaldi (1955):

$$p_2=1/(a \sin \beta)=0.69046$$
$$r_2=1/(c \sin \beta)=0.63467$$
$$\mu=180°-\beta=65°\ 41'$$

Only those faces indicated by solid circles or double-barbed arrows were observed.

CORRELATION OF MORPHOLOGY AND STRUCTURE

In their structural study, Ghose and Ulbrich (1972, as modified by communication from Ghose, dated December 15, 1972, addressed to A. Pabst) have adopted the setting implied by the space group symbol $C2/c$, whereas the space group was given in the original description (Milton, Axelrod and Grimaldi, 1955) as Aa or $A2/a$. Thus the a and c axes are interchanged. As the new axes are to be right-handed and also have the angle between the positive ends of the a and c axes obtuse, the transformation matrix becomes $001/0\bar{1}0/100$, the matrix and its inverse being identical in this case.

ACKNOWLEDGMENTS

We are indebted to Subrata Ghose, University of Washington, and to H. H. Ulbrich, formerly of the University of California, Berkeley, for chemical and structural data on Utah garrelsite, prior to publication; to R. C. Erd for unpublished data on the California garrelsite; to D. E. Appleman for

Table 4.—*The observed and calculated 2-circle angles for two crystals of garrelsite*

hkl	Observed		Calculated		Difference of observed and calculated	
	ϕ_2	ρ_2	ϕ_2	ρ_2	ϕ	ρ
Crystal 1 [Mounted to rotate on *b*]						
$(11\bar{1})$	−53°28′	35°51′	−53°26′	35°46′	0°2′	0°5′
$(\bar{2}11)$	[1]162°41′	[2]51°34′	162°41′	51°34′	-------	-------
$(\bar{1}0\bar{1})$	−148°46′	[2]90°00′	−148°32′	90°00′	0°3′	-------
$(00\bar{1})$	−114°16′	[2]90°00′	−114°16′	90°00′	0°3′	-------
(110)	Not observed	Not observed	00°00′	[3]34°37½′	-------	-------
Crystal 2 [Mounted to rotate on [101], which is $\{11\bar{1}\}$ (formerly misdesignated as $\{110\}$), parallel to rotation axis, *b*[4]]						
$(11\bar{3})$[5]	53°11′	56°20′	53°24′	56°12′	0°13′	0°8′

[1] Angle chosen arbitrarily to determine zero point on rotation axis.

[2] Angles used to aline crystal.

[3] Note that the calculated ρ_2 values for (110) and $(11\bar{1})$ differ by only 1°8½′ and that, as shown on the gnomonic projection (fig. 5), the azimuths of these faces referred to the azimuth of $(\bar{2}11)$ differ by only 1°7′; thus the two forms might easily be confused.

[4] Measurement of $(11\bar{1})$ and $(\bar{2}11)$ on six crystals in the same setting as crystal 2 yielded close agreement; mean departures of angles were as follows: $\phi_{(111)}$, 1.9′; $\phi_{(\bar{2}11)}$, 1.25′; $\rho_{(\bar{2}11)}$, 2.75′.

[5] $(11\bar{1})$, $(\bar{2}11)$, $(00\bar{1})$, and $(\bar{1}0\bar{1})$ were also observed on this crystal.

computation of our X-ray powder data; and to Michael Fleischer, R. C. Erd, and Charles L. Christ for critical review. Our garrelsite specimens have been deposited with the U.S. National Museum. This investigation is part of a continuing research program on Green River mineralogy, supported by National Science Foundation Grant GA4433.

REFERENCES CITED

Christ, C. L., 1959, Garrelsite and the datolite structure group: Am. Mineralogist, v. 44, p. 176–177.

Donnay, J. D. H. and Donnay, Gabrielle, eds., 1963, Crystal data determinative tables: Am. Crystallographic Assoc. Mon. 5, p. 2.

Ghose, Subrata, and Ulbrich, Horst H., 1972, The crystal structure of the silicoborate garrelsite, $NaBa_3Si_2B_6O_{13}(OH)_7$ [abs.]: Geol. Soc. America Abs. with Programs, v. 4, no. 7, p. 516

Ghose, S. and Ulbrich H., 1973, The crystal structure of the silicoborate garrelsite, $NaBa_3Si_2B_7O_{16}(OH)_4$: Naturwiss. v. 60, no. 7, 349–350.

Milton, Charles, Axelrod, J. M., and Grimaldi, F. B., 1955, New mineral, garrelsite $(Ba_{0.65}Ca_{0.29}Mg_{0.06})_4H_6Si_2B_6O_{20}$, from the Green River Formation, Utah [abs.]: Geol. Soc. America Bull. v. 66, p. 1597.

Morgan, Vincent, and Erd, R. C., 1969, Minerals of the Kramer borate district, California, Pt. 1: California Div. Mines and Geology Mineral Inf. Service, v. 22, no. 9, p. 143–153; no. 10, p. 165–172.

Strunz, Hugo and Tennyson, C., 1970, Mineralogische Tabellen [5th ed.]: Leipzig, Akademische Verlagsgesellschaft Geest und Portig, 621 p.

Jour. Research U.S. Geol. Survey
Vol. 2, No. 2, Mar.-Apr. 1974, p. 219–232

PHOSPHATIC ZONE IN THE LOWER PART OF THE MAQUOKETA SHALE IN NORTHEASTERN IOWA

by C. ERVIN BROWN, Washington, D.C.

Abstract.—The basal beds of the Maquoketa Shale in northeastern Iowa include a basal silty phosphorite layer that is thickest near Dubuque. In Clayton County, Iowa, the bed averages about 1 foot thick (30 centimeters) and contains 22.5 percent P_2O_5. Phosphatic dolomite that is 8–10 feet (2.4–3 meters) thick and occurs higher in the Maquoketa was observed only in Dubuque County. The thickest and most phosphatic rock in the Maquoketa appears to be coextensive with dark-brown shale, which also occurs mainly in Dubuque County. Rare-earth content of the phosphatic rock decreases southeastward across the area, ranging from 2,000 to about 120 parts per million. The thin low-grade phosphorite is typical of the platform-type phosphorite facies and may be genetically related to the emergence of the Ozark uplift as an island late in the Ordovician period.

The basal beds of the Maquoketa Shale of Late Ordovician age contain phosphatic material along much of the outcrop belt extending from northwestern Illinois to southeastern Minnesota (fig. 1).

During the course of geologic mapping in the vicinity of Dubuque, Iowa (Brown and Whitlow, 1960, and Whitlow and Brown, 1963a), it was noted that the phosphatic zone is thicker and appears to be richer there than elsewhere in the region. The area was revisited in 1964, a few sections were measured, and 14 samples were collected (fig. 2, loc. 1–10) for analysis in order to evaluate the possibility that the phosphatic zone may be economically valuable for fertilizer raw material. Results of this earlier study were reported (Brown, 1966), with the following conclusions:

1. A regionally continuous zone of friable silty phosphorite at the base of the Maquoketa shale has an average thickness of about 2 ft (0.6 m) and an average grade of 15 percent P_2O_5 within about a 4-mi (6.4-km) radius of Dubuque city limits.
2. Dolomite beds as much as 10 ft (3 m) thick in the lower part of the Maquoketa Shale also are phosphatic. Chip samples from these beds contain nearly 17 percent P_2O_5.
3. Although economically marginal in thickness and grade, location of the deposit in a market area, availability of rail, barge, and truck transportation, and proximity to a sulfuric acid plant and superphosphate plant make it potentially commercial as a small-scale operation.

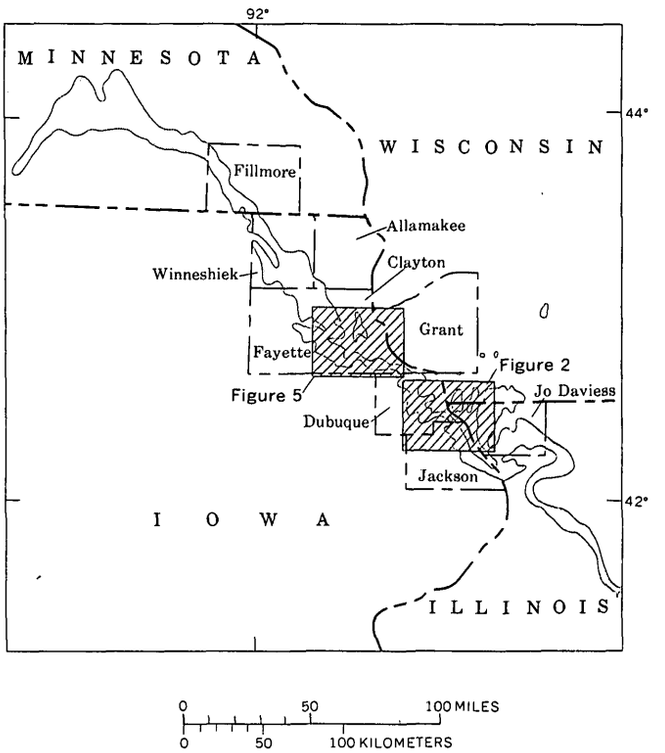

Figure 1.—Index map showing outcrop belt of the Maquoketa Shale (shaded) and counties in the areas of study. Modified from the geologic map of the United States (Stose and Ljungstedt, 1932).

In 1965, the author continued this study in Dubuque, Clayton, and Jackson Counties, Iowa, and in nearby areas of Illinois and Wisconsin. Further research verified the regional continuity of the phosphatic zone at the bottom of the formation and disclosed that deposits in Clayton County, Iowa, are thinner but of higher grade than those near Dubuque. The phosphatic dolomite 20–40 ft (6–12 m) above the base is not continuous and was not seen outside Dubuque County. Spectrographic analyses of bulk samples indicate that the rare-earth content of phosphatic material in Clayton County is also considerably higher than in samples from the vicinity of Dubuque.

The purpose of this report is to summarize the results of the investigation for the entire area of study and to call attention to this submarginal resource of phosphatic material.

GEOLOGIC SETTING

The Middle and Upper Ordovician limestones, dolomites, and shales are thin, relatively flat-lying units that have a regional dip southwestward about 18 ft/mi (3.4 m/km) off the Wisconsin dome.

The regional dip is modified locally by east-trending asymmetric broad warps and small randomly oriented basins and domes having structural relief of 100–200 ft (30–60 m).

Middle and Upper Ordovician rocks are separated by a corrosional disconformity which has associated pyrite and phosphorite and negligible relief. The overlying Silurian dolomites are separated from the Upper Ordovician Maquoketa Shale by an erosional disconformity having more than 100 ft (30 m) of relief.

Topography developed on the southwestward-dipping rocks is cuestaform, the most prominent physiographic feature being a digitate-ridged, dissected escarpment of Silurian dolomite. The underlying Maquoketa Shale comprises mainly poorly indurated dolomitic clay shale and fissile shale that form few outcrops. The topographic surface on the Maquoketa is a smooth gentle slope extending from the escarpment of Silurian dolomite to the bluff-lined stream valleys that are cut in the underlying massive Galena Dolomite of Middle Ordovician age.

The phosphatic zone is in the basal beds of the Maquoketa, and its position can be approximately located by the break in slope at the foot of the long gentle apron cut on the Maquoketa. Because outcrops of the Maquoketa are scarce, it can best be seen at manmade excavations. Trenching is usually necessary to explore the basal phosphatic zone.

STRATIGRAPHY

The Upper Ordovician Maquoketa Shale, as seen on a regional scale in its outcrop belt across northeastern Iowa, is a unit of variable lithology (Ladd, 1929). In contrast, the underlying strata of the Galena Dolomite of Middle Ordovician age are regionally uniform in thickness and appearance. Only the lower part of the Maquoketa is of interest to this study; consequently, the stratigraphic discussion is confined to that part of the section and its immediately adjoining units.

The stratigraphy of the Maquoketa Shale in the outcrop belt across northeastern Iowa was described by Ladd (1929), who also summarized the stratigraphic studies of earlier workers. Agnew (1955) described its subsurface distribution and stratigraphy in Iowa, and Gutstadt (1958) made regional correlations with other Upper Ordovician rocks in the midcontinent region. Brown and Whitlow (1960) described the stratigraphy in the vicinity of Dubuque, Iowa, and Bromberger (1965) studied the mineralogy and petrology of a few exposures of the basal phosphatic beds in northeastern Iowa.

The lateral variability of the Maquoketa Shale was recognized by Ladd (1929), and he described the regional stratigraphy of the formation in two areas separated along an imaginary northeast-trending line extending through southeastern Clayton County, Iowa. The stratigraphy of the Maquoketa Shale in Ladd's (1929) northeastern and southeastern areas, as summarized from older and more recent literature, is shown in figure 3. The Maquoketa Shale in the area southeast of the imaginary line is predominantly shale and was not divided by Ladd. The formation in the area northwest of the line is rather easily divided into four main members, and the ratio of shale to carbonate rocks in the formation there is about 2 to 1.

Dubuque Shaly Member of Galena Dolomite.—Underlying the Maquoketa Shale is the Dubuque Shaly Member of the Galena Dolomite of Middle Ordovician age. This member consists of uniformly bedded carbonate rock in beds a few inches to a few feet thick that are separated by thin shale layers. The carbonate beds grade from limestone to dolomite southeastward across Clayton County. Thicker beds in the lower part grade downward into massive dolomite of the Stewartville Massive Member of the Galena. Beds of the Dubuque Shaly Member are progressively thinner, more impure, and more irregularly bedded toward the top, except in northern Clayton County, where the upper part contains very uniformly bedded limestone.

Except for the change from limestone to dolomite, the Dubuque is amazingly consistent in lithology and thickness throughout the area of study (fig. 4). Templeton and Willman (1963) reported a thickness of 40–45 ft (12–13.5 m) in northern Illinois and progressive thinning to the south. Brown and Whitlow (1960) reported a uniform thickness of 40 ft (12 m) for the member near Dubuque, Iowa. To the northwest in Clayton County, Iowa, Steinhilber, Van Eck, and Feulner (1961) reported a maximum thickness of 50 ft (15 m) although at the only quarry (sec. 9, T. 92 N., R. 5 W.) in which they specified a measured thickness of the entire Dubuque, it has a thickness of 32 ft (9.6 m) (1961, p. 116). Farther northwestward in Fillmore County, Minn., Weiss (1957) reported a thickness of about 34 ft (10.2 m) for the Dubuque. This amounts to an irregular variation in thickness of about 18 ft (5.4 m) in a distance of approximately 130 mi (208 km). Not only is the thickness uniform, but the lithology of well-bedded carbonate and interlayered thin shale partings is also constant throughout. The only major variation is the change from limestone to dolomite southeastward across Clayton County and a slightly increased shaliness of the upper beds in Illinois.

Contact between Galena Dolomite and Maquoketa Shale.—In the area studied, the contact between the Dubuque Shaly Member and the overlying Maquoketa is an abrupt change from dolomite to silty phosphorite. The uppermost Dubuque bed is corrosion pitted and locally perforated. At some exposures the bedding surface has pits only about 2 in. (5 cm) deep; at other places the corrosion effects are greater, but still only inches deep, as at locality 25, half a mile (0.8 km) south of Motor, Iowa, along Turkey River. Here the surface of the

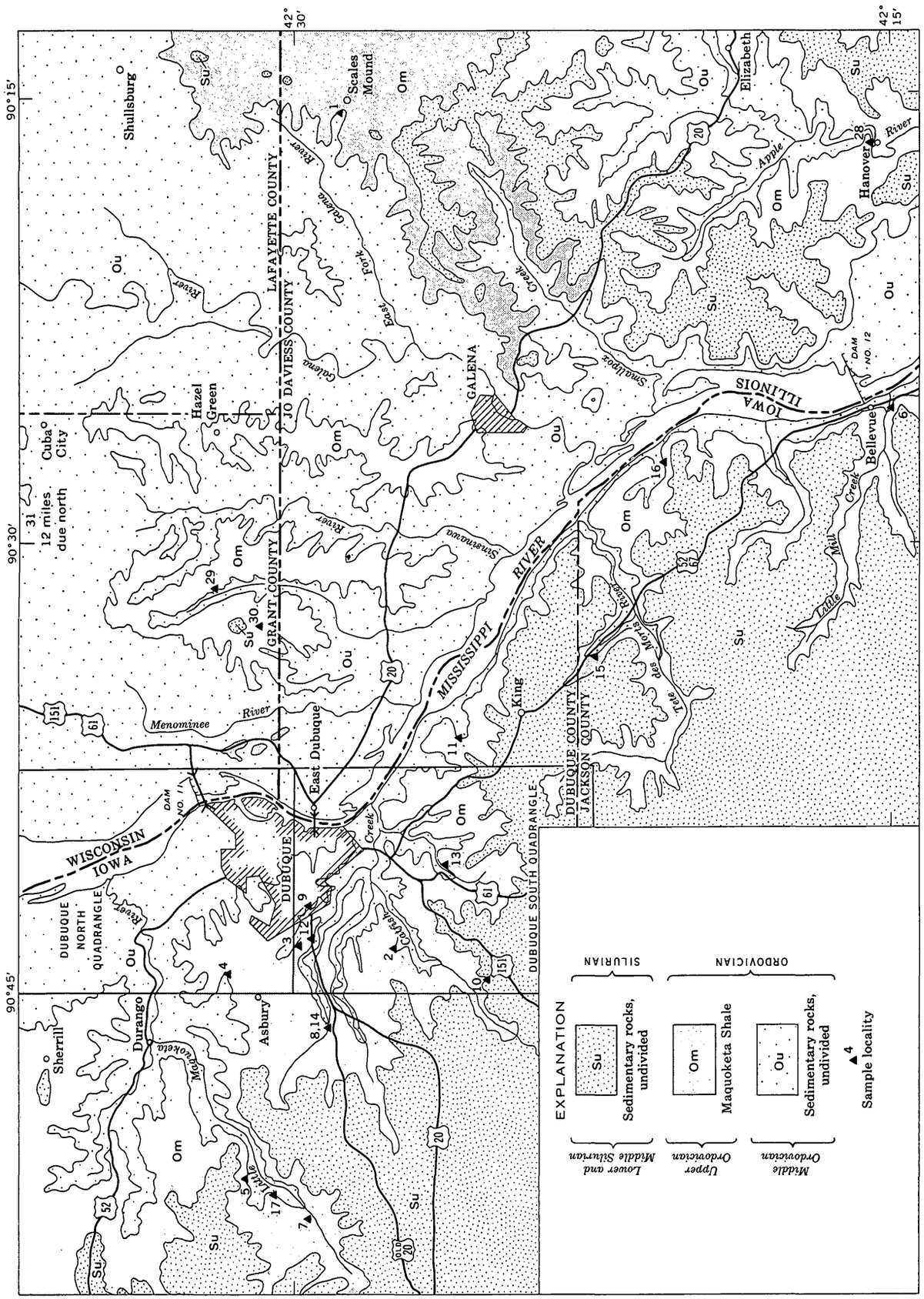

Figure 2.—Generalized geologic map showing the outcrop belt of the Maquoketa Shale and sample localities near Dubuque, Iowa. (Base modified from U.S. Geological Survey 1:250,000 series map, 1962. Geology from Brown, 1966, with additions of new localities.)

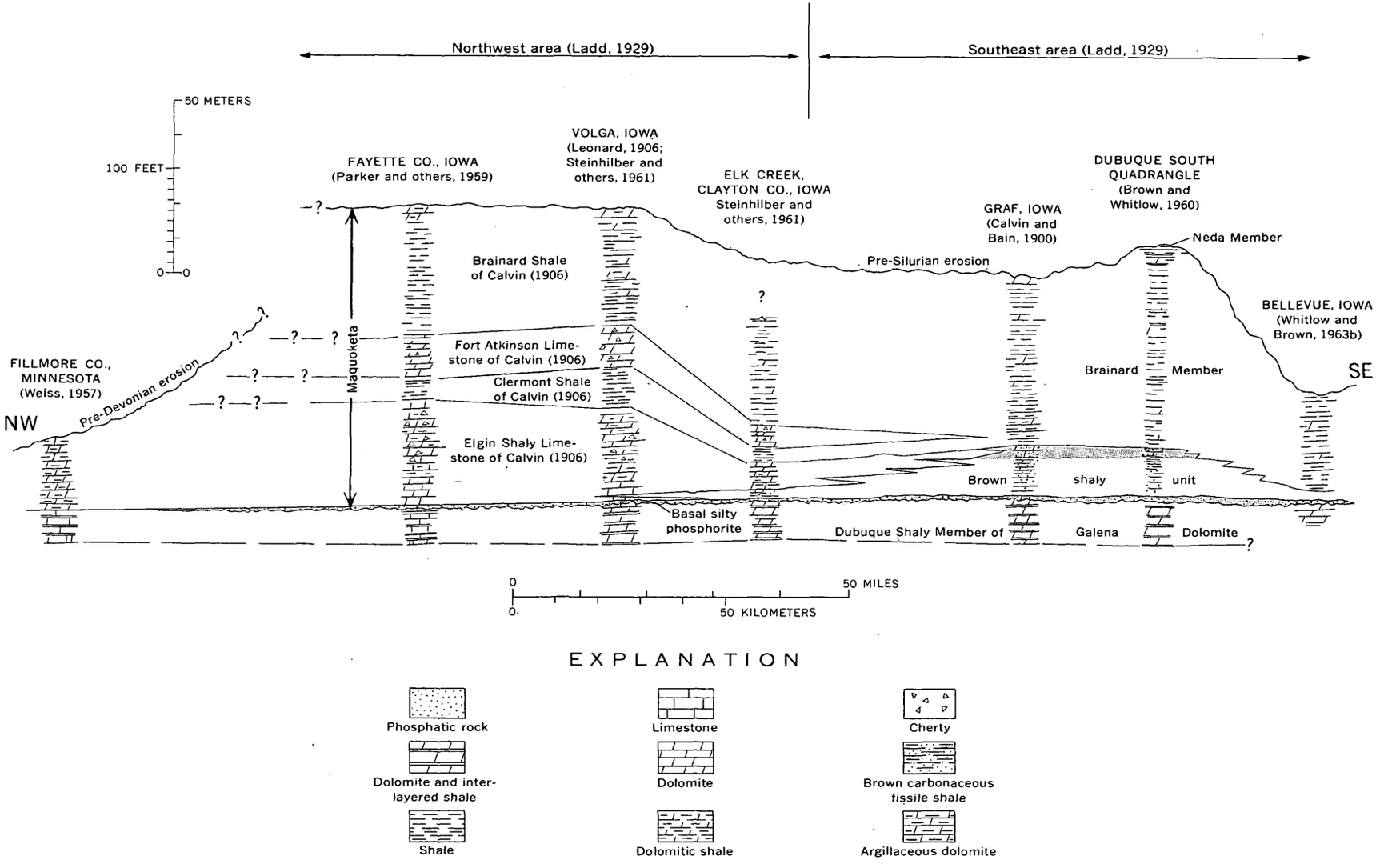

Figure 3.—Stratigraphic diagram showing relations of subdivisions of the Maquoketa Shale southeastward from Fillmore County, Minn., to Bellevue, Jackson County, Iowa.

Figure 4.—Quarry in Dubuque Shaly Member showing even bedding and thin shale partings, 1½ mi (2.4 km) west of Farmersburg, Clayton County, Iowa. SW¼NE¼ sec. 14, T. 94 N., R. 5 W.

uppermost bed of the Dubuque has small pinnacles and ridges as much as 5 in. (12.5 cm) high, and floating in the basal sediment of the Maquoketa are residual pieces of dolomite partly replaced by phosphatic material. A similar phenomenon at Volga, Iowa, was called a corrosion conglomerate by Bromberger (1965). Here (loc. 18, fig. 5) the upper bed locally was also hollowed by corrosion and subsequently filled with dolomite rhombs and phosphatic detritus of the overlying Maquoketa (Brown, 1967, fig. 2). At most places the pitted surface has a crust of iron sulfide and cryptocrystalline phosphatic material. The iron sulfide is commonly disseminated through the upper inch (2.5 cm) of the dolomite and merges with the hard phosphatic crust which is a replacement of the dolomite. The surface of the crust is smooth and is somewhat glossy at fresh exposures. Fine specimens of normal-sized cephalopods, brachipods, and rarely *Flexicalymene* trilobites are also replaced in this crust.

At weathered outcrops the iron sulfide is oxidized, and the phosphatic material weathers free of the dolomite. At an excavation (fig. 2, loc. 9) in the western limit of the city of Dubuque, irregular chunks of the phosphatic crust as much as 2 in. (5 cm) thick and 6 in. (15 cm) square have weathered free and litter the gullies. One analyzed specimen contains 30 percent P_2O_5. The material is iron stained, but on a fresh surface it is a dull grayish brown and fine grained. In thin section the phosphatic material is yellowish brown and appears optically isotropic. It has the X-ray diffraction pattern of apatite and the chemical composition of a carbonate fluorapatite (Brown, 1966).

A specimen of the 2-in. (5 cm)-thick top bed of the Dubuque from Bellevue, Iowa (fig. 2, loc. 6), has a thin irregular and shiny pyritic and phosphatic crust on top but is perforated and hollowed by solution. A mixture of phosphatic fossils, nodules, and pellets as much as half an inch (1.1 cm) across have trickled through these perforations and have filled the hollowed upper bed (fig. 6).

The contact is lithologically abrupt and distinct in the area of study, but to the northwest in Fillmore County, Minn., Weiss (1957, p. 1041) described it as being gradational. He wrote:

> The Dubuque is distinguished from the overlying Maquoketa by the distribution of the detrital fraction in the carbonate. The shale of the Dubuque is almost wholly confined to beds between the limestone layers. * * * In the Maquoketa the clay is uniformly distributed throughout the rock to the extent that bedding planes are scattered and poorly developed. Also, the Maquoketa is dolomitic particularly in the lower part. The change from Dubuque to Maquoketa rock is gradational through a short interval, and the contact is placed at the top of the highest conspicuous shale parting in the succession.

Obviously the sudden change of chemistry and sedimentation processes in the Ordovician sea that produced the corrosion surface and resulted in phosphatic and clastic deposition in northeastern Iowa had little effect on deposition in southeastern Minnesota.

Basal silty phosphorite.—Directly overlying the corroded and phosphate-encrusted top of the Dubuque Shaly Member, over the entire area of study, is the basal silty phosphatic zone known as the depauperate zone because of the small size of the abundant fossils in it (Ladd, 1929). At most places this is a single bed of poorly indurated phosphorite as much as 1.5 ft (0.45 m) thick; locally in Clayton County it is in two thin beds separated by shale or siltstone as at localities 18 and 26 (fig. 5 and table 1). In Dubuque County, from the southern part of Dubuque southeastward to the Tete des Morts River, the phosphorite occurs in two or three thin layers interbedded with clayey silt through as much as 4 ft (1.2 m) of section. The section measured at locality 13 shown on table 1 is typical for that area.

In the Illinois and Wisconsin part of the study area the phosphorite is commonly in two layers separated by as much as 4 ft (1.2 m) of silty shale. Northwest of the area of study near the common corner of Clayton, Fayette, Allamakee, and Winneshiek Counties (fig. 1), the basal fossiliferous phosphatic bed is about 6 in. (15 cm) thick (Ladd, 1929) (H. G. Hershey, written commun., 1965). Ladd reported only about 1 in. (2.5 cm) of depauperate zone exposed in a gully about 4 mi (6.4 km) south of Decorah, in Winneshiek County, Iowa, and 15 mi (24 km) north of Decorah in Fillmore County, Minn., Weiss found no depauperate material (1957, p. 1040) at the contact. As mentioned previously, the contact there is gradational. Apparently Decorah, Iowa, is near the northwestern fringe of basal phosphatic material.

The rock in the basal silty phosphorite consists of phosphatic fossils as much as 1 cm across and irregular smooth-

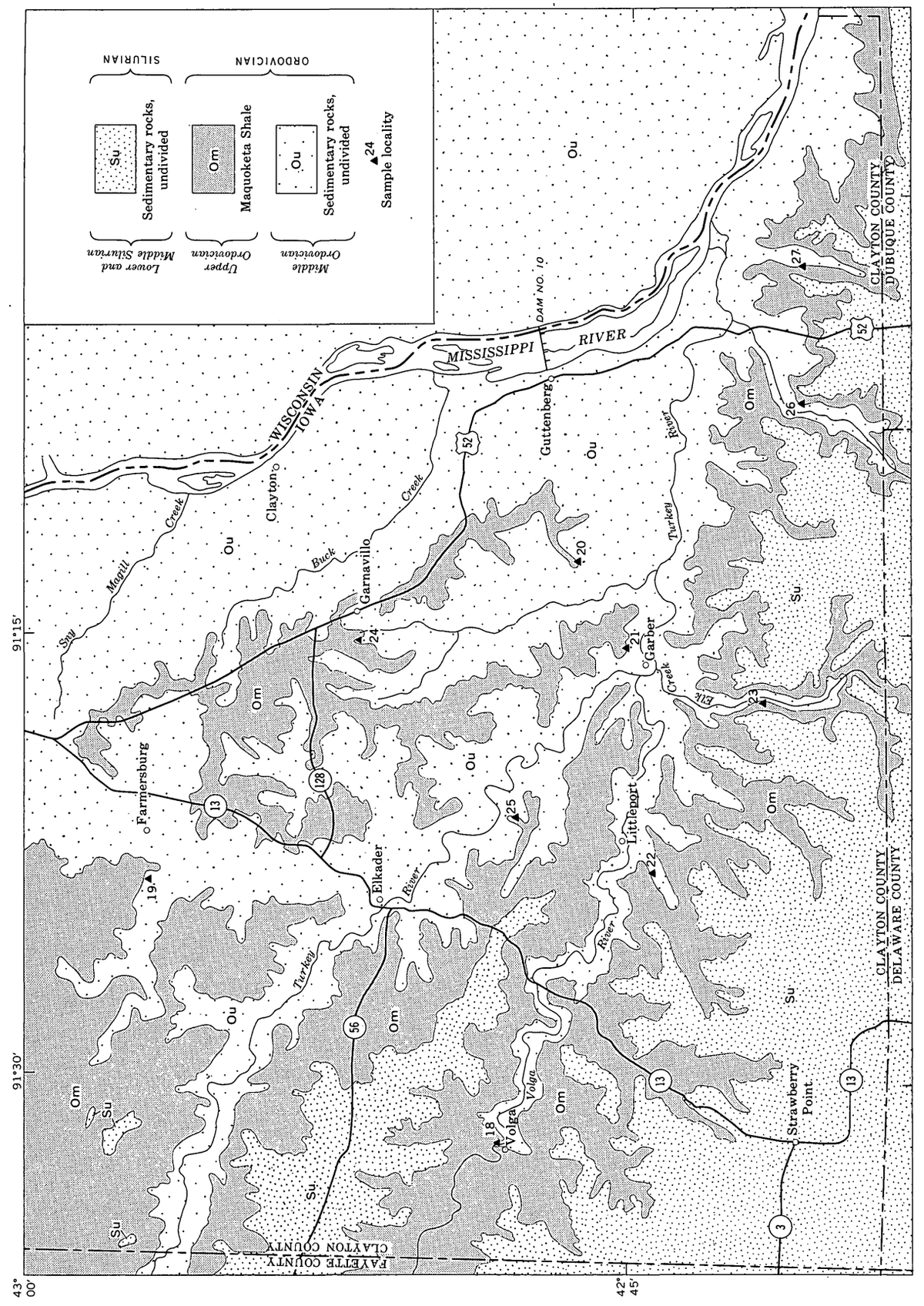

Figure 5.—Generalized geologic map showing the outcrop belt of the Maquoketa Shale and sample localities in Clayton County, Iowa. (Base from Clayton County highway and transportation map, 1964. Geology modified from Steinhilber and others, 1961, and Leonard, 1906.)

surfaced phosphatic nodules as much as several centimeters in largest dimension, set in a matrix of randomly oriented discoidal pellets less than ½ mm across, and clay, silt, and dolomite. The pellets are concentrically banded around cores of minute fossils or comminuted shells (fig. 7*A*). Generally the rock is earthy and friable, although at Bellevue, Iowa (Fig. 2, loc. 6), and at some localities in Clayton County (fig. 7*B*) the rock is moderately well cemented by carbonate. Elsewhere the material is grayish brown and locally has yellowish-gray lenses of clayey silt. A pyritic zone is present in the lower few inches. This zone is ocherstained at most exposures because of the weathering of the pyrite. At many places a second ocher-stained layer is near the top of the basal phosphatic zone, presumably also an oxidized pyritic zone.

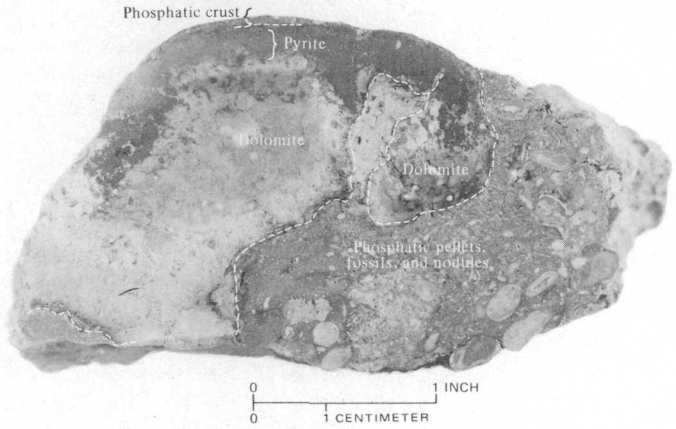

Figure 6.—Polished slab showing corroded top bed of the Dubuque Shaly Member of the Galena Dolomite with cavities filled by phosphatic pellets, fossils, and nodules. Specimen from Bellevue, Iowa (fig. 2, loc. 6).

Brown shaly unit.—In the vicinity of Dubuque County the basal silty phosphatic zone and a second zone of phosphatic dolomite are included in the brown shaly unit (fig. 3) which was described by Brown and Whitlow (1960). The brown shaly unit ranges in thickness from 35 to 50 ft (10.5–15 m) in the Dubuque South quadrangle and averages about 40 ft (12 m). It comprises hard chocolate-brown carbonaceous fissile shale; soft silty carbonaceous brown shale; and, in the upper part, about 10 ft (3 m) of interlayered grayish-orange phosphatic fossiliferous dolomite. Most of these rocks have a strong petroliferous odor when broken and, when churn drilled,

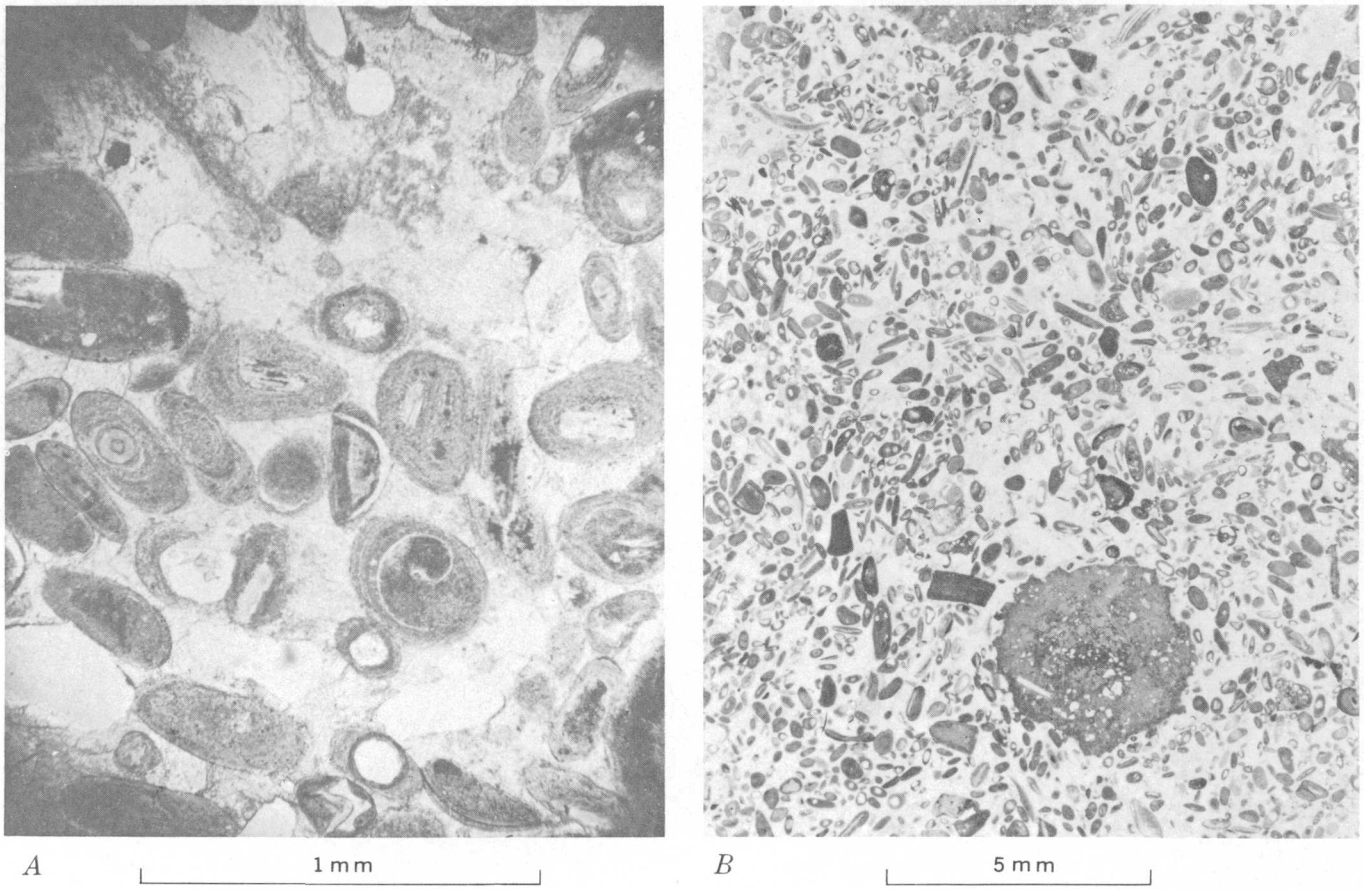

Figure 7.—Photomicrographs of basal silty phosphorite (plain light) near Farmersburg, Iowa (fig. 5, loc. 19). *A*, Concentrically layered phosphatic pellets with nuclei of fossil detritus (enlarged from part of *B*). *B*, Carbonate-cemented phosphorite; cores of many concretions have been plucked during polishing.

commonly produce a dark-brown oily scum on the drilling water. The best exposure of typical rocks of the brown shaly unit is a roadcut at Graf, Iowa. The unit is thickest principally in Dubuque County. To the southeast at Bellevue, Jackson County, Iowa (fig. 2, loc. 6), the brown fissile shale directly overlying the basal phosphatic zone is about 10 ft (3 m) thick, and the dolomite is absent. Seven mi (11.2 km) east of Bellevue, at Hanover, Ill. (fig. 2, loc. 28), there is only about 1.5 ft (0.45 m) of brown fissile shale between the basal phosphatic layers. Twenty mi (32 km) east of Dubuque at Scales Mound, Ill. (Brown, 1966, loc. 1), soft olive-gray to brown shale occurs near the base of the Maquoketa, unlike the hard fissile highly bituminous shale that occurs in Dubuque County. To the northeast near Sinsinawa Mound in Grant County, Wis., about 2 ft (0.6 m) of fissile hard shale occurs in the basal beds, and farther north in Wisconsin, near the Platte Mounds, there is none (Taylor, 1964, p. 303). The fossiliferous grayish-yellow phosphatic dolomite that occurs directly above the brown fissile shale in Dubuque County apparently does not occur in Wisconsin and Illinois. Instead, the basal phosphatic zone is overlain by soft gray silty shale with thin argillaceous limestone layers. Templeton and Willman (1963) reported brown to black shales in northwestern Illinois and also have located another thin zone of depauperate fossils well above the base of the formation.

The carbonaceous brown fissile shale thins abruptly to the northwest in Clayton County, Iowa. The thickest section of brown fissile shale observed by the author in Clayton County is at locality 23 (fig. 5) along Elk Creek, where 7 ft (2.1 m) of this shale occurs above the basal phosphatic bed. The brown shale occurs mainly southeast of Elkader (fig. 5). At Volga, Iowa (fig. 5, loc. 18), less than 1 ft (30 cm) of fissile brown shale occurs. This is the farthest northwest that the fissile-brown-shale lithology was noticed by the author.

The phosphatic dolomite zone in the upper part of the brown shaly unit in Dubuque County consists of about 10 ft (3 m) of yellowish-gray to grayish-orange fossiliferous phosphatic dolomite and thin interlayered silty brown shale. The phosphatic material in the dolomite comprises phosphatized depauperate fauna and many disseminated minute oolitic pellets and nodules. Locally, these beds contain abundant tests of orthoceracone cephalopods. At Graf, Iowa (fig. 2, loc. 7), the cephalopods are jumbled, penetrate each other, and are telescoped together, suggesting strong current or wave action (Miller and Youngquist, 1949). Subsurface studies in the Dubuque South quadrangle (Brown and Whitlow, 1960) show the dolomitic zone at the top of the brown shaly unit in all but the extreme southwest part of the quadrangle. The dolomitic zone was also seen by the author in outcrops near Sherrill, Iowa, in the northern part of Dubuque County.

Elgin Shaly Limestone of Calvin (1906).—In Clayton County, well-bedded slabby yellowish-gray argillaceous limestone of the Elgin Shaly Limestone of Calvin (1906) overlies the basal phosphatic zone and brown shale. The brown shaly unit of Dubuque County is considered to be correlative with and a facies of Calvin's Elgin Shaly Limestone (fig. 3), and the phosphatic dolomite in the upper part probably is a southeast-extending featheredge of the carbonate rocks of the Elgin.

The Elgin Shaly Limestone in Clayton County and adjoining areas to the north and west is a distinct stratigraphic unit with recognizable faunal zones. Its salient features were summarized by Steinhilber, Van Eck, and Feulner (1961, p. 88), as follows:

> The Elgin Limestone Member in Clayton County consists of clayey gray to buff dolomite and shale. It is slightly darker and more clayey to the south and it contains chert to the north. Where not eroded, the minimum observed thickness of the Elgin is 38 feet * * * measured in a stream cut * * * south of Garber; whereas in a well at Postville [southwest corner, Allamakee County], the thickness is 110 feet. The Elgin thins toward the south and east * * *.

The increasing shaliness, darker color, and decreasing thickness of the Elgin southeastward are in keeping with an interfingering relationship with the brown shaly unit.

Other units of the Maquoketa Shale.—Overlying Calvin's Elgin Shaly Limestone in Clayton County are three distinct stratigraphic units, which are, in ascending order, the Clermont Shale, Fort Atkinson Limestone, and Brainard Shale of Calvin (1906) (fig. 3). The lower two units wedge out or lose their identity southeastward, and only the Brainard Shale—a grayish-green, dolomitic, soft silty shale—is recognized overlying the brown shaly unit in Dubuque and Jackson Counties. The sedimentary conditions that produced the southeastward facies change from the Elgin Shaly Limestone to the brown shaly unit and the wedgeout of the Fort Atkinson Limestone and possibly the Clermont Shale in southeastern Clayton County did not affect the deposition of the Brainard, as it appears to blanket the region and is the commonly recognized lithology of the Maquoketa Shale.

The difference in stratigraphic section between the Northwest and Southeast areas of Ladd (1929) is readily apparent in figure 3, as is the association of phosphatic sediments and the carbonaceous brown shale of the brown shaly unit of Brown and Whitlow (1960). Although the basal silty phosphatic zone extends to the south and east beyond the area of the brown shaly unit, it is only a few inches thick in these areas. The area of thick basal phosphorite, that is, greater than 1.5 ft (0.45), is confined to the area covered by the highly organic fissile shale of the brown shaly unit.

SPECULATION ON ORIGIN OF MAQUOKETA PHOSPHORITE

McKelvey (1963) described the origin and environment of deposition of phosphorites. In essence they are as follows:

The solubility of phosphate in sea water increases with decreasing pH and temperature, and therefore it is concentrated in deep cold sea water. These deep phosphate-rich waters are moved by the natural circulating system of the oceans, and sea life flourishes where the waters are forced to upwell by divergence or other means along continental shelves.

In this shallower environment the waters are also warmed, resulting in the deposition of phosphate both inorganically and biochemically. The resulting sediments are phosphorites associated with carbonaceous shales and cherty carbonate rocks. Kazakov (1937) called this rock association the "phosphorite facies." The phosphorite facies are of two types, geosynclinal and platform (Gulbrandsen, 1969, p. 367). The geosynclinal type is the richest and thickest; the platform type is nodular, lean in grade, and shows interrupted sedimentation caused by transgressions and regressions. The basal part of the Maquoketa Shale in northeastern Iowa does not have much chert but otherwise is typical of the platform-type phosphorite facies. Cherty sediments are in this zone to the southwest in Iowa (Agnew, 1955).

Interpretations of the paleoenvironment of the Maquoketa sea have been attempted by many workers (Gutstadt, 1958; Ireland, 1966; Bretsky and Bermingham, 1970, p. 916). This is a difficult task because pre-Devonian erosion has destroyed part of the sedimentary record of the Maquoketa Shale. Nevertheless, a few valid conclusions can be made, as follows:

1. Carbonate sedimentation in southern Minnesota and northwestern Iowa was gradational from the limestone or dolomite and interlayered thin shales of the Galena to the argillaceous dolomite of the Maquoketa (Weiss, 1957; Agnew, 1955). These sediments are the result of slow carbonate deposition in a shallow warm sea bordering probably arid low land to the northwest.
2. Sedimentary deposition in northeastern Iowa changed abruptly at the Galena-Maquoketa contact from well-layered carbonate to marine apatite as a replacement of fossil debris and the carbonate sea floor and as deposition of concretionary pellets and nodules. The accumulation of phosphatic fossil debris of the depauperate zone is a result of a change in physiochemical condition of the sea water and a low supply of clastic materials or a gentle winnowing away of fine clastic materials by currents.
3. The proportion of clastic sediments in the Maquoketa increases, and stratigraphic units thin regularly toward the Ozark uplift to the south (Gutstadt, 1958), indicating that the uplift probably emerged as a positive area at this time and was a locally dominant source of clastic materials. Other structural highs such as the Nemaha uplift and the Wisconsin arch (Gutstadt, 1958, p. 540) apparently had not risen as yet.

Because of these observations, I believe that oscillatory rising of the Ozark uplift was responsible for the clastic sediments that first show up as partings in the Dubuque Shaly Member. Emergence of the Ozark uplift as an island could mark the abrupt change in deposition at the top of the Dubuque in northeastern Iowa. This change might have been brought about because the "Ozark Island" obstructed the normal circulation of waters in the epicontinental sea and produced an upwelling of deep cold nutrient-rich waters into the warm shallow environment of a carbonate shelf.

Gulbrandsen (1969, p. 379–380) discussed optimum conditions for the precipitation of marine apatite. They include a low rate of supply of detritus, low continental runoff, and upwelling cold water with low pH and high content of phosphorus into a shallow continental sea. These conditions appear to have been attained in the Maquoketa sea.

SAMPLING AND ANALYTICAL DATA

Because of the poorly indurated nature of the Maquoketa Shale, few natural exposures exist; consequently, most samples were collected at quarries or roadcuts. Natural outcrops of the zone generally occur only where an accident of erosion, such as a recently slumped creek bank, has exposed the section. These are quickly covered by slumping soil and shale. At most sampling sites, trenching by hand was necessary to expose the contact zone and to produce a clean surface for sampling. All samples from the basal silty zone are from channels 1 in. (2.5 cm) deep and 3 in. (7.5 cm) wide, cut vertically through the beds. The phosphatic dolomite zone in the upper part of the brown shaly unit was not channel sampled, but rather, nearly contiguous chip samples were collected from across the zone.

The lithology, thickness, and P_2O_5 content of the sampled beds are given in tables 1 and 2.

Analyses of 14 samples of phosphatic rock from the vicinity of Dubuque were previously published (Brown, 1966). Additional analyses for major- and minor-element content of the samples are given in tables 3 and 4. The samples were analyzed in laboratories of the U.S. Geological Survey, using X-ray fluorescence supplemented by methods described by Shapiro and Brannock (1962). The minor-element content was determined by semiquantitative spectrographic analysis. Fluorine was determined in 14 of the samples. At two localities, 18 and 13, where the phosphorite occurs in more than one bed, the intervening shale was also analyzed and found to contain only a few percent P_2O_5. The average P_2O_5 content of 11 samples from the basal silty phosphorite in Dubuque and Jackson Counties is 14.5 percent. Eleven samples of the same zone in Clayton County average 22.5 percent P_2O_5. The highest grade sample in Clayton County was collected near Garnavillo (fig. 5, loc. 23), where the phosphorite contains 25.1 percent P_2O_5 and is 1.2 to 1.4 ft (0.36–0.42 m) thick. Both thickness and grade in Clayton County are more uniform than in the vicinity of Dubuque. Unfortunately, the thickness averages only 1.1 ft (0.33 m).

The area having the thickest zone of basal silty phosphorite is along the outcrop belt in Iowa within a radius of 4 mi (6.4 km) of Dubuque. The material here averages 2 ft (0.6 m) thick and contains about 15 percent P_2O_5 (Brown, 1966). Although low in grade, the earthy friable character of this material makes it particularly adaptable for upgrading by washing and screening. It possibly could be recovered in a small-scale operation.

The greatest thickness of phosphatic rock is in the dolomitic zone of the upper part of the brown shaly unit in Dubuque

Table 1.—*Location, lithologic description, and P_2O_5 content of beds in the Maquoketa Shale in the vicinity of Dubuque, Iowa (see figure 2)*

Locality (fig. 2)	Location description	Lithology	Thickness (feet)	Sample	P_2O_5 content (wt percent)
11	Excavation. E¼ cor. sec. 16, T. 88 N., R. 3 E. Dubuque County, Iowa.	Shale, weathered; phosphatic nodules	0.6+		
		Clay, bluish-gray; phosphatic pellets and fossils in thin lenses.	1.4		
		Phosphorite, silty, dark-gray, pelletal, heavily iron stained.	.1		
		Clay, bluish-gray	.9		
		Phosphorite, pelletal and nodular, silty, grayish-yellow; lies on knobby upper surface of Galena Dolomite.	.6	B-65-1	17.48
12	Composite section, roadcut and excavation, NE¼SW¼ sec. 27, T. 89 N., R. 2 E. North of U.S. Route 20, near Center Grove, Dubuque County, Iowa.	Dolomite, yellowish-brown, phosphatic, well-bedded; thin shale partings; overlain by brown shale.	5	B-65-4	11.5
		Shale, fissile, chocolate-brown, carbonaceous	2+		
		Dolomite, yellowish-brown, phosphatic	4	B-65-3	17.2
		Shale, chocolate-brown; fissile, carbonaceous, weathers to bluish gray.	5+		
13	Stream bank, NE¼ SW¼ sec. 13, T. 88 N., R. 2 E. 1,200 ft (360 m) southeast of Granger Creek.	Siltstone, yellowish-brown, weathered, phosphatic nodules in lower part.	.8		
		5. Phosphorite, pelletal, fossiliferous; iron-stained upper part.	.5		
		4. Siltstone, soft, light-brown	.9	B-65-5 (beds 1, 3, 5).	17.4
		3. Phosphorite; fossils with pelletal matrix	.6		
		2. Siltstone, soft, light-brown; scattered phosphatic nodules.	.6	B-65-6 (beds 2, 4).	2.0
		1. Phosphorite, silty, pelletal; iron-stained top and bottom.	.9		
		Irregular top of Galena Dolomite.			
14	Creek bank north of old U.S. Route 20 in SW¼ sec. 29, T. 89 N. R. 2 E., Dubuque County, Iowa. (See loc. 8, Brown, 1966.)	Shale, dolomitic, phosphatic	6	B-64-1	6.1
		Dolomite, yellowish-brown, phosphatic	8.7	B-65-7[1]	[1]14.2
		Shale, fissile, grayish-brown	10+	B-64-6	3.6
15	Gully west of Lux Creek, SE¼ NW¼ sec. 1, T. 87 N., R. 3 E., Jackson County, Iowa.	Clay, yellowish-gray (weathered shale)	3+		
		Phosphorite, dark-gray, pelletal and nodular; iron stained at top.	.3		
		Siltstone, soft, yellowish-gray; thin lenses of phosphatic pellets.	1.4	B-65-8	11.2
		Phosphorite, pelletal, dark-gray, earthy; hard crust on pitted top of Galena Dolomite.	.7		
16	Gully SW¼ sec. 13, T. 87 N., R. 4 E., Jackson County, Iowa.	Clay, grayish-yellow (weathered shale)	4+		
		Phosphorite, pelletal, fossiliferous, iron stained at top; hard crust at bottom attached to pitted surface of Galena Dolomite.	.9	B-65-24	18.71
17	Roadcut NE¼SE¼ sec. 20, T. 89 N., R. 1 E.	Shale, fissile, dark-brown	4+		
		Phosphorite, silty, fossiliferous, pelletal; overlies irregular top surface of Galena Dolomite.	1.5	B-65-26	11.0
28	Hanover, Jo Daviess County, Ill., outcrop on right bank at dam.	Shale, brown, soft; green clay above	2+		
		Phosphorite, fossiliferous, pelletal; lower third of bed is brown silty dolomite. Contact between is very irregular	.7	B-65-28	11.0
		Shale, soft, fissile, brown	1.4		
		Phosphorite, pelletal, iron-stained	.1		
		Top of Galena Dolomite.			
		Dolomite, wavy-bedded	15		
29	Northeast of Sinsinawa Mound, stream bottom, SW¼SW¼ sec. 20, T 1 N., R. 1 W., Grant County, Wis.	Phosphorite, pelletal and nodular, iron-stained	.3		
		Dolomite, silty, brownish-gray, hard; phosphatic nodules embedded in bottom part.	.5	B-65-30 (only phosphorite beds included).	10.8
		Phosphorite, silty, fossiliferous and pelletal	.4		
		Shale, dark-brown, fissile	1+		
30	Road ditch 0.5 mile south of Sinsinawa Mound, Grant County, Wis. E¼ cor., sec. 36, T. 1 N., R 2 W.	Shale, brown, weathered to yellowish clay	2+		
		Phosphorite, clayey, pelletal and nodular, iron stained on top.	.7	B-65-32	16.85

[1] Careful resampling of section represented by sample B-64-3 (Brown, 1966).

Table 2.—*Location, lithologic description, and P_2O_5 content of basal beds of the Maquoketa Shale in Clayton County, Iowa (fig. 5)*

Locality (fig.5)	Location description	Lithology	Thickness (feet)	Sample	P_2O_5 content (wt percent)
18	Outcrop left bank of Volga River above abandoned damsite Volga, Iowa, SE¼SW¼ sec. 3, T. 92 N., R. 6 W. (see Brown 1967, Fig. 3)	Dolomite, buff to gray, argillaceous, locally cherty; shale partings.	20+		
		Siltstone, limy, weathers to gray	1.1		
		Limestone, dolomitic, hard yellowish-gray	.5		
		Shale, fissile, brown	.3		
		3. Phosphorite, dark-brown, dolomitic, pelletal	.4	B-65-11	21.2
		2. Shale, laminated, silty, phosphatic and dolomitic.		(beds 1	
		1. Phosphorite, brown, dolomitic, pelletal; fluorite-lined vugs in bottom layer on pitted Galena Dolomite surface.	.7 .6	and 3) B-65-12	3.8
19	Roadcut 1.5 mi. west of Farmersburg, Iowa, SE¼NE¼ sec.14, T. 94 N., R. 5 W.	Limestone, grayish-yellow, slabby	1+		
		Clay, sticky, grayish-yellow to brown	.8		
		Phosphorite, pelletal, fossiliferous and nodular; lower 3 in. is well indurated; lies on irregular upper surface of Galena Dolomite.	1.2	B-65-13	21.4
20	New roadcut NW¼ sec. 21, T. 92 N., R. 3 W.	Clay, brown (weathered shale and dolomite)	15+		
		Phosphorite, nodular with pelletal matrix, dark-brown; lies on irregular top of Galena Dolomite.	.8	B-65-15	24.8
21	New roadcut, SW¼SE¼ sec. 25, T. 92 N., R. 4 W.	Shale, brown, finely laminated	5+		
		Silt and clay, unindurated	.3		
		Phosphorite, dark-grayish-brown, pelletal, locally hard and well indurated; lies on knobby upper surface of Galena Dolomite.	.7	B-61-16	21.9
22	Quarry 1 mile southwest of Littleport, Iowa, SW¼SW¼ sec. 25, T. 92 N., R. 5 W.	Siltstone, silty dolomite, shale and cherty dolomite.	12+		
		Shale, dark-brown, fissile	3.4		
		Phosphorite, dolomitic, pelletal, dark-brown	.8		
		Phosphorite, hard, nodular; fills deeply pitted surface of Galena Dolomite.	0 to 0.2	B-65-17	24.0
23	Roadcut along west side of Elk Creek valley, SW¼ sec.14, T. 91 N., R. 4 W.	Dolomite, yellowish-brown	3+		
		Shale, brown, fissile	7		
		Phosphorite, dark-brown, pelletal; indurated in bottom 3 in.	0.9 to 1.1	B-65-18	22.1
		Top surface of Galena Dolomite has 0.2-ft-deep pits.			
24	Roadcut 1 mile west of Garnavillo, NE¼NE¼ sec. 3, T. 93 N., R. 4 W.	Shale, yellowish-brown, weathered	2+		
		Phosphorite, pelletal, dark-brown; many coarse nodules.	1.0		
		Phosphorite, hard, nodular; fills pits in surface of Galena Dolomite.	0.2 to 0.4	B-65-19	25.1
25	Quarry along county road south of Turkey River, NW¼NE¼ sec. 7, T. 92 N., R. 4 W.	Dolomite, silty; and yellowish-brown dolomitic siltstone.	10		
		Shale, brown, fissile; phosphatic nodules near bottom.	4.4		
		Phosphorite, pelletal, nodular and fossiliferous; upper part well indurated; iron stained at top and middle.	1.1		
		Phosphorite, nodular; fills pits and replaces isolated remnants of Galena Dolomite; very irregular top surface on Galena.	0.4 to 0.5	B-65-20	19.7
26	Gully outcrop east side of Little Turkey River valley, SW¼ NE¼ sec. 30, T. 91 N., R. 2 W.	Siltstone, limy, gray, wavy-bedded	20+		
		Dolomite, argillaceous, brown	3		
		Phosphorite, shaly, dark-brown, fossiliferous	.5	B-65-22	22.0
		Shale, chocolate-brown, fissile	1.1		
		Phosphorite, silty, pelletal; iron stained on top; hard lumpy nodular material fills pits in Galena Dolomite surface.	0.7 to 0.8	B-65-21	16.87
27	Quarry west side of Bluebell Creek SW¼SW¼ sec. 24, T. 91 N., R. 2 W.	Shale, brown, fissile, weathered	3+		
		Phosphorite, soft and pelletal; also thin, hard, and nodular layers; lies on knobby surface of Galena Dolomite.	1.0	B-65-23	18.2

Table 3.—*Analyses of phosphatic rock from the Maquoketa Shale in Clayton County, Iowa*

[Rapid rock analyses by Paul Elmore, Sam Botts, Lowell Artis, John Glenn, H. Smith, G. Chloe, P. Taylor, and S. M. Berthold. Fluorine determinations by Joseph Budinsky. Semiquantitative spectrographic analyses by J. L. Harris for minor elements and for major elements (not oxides) where values are shown in parentheses. Spectrographic analyses are reported to the nearest number in the series 1, 0.7, 0.5, 0.3, 0.2, 0.15, 0.1, and so forth, which represent approximate midpoints of group data on a geometric scale. The assigned group for semiquantitative results will include the quantitative value about 30 percent of the time. Elements looked for, but not detected: As, Au, Bi, Cd, Dy, Er, Eu, Gd, Ge, Hf, Hg, Ho, In, Li, Lu, Nb, Pd, Pr, Pt, Re, Sb, Sm, Sn, Ta, Tb, Te, Th, Tl, Tm, U, W, and Zn. N.d., not determined; M, major constituent > 10 percent]

Locality (fig.5)	18		19	20	21	22	23	24	25	26		27
Laboratory No.	W165668	W165676	W165669	165992	165993	165994	165995	165996	W165670	165997	165998	W165671
Sample	65-11	65-12	65-13	65-15	65-16	65-17	65-18	65-19	65-20	65-21	65-22	65-23
Major constituents (in weight percent)												
SiO_2	5.5	45.8	5.9	(5)	(3)	(2)	(3)	(5)	10.8	(3)	(2)	22.3
Al_2O_3	1.2	7.0	1.7	(2)	(1.5)	(1)	(2)	(2)	2.5	(2)	(1.5)	6.6
Fe_2O_3	1.5	.79	1.4	(2)	(3)	(2)	(5)	(3)	3.6	(2)	(1)	6.5
FeO	.20	.92	.56						.26			.20
MgO	1.2	5.8	1.0	(.3)	(3)	(1)	(1.5)	(.3)	5.4	(3)	(3)	2.6
CaO	47.0	15.1	47.5	M	M	M	M	M	38.7	M	M	30.7
Na_2O	.24	.14	.22	(.3)	(.2)	(.2)	(.2)	(3)	.23	(.2)	(.3)	.24
K_2O	.45	3.4	.50	(1)	(1)	(.7)	(.7)	(1)	.93	(1.5)	(.7)	2.0
H_2O-	.43	.42	1.1	N.d.	N.d.	N.d.	N.d.	N.d.	.63	N.d.	N.d.	2.4
H_2O+	.87	2.0	.50	N.d.	N.d.	N.d.	N.d.	N.d.	1.3	N.d.	N.d.	1.4
TiO_2	.12	.53	.12	(.05)	(.05)	(.05)	(.07)	(.07)	.18	(.07)	(.05)	.35
P_2O_5	21.2	3.8	21.4	24.8	21.9	24.0	22.1	25.1	19.7	16.87	22.0	18.2
MnO	.05	.19	.06	(.03)	(.03)	(.007)	(.02)	(.03)	.06	(.02)	(.01)	.06
CO_2	17.2	12.0	16.7	N.d.	N.d.	N.d.	N.d.	N.d.	14.2	N.d.	N.d.	5.8
F	1.95	.62	1.97	N.d.	N.d.	N.d.	N.d.	N.d.	1.80	N.d.	N.d.	1.18
SO_3	2.9	1.1	.54	N.d.	N.d.	N.d.	N.d.	N.d.	.34	N.d.	N.d.	.35
Total	102.01	99.61	101.17						100.63			100.88
Minor elements (in weight percent)												
Ag	0	0	0	0	0	0	0	0	0	0	0	0
B	0	.003	0	0	0	0	0	0	0	0	0	0
Ba	.01	.02	.01	.03	.3	.01	.3	.02	.01	.015	.01	.02
Be	0	0	0	0	0	0	0	0	0	0	0	0
Ce	.03	0	.05	.05	.05	.07	.07	.07	.05	.05	.07	.05
Co	0	0	0	.0005	0	0	0	0	0	.0003	0	.0007
Cr	.003	.005	.003	.007	.005	.003	.003	.007	.003	.005	.005	.005
Cu	.002	.002	.015	.005	.007	.003	.01	.001	.007	.007	.01	.01
Ga	0	.0007	.0001	.0005	.0003	.001	.0002	.0007	.0001	.0005	.00015	.0007
La	.03	.007	.05	.015	.03	.05	.05	.05	.03	.02	.05	.02
Mo	0	0	0	0	.0003	.0003	.0005	.0005	0	0	0	.0007
Nd	.03	0	.05	0	0	0	0	0	.03	0	0	.02
Ni	.003	.003	.003	.005	.005	.003	.007	.007	.003	.003	.003	.005
Pb	.0005	.0005	.003	.005	.003	.002	.007	.005	.005	.003	.003	.015
Sc	.0007	.0005	.0007	.001	.001	.0007	.001	.001	.0007	.0007	.0007	.0007
Sr	.15	.05	.15	.07	.05	.07	.07	.05	.07	.03	.1	.05
V	.001	.003	.002	.003	.002	.0015	.0015	.005	.002	.002	.002	.005
Y	.03	.007	.05	.05	.03	.05	.03	.03	.03	.02	.03	.02
Yb	.0015	.0005	.0002	.002	.0015	.002	.002	.002	.0015	.0007	.0015	.0007
Zr	.0005	.015	.001	.003	.007	.002	.003	.005	.001	.002	.002	.005

County. Samples of this rock contain about 14 percent P_2O_5 with thicknesses of 8–10 ft (2.4–3 m). However, carbonate content is objectionable in the present methods of phosphate-rock treatment because excess acid is consumed.

Rare earths and other minor elements.—About 20 elements were detected in minor quantities by semiquantitative spectrographic analyses in most of the samples. Strontium, barium, cerium, copper, and lanthanum are most abundant.

The rare-earth content of the phosphatic rocks is higher in Clayton County than to the southeast and appears to decrease uniformly from northwest to southeast. Samples in Clayton County contain 900 to about 2,000 p/m combined lanthanum, cerium, neodymium, scandium, yttrium, and ytterbium. The greatest amount is in the material at Farmersburg, locality 19, which contains more than 2,000 p/m. In the vicinity of Dubuque, samples contain about 120–850 p/m, and neodymium, which was found in four samples in Clayton County, has not been detected here. The sample from Hanover, Ill., locality 28, has the smallest rare-earth content, with only 127 p/m. It is possibly coincidental that the highest and lowest

Table 4.—*Analyses of phosphatic rock from the Maquoketa Shale in the vicinity of Dubuque, Iowa*

[Rapid rock analyses by Paul Elmore, Sam Botts, Lowell Artis, John Glenn, H. Smith, G. Chloe, P. Taylor, and S. M. Berthold, Fluorine determinations by Joseph Budinsky. Semiquantitative spectrographic analyses by J. L. Harris for minor elements and for major elements (not oxides) where values are shown in parentheses. Spectrographic analyses are reported to the nearest number in the series 1, 0.7, 0.5, 0.3, 0.2, 0.15, 0.1, and so forth, which represent approximate midpoints of group data on a geometric scale. The assigned group for semiquantitative results will include the quantitative value about 30 percent of the time. Elements looked for, but not detected: As, Au, Bi, Cd, Cy, Er, Eu, Gd, Ge, Hf, Hg, Ho, In, Li, Lu, Nb, Pd, Pr, Pt, Re, Sb, Sm, Sn, Ta, Tb, Te, Th, Tl, Tm, U, W, and Zn. Nd., not determined; M, major constituent >10 percent]

Locality (fig.2)	11	12		13		14	15	16	17	31	28	29	30
Laboratory No.	W165991	W165663	W165664	W165666	W165675	W165665	W165667	W165999	W165672	W166619[1]	W165673	W165674	W166001
Sample	65-1	65-3	65-4	65-5	65-6	65-7	65-8	65-24	65-26	65-50	65-28	65-30	65-32
Major constituents (in weight percent)													
SiO_2	(5)	12.2	18.2	17.8	35.3	10.8	21.4	(7)	25.7	(3)	10.08	24.0	(3)
Al_2O_3	(3)	1.8	2.6	5.4	10.9	1.8	6.6	(5)	6.4	(1)	3.4	7.1	(2)
Fe_2O_3 } FeO	(3)	1.6 / .12	1.9 / .28	4.7 / .28	2.5 / .52	1.3 / .18	5.5 / .40	(7)	5.5 / .20	(1.5)	4.1 / .48	4.9 / .60	(2)
MgO	(3)	8.4	9.0	5.2	9.1	10.2	7.2	(.7)	5.7	(.3)	12.2	6.5	(3)
CaO	M	36.0	30.0	31.0	14.1	35.0	26.0	M	25.2	M	29.0	23.6	M
Na_2O	(.2)	.22	.18	.24	.18	.18	.21	(.3)	.12	(.2)	.16	.22	(.15)
K_2O	(1.5)	.62	1.1	2.0	3.9	.68	2.3	(2)	2.4	(0)	1.0	2.4	(1)
H_2O^-	N.d.	.57	.45	.91	1.3	.48	1.0	N.d.	1.0	N.d.	.61	.84	(.07)
H_2O+	N.d.	.73	1.0	1.9	2.0	1.2	1.9	N.d.	2.1	N.d.	1.4	2.4	N.d.
TiO_2	(.07)	.12	.20	.31	.63	.15	.40	(1.5)	.39	(.05)	.23	.47	N.d.
P_2O_5	17.48	17.2	11.5	17.4	2.0	14.2	11.2	18.71	11.0	M	11.0	10.8	16.85
MnO	(.03)	.08	.08	.07	.07	.08	.08	(.05)	.08	(0)	.12	.07	(.07)
CO_2	N.d.	18.7	21.9	11.1	16.9	22.7	15.4	N.d.	12.9	N.d.	24.2	14.4	N.d.
F	N.d.	1.65	1.08	1.40	.32	1.37	.78	N.d.	.88	N.d.	.80	.72	N.d.
SO_3	N.d.	.24	.15	.33	.03	.22	.25	N.d.	.37	N.d.	.73	.65	N.d.
Total		100.25	99.62	100.04	99.75	100.54	100.62		99.94		100.51	99.67	
Minor elements (in weight percent)													
Ag	0	0	0	0	0	0	0	.00015	0	0	0	0	0
B	0	0	0	0	.007	0	0	0	0	0	0	0	0
Ba	.03	.015	.01	.02	.02	.007	.02	.03	.02	.015	.015	.02	.03
Be	0	0	0	0	.0001	0	0	0	0	0	0	0	0
Ce	.05	.05	0	.03	0	0	.03	.05	.03	.07	0	.03	.03
Co	.0005	0	0	.0007	0	0	.001	.003	0	0	0	.0007	.0015
Cr	.007	.003	.003	.007	.007	.002	.007	.01	.005	.0015	.007	.007	.003
Cu	.005	.005	.005	.005	.002	.003	.003	.007	.005	.01	.005	.003	.007
Ga	.0005	.0001	.0001	.0005	.001	.0001	.0007	.001	.0007	0	.0003	.0007	.0003
La	.015	.02	.007	.01	0	.007	.01	.015	.01	.03	.007	.01	.015
Mo	0	0	0	.0003	0	0	.0003	.0005	.0007	0	0	.0003	.0003
Nd	0	0	0	0	0	0	0	0	0	0	0	0	0
Ni	.005	0	0	.005	.003	0	.005	.01	.005	.003	.003	.003	.007
Pb	.005	.003	.003	.015	.002	.02	.007	.015	.005	.015	.007	.007	.003
Sc	.001	0	0	.0007	.0007	0	.0007	.0015	.0007	.0007	.0005	.0007	.0007
Sr	.05	.05	.02	.05	.01	.05	.03	.03	.03	.1	.02	.03	.03
V	.002	.0015	.0015	.003	.005	.001	.003	.007	.003	.003	.001	.003	.0015
Y	.015	.03	.01	.015	.0015	.01	.01	.02	.01	.03	.005	.007	.015
Yb	.0007	.001	.0005	.0005	.00015	.0005	.0005	.0007	.0005	.001	.0002	.0003	.0007
Zr	.003	.0005	.001	.003	.005	.0003	.003	.01	.003	.002	.0007	.003	.002

[1] Specimen of phosphatic pellets and fossils from near Belmont Mound, Wis.

values are from the extreme northwest and southeast sample localities, but other values verify the decrease southeastward.

SUMMARY OF CONCLUSIONS

The phosphatic zone in the basal beds of the Maquoketa Shale overlies the corrosion-pitted surface of the Galena Dolomite. This surface is a result of an abrupt physicochemical change in the marine environment. The corrosional disconformity and associated phosphatic sediment extends southeastward from near the Minnesota-Iowa line. In Minnesota the contact is gradational and difficult to identify.

The phosphatic zone at the base of the Maquoketa Shale is thin and of low grade. The area where the deposit is thickest is in Iowa within a radius of about 4 mi (6.4 km) of Dubuque. A strip 100 ft (30 m) wide, along the outcrop belt in this area is estimated to contain 9 million short tons (8.1 million tonnes) of rock containing 15 percent P_2O_5 (Brown, 1966). The same zone in Clayton County is more uniform in thickness and

grade. Samples there average 22.5 percent P_2O_5, but the average thickness is only about 1 ft (30 cm) and therefore mainly of academic interest.

Rare-earth content of the basal phosphorite in Clayton County is as much as 2,000 p/m. The content decreases sharply to the southeast, and the lowest determined value is about 120 p/m at Hanover, Ill.

The thickest deposits near Dubuque are possibly minable, particularly if done as a small operation supplying raw material to a local plant, because of their location in a farming area and because of the availability of transportation by highway, railroad, and barge. A sulfuric acid plant 1 mi (1.6 km) south of Dubuque and a superphosphate plant, presently using rock barged from Florida, are additional advantages in using locally available phosphatic raw material. A large-scale mining operation is unlikely, however, because the land near Dubuque is principally utilized for farms and residences and would not warrant disruption for the recovery of a submarginal resource.

REFERENCES CITED

Agnew, A. F., 1955, Facies of Middle and Upper Ordovician strata in Iowa: Am. Assoc. Petroleum Geologists Bull., v. 39, no. 9, p. 1703–1752.

Bretsky, P. W., and Bermingham, J. J., 1970, Ecology of the Paleozoic scaphopod genus *Plagioglypta* with special reference to the Ordovician of eastern Iowa: Jour. Paleontology, v. 44, no. 5, p. 908–924.

Bromberger, S. H., 1965, Mineralogy and petrology of basal Maquoketa (Ordovician) phosphatic beds, Iowa: Ames, Iowa., State Univ., M.S. thesis.

Brown, C. E., 1966, Phosphate deposits in the basal beds of the Maquoketa Shale near Dubuque, Iowa, *in* Geological Survey research 1966: U.S. Geol. Survey Prof. Paper 550-B, p. B152–B158.

—— 1967, Fluorite in crystal-lined vugs in the Maquoketa Shale at Volga, Clayton County, Iowa: Am. Mineralogist, v. 52, nos. 11-12, p. 1735–1750.

Brown, C. E., and Whitlow, J. W., 1960, Geology of the Dubuque South quadrangle, Iowa-Illinois: U.S. Geol. Survey Bull. 1123-A, 93, p.

Calvin, Samuel, 1906, Geology of Winneshiek County [Iowa]: Iowa Geol. Survey Ann. Rept., v. 16, p. 39–146.

Calvin, Samuel, and Bain, H. F., 1900, Geology of Dubuque County [Iowa]: Iowa Geol. Survey Ann. Rept., v. 10, p. 379–622.

Gulbrandsen, R. A., 1969, Physical and chemical factors in the formation of marine apatite: Econ. Geology, v. 64, no. 4, p. 365–382.

Gutstadt, A. M., 1958, Upper Ordovician stratigraphy in eastern interior region: Am. Assoc. Petroleum Geologists Bull., v. 42, no. 3, p. 513–547.

Ireland, H. A., 1966, Résumé and setting of Middle and Upper Ordovician stratigraphy, midcontinent and adjacent regions: Tulsa Geol. Soc. Digest, v. 34, p. 26–40.

Kazakov, A. V., 1937, [The phosphorite facies and genesis of phosphorites], *in* Kazakov, A. V., ed., [Agronomical ores of USSR, vol. III, pt. 1]: Leningrad, [Sci. Inst. Fertilizers and Insecto-Fungicides Trans.], no. 142, p. 95–113 (in Russian).

Ladd, H. S., 1929, The stratigraphy and paleontology of the Maquoketa Shale of Iowa: Iowa Geol. Survey Ann. Rept., v. 34, p. 305–448.

Leonard, A. G., 1906, Geology of Clayton County [Iowa]: Iowa Geol. Survey Ann. Rept., v. 16, p. 213–307.

McKelvey, V. E., 1963, Successful new techniques in prospecting for phosphate deposits, *in* Natural resources–minerals and mining, mapping and geodetic control–United Nations Conf. Application Sci. and Technology Benefit Less Developed Areas, Geneva, 1963, U.S. Papers, v. 2: Washington, D.C., U.S. Dept. State, p. 163–172.

Miller, A. K., and Youngquist, W. L., 1949, The Maquoketa coquina of cephalopods: Jour. Paleontology, v. 23, no. 2, p. 199–204.

Mullens, T. E., 1964, Geology of the Cuba City, New Diggings, and Shullsburg quadrangles, Wisconsin and Illinois: U.S. Geol. Survey Bull. 1123–H, p. 437–531.

Parker, M.C., Dorheim, F. H., and Campbell, R. B., 1959, Resolving discrepancies between subsurface studies of the Maquoketa Formation of northeast Iowa: Iowa Acad. Sci. Proc. 1959, v. 66, p. 248–256.

Shapiro, Leonard, and Brannock, W. W., 1962, Rapid analysis of silicate, carbonate, and phosphate rocks: U.S. Geol. Survey Bull. 1144-A, 56 p.

Shaw, E. W., and Trowbridge, A. C., 1916, Description of the Galena-Elizabeth quadrangles [Illinois-Iowa]: U.S. Geol. Survey Geol. Atlas, Folio 200, 13 p.

Steinhilber, W. L., Van Eck, O. J., and Feulner, A. J., 1961, Geology and ground-water resources of Clayton County, Iowa: Iowa Geol. Survey Water-Supply Bull. 7, 142 p.

Stose, G. W., and Ljungstedt, O. A., 1932, Geologic map of the United States: U.S. Geol. Survey, scale 1:2,500,000.

Taylor, A. R., 1964, Geology of the Rewey and Mifflin quadrangles, Wisconsin: U.S. Geol. Survey Bull. 1123-F, p. 279–360.

Templeton, J. S., and Willman, H. B., 1963, Champlainian Series (Middle Ordovician) in Illinois: Illinois Geol. Survey Bull. 89, 260 p.

Weiss, M. P., 1957, Upper Middle Ordovician stratigraphy of Fillmore County, Minnesota: Geol. Soc. America Bull., v. 68, no. 8, p. 1027–1062.

Whitlow, J. W., and Brown, C. E., 1963a, Geology of the Dubuque North quadrangle, Iowa-Wisconsin-Illinois: U.S. Geol. Survey Bull. 1123-C, p. 139–168.

—— 1963b, The Ordovician-Silurian contact in Dubuque County, Iowa, *in* Short papers in geology and hydrology: U.S. Geol. Survey Prof. Paper 475–C, p. C11–C13.

Whitlow, J. W., and West, W. S., 1966, Geologic map of the Kieler quadrangle, Grant County, Wisconsin, and Jo Daviess County, Illinois: U.S. Geol. Survey Geol. Quad. Map GQ-487.

Jour. Research U.S. Geol. Survey
Vol. 2, No. 2, Mar.-Apr. 1974, p. 233–248

WATEQ, A COMPUTER PROGRAM FOR CALCULATING CHEMICAL EQUILIBRIA OF NATURAL WATERS

By ALFRED H. TRUESDELL and BLAIR F. JONES,
Menlo Park, Calif., Washington, D.C.

Abstract.—The computer program, WATEQ, calculates the equilibrium distribution of inorganic aqueous species of major and important minor elements in natural waters using the chemical analysis and *in situ* measurements of temperature, pH, and redox potential. From this model, the states of reaction of the water with solid and gaseous phases are calculated. Thermodynamic stabilities of aqueous species, minerals, and gases have been selected from a careful consideration of all available experimental data. The program is written in PL-1 for IBM 360 computers.

The chemistry of water-rock interactions is determined in part by possible reactions with regard to the states of the water (undersaturated or supersaturated with respect to a solid phase or to a gas at a certain pressure). The reaction states may be calculated from an equilibrium chemical model of the water and from the stabilities of phases with which it may react. The examination of reaction states may suggest the origin of dissolved constituents and assist in the prediction of the chemical effects of ground-water production, recharge, and irrigation. Although the use of inorganic equilibrium models for the processes of mineral solution and precipitation cannot produce a complete description of these processes, an equilibrium model is a useful reference. It can indicate which processes are impossible for a given water-rock system and suggest which processes may control water compositions and which processes are so hindered by kinetic factors that the water compositions are indifferent to them.

Calculations of the states of saturation of natural waters with minerals are complicated by the consideration of all the factors which affect the activity of the ions involved in the solution equilibria. One simple approach for multicomponent water solutions is to assume the existence of complexes whose formation is described by mass-action expressions and to assume that the activity coefficients of simple ions and complexes can be described by equations depending only on the temperature and a function of the water composition, the ionic strength. The number of possible ions, complexes, and minerals and the use of iteration for the solution of simultaneous equations and for the calculation of activity coefficients practically necessitate the use of computer methods.

This report is an attempt to provide a general computer program, for the calculation of chemical equilibria in natural waters at low temperatures, that may be expanded and updated by the user as additional stability data on complexes and minerals become available. The complete computer program is available from the National Technical Information Service, Springfield, VA 22151, as document No. PB-220 464 at a cost of $1.45 per microfiche and $4.85 per paper copy.
The study was financed in part by the Defense Advanced Research Projects Agency of the Department of Defense under Order 1813, Amendment 1.

Acknowledgments.—Our thanks are extended to Ivan Barnes, whose earlier program suggested the format, and to C. L. Christ, J. Haas, G. M. Lafon, F. J. Pearson, Jr., Y. Karaka and E. A. Jenne for data and for corrections to the program. We are especially grateful to Manuel Nathenson for checking the thermodynamic data. The thermodynamic approach has been influenced by Garrels and Christ (1965), Sillen and Martell (1964), and Denbigh (1955). Many readers find the approach familiar, and they may wish to omit the next sections in which the minimum thermodynamic theory necessary to explain the calculations is presented.

MASS-ACTION EQUILIBRIUM EQUATIONS

In a mixture at equilibrium, the activities of the chemical species present are related by a set of mass-action equilibrium equations (Garrels and Christ, 1965, p. 6, 342; Denbigh, 1955, p. 138, 307). For each possible reaction of the form,

$$aA+bB=cC+dD, \quad (1)$$

in which lowercased letters are the stoichiometric coefficients of the chemical species represented by the uppercased letters, there is a mass action equation of the form,

$$K=\frac{[C]^c[D]^d}{[A]^a[B]^b} \quad (2)$$

In this equation, K is the mass action or equilibrium constant, and the brackets represent activities. For equilibria involving low-pressure gases, the partial pressure of the gas may be used instead of activity, and for gas-aqueous solution equilibria, activities and partial pressures may be used in the same equation.

The equilibrium constants may be derived from experimental measurement of concentrations in a series of equilibrium mixtures of different total concentration with extrapolation to infinite dilution. Alternatively, the experimental concentrations may be corrected to activities by means of calculated activity coefficients (see later discussion). Useful compilations of experimentally derived equilibrium constants have been made by Sillen and Martel (1964), Barnes, Helgeson, and Ellis (1966), Ellis (1967) and Helgeson (1969).

The equilibrium constant for a reaction may also be derived from the standard free energy change of that reaction. For the reaction given by equation 1, the sum of the standard free energies of formation, ΔG_f°, of the products times their stoichiometric coefficients less that of the reactants times their stoichiometric coefficients is the standard free energy change of reaction:

$$\Delta G_r^\circ = c\Delta G_f^\circ, C + d\Delta G_f^\circ, D - (a\Delta G_f^\circ, A + b\Delta G_f^\circ, B) . \quad (3)$$

This standard free energy change of reaction is related to the equilibrium constant of the reaction by the equation,

$$\Delta G_r^\circ = -2.303\, RT \log K \quad (4)$$

In which R is the gas constant and T is the absolute temperature. By the use of these equations, experimental equilibrium data may be related to thermochemical data derived from calorimetric measurements. Useful compilations of standard free energies of formation (and other thermochemical data) have been made by the National Bureau of Standards (Rossini and others, 1952; Wagman and others, 1968 and 1969) and by Latimer (1952), Garrels and Christ (1965), Robie and Waldbaum (1968) and Helgeson (1969).

No single source of equilibrium constants or thermochemical data is of sufficient scope or of recent enough publication to include all the data relevant to near-surface rock-water reactions. The data contained in WATEQ (table 1) are from a compilation in preparation by the authors of this program and Manuel Nathenson.

The effect of temperature and pressure on mass action equations will be considered in a later section.

Table 1.—*Reactions and thermodynamic data*

[Log K_{298} (logarithm of equilibrium constant at 298 K) and $\Delta H_{r,298}$ (heat of reaction at 298 K), unless otherwise noted, are calculated from free energies and enthalpies. Data source values are given for the reactions as considered by the original reference, not necessarily as printed here. R and W refer to Robie and Waldbaum (1968); 270-3 and 270-4 refer to Wagman and others (1968) and (1969), respectively. S°, standard state of entropy. Sources for ΔG_f and ΔH_f of individual ion species in solution are all from 270-3 or 270-4, except that Mg^{+2}, Ca^{+2}, Sr^{+2}, Ba^{+2}, and Li^+ are from Latimer (1952), $H_4SiO_4^\circ$ is from Helgeson (1969), and H^+ plus e^- are 0 by definition. ΔG and ΔH values are given in calories]

Reaction No.	Mineral or species name	Reaction	log K	ΔH_r	Data source
0	Fe^{+2}	$Fe^{+2}=Fe^{+3}+e^-$	-13.013	9,700	ΔG_f and ΔH_f from 270-4.
1	$FeOH^{+2}$	$Fe^{+2}+H_2O=FeOH^{+2}+e^-+H^+$	-15.473	20,115	$Fe^{+3}+H_2O=FeOH^+ + H^+$, log K=-2.46; Lamb and Jacques as quoted in Langmuir (1969), ΔH_f from 270-4.
2	$FeOH^+$	$Fe^{+2}+H_2O=FeOH^++H^+$	- 9.319	13,218	From ΔH_r and ΔS_r of magnetite hydrolysis (Sweeton and Baes, 1970).
3	$Fe(OH)_3^-$	$Fe^{+2}+3H_2O=Fe(OH)_3^-+3H^+$	-29.458	32,995	Do.
4	$FeSO_4^+$	$Fe^{+2}+SO_4^{-2}=FeSO_4^++e^-$	- 8.886	15,920	ΔG_f and ΔH_f from 270-4.
5	$FeCl^{+2}$	$Fe^{+2}+Cl^-=FeCl^{+2}+e^-$	-11.600	18,152	Do.
6	$FeCl^+$	$Fe^{+2}+2Cl^-=FeCl_2^++e^-$	-10.919	----------	ΔG_f from 270-4.
7	$FeCl_3^\circ$	$Fe^{+2}+3Cl^-=FeCl_3^\circ+e^-$	-11.925	----------	Do.
8	$FeSO_4^\circ$	$Fe^{+2}+SO_4^{-2}=FeSO_4^\circ$	2.200	560	Log K=2.20, ΔH_r=560 (Izatt and others, 1969).
9	Siderite	$FeCO_3=Fe^{+2}+CO_3^{-2}$	-10.55	-5,328	Langmuir (1969), ΔH_f from R and W.
10	Magnesite	$MgCO_3=Mg^{+2}+CO_3^{-2}$	- 8.029	-6,169	Do.
11	Dolomite	$CaMg(CO_3)_2=Ca^{+2}+Mg^{+2}+2CO_3^{-2}$	-17.000	-8,290	Log K_{298}=-17.0 (Berner, 1967), ΔH_r=-8,290 (Helgeson, 1969).
12	Calcite	$CaCO_3=Ca^{+2}+CO_3^{-2}$	- 8.370	-3,190	Log K_{298}=-8.37 (Berner, 1967), ΔH_r= -3,190 (Helgeson, 1969).

Table 1.—*Reactions and thermodynamic data*—Continued

Reaction No.	Mineral or species name	Reaction	log K	ΔH_r	Data Source
13	$H_3SiO_4^-$	$H_4SiO_4^\circ = H_3SiO_4^- + H^+$	- 9.930	8,935	Log K=-9.929, ΔH_r=8,935 from log $K(T)$ expression (Ryzhenko, 1967).
14	$H_2SiO_4^{-2}$	$H_4SiO_4^\circ = 2H^+ + H_2SiO_4^{-2}$	-21.619	29,714	Log K=-21.617, ΔH_r=29,714 from log $K(T)$ expression (Ryzhenko, 1967).
15	HPO_4^{-2}	$H^+ PO_4^{-3} = HPO_4^{-2}$	12.346	-3,530	ΔG_f and ΔH_f from 270-3.
16	$H_2PO_4^-$	$2H^+ + PO_4^{-3} = H_2PO_4^-$	19.553	-4,520	Do.
17	Anhydrite	$CaSO_4 = Ca^{+2} + SO_4^{-2}$	- 4.637	-3,769	ΔG_f and ΔH_f from R and W.
18	Gypsum	$CaSO_4 \cdot 2H_2O = Ca^{+2} + SO_4^{-2} + 2H_2O$	- 4.848	261	Do.
19	Brucite	$Mg(OH)_2 = Mg^{+2} + 2OH^-$	-11.204	850	ΔG_f and ΔH_f from R and W.
20	Chrysotile	$Mg_3Si_2O_5(OH)_4 + 5H_2O = 3Mg^{+2} + 2H_4SiO_4^\circ + 6OH^-$	-51.800	27,585	Log K=-51.8 (Hostetler and Christ, 1968), ΔH_f from R and W.
21	Aragonite	$CaCO_3 = Ca^{+2} + CO_3^{-2}$	-8.305	-2,959	ΔG_f and ΔH_f from R and W.
22	MgF^+	$Mg^{+2} + F^- = MgF^+$	1.820	4,674	Log K=1.82, ΔH_r=24 (Sillen and Martell, 1964).
23	$CaSO_4^\circ$	$Ca^{+2} + SO_4^{-2} = CaSO_4^\circ$	2.309	1,650	Log K=2.309, ΔH_r=1,650 (Bell and George, 1953).
24	$MgOH^+$	$Mg^{+2} + OH^- = MgOH^+$	2.600	2,140	Log K=2.6 (Hostetler, 1963); ΔH_r=2,140 (Helgeson, 1969).
25	H_3BO_3	$H_3BO_3 = H^+ + H_2BO_3^-$	-9.240	3,224	Log K=4.757-log KW, ΔH_r=-10,121 -$(\Delta H_r)_{KW}$ from log $K(T)$ expression (Mesmer and others, 1972).
26	NH_3°	$NH_4^+ = NH_3^\circ + H^+$	-9.252	12,480	ΔG_f and ΔH_f from 270-3.
27	Forsterite	$Mg_2SiO_4 + 4H_2O = 2Mg^{+2} + 2H_4SiO_4 + 4OH^-$	-27.694	4,870	ΔG_f and ΔH_f from R and W.
28	Diopside	$CaMgSi_2O_6 + 6H_2O = Ca^{+2} + Mg^{+2} + 2H_4SiO_4^\circ + 4OH^-$	-36.106	21,100	Do.
29	Clinoenstatite	$MgSiO_3 + 3H_2O = Mg^{+2} + H_4SiO_4^\circ + 2OH^-$	-16.658	6,675	Do.
30	$NaHPO_4^-$	$Na^+ + HPO_4^{-2} = NaHPO_4^-$	1.200	----------	Log K=1.20 obtained by calculation from data of Smith and Alberty (1956) by using $K_{equiv} = \gamma NaHPO_4^- / (\gamma Na^+ \gamma HPO_4^{-2})$ and K_{approx} and by assuming $\gamma HPO_4^{-2} = \gamma SO_4^{-2} = 0.25$, $\gamma Na^+ = 0.75$, and $\gamma NaHPO_4^- = \gamma Na^+$.
31	Tremolite	$Ca_2Mg_5Si_8O_{22}(OH)_2 + 22H_2O = 2Ca^{+2} + 5Mg^{+2} + 8H_4SiO_4^\circ + 14OH^-$	-139.426	90,215	ΔG_f and ΔH_f from R and W.
32	$KHPO_4^-$	$K^+ + HPO_4^{-2} = MgHPO_4^\circ$	1.090	----------	Log K=1.09 obtained by calculation from data of Smith and Alberty (1956) in a similar manner to $NaHPO_4^-$.
33	$MgHPO_4^\circ$	$Mg^{+2} + HPO_4^{-2} = MgHPO_4^\circ$	2.870	3,300	Log K=2.87 (Sillen and Martell, 1964), ΔH_r=3,300 by analogy to $CaHPO_4^\circ$ data of Chughtai, Marshall, and Nancollas (1968).
34	$CaHPO_4^\circ$	$Ca^{+2} + HPO_4^{-2} = CaHPO_4^\circ$	2.739	3,300	Log K=2.739, ΔH_r=3,300 (Chughtai and others, 1968).
35	HCO_3^-	$H_2CO_3^\circ = HCO_3^- + H^+$	-6.379	1,976	Log K=-6.379, ΔH_r=1,976 from log $K(T)$ expression (Ryzhenko, 1963).
36	Sepiolite	$Mg_2Si_3O_{7.5}OH \cdot 3H_2O + 4.5H_2O = 2Mg^{+2} + 3H_4SiO_4^\circ + 4OH^-$	-40.079	26,532	ΔG_f=-1,105,600; S°=90.1 (Christ and others, 1973).
37	Talc	$Mg_3Si_4O_{10}(OH)_2 + 10H_2O = 3Mg^{+2} + 4H_4SiO_4^\circ + 6OH^-$	-60.933	45,065	ΔG_f from Hostetler and others (1971); ΔH_f from R and W.
38	Hydromagnesite	$Mg_5(CO_3)_4(OH)_2 \cdot 4H_2O = 5Mg^{+2} + 4CO_3^{-2} + 2OH^- + 4H_2O$	-36.762	-25,520	ΔG_f and ΔH_f from Robie and Hemingway (1972).
39	Adularia	$KAlSi_3O_8 + 8H_2O = K^+ + Al(OH)_4^- + 3H_4SiO_4^\circ$	-20.573	30,820	ΔG_f and ΔH_f from R and W.

Table 1.—*Reactions and thermodynamic data*—Continued

Reaction No.	Mineral or species name	Reaction	log K	ΔH_r	Data source
40	Albite	$NaAlSi_3O_8 + 8H_2O = Na^+ + Al(OH)_4^- + 3H_4SiO_4^\circ$	-18.002	25,896	Do.
41	Anorthite	$CaAl_2Si_2O_8 + 8H_2O = Ca^{+2} + 2Al(OH)_4^- + 2H_4SiO_4^\circ$	-19.424	17,530	ΔG_f and ΔH_f from R and W.
42	Analcime	$NaAlSi_2O_6 \cdot H_2O + 5H_2O = Na^+ + Al(OH)_4^- + 2H_4SiO_4^\circ$	-12.701	18,206	Do.
43	K-mica	$KAl_3Si_3O_{10}(OH)_2 + 12H_2O = K^+ + 3Al(OH)_4^- + 3H_4SiO_4^\circ + 2H^+$	-49.102	67,860	Do.
44	Phlogopite	$KMg_3AlSi_3O_{10}(OH)_2 + 10H_2O = K^+ + 3Mg^{+2} + Al(OH)_4^- + 3H_4SiO_4^\circ + 6OH^-$	----------	----------	No data.
45	Illite	$K_{0.6}Mg_{0.25}Al_{2.3}Si_{3.5}O_{10}(OH)_2 + 11.2H_2O = 0.6K^+ + 0.25Mg^{+2} + 2.3Al(OH)_4^- + 3.5H_4SiO_4^\circ + 1.2H^+$	-40.267	54,684	ΔG_f and ΔH_f from Helgeson (1969).
46	Kaolinite	$Al_2Si_2O_5(OH)_4 + 7H_2O = 2Al(OH)_4^- + 2H_4SiO_4^\circ + 2H^+$	-36.921	49,150	Kaolinite + $6H^+ = 2Al^{+3} + 2H_4SiO_4 + H_2O$; log K=7.185 (Kittrick, 1966); ΔH_f from R and W.
47	Halloysite	$Al_2Si_2O_5(OH)_4 + 7H_2O = 2Al(OH)_4^- + 2H_4SiO_4^\circ + 2H^+$	-32.830	44,680	ΔG_f and ΔH_f from R and W.
48	Beidellite	$(Na,K,\frac{1}{2}Mg)_{0.33}Al_{2.33}Si_{3.67}O_{10}(OH)_2 + 12H_2O = 0.33(Na,K,\frac{1}{2}Mg)^+ + 2.33Al(OH)_4^- + 3.67H_4SiO_4^\circ + 2H^+$	-45.272	60,355	ΔG_f and ΔH_f from Helgeson (1969) for Na end member.
49	Chlorite	$Mg_5Al_2Si_3O_{10}(OH)_8 + 10H_2O = 5Mg^{+2} + 2Al(OH)_4^- + 3H_4SiO_4^\circ$	-89.563	54,760	ΔG_f and ΔH_f taken as average of Helgeson (1969) and Zen (1972).
50	Alunite	$KAl_3(SO_4)_2(OH)_6 = K^+ + 3Al^{+3} + 2SO_4^{-2} + 6OH^-$	-85.334	29,820	ΔG_f and ΔH_f from Hemley and others (1969).
51	Gibbsite (crystalline)	$Al(OH)_3 = Al^{+3} + 3OH^-$	-32.774	14,470	ΔG_f and ΔH_f from R and W.
52	Boehmite	$AlO(OH) + H_2O = Al^{+3} + 3OH^-$	-33.416	11,905	Do.
53	Pyrophyllite	$Al_2Si_4O_{10}(OH)_2 + 12H_2O = 2Al(OH)_4^- + 4H_4SiO_4^\circ + 2H^+$	-48.314	----------	ΔG_r=65,900 from data in tables 4 and 5 in Reesman and Keller (1968).
54	Phillipsite	$Na_{0.5}K_{0.5}AlSi_3O_8 \cdot H_2O + 7H_2O = 0.5Na^+ + 0.5K^+ + Al(OH)_4^- + 3H_4SiO_4^\circ$	-19.874	----------	Log K=0.7 for reaction phillipsite + $0.5K^+ = K$-feldspar + $0.5Na^+ + H_2O$; ΔG_f of K-feldspar from R and W; (Hess, 1966).
55	Erionite	$NaAlSi_{3.5}O_9 \cdot 3H_2O + 6H_2O = Na^+ + Al(OH)_4^- + 3.5H_4SiO_4^\circ$	----------	----------	No data.
56	Clinoptilolite	$(K,Na)AlSi_5O_{12} \cdot 3.5H_2O + 8.5H_2O = (K,Na)^+ + Al(OH)_4^- + 5H_4SiO_4^\circ$	----------	----------	Do.
57	Mordenite	$(Na,K)AlSi_{4.5}O_{11} \cdot 3H_2O + 8H_2O = (Na,K)^+ + Al(OH)_4^- + 4.5H_4SiO_4^\circ$	----------	----------	Do.
58	Nahcolite	$NaHCO_3 = Na^+ + HCO_3^-$	-0.548	3,720	ΔG_f and ΔH_f from Latimer (1952).
59	Trona	$NaHCO_3 \cdot Na_2CO_3 \cdot 2H_2O = 2H_2O + 3Na^+ + CO_3^{-2} + HCO_3^-$	-0.795	-18,000	From data on natron (this study), nahcolite (Latimer, 1952), and trona-nahcolite-soda in equilibrium at 21.1°C (Linke and Seidell, 1965, p. 925).
60	Natron	$Na_2CO_3 \cdot 10H_2O = 2Na^+ + CO_3^{-2} + 10H_2O$	-1.311	15,745	$Na_2CO_3 \cdot 10H_2O = Na_2CO_3 \cdot H_2O + 9H_2O$ (g); ΔG_r=20,435; ΔH_r=113,218 (Waterfield and others, 1968); ΔG_f and ΔH_f of thermonatrite computed in this study.
61	Thermonatrite	$Na_2CO_3 \cdot H_2O = 2Na^+ + CO_3^{-2} + H_2O$	0.125	-2,802	$Na_2CO_3 \cdot H_2O = Na_2CO_3 + H_2O$ (g); ΔG_r=2,944; ΔH_r=14,037; Waterfield and others (1968); ΔG_f of Na_2CO_3 from ΔH_f of Latimer (1952) and S° of Waterfield and others (1968).
62	Fluorite	$CaF_2 = Ca^{+2} + 2F^-$	-9.046	1,530	ΔG_f and ΔH_f from R and W.
63	Ca montmorillonite	$Ca_{0.17}Al_{2.33}Si_{3.67}O_{10}(OH)_2 + 12H_2O = 0.17Ca^{+2} + 2.33\ Al(OH)_4^- + 3.67H_4SiO_4^\circ + 2H^+$	-45.027	58,373	ΔG_f and ΔH_f from Helgeson (1969).
64	Halite	$NaCl = Na^+ + Cl^-$	1.582	918	ΔG_f and ΔH_f from R and W.
65	Thenardite	$Na_2SO_4 = 2Na^+ + SO_4^{-2}$	-0.179	-572	Do.

Table 1.—*Reactions and thermodynamic data*—Continued

Reaction No.	Mineral or species name	Reaction	log K	ΔH_r	Data source
66	Mirabilite	$Na_2SO_4 \cdot 10H_2O = 2Na^+ + SO_4^{-2} + 10H_2O$	-1.114	18,987	Do.
67	Mackinawite	$FeS + H^+ = Fe^{+2} + HS^-$	-4.648	----------	Log K=-17.566 (Berner, 1967).
68	CO_3^{-2}	$HCO_3^- = H^+ + CO_3^{-2}$	-10.330	3,550	ΔG_f and ΔH_f from 270-3.
69	$NaCO_3^-$	$Na^+ + CO_3^{-2} = NaCO_3^-$	1.268	8,911	Log K=-1.268 (Garrels and others, 1961), ΔH_r=-8,911 (Lafon, 1969).
70	$NaHCO_3^\circ$	$Na^+ + HCO_3^- = NaHCO_3^\circ$	-0.250	----------	Log K=0.25 (Garrels and Thompson, 1962).
71	$NaSO_4^-$	$Na^+ + SO_4^{-2} = NaSO_4^-$	0.226	2,229	Log K=0.226, ΔH_r=308 from log $K(T)$ expression (Lafon and Truesdell, 1971).
72	KSO_4^-	$K^+ + SO_4^{-2} = KSO_4^-$	0.847	3,082	Log K=0.847, ΔH_r=3,082 from log $K(T)$ expression (Truesdell and Hostetler, 1968).
73	$MgCO_3^\circ$	$Mg^{+2} + CO_3^{-2} = MgCO_3^\circ$	3.398	58	Log K=3.398 (Garrels and others, 1961); ΔH_r=58 (Lafon, 1969).
74	$MgHCO_3^-$	$Mg^{+2} + HCO_3^- = MgHCO_3^+$	0.928	10,370	$MgHCO_3^+ = MgCO_3^\circ + H^+$, log K=-7.86 (Hostetler, 1963); ΔH_r=+10,370 (Lafon, 1969).
75	$MgSO_4^\circ$	$Mg^{+2} + SO_4^{-2} = MgSO_4^\circ$	2.238	4,920	Log K=-2.238 (Hanna and others, 1971); ΔH_r=-4,920 (Helgeson, 1969).
76	$CaOH^+$	$Ca^{+2} + OH^- = CaOH^+$	1.400	1,190	Log K=1.40; ΔH_r=1,190 (Sillen and Martell, 1964).
77	$CaHCO_3^+$	$Ca^{+2} + HCO_3^- = CaHCO_3^+$	1.260	6,331	Log K=-1.26 (Garrels and Thompson, 1962); ΔH_r=-6,331 (Lafon, 1969).
78	$CaCO_3^\circ$	$Ca^{+2} + CO_3^{-2} = CaCO_3^\circ$	3.200	3,130	Log K=-3.2 (Garrels and Thompson, 1962); ΔH_r=-3,130 (Helgeson, 1969).
79	$Na_2CO_3^\circ$	$2Na^+ + CO_3^{-2} = Na_2CO_3^\circ$	0.672	---------	Log K=-0.672 (Garrels and Christ, 1965, p. 109).
80	$AlOH^{+2}$	$Al^{+3} + OH^- = AlOH^{+2}$	8.998	1,990	$Al^{+3} + H_2O = AlOH^{+2} + H^+$; log K=-5.00 (Hem and others 1973). ΔH_r=1,990 (Helgeson, 1969).
81	$Al(OH)_2^+$	$Al^{+3} + 2OH^- = Al(OH)_2^+$	18.235	----------	$Al^{+3} + 2H_2O = Al(OH)_2^+ + 2H^+$; log K=-9.76 (Hem and others, 1973).
82	$Al(OH)_4^-$	$Al^{+3} + 4OH^- = Al(OH)_4^-$	33.938	-9,320	$Al(OH)_3$ (microcryst)=Al^{+3}+3OH, log K=32.65; $Al(OH)_3$ (microcryst) +H_2O=$Al(OH)_4^-$+H^+; log K=-12.71. (Hem and Roberson, 1967); ΔH_f from 270-3.
83	AlF^{+2}	$Al^{+3} + F^- = AlF^{+2}$	7.010	----------	Log K=7.01 (Hem, 1968).
84	AlF_2^+	$Al^{+3} + 2F^- = AlF_2^+$	12.750	20,000	Log K=12.75 (Hem, 1968), ΔH_f from 270-3.
85	AlF_3°	$Al^{+3} + 3F^- = AlF_3^\circ$	17.020	2,500	Log K=17.02 (Hem, 1968), ΔH_f from 270-3.
86	AlF_4^-	$Al^{+3} + 4F^- = AlF_4^-$	19.720	----------	Log K=19.72 (Hem, 1968).
87	$AlSO_4^+$	$Al^{+3} + SO_4^{-2} = AlSO_4^+$	3.200	2,290	Log K=3.2 (Hem, 1968); ΔH_r=2,290 (Izatt and others, 1969).
88	$Al(SO_4)_2^-$	$Al^{+3} + 2SO_4^{-2} = Al(SO_4)_2^-$	5.100	3,070	Log K=5.1 (Hem, 1968); ΔH_r=3,070 (Izatt and others, 1969).
89	HSO_4^-	$H^+ + SO_4^{-2} = HSO_4^-$	1.987	4,910	Log K=-1.987, ΔH_r=-4,910 from log $K(T)$ expression (Lietzke and others, 1961).
90	SO_4^{-2}/H_2S	$SO_4^{-2} + 10H^+ + 8e^- = H_2S^+ + 4H_2O$	40.644	-65,440	ΔG_f and ΔH_f from 270-3.
91	HS^-	$H_2S = H^+ + HS^-$	-6.994	5,300	Do.
92	S^{-2}	$HS^- = H^+ + S^{-2}$	-12.918	12,100	Do.
93	H_2O/O_2(gas)	$0.5H_2O = 0.25O_2(g) + H^+ + e^-$	-20.780	34,157	Definition.
94	HCO_3^-/CH_4(gas)	$HCO_3^- + 8e^- + 9H^+ = CH_4 + 3H_2O$	30.741	-57,435	ΔG_f and ΔH_f from 270-3.

Table 1.—*Reactions and thermodynamic data*—Continued

Reaction No.	Mineral or species name	Reaction	Log K	ΔH_r	Data source
95	OH apatite	$Ca_5(PO_4)_3(OH)+3H_2O=5Ca^{+2}+3HPO_4^{-2}+4OH^-$	-59.421	17,225	OH apatite $=5Ca^{+2}+3PO_4^{-3}+OH^-$; log K= -54.408 (Brown, 1960); ΔH_f from R and W.
96	F apatite	$Ca_5(PO_4)_3F+3H_2O=5Ca^{+2}+3HPO_4^{-2}+3OH^-+F^-$	-67.243	19,695	ΔG_f and ΔH_f from Roberson (1966).
97	Chalcedony	$SiO_2+2H_2O=H_4SiO_4^\circ$	-3.523	4,615	Log K and ΔH_r obtained from data of R. O. Fournier and J. J. Rowe (in Fournier, 1973).
98	Magadiite	$NaSi_7O_{13}(OH)_3 \cdot 3H_2O+H^++9H_2O=Na^++7H_4SiO_4^\circ$	-14.300	----------	Log K=-14.3 (Bricker, 1969).
99	Cristobalite	$SiO_2+2H_2O=H_4SiO_4^\circ$	-3.587	5,500	ΔG_f and ΔH_f from R and W.
100	Silica gel	$SiO_2+2H_2O=H_4SiO_4^\circ$	-3.018	4,440	Do.
101	Quartz	$SiO_2+2H_2O=H_4SiO_4^\circ$	-4.006	6,220	Do.
102	$Fe(OH)_2^+$	$Fe^{+2}+2H_2O=Fe(OH)_2^++2H^++e^-$	-20.173	----------	$FeOH^{+2}+H_2O=Fe(OH)_2^++H^+$; log K=-4.7, Lamb and Jacques as quoted in Langmuir (1969).
103	$Fe(OH)_3^\circ$	$Fe^{+2}+3H_2O=Fe(OH)_3^\circ+3H^++e^-$	-26.571	----------	$Fe(OH)_3^\circ=Fe(OH)_2^++OH^-$; log K=7.6, Hem and Cropper as quoted in Langmuir (1969).
104	$Fe(OH)_4^-$	$Fe^{+2}+4H_2O=Fe(OH)_4^-+4H^++e^-$	-34.894	----------	Rough estimate from $Fe^{+3}+4OH^-=Fe(OH)_4^-$; log K=34.11 in 3 M $NaClO_4$ solution (Langmuir, 1969).
105	$Fe(OH)_2^\circ$	$Fe^{+2}+2H_2O=Fe(OH)_2^\circ+2H^+$	-20.570	28,565	From ΔH_r and ΔS_r of magnetite hydrolysis (Sweeton and Baes, 1970).
106	Vivianite	$Fe_3(PO_4)_2 \cdot 8H_2O=3Fe^{+2}+2PO_4^{-3}+8H_2O$	-36.000	----------	Vivianite = $3Fe^{+2}+2PO_4^{-3}+8H_2O$; log K=-36 (Nriagu, 1972b).
107	Magnetite	$Fe_3O_4+8H^+=3Fe^{+3}+4H_2O+e^-$	-9.565	-40,660	ΔG_f and ΔH_f from R and W.
108	Hematite	$Fe_2O_3+6H^+=2Fe^{+3}+3H_2O$	-4.008	-30,845	Do.
109	Maghemite	$Fe_2O_3+6H^+=2Fe^{+3}+3H_2O$	6.386	----------	Maghemite + $3H_2O$ = $2Fe^{+3}+6OH^-$; log K=-77.6 (Doyle as quoted in Langmuir, 1969).
110	Goethite	$FeO(OH)+H_2O=Fe^{+3}+3OH^-$	-41.200	25,555	2 goethite = hematite + H_2O; ΔG_r= 545 (Langmuir, 1971); ΔH_f from R and W.
111	Greenalite	$Fe_3Si_2O_5(OH)_4+5H_2O=3Fe^{+2}+2H_4SiO_4^\circ+6OH^-$	----------	----------	No data.
112	$Fe(OH)_3$ (amorphous)	$Fe(OH)_3+3H^+=Fe^{+3}+3H_2O$	4.891	----------	$Fe(OH)_3$ (amorphous)$=Fe^{+3}+3OH^-$; log K = -37.1 (Langmuir, 1969).
113	Annite	$KFe_3AlSi_3O_{10}(OH)_2+10H_2O=K^++3Fe^{+2}+Al(OH)_4^-+3H_4SiO_4^\circ$	-85.645	62,480	ΔG_f and ΔH_f from Helgeson (1969).
114	Pyrite	$FeS_2+2H^++2e^-=Fe^{+2}+2HS^-$	-18.479	11,300	ΔG_f and ΔH_f from R and W.
115	Montmorillonite (Belle Fourche)	$(H,Na,K)_{0.28}Mg_{0.29}Fe^{+3}_{0.23}Al_{1.58}Si_{3.93}O_{10}(OH)_2+10.04H_2O=0.28(H,Na,K)^++0.29Mg^{+2}+0.23Fe^{+3}+1.58Al(OH)_4^-+3.93H_4SiO_4^\circ+0.23Fe^{+3}$	-34.913	----------	Recalculated from data in table 2 of Kittrick (1971a) assuming hydrogen montmorillonite was dissolved in equilibrium with $Fe(OH)_3$ (amorph) rather than hematite.
116	Montmorillonite (Aberdeen)	$(H,Na,K)_{0.42}Mg_{0.45}Fe^{+3}_{0.34}Al_{1.47}Si_{3.82}O_{10}(OH)_2+9.16H_2O+0.84H^+=0.42(H,Na,K)^++0.45Mg^{+2}+0.34Fe^{+3}+1.47Al(OH)_4^-+3.82H_4SiO_4^\circ$	-29.688	----------	Recalculated from data in table 2 of Kittrick (1971b) assuming hydrogen montmorillonite was dissolved in equilibrium with $Fe(OH)_3$ (amorph) rather than hematite.
117	Huntite	$CaMg(CO_3)_4=3Mg^{+2}+Ca^{+2}+4CO_3^{-2}$	-29.968	-25,760	ΔG_f and ΔH_f from Hemingway and Robie (1972).
118	Greigite	$Fe_3S_4+4H^++2e^-=3Fe^{+2}+4HS^-$	-18.959	----------	Log K=-70.63 (Berner, 1967).

Table 1.—*Reactions and thermodynamic data*—Continued

Reaction No.	Mineral or species name	Reaction	Log K	ΔH_r	Data source
119	FeS (precipitate)	$FeS+H^+=Fe^{+2}+HS^-$	-3.915	----------	Log K=-16.833 (Berner, 1967).
120	FeH_2PO_4	$Fe^{+2}+H_2PO_4^-=FeH_2PO_4^+$	2.700	----------	Log K=2.7 (Nriagu, 1972b).
121	$CaPO_4^-$	$Ca^{+2}+PO_4^{-3}=CaPO_4^-$	6.459	3,100	Log K=6.459, ΔH_r=3,100 (Chughtai and others, 1968).
122	$CaH_2PO_4^+$	$Ca^{+2}+H_2PO_4^-=CaH_2PO_4^+$	1.408	3,400	Log K=1.408, ΔH_r=3,400 (Chughtai and others, 1968).
123	$MgPO_4^-$	$Mg^{+2}+PO_4^{-3}=MgPO_4^-$	6.589	3,100	Log K adjusted from $CaPO_4^-$ by using analogy between $CaHPO_4^-$ and $MgHPO_4^\circ$; that is, log K=6.459+(2.87-2.74)=6.589, ΔH_r=3,100 by analogy with $CaPO_4^-$.
124	$MgH_2PO_4^+$	$Mg^{+2}+H_2PO_4^-=MgH_2PO_4^+$	1.513	3,400	Log K adjusted from $CaH_2PO_4^-$ by using analogy between $CaHPO_4^-$ and $MgHPO_4^\circ$; that is, log K=1.408+(2.87-2.74)=1.513, ΔH_r=3,400 by analogy with $CaH_2PO_4^-$.
125	$LiOH^\circ$	$Li^++OH^-=LiOH^\circ$	0.200	4,832	ΔG_r=-273, ΔH_r=4,832 obtained by fitting best straight line in log K vs. $1/T$ plot of data in Sillen and Martell (1964).
126	$LiSO_4^-$	$Li^++SO_4^{-2}=LiSO_4^-$	0.640	----------	Log K=0.64 (Sillen and Martell, 1964).
127	NO_3^-/NH_4^+	$NO_3^-+10H^++8e^-=NH_4^++3H_2O$	119.077	-187,055	ΔG_f and ΔH_r from 270-3.
128	Laumontite	$CaAl_2Si_4O_{12}\cdot 4H_2O+8H_2O=Ca^{+2}+2Al(OH)_4^-+4H_4SiO_4^\circ$	-31.053	39,610	ΔG_f and ΔH_f from Zen (1972).
129	$SrOH^+$	$Sr^{+2}+OH^-=SrOH^+$	0.820	1,150	Log K=0.82, ΔH_r=1,150 (Sillen and Martell, 1964).
130	$BaOH^+$	$Ba^{+2}+OH^-=BaOH^+$	0.640	1,750	Log K=0.64, ΔH_r=1,750 (Sillen and Martell, 1964).
131	$NH_4SO_4^-$	$NH^++SO_4^{-2}=NH_4SO_4^-$	1.110	----------	Log K=1.110 (Sillen and Martell, 1964).
132	HCl°	$H^++Cl^-=HCl^\circ$	-6.100	18,630	Log K=-6.1, ΔH_r=18,630 (Helgeson, 1969).
133	$NaCl^\circ$	$Na^++Cl^-=NaCl^\circ$	-1.602	----------	Log K=-1.602 (Hanna and others, 1971).
134	KCl°	$K^++Cl^-=KCl^\circ$	-1.585	----------	Log K=-1.585 (Hanna and others, 1971).
135	$H_2SO_4^\circ$	$2H^++SO_4^{-2}=H_2SO_4^\circ$	-1.000	----------	$H^++HSO_4^-=H_2SO_4^\circ$; log K=-3, (Sillen and Martell, 1964).
136	H_2O/O_2 (aqueous)	$0.5H_2O=0.25\ O_2(aq)+H^++e^-$	-11.385	----------	Eh=0.70 from equation (1) of Sato (1960).
137	H_2CO_3	$CO_2(g)+H_2O=H_2CO_3$	-1.452	-5,000	ΔG_f and ΔH_f from 270-3.
138	$FeHPO_4^\circ$	$Fe^{+2}+HPO_4^{-2}=FeHPO_4^\circ$	3.600	----------	Log K=-3.6 (Nriagu, 1972b).
139	$FeHPO_4^+$	$Fe^{+2}+HPO_4^{-2}=FeHPO_4^++e^-$	-7.613	----------	$Fe^{+3}+HPO_4^{-2}=FeHPO_4^+$; log K=5.4 (Nriagu, 1971).
140	$Al(OH)_3$ (amorphous)	$Al(OH)_3=Al^{+3}+3OH^-$	-31.611	12,990	ΔG_f and ΔH_f from Latimer (1952).
141	Prehnite	$Ca_2Al_2Si_3O_{10}(OH)_2+8H_2O+2H^+=2Ca^{+2}+2Al(OH)_4^-+3H_4SiO_4^\circ$	-11.695	10,390	ΔG_f and ΔH_f from Zen (1972).
142	Strontianite	$SrCO_3=Sr^{+2}+CO_3^{-2}$	-11.789	2,361	ΔG_f and ΔH_f from R and W.
143	Celestite	$SrSO_4=Sr^{+2}+SO_4^{-2}$	-6.349	-1,054	Do.
144	Barite	$BaSO_4=Ba^{+2}+SO_4^{-2}$	-9.773	6,141	ΔG_f and ΔH_f from R and W.
145	Witherite	$BaCO_3=Ba^{+2}+CO_3^{-2}$	-13.335	6,950	Do.
146	Strengite	$FePO_4\cdot 2H_2O=Fe^{+3}+PO_4^{-3}+2H_2O$	-26.400	-2,030	Log K=-26.4 (Nriagu, 1972b); ΔH_f from R and W.
147	Leonhardite	$Ca_2Al_4Si_8O_{24}\cdot 7H_2O+17H_2O=2Ca^{+2}+4Al(OH)_4^-+8H_4SiO_4^\circ$	-69.756	90,070	ΔG_f and ΔH_f from R and W.
148	$Na_2SO_4^\circ$	$2Na^++SO_4^{-2}=Na_2SO_4^\circ$	1.512	-2,642	Log K=1.512, ΔH_r=2,642 from log $K(T)$ expression in Lafon and Truesdell (1971).

Table 1.—*Reactions and thermodynamic data*—Continued

Reaction No.	Mineral or species name	Reaction	log K	ΔH_r	Data source
149	Nesquehonite	$MgCO_3 \cdot 3H_2O = Mg^{+2} + CO_3^{-2} + 3H_2O$	4.999	−4,619	ΔG_f and ΔH_f from Robie and Hemingway (1972).
150	Artinite	$MgCO_3 \cdot Mg(OH)_2 \cdot 3H_2O = 2Mg^{+2} + CO_3^{-2} + 2OH^- + 3H_2O$	−17.980	498	ΔG_f and ΔH_f from Hemingway and Robie (1972).
151	H_2O/O_2 (aqueous)	$0.5H_2O = 0.25O_2(aq) + H^+ + e^-$	−21.495	33,457	ΔG_f and ΔH_f from 270-3.
152	H_2O	$H_2O = H^+ + OH^-$	−13.998	13,345	Do.
153	Sepiolite (precipitate)	$Mg_2Si_3O_{7.5}(OH) \cdot 3H_2O + 4.5H_2O = 2Mg^{+2} + 3H_4SiO_4^\circ + 4OH^-$	−37.212	----------	Log K=−37.212 (Wollast and others, 1968).
154	Diaspore	$AlOOH + H_2O = Al^{+3} + 3OH^-$	−35.121	15,405	ΔG_f and ΔH_f from 270-3.
155	Wairakite	$CaAl_2Si_4O_{12} \cdot 2H_2O + 10H_2O = Ca^{+2} + 2Al(OH)_4^- + 4H_4SiO_4^\circ$	−26.708	26,140	ΔG_f and ΔH_f from Zen (1972).
156	$FeH_2PO_4^{+2}$	$Fe^{+2} + H_2PO_4^- = FeH_2PO_4^{+2} + e^-$	−7.583	----------	$Fe^{+3} + H_2PO_4^- = FeH_2PO_4^{+2}$; log K= −5.43 (Nriagu, 1972b).

ACTIVITY COEFFICIENTS

In the limit of infinite dilution, a consequence of the definition of the standard state for ions in solution is that all ionic activities approach ionic concentrations and activity coefficients (defined as the ratios of activities to concentrations) approach unity. This property is useful in experimental studies where mass action expressions are written in which concentrations may be extrapolated to infinite dilution to yield equilibrium constants, but the property gives no clue to activity coefficients in real solutions of finite concentration. In real solutions of more than a few components, it is necessary to use single-ion activities and single-ion activity coefficients. These are formally defined by the equation,

$$a_i = \gamma_i m_i , \tag{5}$$

in which a_i, γ_i, and m_i are respectively the activity, the activity coefficient, and the molality of the ith ion. The convention that activities are dimensionless requires that single-ion activity coefficients have dimensions of molality $^{-1}$.

Single-ion activities and single-ion activity coefficients cannot be defined thermodynamically or exactly measured or calculated because measurement of the activity (and therefore the chemical potential) of a single charged ion would require the measurement of the finite free energy change of the solution resulting from a finite change in concentration of the single charged ion while the concentrations of all other ions and the electrical potential of the phase are held constant. This measurement obviously cannot be made. We must, therefore, use nonthermodynamic models to evaluate single-ion activity coefficients. The reader should be aware of the additional uncertainties introduced by this approach.

Two models have been used in WATEQ for the calculation of single-ion activity coefficients, the Debye-Hückel equation and the MacInnes assumption. These are not the only models available but are perhaps the most widely used and are generally consistent with the functions used to correct experimental determinations to infinite dilution. The Debye-Hückel theory provides an equation which describes single-ion activity coefficient behavior of ions in dilute solutions and which can be extended with adjustable parameters to more concentrated solutions. The MacInnes assumption provides information on the behavior of single-ion activities at higher concentrations with which to fit the parameters of the extended Debye-Hückel equation.

The Debye-Hückel theory

The Debye-Hückel theory considers the effect, on the free energy of a single ion, of electrical interactions with other ions by assuming that oppositely charged ions can be considered as forming a spherical shell around the ion. This assumption is valid only for very dilute solutions, and activity coefficients derived from the theory deviate increasingly from experimental results as the concentration increases. The original equation (Robinson and Stokes, 1955, p. 229) states that,

$$\log \gamma = -\frac{A z^2 \sqrt{I}}{1 + Ba\sqrt{I}} \tag{6}$$

where A and B are constants depending only on the dielectric constant, density, and temperature; z is the ionic charge; and I is the ionic strength (defined as half the sum of the products of the molality and the square of the charge of all ions in the solution) and contains one parameter, a, the "hydrated ion size" that must be estimated from experimental data. The extended form of the equation (Robinson and Stokes, 1955, p. 231),

$$\log \gamma = -\frac{A z^2 \sqrt{I}}{1 + Ba\sqrt{I}} + bI, \quad (7)$$

adds a second adjustable parameter, b, which allows for the effect of the decrease in concentration of solvent in concentrated solutions. This equation is used in WATEQ for major ions with a and b values calculated from experimental mean salt single-ion activity coefficients (see "The MacInnes Assumption") and for minor ions with values of a from Kielland (1937) and b set to zero. The constants A and B are calculated from the dielectric constant, density, and temperature by the equations (Hamer, 1968)

$$A = \frac{1.82483 \times 10^6 d^{1/2}}{(\epsilon T)^{3/2}} \text{ moles}^{-1/2} (10^3 \text{ g } H_2O)^{1/2} \quad (8)$$

and

$$B = \frac{50.2916 \times 10^8 d^{1/2}}{(\epsilon T)^{1/2}} \text{ cm}^{-1} \text{ mole}^{-1/2} (10^3 \text{ g } H_2O)^{1/2} \quad (9)$$

where d is the density of water (Keenan and Keyes, 1936), T is the absolute temperature, and ϵ is the dielectric constant of water (Malmberg and Maryott, 1956; Akerlof and Oshery, 1950).

The MacInnes assumption

In order to assign the adjustable parameters in equation 7, it is necessary to know the variation of single-ion activity coefficients with ionic strength in a single solution. Experimental values are available for the mean molal activity coefficients, $\gamma\pm$, of many salts, and if the activity coefficient of one ion can be calculated, then others may be derived from it. The MacInnes assumption (MacInnes, 1939) that the single-ion activity coefficients of K^+ and Cl^- are equal to each other and to the mean activity coefficient of KCl allows this to be done. By definition,

$$\gamma_+ \gamma_- \equiv \gamma_\pm^2 . \quad (10)$$

If

$$\gamma_\pm KCl = \gamma K^+ = \gamma Cl^- , \quad (11)$$

then

$$\gamma Na^+ = \frac{\gamma_\pm^2 NaCl}{\gamma_\pm KCl}, \quad (12)$$

$$\gamma Ca^{+2} = \frac{\gamma_\pm^3 CaCl_2}{\gamma_\pm^2 KCl}, \quad (13)$$

and

$$\gamma Br^- = \frac{\gamma_\pm^2 KBr}{\gamma_\pm KCl} , \quad (14)$$

and so forth.

In deriving these mean salt activity coefficients, one must be careful to avoid solutions in which the ions are highly associated. In calculating $\gamma_{SO_4^{-2}}$, for example, $\gamma\pm K_2SO_4$ cannot be used because of the formation of the KSO_4^- ion pair. In this calculation, the most reasonable values of γSO_4^{-2} can be obtained from $\gamma\pm Cs_2SO_4$, $\gamma\pm CsCl$, and $\gamma\pm KCl$ by the relation,

$$\gamma SO_4^{-2} = \frac{\gamma_\pm^3 Cs_2SO_4 \ \gamma_\pm^2 KCl}{\gamma_\pm^4 CsCl} . \quad (15)$$

Even here, the results must be used with caution because Cs^+ and Cl^- may be weakly associated and γSO_4^{-2} values derived in this way may be somewhat too high at high ionic strengths.

Values of a and b for major ions obtained from computer fitting of calculated mean salt activity coefficients as well as values of a for minor ions derived from Kielland (1937) are shown in table 2.

Table 2.—*Parameters of the Debye-Hückel equation*

Major ions[1]	a	b
Ca^{+2}	5.0	0.165
Mg^{+2}	5.5	.20
Na^+	4.0	.075
K^+	3.5	.015
Cl^-	3.5	.015
SO_4^{-2}	5.0	−.04
HCO_3^-	5.4	.0
CO_3^{-2}	5.4	.0

Minor ions[2]	a
$H_2BO_3^-$, NH_4^+	2.5
NO_3^-	3.0
OH^-, F^-, HS^-	3.5
$MgHCO_3^+$, $H_3SiO_4^-$,	4.0
MgF^+, $Al(OH)_4^-$, AlF_4^-, $AlSO_4^+$, $Al(SO_4)_2^-$, HSO_4^-	4.5
$FeOH^{+2}$, $FeOH^+$, $FeSO_4^+$, $FeCl^{+2}$, $FeCl_2^+$, PO_4^{-3}, HPO_4^{-2}, S^{-2}, $LiSO_4^-$, Sr^{+2}, $SrOH^+$, Ba^{+2}, $BaOH^+$, NH_4SO_4	5.0
$H_2SiO_4^{-2}$, $CaPO_4^-$, $CaH_2PO_4^+$, $MgPO_4^-$, $MgH_2PO_4^+$, $NaCO_3^-$ $NaSO_4^-$, KSO_4^-, $H_2PO_4^-$, $NaHPO_4^-$, $KHPO_4^-$, $AlOH^{+2}$, $Al(OH)_2^+$, AlF^{+2}, AlF_2^+, $Fe(OH)_4^-$, $FeHPO_4^+$, $FeH_2PO_4^+$	5.4
Fe^{+2}, $CaOH^+$, $CaHCO_3^+$, Li^+	6.0
Fe^{+3}, Al^{+3}, H^+	9.0

[1] a and b values calculated from experimental mean salt single-ion activity coefficients.

[2] a values from Kielland (1937); b values set to zero.

Single-ion activity coefficients have been calculated for concentrated single-salt solutions by use of the Stokes-Robinson equation (Bates and others, 1970). Where compari-

sons are possible, these values agree reasonably with activity coefficients based on mean salt calculations. In table 3, values of single-ion activity coefficients used in WATEQ are compared with mean salt coefficients and with those calculated by Bates and others (1970).

The use of any model of single-ion activity coefficients based on experimental measurements made on single salt solutions requires the assumption that, at a given temperature, activity coefficients in simple solutions are equal to those in complex solutions of the same ionic strength. This assumption is reasonable in dilute solutions, but limited experimental work in concentrated (>1 molal) mixed electrolyte solutions indicates that it is not always true. The extent of deviation from ionic strength dependence is small except for ions that differ greatly in size and hydration such as H^+ and Cs^+. However, for models in which all ion associations are considered (as in WATEQ), these deviations have proved to be insignificant (Pytkowicz and Kester, 1969; Yeatts and Marshall, 1972). For further discussion and comparison of activity coefficient equations, see Truesdell and Jones (1969).

Table 3.—*Single-ion activity coefficients at 25°C from a two-parameter equation used in WATEQ compared with mean salt, Stokes-Robinson, and other single-ion activity coefficients*

Ionic strength		0.01	0.1	0.5	1.0	2.0	3.0	4.0
γ_{Na^+} ...	DH[1] ...	0.903	0.782	0.708	0.715	0.789	0.901	1.043
	MS[2]	.904	.786	.713	.716	.779	.896	1.062
	SR[3]		.783	.701	.697	.756	.870	1.038
γ_{K^+}	DH[1] ...	.900	.763	.642	.600	.570	.562	.563
	MS[2]	.901	.770	.649	.604	.573	.569	.577
	SR[3]	.....	.773	.659	.623	.610	.626	.659
$\gamma_{Ca^{+2}}$ ..	DH[1] ...	.670	.389	.266	.247	.289	.376	.509
	MS[2]	.680	.382	.266	.251	.291	.385	.553
	SR[3]	.....	.380	.234	.210	.220	.265	.340
	Davies[4] .	.661	.372	.288				
$\gamma_{Mg^{+2}}$ ..	DH[1] ...	.674	.406	.292	.297	.389	.554	.822
	MS[2]	.685	.400	.289	.293	.380	.567	.945
	SR[3]	.....	.390	.247	.230	.265	.350	.470
γ_{Cl^-} ...	DH[1] ...	.900	.763	.642	.600	.570	.562	.563
	MS[2]	.901	.770	.649	.604	.573	.569	.577
	SR[3]	.....	.773	.661	.620	.590	.586	.591
$\gamma_{SO_4^{-2}}$.	DH[1] ...	.667	.371	.205	.155	.112	.091	.077
	MS[2]	.653	.368	.214	.155	.108	.085	.070
$\gamma_{HCO_3^-}$.	DH[1] ...	.905	.788	.692	.654	.623	.606	.596
	WBJ[5] ...	.904	.790	.692	.654	.627	.600	.580
$\gamma_{CO_3^{-2}}$.	DH[1] ...	.671	.386	.229	.184	.150	.135	.126
	WBJ[5] ...	.668	.388	.230	.183	.154	....	.....

[1] From parameters of Debye-Hückel equation (table 2).
[2] Mean salt.
[3] In chloride solutions (Bates and others, 1970); γ_{Cl^-} from NaCl solution.
[4] No adjustable parameters (Davies, 1962).
[5] From Walker, Bray, and Johnson (1927).

SOLUTION OF MASS ACTION AND MASS BALANCE EQUATIONS

Computation of solution species distribution is accomplished by means of a chemical model (Garrels and Thompson, 1962) which uses analytical concentrations, experimental solution equilibrium constants, mass balance equations, and the measured pH. The distribution of anionic weak acid species is calculated first from total analyzed concentrations, the pH, and activity coefficients of individual species, as illustrated by silicate equilibria,

$$H_4SiO_4 = H^+ + H_3SiO_4^- \quad (16)$$

and

$$H_3SiO_4^- = H^+ + H_2SiO_4^{-2}. \quad (17)$$

The concentration of each species is calculated from the total or analytical concentration, the pH, and the activity coefficients of the species. From the preceding equations,

$$K_1 = \frac{m_{H_3SiO_4^-}\ \gamma_{H_3SiO_4^-}\ 10^{-pH}}{m_{H_4SiO_4}\ \gamma_{H_4SiO_4}}, \quad (18)$$

and

$$K_2 = \frac{m_{H_2SiO_4^{-2}}\ \gamma_{H_2SiO_4^{-2}}\ 10^{-pH}}{m_{H_3SiO_4^-}\ \gamma_{H_3SiO_4^-}}. \quad (19)$$

The mass balance equation for total silica (silicic acid and silicate ions) is

$$m_{Si\ total} = m_{H_4SiO_4} + m_{H_3SiO_4^-} + m_{H_2SiO_4^{-2}}. \quad (20)$$

The mass action equations can be combined with the mass balance equation to solve for $m_{H_4SiO_4}$, as follows:

$$m_{H_4SiO_4} = \frac{m_{Si\ total}}{1 + \gamma_{H_4SiO_4}\left(\frac{K_1\ 10^{pH}}{\gamma_{H_3SiO_4^-}} + \frac{K_1\ K_2\ 10^{2pH}}{\gamma_{H_2SiO_4^{-2}}}\right)}; \quad (21)$$

$m_{H_4SiO_4}$ is then substituted into the mass action equations to solve for $m_{H_3SiO_4^-}$ and $m_{H_2SiO_4^{-2}}$. The activity coefficients are calculated from the ionic strength by an iterative procedure. The same method is employed for phosphate, borate, and sulfide species and for the carbonate-bicarbonate distribution from pH and the alkalinity determination, after correction for other weak acid radicals (if the alkalinity has been corrected during the chemical analysis, this step may be bypassed in the program). The concentration of H_2CO_3 is calculated from the re-computed bicarbonate molality and the first dissociation constant of carbonic acid.

Calculation of the concentrations of ion pairs is accomplished by a procedure similar to that for weak acid species, but the analyzed or computed values for the anion concentrations are utilized in place of the pH and equilibrium association constants are employed. The calculations may be illustrated for the calcium ion species. The major ion-pairing reactions are

$$Ca^{+2} + OH^{-2} = CaOH^{+}, \quad (22)$$

$$Ca^{+2} + HCO_3^{-} = CaHCO_3^{+}, \quad (23)$$

$$Ca^{+2} + CO_3^{-2} = CaCO_3^{\circ}, \quad (24)$$

and

$$Ca^{+2} + SO_4^{-2} = CaSO_4^{\circ}. \quad (25)$$

From equations 22–25, equilibrium constants for the association reactions are

$$K_1 = \frac{a_{CaOH^+}}{a_{Ca^{+2}}\, a_{OH^-}}, \quad (26)$$

$$K_2 = \frac{a_{CaHCO_3^+}}{a_{Ca^{+2}}\, a_{HCO_3^-}}, \quad (27)$$

$$K_3 = \frac{a_{CaCO_3^\circ}}{a_{Ca^{+2}}\, a_{CO_3^{-2}}}, \quad (28)$$

and

$$K_4 = \frac{a_{CaSO_4^\circ}}{a_{Ca^{+2}}\, a_{SO_4^{-2}}}. \quad (29)$$

From these quations the expressions,

$$m_{CaOH^+} = \frac{K_1\, a_{OH^-}\, m_{Ca^{+2}}\, \gamma_{Ca^{+2}}}{\gamma_{CaOH^+}}, \quad (30)$$

$$m_{CaHCO_3^+} = \frac{K_2\, a_{HCO_3^-}\, m_{Ca^{+2}}\, \gamma_{Ca^{+2}}}{\gamma_{CaHCO_3^{+2}}}, \quad (31)$$

$$m_{CaCO_3^\circ} = \frac{K_3\, a_{CO_3^{-2}}\, m_{Ca^{+2}}\, \gamma_{Ca^{+2}}}{\gamma_{CaCO_3^\circ}}, \quad (32)$$

and

$$m_{CaSO_4^\circ} = \frac{K_4\, a_{SO_4^{-2}}\, m_{Ca^{+2}}\, \gamma_{Ca^{+2}}}{\gamma_{CaSO_4^\circ}} \quad (33)$$

may be substituted into the mass balance equation for calcium as follows:

$$m_{Ca\ total} = m_{Ca^{+2}} + m_{CaOH^+} + m_{CaHCO_3^+} + m_{CaCO_3^\circ} + m_{CaSO_4^\circ}$$

to obtain an expression for free (uncomplexed) Ca^{+2} ion,

$$m_{Ca^{+2}} = \frac{m_{Ca\ total}}{1 + \gamma_{Ca^{+2}}\left(\frac{K_1 a_{OH^-}}{\gamma_{CaOH^+}} + \frac{K_2 a_{HCO_3^-}}{\gamma_{CaHCO_3^+}} + \frac{K_3 a_{CO_3^{-2}}}{\gamma_{CaCO_3^\circ}} + \frac{K_4 a_{SO_4^{-2}}}{\gamma_{CaSO_4}}\right)} \quad (34)$$

In actuality, these computations in WATEQ also include phosphate species. The computed concentration of free calcium ion, $m_{Ca^{+2}}$, is substituted back into the mass action expressions to solve for the concentrations of ion pairs. The concentrations assigned to ion pairs and weak acids reduce the concentrations of the free ions and change the ionic strength and therefore the activity coefficients. The corrected values are calculated by iteration. In each iteration, the program reduces, if necessary, the molalities of the free anions HCO_3^- CO_3^{-2}, SO_4^{-2}, Cl^-, F^-, and PO_4^{-3} and recalculates the ionic strength and the activity coefficients. Then the calculations of free Ca^{+2} and Ca complexes along with similar calculations for Na, K, Mg, Fe, and H complexes are repeated. When the sums of all weak acids, complex ions, and free ions for all anions agree with the analytical values within 0.5 percent, the iteration is stopped.

ION RATIOS

When the chemical model is complete, it is useful to calculate molal concentration ratios and ion activity ratios for plotting on water composition and mineral stability diagrams, respectively. Comparison of these ratios with those of related waters can suggest possible origins of dissolved constituents and possible controls by mineral reactions. A number of these ratios are calculated in WATEQ.

ACTIVITY PRODUCTS AND SOLUBILITY PRODUCTS

The equilibrium of a solid phase with an aqueous solution can be characterized by a mass action equation. For a solid of formula AX which dissolves to form ions A^+ and X^-, this expression is

$$K = \frac{a_{A^+}\, a_{X^-}}{a_{AX}}, \quad (35)$$

where K is the equilibrium constant of solubility. If the solid is a pure substance, not a solid solution, its activity is equal to one because it is in its standard state (Garrels and Christ, 1965, p. 5), and the expression for the equilibrium constant reduces to the "solubility product,"

$$K_{SP} = a_{A^+}\, a_{X^-}. \quad (36)$$

In hydrolysis reactions, water is considered explicitly as part of the reaction. In the solution of quartz to form silicic acid, for example,

$$SiO_{2\,(quartz)}+2H_2O=H_4SiO_4, \qquad (37)$$

the water is written as part of the reaction, and its activity appears in the equilibrium expression.

A water sample when collected is usually no longer in contact with mineral phases, and these phases may not be accessible to observation. It is of interest then to determine with what mineral phases the water is saturated or nearly so. The calculated activities of the dissolved ions in a water may be combined to produce the appropriate activity product which may be compared with the solubility equilibrium constant to show the degree of saturation of the water with each mineral considered.

This comparison may be made by means of the ratio of the activity product to the equilibrium solubility product which is given in the program as "AP/K" and "LOG AP/K" and by means of the free energy change of the reaction ΔG_r (which is zero at equilibrium) and is given as "DELGR" in the program. These quantities are related by the expression

$$\Delta G_r=2.303RT\log(\mathrm{AP/K}). \qquad (38)$$

Some mineral formulas contain a relatively large number of atoms, and the ΔG_r values for these minerals will deviate from zero more rapidly with dilution of concentration than will those values for minerals with simple formulas. This deviation can be illustrated by comparing the activity product of dolomite, $a_{Ca^{+2}}a_{Mg^{+2}}a^2_{CO_3^{-2}}$ with that of calcite, $a_{Ca^{+2}}a_{CO_3^{-2}}$. If a water initially saturated with both minerals is diluted with pure water, ΔG_r dolomite will be twice ΔG_r calcite. To correct this, ΔG_r values are divided by the number of negative charges in the formula of the mineral and presented as (for want of a better label) "PER EQUIV" ΔG_r.

The compilation of a consistent set of stability constants for minerals suffers from several uncertainties. The standard enthalpy of formation and standard entropy of most minerals have been measured by calorimetric methods, and the standard free energy of formation calculated from these quantities is often referenced to the free energies of formation of the elements rather than to the free energies of formation of the ions formed on solution of the mineral. The combination of such values with those for solution species involving aqueous ions may lead to erroneous stability constants. The use of experimental solubility products or resulting free energy values is free from this inconsistency. The main uncertainty in the use of these data lies in the precise definition of reactants and products involved in the experiment and in the difficulty of reversing the equilibrium.

Because of these uncertainties, the logarithms of the maximum and minimum solubility products are calculated in WATEQ and presented in addition to the logarithm of the most probable value for visual comparison with the logarithm of the activity product. Because of space limitations only the most probable solubility product is used in calculating values of AP/K, $\log$ (AP/K), ΔG_r, and ΔG_r per equivalent. Enthalpy values and solubility products used in the program, together with the sources of all data, are given in table 1.

EFFECTS OF TEMPERATURE AND PRESSURE

In the relationships developed in the previous sections, temperature and pressure have been assumed to be constant and their effect on the equilibria has not been discussed. The great majority of experimental determinations of equilibrium constants and of free energy values has been made at 25°C and, particularly for solution equilibria, data at other temperatures may be entirely lacking. If experiments have been made over a wide range of temperatures or if complete thermochemical data are available for all species of a reaction, then the equilibrium constant may be expressed as a power function of the absolute temperature

$$\log K=A+BT+C/T+D\log T, \qquad (39)$$

in which one or more coefficients may be zero. Where this type of expression was available in the literature, it has been used in WATEQ (table 4). If experimental determinations at only two or three temperatures are available, a linear dependence of $\log K$ with the reciprocal of the absolute temperature may be indicated (that is, B and D are zero in eq. 39) which is equivalent to a constant value of the enthalpy (heat content) change of the reaction, ΔH. This is expressed by the Van't Hoff relation,

$$\log K=\log K_{Tr}-\frac{\Delta H_{Tr}}{2.3R}\left(\frac{1}{T}-\frac{1}{Tr}\right), \qquad (40)$$

in which Tr is the reference temperature (298.15 K (= 25°C) in WATEQ) and the constants A and C in equation 39 are equal to

$$\log K_{Tr}+\frac{\Delta H_{Tr}}{2.3RT} \text{ and } \frac{\Delta H_{Tr}}{2.3R},$$

respectively.

The enthalpy change of reaction can be obtained by determining the slope of a plot of experimental values of $\log K$ versus $(1/T)$, from tabulated values of the standard enthalpy of formation of the species in the reaction by using a relation analogous to equation 3 or from direct measurements. The enthalpy of reaction at 25°C has been calculated for most of the equilibria used in WATEQ (table 1), and equation 40 is used to calculate the value of the equilibrium constant for the

Table 4. *Analytical expressions for log* K(T) *used in WATEQ*
[*T*, in kelvins]

Identifier	Reaction	Expression for log *K*(*T*)	Reference
KT(13)	$H_4SiO_4^\circ = H_3SiO_4^- + H^+$	6.368-0.016346 *T*-3405.9/*T*	Ryzhenko (1967).
KT(14)	$H_4SiO_4^\circ H_2SiO_4^{-2} + 2H^+$	39.478-0.065927 *T*-12355.1/*T*	Do.
KT(25)	$H_3BO_3^\circ = H_2BO_3^- + H^+$	1573.21/*T*+28.6059+0.012078 *T* -13.2258 log *T*+log *KW*.	Mesmer, Baes, and Sweeton (1972).
KT(26)	$NH_4^+ = NH_3^\circ + H^+$	0.6322-0.001225 *T*-2835.76/*T*	Wright, Lindsay, and Druga (1961).
KT(35)	$H_2CO_3^\circ = HCO_3^- + H^+$	8.153-0.02194 *T*-2382.3/*T*	Ryzhenko (1963).[1]
KT(68)	$HCO_3^- = H^+ + CO_3^{-2}$	5.388-0.02199 *T*-2730.7/*T*	Do.
KT(72)	$K^+ + SO_4^{-2} = KSO_4^-$	3.106-673.6/*T*	Truesdell and Hostetler (1968).
KT(89)	$H^+ + SO_4^{-2} = HSO_4^-$	-5.3505+0.0183412 *T*+557.2461/*T*	Lietzke, Stoughton, and Young (1961).
KT(91)	$H_2S^\circ = H^+ + HS^-$	11.17-0.02386 *T*-3279/*T*	D'yachkova and Khodakovskiy (1968).

[1] In more recent practice, the expressions based on the original work of Harned and co-workers (Harned and Owen, 1958) have been utilized, despite being limited to 50°C maximum temperature.

temperature of the water. For a few reactions in which data at temperatures other than 25°C were not available, the 25°C value of the equilibrium constant is used at all temperatures.

The effect of pressure has not been calculated in WATEQ because the necessity of inputing a measured pH value virtually limits WATEQ to surface and near-surface waters and because much necessary data is not available for ion pairs. Correlations suggested by Ellis and McFadden (1972) allow the calculation of the pressure effect on equilibria involving only minerals and simple ions (not ion pairs) to be made for temperatures to 250°C. These calculations suggest that pressure effects are not large for pressures less than a few hundred atmospheres.

REDOX REACTIONS

Oxidation-reduction equilibria have been treated in the same manner as other reactions in WATEQ. To achieve this, the measured Eh value, or the Eh value calculated from the measured concentration of dissolved oxygen, is converted to the negative logarithm of the conventional activity of the electron (or pE) by the relation,

$$pE \equiv Eh/(2.303RT/F), \quad (41)$$

in which F is the faraday and $2.303RT/F$ is the Nernst slope. pE is related to the conventional activity of the electron by

$$a_{e^-} = 10^{-pE} \quad (42)$$

This equation is similar to that assumed for pH, and because both measurements have an unknown liquid junction potential, the relations of pE to electron activity and of pH to hydrogen ion activity are equally uncertain. It is necessary, however, to use these relations despite the uncertainty. The standard free energy and enthalpy of the hydrated electron in aqueous solution are zero by convention. The conventional electron activity thus ranges from 10^{-20} to 10^{+20} while the actual electron activity is about 10^{-60} to 10^{-100}. These conventions are discussed by Sillen and Martell (1964) and by Truesdell (1968).

An advantage of the use of electron activity is that it is not necessary to set up separate redox equilibrium expressions. For example, the equilibrium between Fe^{+2} and Fe^{+3} is expressed by a conventional equilibrium constant,

$$K = \frac{a_{Fe^{+3}}\, a_{e^-}}{a_{Fe^{+2}}} \quad (43)$$

and the value of the equilibrium constant may be calculated from G_f°, Fe^{+3}, and G_f°, Fe^{+2} (G_f°, electron = 0 by convention). Other redox equilibria are treated similarly, and the method of calculation of the concentration of ion pairs involving iron is the same as that involving metals that are not redox active.

In natural waters that contact the atmosphere the dissolved oxygen (DOX) content may have been measured in addition to or in place of the Eh. If the dissolved oxygen has been measured, it is read into the program after the normal data as a statement, "DOX = (parts per million of dissolved oxygen),". Two values of pE are calculated in WATEQ from the relation,

$$pE = -\log K - pH - 0.5 \log a_{H_2O} + 0.25 \log a_{DOX}, \quad (44)$$

in which log K values are from thermodynamic data ("PE CALC O") and from the empirical Eh-pH relation for waters in contact with the atmosphere (Sato, 1960). ("EMPIR PE O") and DOX activities are on a molal scale. If a DOX measurement is given without an Eh value, the value of PE CALC O is used throughout the program. If instead, EMPIR PE O is to be

adopted, the statement "EMPOX = 1" is added to the optional data.

Separate analyses of reduced and oxidized species allow the calculation of pE values which may be compared with each other or the measured pE to estimate the degree of internal redox equilibrium. Two such pairs are sulfide-sulfate and ammonia-nitrate. The equilibrium between sulfide and sulfate can be written,

$$H_2S+4H_2O=SO_4^{-2}+10H^++8e^-, \quad (45)$$

and the mass action expression can be rearranged to give

$$pE=(\log K+\log a_{SO_4^{-2}}-\log a_{H_2S}-10pH-4\log a_{H_2O})/8. \quad (46)$$

Similarly, the equilibrium between ammonium and nitrate yields the expression

$$pE=(-\log K+\log a_{NO_3^-}-\log a_{NH_4^+}-10pH-3\log a_{H_2O})/8. \quad (47)$$

These quantities, PE CALC S and PE CALC N, are calculated in WATEQ.

GAS PARTIAL PRESSURES

Although gas partial pressures are seldom measured in natural waters, in some solutions they may be calculated from the gas solubility constants and the water analysis. The partial pressures of CO_2, O_2, and CH_4 are calculated from the following equations,

$$\log P_{CO_2}=\log K+\log a_{HCO_3^-}+\log a_{H^+}-\log a_{H_2O}, \quad (48)$$

$$\log P_{O_2}=\log K'+2\log a_{H_2O}+4pH+4pE, \quad (49)$$

$$\log P_{CH_4}=\log K''+\log a_{HCO_3^-}-9pH-9pE-3\log a_{H_2O}. \quad (50)$$

ACTIVITY OF WATER

The activity of water is calculated in WATEQ by the approximate relation (Garrels and Christ, 1965, p. 66)

$$a_{H_2O}=1-0.017\Sigma m_i. \quad (51)$$

where Σm_i is the sum of the molalities of dissolved anions, cations, and neutral species. The equation yields reasonable values if Σm_i is less than molal.

INPUT

Input to WATEQ consists of a complete chemical analysis of the water sample and field measurements of its temperature and pH. If available, measurements of Eh and dissolved oxygen as well as some trace element analyses may be included. In order to allow the inclusion of optional data, the last space on the first card is coded with ISTDATA which is the number of cards containing the necessary data including the normal chemical analysis and the sample description. Cards after the chemical analysis are used for optional data. A blank card must be included after each data set to separate data sets. The required data is coded in free field (that is, one space between each number) in the order indicated below. See list of identifiers in the complete computer program for detailed descriptions. Sample sets of data are given with the resulting printout after the program.

Card 1 . . . . Sample Description (79 spaces) and ISTDATA (space 80).
Card 2 . . . . TEMP, PH, EHM (in volts, code 9.9 if data is not available), FLAG (='PPM', 'MG/L', 'MEQ/L' or 'MOL').
Card 3 . . . . Chemical analysis in PPM, MG/L, and MEQ/L or MOL/L (set FLAG) in the order Ca, Mg, Na, K, Cl, SO_4, HCO_3, Fe, H_2S, CO_3, SiO_2, NH_4, B, PO_4, Al, F, NO_3.
Succeeding cards . . . . Other data (identifier, equality sign, numerical value, and comma) including: "DENS=□" (if not specified, density is set equal to 1); if alkalinity is corrected for noncarbonate alkalinity "CORALK=1," (omitted if not corrected); electrical potential (volts) of the Eh cell including the calomel reference electrode "EHMC=□,"; electrical potential (volts) of the Eh cell with Zobell's solution for calibration, "EMFZSCE=□,"; parts per million of dissolved oxygen, "DOX=□,"; and certain trace elements including Li (I=80), Sr (I=87), Ba (I=89) in the form, "CUNITS(I)=□,". A semicolon in place of a comma follows the last data statement.
Last card . . . . Blank.

REFERENCES CITED

Akerlof, G. C., and Oshery, H. I., 1950, The dielectric constant of water at high temperatures and in equilibrium with its vapor: Am. Chem. Soc. Jour., v. 72, p. 2844–2847.

Barnes, H. L., Helgeson, H. C., and Ellis, A. J., 1966, Ionization constants in aqueous solutions: Geol. Soc. America Mem. 97, 401–413.

Bates, R. G., Staples, B. R., and Robinson, R. A., 1970, Ionic hydration and single ion activities in unassociated chlorides at high ionic strength: Anal. Chemistry, v. 42, No. 8, p. 867–871.

Bell, R. P., and George, J. H. B., 1953, The incomplete dissociation of some thallous and calcium salts at different temperatures: Faraday Soc. Trans., v. 49, p. 619–627.

Berner, R. A., 1967, Comparative dissolution characteristics of carbonate minerals in the presence and absence of aqueous magnesium ion: Am. Jour. Sci., v. 265, p. 45–70.

——1967, Thermodynamic stability of iron sulfides: Am. Jour. Sci., v. 265, p. 773–785.

Bricker, O. P., 1969, Stability constants and Gibbs free energies of formation of magadiite and kenyaite: Am. Mineralogist, v. 54, p. 1026–1033.

Brown, W. E., 1960, Behavior of slightly soluble calcium phosphates as revealed by phase-equilibrium calculations: Soil Sci., v. 90, p. 51–57.

Christ, C. L., Hostetler, P. B., and Siebert, R. M., 1973, Studies in the system MgO-SiO_2-CO_2-H_2O(III): the activity-product constant of sepiolite: Am. Jour. Sci., No. 293, p. 65–83.

Chughtai, A., Marshall, R., and Nancollas, G. H., 1968, Complexes in calcium phosphate solutions: Jour. Phys. Chemistry, v. 72, p. 208–211.

Davies, C. W., 1962, Ion Association: Washington, Butterworths, 190 p.

Denbigh, Kenneth, 1955, The Principles of Chemical Equilibrium: Cambridge, England, University Press, 491 p.

D'yachkova, I. B., and Khodakovskiy, I. L., 1968, Thermodynamic equilibria in the systems S-H_2O, Se-H_2O and Te-H_2O in the 25–300°C temperature range and their geochemical interpretatons: Geochemistry Internat., p. 1108–1125.

Ellis, A. J., 1967, The chemistry of some explored geothermal systems, *in* Barnes, H. L., ed., Geochemistry of hydrothermal ore deposits: New York, Holt, Rinehart, Winston, p. 465–514.

Ellis, A. J., and McFadden, I. M., 1972, Partial molal volumes of ions in hydrothermal solutions: Geochim. et Cosmochim. Acta, v. 36, p. 413–426.

Fournier, R. O., 1973, Silica in thermal waters: Laboratory and field investigations, *in* Proceedings of International Symposium on Hydrogeochemistry and Biochemistry, Japan 1970: Washington, D.C., J. W. Clarke, p. 122–139.

Garrels, R. M., and Christ, C. H., 1965, Solutions, minerals, and equilibria: New York, Harper & Row, 450 p.

Garrels, R. M., and Thompson, M. E., 1962, A chemical model for sea water at 250°C and one atmosphere total pressure: Am. Jour. Sci., v. 260, p. 57–66.

Garrels, R. M., Thompson, M. E., and Siever, Raymond, 1961, Control of carbonate solubility by carbonate complexes: Am. Jour. Sci., v. 259, p. 24–25.

Hamer, W. J., 1968, Theoretical mean activity coefficients of strong electrolytes in aqueous solutions from 0 to 100°C: U.S. Natl. Bur. Standards, Natl. Standard Reference Data Ser. 24, 271 p.

Hanna, E. M., Pethybridge, A. D., and Prue, J. E., 1971, Ion association and the analysis of precise conductimetric data: Electrochim. Acta, v. 16, p. 677–686.

Harned, H. S., and Owen, B. B., 1958, The physical chemistry of electrolytic solutions [3d ed.]: New York, Reinhold, 803 p.

Helgeson, H. C., 1969, Thermodynamics of hydrothermal systems at elevated temperatures and pressures: Am. Jour. Sci., Vo. 267, p. 729–804.

Hem, J. D., 1968, Graphical methods for studies of aqueous aluminum hydroxide, fluride and sulfate complexes: U.S. Geol. Survey Water-Supply Paper 1827-B, 33 p.

Hem, J. D., and Roberson, C. E., 1967, Form and stability of aluminum hydroxide complexes in dilute solution: U.S. Geol. Survey Water-Supply Paper 1827-A, 55 p.

Hem, J. D., Roberson, C. E., Lind, C. J., and Polzer, W. L., 1973, Chemical interactions of aluminum with aqueous silica at 25°C: U.S. Geol. Survey Water-Supply Paper 1827-E, 57 p.

Hemingway, B. S., and Robie, R. A., 1973, A calorimetric determination of the standard enthalpies of formation of huntite, $CaMg_3(CO_3)_4$, and artinite, $Mg_2(OH)_2CO_3 \cdot 3H_2O$, and their standard Gibbs free energies of formation: U.S. Geol. Survey Jour. Research, v. 1, No. 5, p. 535–541.

Hemley, J. J., Hostetler, P. B., Gude, A. J., and Mountjoy, W. T., 1969, Some stability relations of alunite: Econ. Geology, v. 64, p. 599–612.

Hess, P. C., 1966, Phase equilibria of some minerals in the K_2O-NA_2O-Al_2O_3-SiO_2-H_2O system at 25°C and 1 atmosphere: Am. Jour. Sci., v. 264, p. 289–309.

Hostetler, P. B., 1963a, Complexing of magnesium with bicarbonate: Jour. Phys. Chemistry, v. 67, p. 720–721.

——1963b, The stability and surface energy of brucite in water at 25°C: Am. Jour. Sci., v. 261, p. 238–258.

Hostetler, P. B., and Christ, C. L., 1968, Studies in the system MgO-SiO_2-CO_2-H_2O (I): The activity-product constant of chrysotile: Geochim. et Cosmochim. Acta, v. 32, p. 485–497.

Hostetler, P. B., Hemley, J. J., Christ, C. O., and Montoya, J. J., 1971, Talc-chrysotile equilibrium in aqueous solutions: Geol. Soc. America Abs, with Programs v. 3, p. 605.

Izatt, R. M., Eatough, Delbert, Christensen, J. J., and Bartholomew, C. H., 1969, Calorimetrically determined log K, $\Delta H°$, and $\Delta S°$ values for the interaction of sulphate ion with several bi- and ter-valent metal ions: Chem. Soc. [London] Jour., sec. A, pt. 1, p. 47–53.

Keenan, J. H., and Keys, Frederick, 1936, Thermodynamic properties of steam: New York, John Wiley and Sons, Inc., 89 p.

Kielland, J., 1937, Individual activity coefficients of ions in aqueous solutions: Am. Chem. Soc. Jour., v. 59, p. 1675–1678.

Kittrick, J. A., 1966, Free energy of formation of kaolinite from solubility measurements: Am. Mineralogist, v. 51, p. 1457–1466.

——1971a, Stability of montmorillonites: I. Belle Fourche and Clay Spur montmorillonites: Soil Sci. Soc. America Proc., v. 35, p. 140–145.

——1971b, Stability of montmorillonites: II. Aberdeen montmorillonite: Soil Sci. Soc. America Proc., v. 35, p. 820–823.

Lafon, G. M., 1969, Some quantitative aspects of the chemical evolution of the oceans: Northwestern Univ., Ph. D. dissert., 136 p.

Lafon, G. M., and Truesdell, A. H., 1971, Temperature dependence of sodium sulfate complexing in aqueous solutions [abs.]: Am. Geophys. Union Trans., v. 52, p. 362.

Langmuire, Donald, 1969, The Gibbs free energies of substances in the system Fe-O_2-H_2O-CO_2 at 25°C, *in* Geological Survey research 1969: U.S. Geol. Survey Prof. Paper 650-B, p. B180–B183.

——1971, Particle size effect on the reaction geothite-hematite + water: Am. Jour. Sci, v. 271, p. 147–156.

Latimer, W. M., 1952, The oxidation states of the elements and their potential in aqueous solutions [2d ed.]: New York, Prentice-Hall, Inc., 392 p.

Lietzke, M. H., Stoughton, R. W., and Young, T. F., 1961, The bisulfate acid constant from 25 to 225° as computed from solubility data: Jour. Phys. Chemistry, v. 65, p. 2247–2249.

Linke, M. F., and Seidell, A., 1965, Solubilities of inorganic and metal-organic compounds: Washington, Am. Chem. Soc., v. 2, 1914 p.

MacInnes, D. A., 1939, The principles of electrochemistry: New York, Reinhold, 478 p.

Malmberg, C. G., and Maryott, A. A., 1956, Dielectric constant of water from 0° to 100°C: U.S. Natl. Bur. Standards Jour. Research, v. 56, p. 1–8.

Mesmer, R. E., Baes, C. F., Jr., and Sweeton, F. H., 1972, Acidity measurements at elevated temperatures: VI. Boric acid equilibria: Inorganic Chemistry, v. 11, No. 3, p. 537–543.

Nriagu, J. O., 1971, Solubility studies on vivianite and strengite: Geol. Soc. America Abs. with Programs, v. 3, p. 662.

——1972a, Solubility equilibrium constant of strengite: Am. Jour. Sci., v. 272, p. 476–484.

——1972b, Stability of vivianite and ion pair formation in the system $Fe_3(PO_4)_2$-H_3PO_4-H_2O: Geochim. et Cosmochim. Acta, v. 36, p. 459–470.

Pytkowicz, R. M., and Kester, D. R., 1969, Harned's rule behavior of NaCl-Na_2SO_3 solutions explained by an ion-association model: Am. Jour. Sci., v. 267, p. 217–229.

Reesman, A. L., and Keller, W. D., 1968, Aqueous solubility studies of high-alumina and clay minerals: Am. Mineralogist, v. 53, p. 929–942.

Roberson, C. E., 1966, Solubility implications of apatite in sea water, *in* Geological Survey research 1966: U.S. Geol. Survey Prof. Paper 550-D, p. D178–D185.

Robie, R. A., and Hemingway, B. S., 1973, The enthalpies of formation of nesquehonite, $MgCO_3 \cdot 3H_2O$, and hydromagnesite, $5MgO \cdot 4CO_2 \cdot 5H_2O$: U.S. Geol. Survey Jour. Research, v. 1, No. 5, p. 543–547.

Robie, R. A., and Waldbaum, D. R., 1968, Thermodynamic properties of minerals and related substances at 298.15°K (25.0°C) and one atmosphere (1.013 bars) pressure and at higher temperatures: U.S. Geol. Survey Bull. 1259, 256 p.

Robinson, R. A., and Stokes, R. H., 1955, Electrolyte solutions: London, Butterworths Scientific Publications. 559 p.

Rossini, F. D., Wagman, D. D., Evans, W. H., Levine, Samuel, and Jaffe, Irving, 1952, Selected values of chemical thermodynamic properties: U.S. Natl. Bur. Standards Circ. 500, 1,268 p. Part I. Tables, p. 1–822, reprinted in 1961.

Ryzhenko, B. N., 1963, Determination of dissociation constants of carbonic acid and the degree of hydrolysis of the CO_3^{-2} and HCO_3^- ions in solutions of alkali carbonates and bicarbonates at elevated temperatures: Geochemistry, No. 2, p. 151-163; translated from Geokhimya.

——1967, Determination of the hydrolysis of sodium silicate and calculation of dissociation constants of orthosilicic acid at elevated temperatures: Geochemistry Internat., v. 4, p. 99–107.

Sato, Motaki, 1960, Oxidation of sulfide ore bodies: Econ. Geology, v. 55, p. 928–1231.

Sillen, L. G., and Martell, A. E., 1964, Stability complexes of metal-ion complexes: Chem. Soc. [London] Spec. Pub. 17, 754 p.

Smith, R. M., and Alberty, R. A., 1956, The apparent stability constants of ionic complexes of various adenosine phosphates with monovalent cations: Jour. Phys. Chemistry, v. 60, p. 180–184.

Sweeton, F. H., and Baes, C. F., Jr., 1970, The solubility of magnetite and hydrolysis of ferrous iron in aqueous solutions at elevated temperatures: Jour. Chem. Thermodynamics, v. 2, No. 4, p. 479-500.

Truesdell, A. H., 1968, The advantage of using pE rather than Eh in redox equilibrium calculations: Jour. Geol. Education, v. 16, p. 17–20.

Truesdell, A. H., and Hostetler, P. B., 1968, Dissociation constants of KSO_4^- from 10° to 50°C: Geochim. et Cosmochim. Acta, v. 32, p. 1019–1022.

Truesdell, A. H., and Jones, B. F., 1969, Ion association in natural brines: Chem. Geology, v. 4, p. 51–62.

Wagman, D. D., Evans, W. H., Parker, V. B., Halow, I., Baily, S. M., and Schumm, R. H., 1968, Selected values of chemical thermodynamic properties: U.S. Natl. Bur. Standards Tech. Note 270-3, 264 p.

——1969, Selected values of chemical thermodynamic properties: U.S. Natl. Bur. Standards Tech. Note 270-4, 141 p.

Walker, A. C., Bray, U. B., and Johnson, John, 1927, Equilibrium in solutions of alkali carbonates: Am. Chem. Soc. Jour., v. 49, p. 1235–1256.

Waterfield, C. G., Linford, R. G., Goalby, B. B., Bates, T. R., Elyard, C. A., and Staveley, L. A. K., 1968, Thermodynamic investigation of disorder in the hydrates of sodium carbonate: Faraday Soc. Trans., v. 64, p. 868–874.

Wollast, Roland, Mackenzie, F. T., and Bricker, O. P., 1968, Experimental precipitation and genesis of sepiolite at Earth-surface conditions: Am. Mineralogist, v. 53, p. 1645–1662.

Wright, J. M., Lindsay, W. T., Jr., and Druga, T. R., 1961, The behavior of electrolytic solutions at elevated temperatures as derived from conductance measurements: Washington, D.C., U. S. Atomic Energy Comm. R & D rept. WAPD-TM-204, 32 p.

Yeatts, L. B., and Marshall, W. L., 1972, Solubility of calcium sulfate dihydrate and association equilibria in several aqueous mixed electrolyte salt systems at 25°C: Jour. Chem. and Eng. Data, v. 17, p. 163–168.

Zen, E-an, 1972, Gibbs energy, enthalpy, and entropy of ten rock-forming minerals, calculations, discrepancies, implications: Am. Mineralogist, v. 57, p. 524–553.

Jour. Research U.S. Geol. Survey
Vol. 2, No. 2, Mar.-Apr. 1974, p. 249—252

HYDROGEOLOGY OF ANTIETAM CREEK BASIN

By LARRY J. NUTTER, Parkville, Md.

Work done in cooperation with the Maryland Geological Survey

Abstract.—The Antietam Creek basin in the Great Valley of Maryland and Pennsylvania is underlain almost entirely by intensely folded and faulted lower Paleozoic carbonate rocks. The ground-water discharge of the basin is about 85 percent of the total discharge, in contrast with less than 70 percent of the total discharge in two small basins underlain by igneous and metamorphic rocks in the Maryland Piedmont. Large quantities of ground water are stored in a thick residual mantle, which overlies the carbonate rocks in the valley and adjacent metamorphic rocks in mountain areas on the east edge of the basin. Streams that flow off the mountain areas are major sources of recharge to the carbonate-rock aquifers. Several streams lose a large part of their flow within a mile after reaching the carbonate rocks in the valley, and a few flow directly into swallow holes (sinkholes). The low density of perennial streams in the basin is a result of subsurface drainage through solution cavities along joints, faults, and bedding in the carbonate rocks. The major orientations of straight stream reaches along Antietam Creek and the strikes of major joint sets in quarries are nearly coincident, suggesting that the stream network throughout the basin is joint controlled.

Carbonate-rock aquifers in the Great Valley and the Frederick Valley of Maryland are among the most productive in the State. Recognizing the importance of these aquifers, the U.S. Geological Survey, in cooperation with the Maryland Geological Survey, undertook a study of the hydrogeology of the Great Valley and the Frederick Valley. Antietam Creek basin in the Great Valley (fig. 1) was used as a type area because it is almost entirely underlain by carbonate rocks and because streamflow and weather records were available for the basin. The purpose of the study was to evaluate the relationship between ground-water runoff and surface runoff within the basin and to investigate the role of the thick residual mantle on the east margin of the basin in storing ground water and transmitting it to the underlying carbonate rocks.

Antietam Creek basin drains a large part of the Great Valley in western Maryland and extends northward into Pennsylvania. Nearly 90 percent of the basin is in the Great Valley, which is underlain by intensely folded and faulted Cambrian and Ordovician carbonate rocks (fig. 1). The remaining part is in the Blue Ridge physiographic province, which is underlain by Lower Cambrian and Precambrian metamorphic rocks.

HYDROGEOLOGY

General features

Water in the bedrock occurs almost exclusively in joints, faults, bedding-plane partings, and in solution cavities along these features (fig. 2). Water also occurs in the residuum that overlies the carbonate rocks throughout most of the basin and in thick mountain wash that overlies the bedrock along the east margin of the basin (fig. 1). The term "residuum," as used in this paper, refers to a mantle of relatively insoluble material that is left after soluble rock material is dissolved and removed, chiefly by percolating recharge water (fig. 2). The original rock structures are only partly preserved, if at all, in the residuum. Mountain wash refers to thick deposits that, in most places, are probably entirely composed of colluvium. However, in some places the mountain wash seems to include colluvium that is underlain by thick residual clay.

Hydrologic equation

Streamflow records from Sharpsburg and precipitation records from Hagerstown for 1951-70 were used in the hydrologic equation for Antietam Creek basin, where the surface-water and ground-water divides are fairly coincident and import or export of water is small. The basic equation is

$$P=Rg+Rs+ET\pm\Delta s,$$

where P is the precipitation, Rg is the ground-water runoff, Rs is the surface-water runoff, ET is the evapotranspiration, and Δs is the change in ground-water storage. All terms are expressed in inches.

The other factors to be considered in a hydrologic equation include the change in soil moisture, flow of ground water across basin divides or underflow past the gage, and diversions of water to or from the basin. All these factors seem to be negligible in the study area, or appropriate adjustments have been made. The change in soil moisture is negligible if a period of several years is considered. The ground-water basin divide seems to coincide with the surface-water basin divide, and there are no data to indicate that significant quantities of

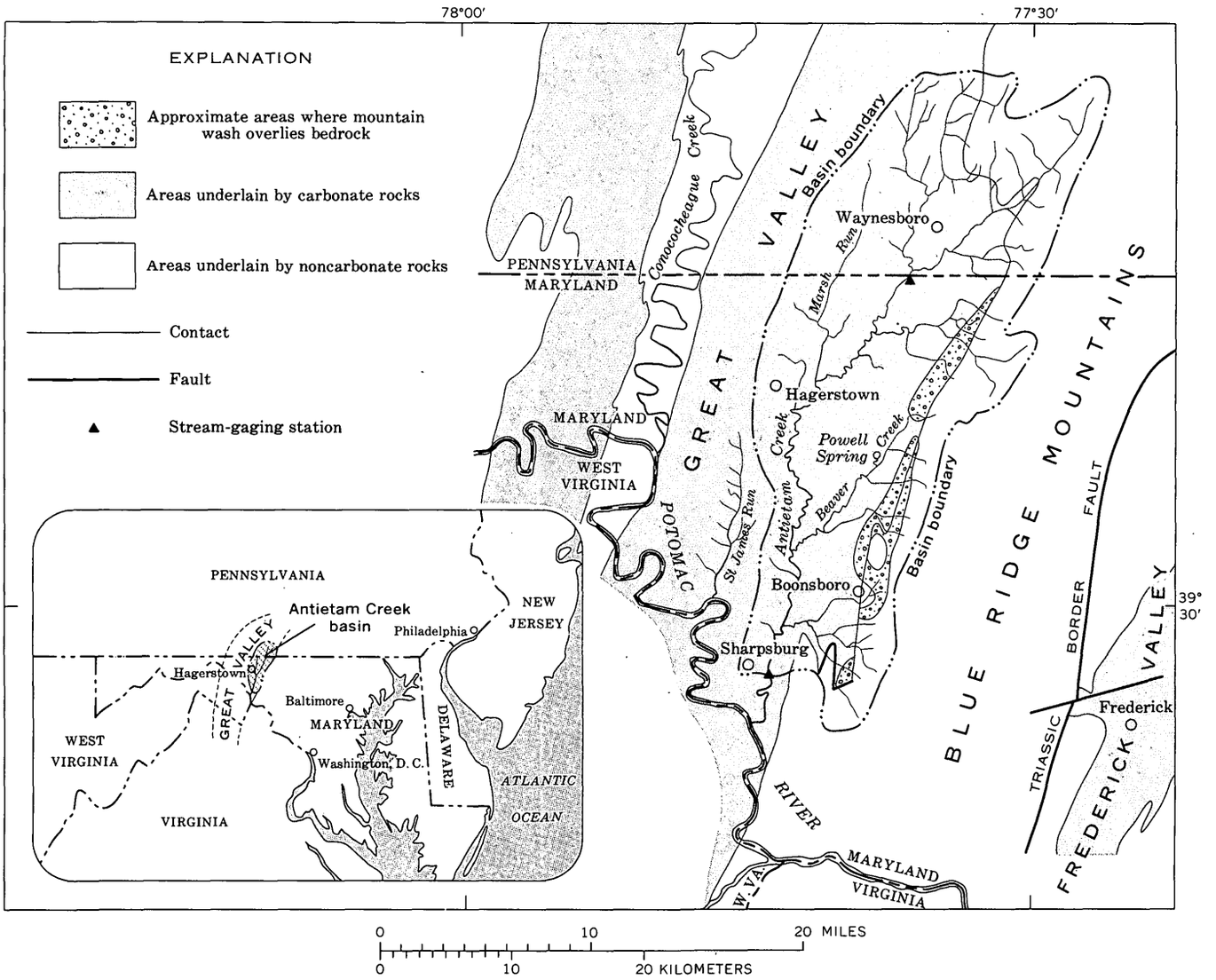

Figure 1.—Antietam Creek basin and areas underlain by carbonate rocks and mountain wash deposits. Geology adapted from Cloos (1941) and Gray and others (1960).

ground water flow under the gage. Water imported from outside the basin enters Antietam Creek through the sewage-treatment plant, but the streamflow data used in preparing the water budget have been adjusted for the imported water.

In the hydrologic equation the streamflow is represented by *Rg* and *Rs*. The relative proportion of *Rg* and *Rs* was determined by hydrograph separation, a method of determining ground-water runoff and surface runoff by using a hydrograph of the mean daily discharge. The change in ground-water storage (Δs) over a long period is considered to be zero. During years of above-normal precipitation, Δs is positive; during years of below-normal precipitation, Δs is negative. The value of Δs for short periods can be determined from observation-well records, or it can be computed as a residual if the other elements in the equation are known. Evapotranspiration (*ET*) is commonly computed as a residual, or it can be determined by formulas involving heat energy (Thornthwaite and Mather, 1955).

The following represent average annual quantities for the hydrologic equation determined for Antietam Creek basin above the streamflow gage near Sharpsburg during 1951–70:

$$P=(Rg+Rs)+ET\pm\Delta s,$$

or $$35.39=(11.48)+ET+0,$$

and therefore $ET=23.91$ inches (60.73 cm).

On the basis of hydrograph separations of the 1967 and 1970 water years (October through September) for the Antietam Creek gaging stations near Sharpsburg and near Waynesboro, the ground-water runoff (*Rg*) from the basin is about 85 percent of the total discharge. The long-term average discharge of Antietam Creek near Sharpsburg (drainage area 281 mi^2, or 452 km^2 is 256 ft^3/s(7.25 m^3/s). During the 1967

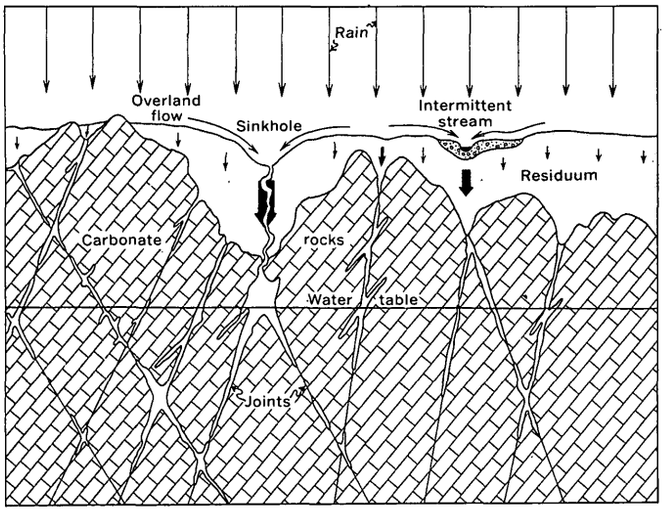

Figure 2.—Schematic diagram showing localized recharge and control of solution cavities by joints and bedding in carbonate rocks. (Not drawn to scale.)

water year, the average discharge was 244 ft^3/s (6.91m^3/s), slightly below the long-term average; during the 1970 water year, the average discharge was 311 ft^3/s (8.81 m^3s), substantially above the long-term average. Ground-water discharge at the Sharpsburg gage was 87 percent of the total discharge in 1970 and 88 percent of the total discharge in 1967. At the Waynesboro gage (drainage area 93.5 mi^2, or 150 km^2), the ground-water discharge was 82 percent of the total discharge in 1970 and 84 percent of the total discharge in 1967.

In contrast, the ground-water discharge of two small basins underlain by igneous and metamorphic rocks in the Maryland Piedmont was computed to be slightly less than 70 percent of the total discharge (Dingman and Meyer, 1954, p. 39; Dingman and Ferguson, 1956, p. 52). The water budget of these two basins seems to be typical of most areas in the Maryland Piedmont.

Recharge

The abundance of large springs, the high base flow, and the low density of perennial streams all indicate that ground-water bodies are recharged readily in the study area.

The thick wash along the mountain areas bordering the Antietam Creek basin on the east stores large quantities of water and slowly recharges the underlying carbonate rocks. The permeability of the wash is generally low, but the storage capacity is high. This wash, in places more than 400 ft (122 m) thick, is mostly colluvium composed of boulders, cobbles, and sand, usually in a clay matrix. In places, the apparent great thickness may be caused by thick residual clay beneath the colluvium, as in the Shenandoah Valley of Virginia (Hack, 1965, p. 67). The thickest deposits of residual clay beneath the colluvium are at the contact between the Antietam Quartzite and the Tomstown Formation (fig. 3). The great thickness is apparently due to the reaction of the slightly acid ground water percolating through the quartzite with the soluble carbonate-rock material at the contact.

Streams that flow off the mountain areas are major sources of recharge to the carbonate rocks. Several, which begin in Precambrian metamorphic rocks of the Blue Ridge physiographic province, lose large quantities of water within a mile after reaching the carbonate rocks in the valley. Discharge measurements of several of the small streams flowing off the mountain areas confirmed this loss. A few flow directly into swallow holes (sinkholes). Thus, the recharge per square mile in the valley adjacent to the mountain area is substantially greater than in other areas in the Great Valley.

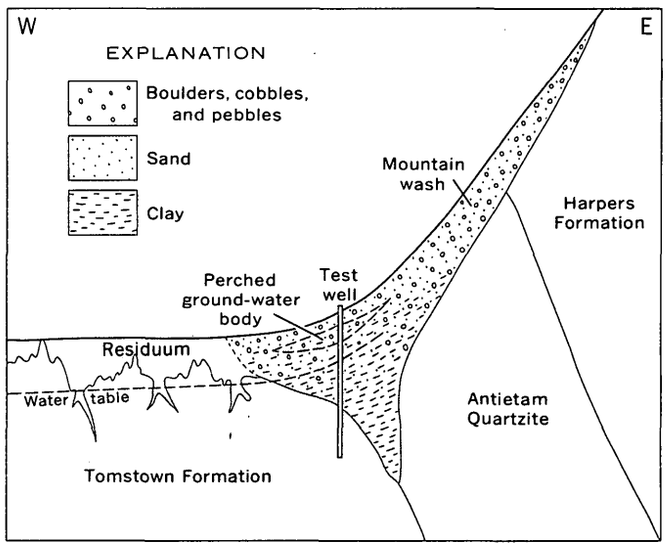

Figure 3.—Schematic cross section showing mountain wash deposits and perched ground-water body. (Not drawn to scale.)

Wells drilled to the bedrock are expensive and difficult to construct in areas of thick mountain wash. Many homeowners in these areas use either cisterns or shallow wells tapping the local perched ground-water bodies within the wash (fig. 3).

Stream network

One of the most common features of areas underlain by carbonate rocks is the low density of perennial streams, as contrasted to the densities in areas underlain by most other rock types. Study of the stream network of Antietam Creek basin reveals that most 7½-minute quadrangle maps of the area show more perennial streams than exist. In many of the valleys, streams shown on quadrangle maps as perennial actually flow only immediately after heavy rain.

Nearly all the base flow in the basin originates from discrete springs. The combined discharge of the three springs forming the headwaters of an unnamed tributary to Marsh Run, which flows into Antietam Creek northeast of Hagerstown, was

found to be equal to the total flow of the tributary. The same conditions were observed in St. James Run west of Hagerstown (Slaughter, 1962, p. 51) and in Rocky Fountain Run in the Frederick Valley (Nutter, 1973).

The springs in the basin are numerous, and many discharge large quantities of water. Powell Spring north of Boonsboro often discharges more than 3,000 gal/min (189 l/s). Some springs act as relief valves—they flow when the water table is above the point of discharge, and they cease to flow when the water table drops below the point of discharge, generally in late summer.

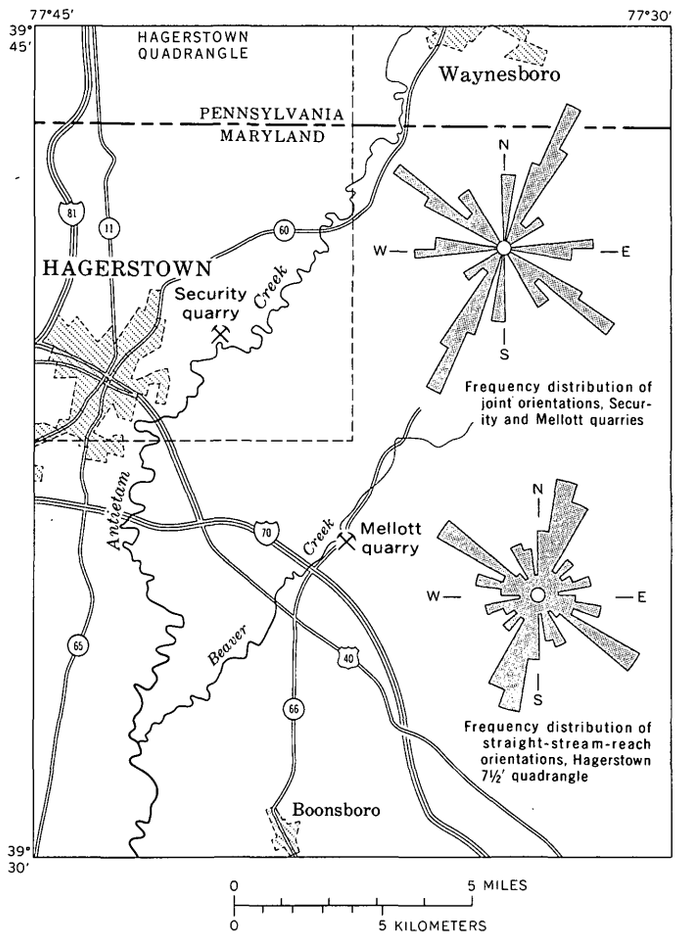

Figure 4.—Drainage pattern of a reach of Antietam Creek and orientation of joints and straight stream segments.

Antietam Creek is a classic example of a joint-controlled drainage pattern (fig. 4). Comparison of rose diagrams showing the orientation of straight stream reaches, measured from 7½-minute quadrangle maps, and joint strikes, measured in quarries and outcrops, indicate a good correlation between joint strikes and stream azimuths. Because solution cavities primarily occur along joint planes in the carbonate rocks of the basin, the correlation between the orientation of straight stream reaches and joint strikes should be helpful in locating wells to obtain moderately large supplies of ground water. Test-drilling sites along extensions of straight stream reaches or at projected intersections of two straight reaches are likely to be located where conditions for penetrating solution cavities are favorable.

REFERENCES CITED

Cloos, Ernst, 1941, Geologic map of Washington County, Maryland: Maryland Geol. Survey.

Dingman, R. J., and Ferguson, H. F., 1956, The ground-water resources of the Piedmont part, *in* The water resources of Baltimore and Harford Counties: Maryland Dept. Geology, Mines and Water Resources. Bull. 17, p. 1–128.

Dingman, R. J., and Meyer, Gerald, 1954, The ground-water resources, *in* The water resources of Howard and Montgomery Counties: Maryland Dept. Geology, Mines and Water Resources Bull. 14, p. 1–139.

Hack, J. T., 1965, Geomorphology of the Shenandoah Valley, Virginia and West Virginia, and origin of the residual ore deposits: U.S. Geol. Survey Prof. Paper 484, 84 p.

Gray, Carlyle, and others (compilers and editors), 1960, Geologic map of Pennsylvania: Pennsylvania Geol. Survey.

Nutter, L. J., 1973, Hydrogeology of the carbonate rocks, Frederick and Hagerstown Valleys, Maryland: Maryland Geol. Survey Rept. Inv. 19, 70 p.

Slaughter, T.H., 1962, The ground-water resources, *in* The water resources of Allegany and Washington Counties: Maryland Dept. Geology, Mines and Water Resources Bull. 24, p. 1–243.

Thornthwaite, C. W., and Mather, J. R., 1955, The water balance: Drexel Inst. Tech., Pub. in Climatology, v. 8, no. 1, 104 p.

Jour. Research U.S. Geol. Survey
Vol. 2, No. 2, Mar.-Apr. 1974, p. 253—257

RATES OF SALT SOLUTION IN THE PERMIAN BASIN

By FRANK A. SWENSON, Denver, Colo.

Work done in cooperation with the U.S. Atomic Energy Commission

Abstract.—For safe, long-term storage of radioactive materials in salt beds, rates of solution of salt which might imperil such storage must be known. For solution to continue, fluid must move through the system. Major fluid discharge from the system is by surface streams. Using U.S. Geological Survey records of streamflow and chemical quality of water, computations of sodium chloride discharges of numerous subbasins have been made. A map has been constructed showing tons of sodium chloride discharged per day and tons of sodium chloride discharged per square mile per year. Also shown are locations of major saline springs and their rate of discharge of sodium chloride in tons per day.

The Permian basin, underlying western Texas, Oklahoma, Kansas, and adjacent eastern parts of New Mexico and Colorado, is a region characterized by a series of bedded halite and associated evaporite deposits in a thick sedimentary sequence largely of Permian age. The thick accumulation of sediments and included salts was deposited in a series of sedimentary basins that were not contemporaneous, so that there are numerous discontinuous salt beds. In general, the salt deposits in Kansas and Oklahoma are older than those to the south, those in the Delaware basin of southeastern New Mexico and adjacent Texas being the youngest.

The salt beds of the Permian basin have been considered for the proposed storage of radioactive materials, and it is important to determine the relative rate of salt solution, which might imperil the long-term safe storage of such materials. In order for solution to continue, there must be movement of water through the system; otherwise water in contact with the salt will become saturated and no further solution will take place.

The major fluid discharge from the system is by surface flow in the streams draining the area. They carry the overland flow and the small amounts of ground-water inflow.

It is known that considerable amounts of sodium chloride are carried by the Arkansas, Canadian, Red, Trinity, Brazos, Colorado, and Pecos Rivers as they leave the area. Numerous streamflow and chemical quality of water measurement stations have been established on these streams, and somewhat detailed studies have been made of fairly localized areas. Using the data gathered at these sites over a period of years (U.S. Geological Survey, 1964, 1966, 1967, 1968, 1969, 1970, 1971) and making certain assumptions and computations, I have been able to compute the approximate rate of salt solution for various subbasins of the major streams draining the Permian basin.

All bedrock formations, from the Santa Rosa Sandstone of Triassic age to the basement rocks of Precambrian age, contain strongly saline water, except locally near outcrops where they may be flushed by recharge. From potentiometric maps prepared by McNeal (1965) and P. R. Stevens, U.S. Geological Survey (written commun., 1972), probable fluid movement through all formations bearing saline ground water is from west to east with local variations. The strongly saline water is under sufficient artesian pressure in all formations to maintain a water column close to the land surface across much of the area. Natural hydraulic interconnections between formations are provided by faults, joints, unconformities which truncate beds, and locally by reefs which may transect boundaries. The thousands of oil and gas tests which have been drilled in the area also provide hydraulic interconnections between the formations. Although potentiometric data indicate easterly movement of fluids, the actual quantity and rate of movement across the entire basin is very small. Using the best data he could obtain in a comprehensive ground-water study, Stevens (written commun., 1972) states that the average velocity of water movement in the Santa Rosa Sandstone is about 0.4 ft/yr. At that rate it would take at least 2.5 m.y. for a water molecule to cross the Permian basin from recharge areas on the west to discharge areas on the east. Stevens estimates that the average velocity of water movement in the San Andres Limestone of Permian age is about 0.015 ft/yr. The recharge areas of the San Andres lie west and the discharge areas lie east, respectively, of the recharge and discharge areas of the Santa Rosa Sandstone. At that rate and increased distance, the time required for a water molecule to cross the Permian basin may be about 80 m.y.

POTENTIAL SALT SOLUTION AT DEPTH

Few specific data are available regarding the potential for salt solution at depths of more than a few hundred feet. As indicated earlier, for any major solution to take place, water must circulate through the system in order to move saturated

solutions out and bring less mineralized fluids into contact with the salt. Much of our evidence bearing on this problem is qualitative in character but will be discussed here because it has an important bearing on the safe, long-term storage of radioactive materials in salt beds at depth. Before any such storage takes place, exhaustive studies must be made.

As may be seen from the map (fig. 1), the major discharge of salt into surface streams is closely related to the geology and topography of the Permian basin. The salt-bearing beds are exposed, or are at very shallow depth, around the flanks of the High Plains, and at these locations salt is discharged from the system. It is known that salt beds exist at depth under much of the area, and to the north and east under Kansas, yet in these areas little or no salt is discharged from the hydrologic system into the streams, which would tend to indicate that major solution does not take place at depths of more than a few hundred feet.

Sinkholes develop in areas where salt is no deeper than several hundred feet from the land surface. Where beds are more deeply buried, there are no indications of sinks (Williams and Lohman, 1949 p. 83–87). Stratigraphic studies based on test holes often indicate thinning of salt-bearing formations for some distances downdip from exposures, but there are few records of such thinning of formations at greater depths which can be attributed to solutional action.

Salt beds are among our least permeable materials, and salt mines hundreds of feet below the water table are invariably dry. Clearly, solution of salt can only take place on the upper, and possibly the lower, parts of thick-bedded salt deposits, except where beds are exposed to surface recharge. In some places the tops of salt beds are marked by a breccia zone formed by collapse of overlying beds where salt has been dissolved. In some places such rubble zones at the upper surface of salt beds were formed shortly after the overlying beds were deposited when the salt beds were not yet deeply buried. Such zones, if they are water bearing, are characterized by the presence of saturated brines.

Some specific data regarding potential salt solution at depth were gathered in the course of a ground-water investigation of the Project Gnome area near Carlsbad, N. Mex. (Cooper, 1962). At this location, some 10 mi. east of the Pecos River and 25 mi. southeast of Carlsbad, the Permian rocks are exposed, or are mantled by a relatively thin sequence of Triassic and Pleistocene rocks. To the west, at lower elevations in the broad valley of the Pecos River, the Permian rocks are exposed and are marked by numerous sinkholes and other solutional features. There is a marked thinning of the Salado Formation toward the west, as determined by deep test holes. The top of the Salado Formation at a depth of 710 ft. is marked by a layer or residuum consisting of red silty clay and claystone with randomly oriented blocks of gypsum, siltstone, and polyhalite. At the shaft prepared for the nuclear explosion, this residuum layer was 60 ft. thick but did not contain any water (Cooper and Glanzman, 1971), although a similar but thicker residuum layer to the west, found at shallower depth, is known to contain a saturated brine. The Salado Formation itself is not known to contain any water, either in the nearby potash mines excavated far below the water table, or in any of the numerous drill holes scattered throughout the area. The salt is virtually impermeable, because the weight of the overlying formations causes plastic flow of the salt and prevents the development of any open spaces which might contain water.

NEAR-SURFACE SALT SOLUTION

Where salt and anhydrite-bearing rocks crop out, solution of salt, conversion of anhydrite to gypsum, and leaching of these materials has resulted in increased permeability through fracturing and collapse. Largely through these weathered zones local recharge enters to dissolve the salt underground; later it issues as salt springs along deeply cut stream courses where the salt-bearing Permian rocks are exposed on the eastern edge of the High Plains. Radioactive-isotope dating of spring discharge by Ward (1963) and Stevens (written commun., 1972) shows that most of the brine-spring discharge on the eastern side of the High Plains is meteoric water that has moved down from the land surface and moved short distances to the discharge area. Only a very minor part is old enough to be of connate origin or to have moved across the Permian basin from western exposure of these rocks.

SPECIFIC DATA

Sodium chloride discharges calculated from U.S. Geological Survey observations of the chemical quality of water from streams draining the area of interest are shown in figure 1. The major river basins are divided into subbasins at the gaging stations where sufficient water-quality data are available. On the map the computed tons of sodium chloride per day discharged by surface-water flow from each subbasin and the tons per square mile per year are shown. Most of the records are for the 1966 water year (U.S. Geological Survey, 1971). Locations of major saline springs and seeps are shown with tonnage of sodium chloride discharged per day. As data on the areas contributing to the spring discharge were not available, the tons of salt dissolved per square mile per year were not calculated.

Two subbasins in the Pecos River drainage show losses of sodium chloride, but these anomalous figures can be explained. Between the gaging stations at Artesia and Carlsbad, N. Mex., a loss of 330 tons of sodium chloride per day (43 tons $mi^{-2}yr^{-1}$) was recorded for 1966. Several factors explain this seemingly enigmatic situation. Considerable water, with contained salt, is lost by seepage from storage in the Lake McMillan reservoir between these gaging stations, and thus does not appear at the Carlsbad station. Much water is diverted for irrigation between these stations, and the water with its dissolved salt load does not pass the Carlsbad gage, although some of the diverted water and salt load returns via drains to

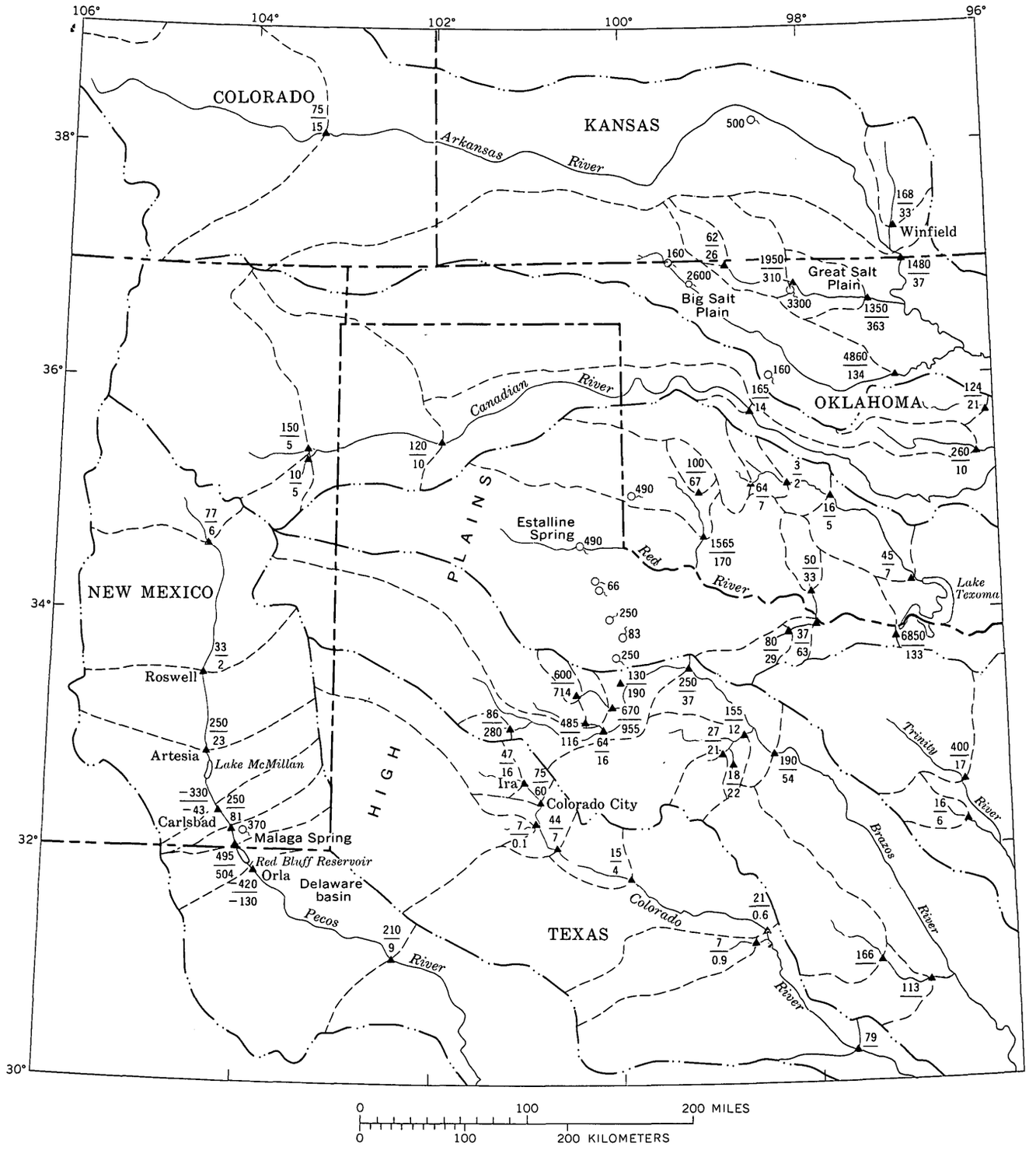

EXPLANATION

62/26 Subbasin gaging station. Upper number, total NaCl, in tons per day, for subbasin. Lower number, average NaCl, in tons per square mile of subbasin per year. Negative values indicate loss of NaCl

160 Major areas of salt springs and yield, in tons of NaCl per day

River basin boundary

Subbasin boundary

Figure 1.—Sodium chloride discharge via surface-water flow from subbasins of major streams draining the Permian basin. Map compiled by F. A. Swenson (1973)

the river below the Carlsbad gage. Between Red Bluff, N.Mex., and Orla, Tex., the Pecos River showed a loss of 420 tons of sodium chloride per day in 1966. This salt loss is believed to take place in the Red Bluff Reservoir. Concentrated brine solution is known to be present in the deeper parts of the reservoir, and precipitation of salt from the brine is believed to occur. There are significant annual variations in the ratio of salt discharge; for instance, in 1967 about 250 more tons of sodium chloride per day were discharged from the reservoir than entered it.

One factor that locally may tend to introduce some error in the calculation of sodium chloride discharge by surface-water flow is the disposal of brines from oil and gas production which has taken place. These brines are drawn from deep bedrock sources and therefore are not part of the natural discharge of salts. Locally, in small drainages, this problem may be important, but it is believed that in the overall study it is not significant.

As may be seen from the map (fig. 1), there is a wide range in the amount of sodium chloride discharged in the surface water draining the various subbasins. The highest discharge is from the 253-mi^2 increment of the Salt Fork of the Brazos River between the gaging stations on Croton Creek and the upper Salt Creek gage. This small subbasin had an average yield of 670 tons of sodium chloride a day and a yield of 955 tons of sodium chloride per square mile per year in 1966. Even though this seems like a very large amount of solution, it would amount to only about half a foot in thickness of salt dissolved in 1,000 yr spread evenly over the 253 mi^2 of the subbasin. In this subbasin the salt-bearing beds crop out or occur at very shallow depth. Local recharge enters the slumped and broken formation, dissolves the salt, and moves underground to discharge at salt springs and seeps along the incised stream within tens of years. It is highly unlikely that any appreciable solution of salt takes place at depths of more than a few hundred feet, or extensively over the basin.

INDIVIDUAL DRAINAGE BASINS

The pattern of sodium chloride discharge is closely related to the geology and topography of the area. The broad valley of the Pecos River is deeply incised into the Permian beds and forms a ground-water drain downstream from Roswell; salt discharge below this point increases greatly. A major point of salt discharge is Malaga Spring, about 20 mi southeast of Carlsbad, where some 370 tons of sodium chloride a day is discharged. The ground-water divide east of the Pecos valley closely follows the outcrop of the Triassic rocks that cap the highlands. Very little recharge from precipitation is believed to occur in the badland escarpment east of the Pecos.

The Colorado River drainage is not deeply incised, and large parts of its upper basin do not contribute any appreciable flow. The 1,027 mi^2 of drainage basin that does contribute water above the Ira, Tex., gaging station discharged only 47 tons of sodium chloride per day, but the 455 mi^2 of drainage basin between the Ira and Colorado City gages contributes an additional 75 tons/d. The reason for this substantial contribution is that this short reach of the Colorado River at the edge of the High Plains is incised into salt-bearing Permian rocks that discharge saline ground water to the river.

The Brazos River is noted for its salinity. Very little flow or salt is contributed in the upper part of the drainage basin on the High Plains, but at the edge of the High Plains the Brazos River is deeply incised into the Permian rocks, and seeps and springs are numerous. It is here that we find the highest rate of sodium chloride discharge—as much as 955 tons $mi^{-2}\ yr^{-1}$.

The Trinity River originates at the edge of the High Plains, and although it has a fairly high sodium chloride load (400 tons/d), it amounts to only 17 tons $mi^{-2}\ yr^{-1}$ from the 8,146 mi^2 of its upper drainage basin.

In the Red River basin there is a zone of high sodium chloride discharge where the stream is deeply incised at the east edge of the High Plains. Although the areas of maximum sodium chloride discharge are shown as springs, only one, Estalline Spring on the Prairie Dog Town Fork, is a true spring; the rest are diffuse areas of seeps and minor spring discharge that cannot be considered point sources. As data on the areas contributing to the spring discharge were not available, the tons of sodium chloride dissolved per square mile per year were not calculated. The total amount of sodium chloride discharged by the drainage basin above Lake Texoma is more than 8,600 tons/d from an area of 24,846 mi^2 contributing flow.

The Canadian River has a large drainage basin, but the basin is narrow where it crosses the zone of salt discharge at the east edge of the High Plains, so that the river does not acquire a heavy sodium chloride load.

The Arkansas River, originating high in the mountains of central Colorado, has by far the largest drainage basin of those streams being considered. The sodium chloride load is low until it reaches south-central Kansas and Oklahoma, where there is major salt discharge from zones of seeps and springs. The sodium chloride discharge at the Great Salt Plain in Oklahoma is about 3,300 tons/d, and that at Big Salt Plain, about 50 mi to the west, totals 2,600 tons/d. These areas of brine discharge and other smaller areas of discharge are the northeastward continuation of the zone of brine discharge in the Brazos and Red Rivers and reflect the northeastward extension of the outcrop of salt-bearing Permian rocks.

Salt beds are present in central Kansas to the north and east, but there the salt is too deeply buried to be within the zone of circulation of the ground water. As a result, streams draining that area discharge relatively little sodium chloride, and much of this possibly results from brine disposal by the oil and gas industry in the past. It is estimated that more than 50 percent of the annual load of sodium chloride in the Walnut River near Winfield, Kan., consists of residual sodium chloride from past brine disposal. In 1966 this drainage basin discharged 168 tons of sodium chloride a day, which is 33 tons $mi^{-2}\ yr^{-1}$—a moderate rate compared to that from some other subbasins.

REFERENCES CITED

Cooper, J. B., 1962, Ground-water investigations of the Project Gnome area, Eddy and Lea Counties, New Mexico: U.S. Geol. Survey TEI-802, issued by U.S. Atomic Energy Comm. Tech. INF' Service, Oak Ridge, Tenn., 67 p., 17 figs.

Cooper, J. B., and Glanzman, V. M., 1971, Geohydrology of Project Gnome site, Eddy County, New Mexico: U.S. Geol. Survey Prof. Paper 712-A, 24 p.

McNeal, R. P., 1965, Hydrodynamics of the Permian Basin, *in* Fluids in subsurface environments—a symposium: Am. Assoc. Petroleum Geologists Mem. 4, p. 308–326.

Swenson, F. A., 1973, Dissolved salts in surface water, *in* Stability of salt in the Permian salt basin of Kansas, Oklahoma, Texas, and New Mexico: U.S. Geol. Survey open-file rept., p. 46–53.

U.S. Geological Survey, 1964, Quality of surface waters of the United States, 1962—Parts 7 and 8, Lower Mississippi River basin and western Gulf of Mexico basins: U.S. Geol. Survey Water-Supply Paper 1944, 645 p.

——1966, Quality of surface waters of the United States, 1963—Parts 7 and 8, Lower Mississippi River basin and western Gulf of Mexico basins: U.S. Geol. Survey Water-Supply Paper 1950, 635 p.

——1967, Quality of surface waters of the United States, 1961 Parts 7 and 8, Lower Mississippi River basin and western Gulf of Mexico basins: U.S. Geol. Survey Water-Supply Paper 1884, 590 p.

——1968, Quality Quality of surface waters of the United States, 1960—Parts 7 and 8, Lower Mississippi River basin and western Gulf of Mexico basins: U.S. Geol. Survey Water-Supply Paper 1755, 548 p.

——1969, Quality of surface waters of the United States, 1964—Parts 7 and 8, Lower Mississippi River basin and western Gulf of Mexico basins: U.S. Geol. Survey Water-Supply Paper 1957, 602 p.

——1970, Quality of surface waters of the United States, 1965—Parts 7 and 8, Lower Mississippi River basin and western Gulf of Mexico basins: U.S. Geol. Survey Water-Supply Paper 1964, 819 p.

——1971, Quality of surface waters of the United States, 1966—Parts 7 and 8, Lower Mississippi River basin and western Gulf of Mexico basins: U.S. Geol. Survey Water-Supply Paper 1994, 815 p.

Ward, P. E., 1963, Geology and ground-water features of salt springs, seeps, and plains in the Arkansas and Red River basins of western Oklahoma and adjacent parts of Kansas and Texas: U.S. Geol. Survey open-file rept., 82 p., 3 pls., 22 figs.

Williams, C. C., and Lohman, S. W., 1949, Geology and ground-water resources of a part of south-central Kansas: Kansas Geol. Survey Bull. 79, 455 p.

RECENT PUBLICATIONS OF THE U.S. GEOLOGICAL SURVEY

(The following books may be ordered from the Superintendent of Documents, Government Printing Office, Washington, DC 20402, to whom remittances should be sent by check or money order. Give series number, title, stock number shown in parentheses in this list, and catalog number shown in brackets)

Professional Papers

485-E. Historic flood information for northern California streams from geological and botanical evidence, by E. J. Helley and V. C. LaMarche, Jr. 1973. p. E1–E16; plate in pocket. $1.65. (2401-02414) [I 19:16:485-E]

574-E. Airborne chemical elements in Spanish moss, by H. T. Shacklette and J. J. Connor. 1973. p. E1–E46. $1.25. (2401-02456) [I 19:16:574-E]

743-C. *Complexiopollis* pollen lineage in Mississippi Embayment rocks, by R. H. Tschudy. 1973. p. C1–C15; 9 plates showing fossils. $1.15. (2401-00345) [I 19:16:743-C]

773. Geologic structures in the Gulf of Mexico basin, by L. E. Garrison and R. G. Martin, Jr. 1973. 85 p.; plate in pocket. $2.95. (2401-00366) [I 19:16:773]

784. Early Paleozoic brachiopods of the Moose River synclinorium, Maine, by A. J. Boucot. 1973. 81 p.; 23 plates showing fossils. $3.20. (2401-00325) [I 19:16:784]

802-A. Principles and measuring techniques of turbulence characteristics in open-channel flows, by R. S. McQuivey. 1973. p. A1–A82. $1.80. (2401-02405) [I 19:16:802-A]

808. Paleontology and stratigraphy of the Rabbit Hill Limestone and Lone Mountain Dolomite of central Nevada, by C. W. Merriam. 1973. 50 p.; 12 plates showing fossils. $1.75 (2401-02379) [I 19:16:808]

809-B. Location and characteristics of the interface between brine and fresh water from geophysical logs of boreholes in the upper Brazos River basin, Texas, by W. S. Keys and L. M. MacCary. 1973. p. B1–B23. 75¢. (2401-02410) [I 19:16:809-B]

812-A. A photometric technique for determining planetary slopes from orbital photographs, by W. J. Bonner and R. A. Schmall. 1973. p. A1–A16. 40¢. (2401-02409) [I 19:16:812-A]

818-A. Hydrothermal alteration associated with beryllium deposits at Spor Mountain, Utah, by D. A. Lindsey, Harold Ganow, and Wayne Mountjoy. 1973. p. A1–A20. 75¢. (2401-02401) [I 19:16:818-A]

822. Water resources of the Delmarva Peninsula, by E. M. Cushing, I. H. Kantrowitz, and K. R. Taylor. 1973. 58 p.; text and plates in case. $12.10. (2401-02412) [I 19:16:822]

825. Ostracodes from Lower Devonian formations in Alaska and Yukon Territory, by J. M. Berdan and M. J. Copeland. 1973. 47 p.; 14 plates showing fossils. $1.75. (2401-02407) [I 19:16:825]

Bulletins

1304. Mineral resources of the Idaho Primitive Area and vicinity, Idaho, by F. W. Cater, D. M. Pinckney, W. B. Hamilton, R. L. Parker, R. D. Weldin, T. J. Close, and N. T. Zilka, *with a section on the* Thunder Mountain district, by B. F. Leonard, *and a section on* Aeromagnetic interpretation, by W. E. Davis. 1973. 431 p.; plates in pocket. $4.65. (2401-02434) [I 19:3:1304]

1305. A geochemical reconnaissance for gold in the sedimentary rocks of the Great Lakes region, Minnesota to New York, by D. A. Seeland. 1973. 16 p. 35¢. (2401-02411) [I 19:3:1305]

1358. Geology of the Istarú quadrangle Costa Rica, by R. D. Krushensky. 1972 (1973). 46 p.; plates in pocket. $2.00. (2401-00263) [I 19:3:1358]

1385-A. Mineral resources of the Chiricahua Wilderness area, Cochise County, Ariz., by Harald Drewes and F. E. Williams, *with a section on* Aeromagnetic interpretation, by G. P. Eaton. 1973. p. A1–A53; plate in pocket. $1.35. (2401-02425) [I 19:3:1385-A]

1394-B. Sturgis formation (Upper Pennsylvanian), a new map unit in the western Kentucky coal field, by T. M. Kehn. 1973. p. B1–B24. 35¢. (2401-02408) [I 19:3:1394-B]

1394-E. The Auld Lang Syne Group of Late Triassic and Jurassic(?) age, north-central Nevada, by D. B. Burke and N. J. Silberling. 1973. p. E1-E14. 35¢. (2401-02431) [I 19:3:1394-E]

Water-Supply Papers

1817-E. Fractionation and characterization of natural organic matter from certain rivers and soils by free-flow electrophoresis, by J. A. Leenheer and R. L. Malcolm. 1973. p. E1-E14. 35¢. (2401-02400) [I 19:13:1817-E]

1974. Water resources of the New Jersey part of the Ramapo River basin, by John Vecchioli and E. G. Miller. 1973. 77 p.; plates in pocket. $2.35. (2401-02417) [I 19:13:1974]

2024. Water resources of the Big Sioux River valley near Sioux Falls, S. Dak., by D. G. Jorgensen and E. A. Ackroyd. 1973. 50 p.; plate in pocket. $2.05. (2401-02413) [I 19:13:2024]

2025. Glossary of selected terms useful in studies of the mechanics of aquifer systems and land subsidence due to fluid withdrawal, by J. F. Poland, B. E. Lofgren, and F. S. Riley. 1972. 9 p. 25¢. (2401-00228) [I 19:13:2025]

2029-C. Use of finite-difference arrays of observation wells to estimate evapotranspiration from ground water in the Arkansas River valley, Colorado, by E. P. Weeks and M. L. Sorey. 1973. p. C1-C27. 50¢. (2401-02451) [I 19:13:2029-C]

2034. Cost analysis of ground-water supplies in the North Altantic Region, 1970, by D. J. Cederstrom. 1973. 48 p. 60¢. (2401-02428) [I 19:13:2034]

U.S. GOVERNMENT
PRINTING OFFICE
PUBLIC DOCUMENTS DEPARTMENT
WASHINGTON, D.C. 20402